Cape Peninsula
University of Technology

Ultrasensitive silver-gold bimetallic interdigitated array sensor for detection of *Escherichia coli* and *Salmonella typhimurium*

By

CALLEB OTIENO DUYA

B. Ed. (Masinde Muliro University of Science and Technology, Kenya), M. Sc. (Kenyatta University, Kenya)

Thesis submitted in fulfilment of the requirements for the degree

Doctor of Philosophy: (Chemistry)

In the Faculty of Applied Sciences

Department of Chemistry

Supervisor: Prof. M. C. Matoetoe

External supervisor: Dr. F. O. Okumu

MARCH, 2023

DECLARATION

I, **Calleb Otieno Duya**, solemny declares that the contents of this thesis represent my own unaided work, and that this thesis has not been previously submitted for any academic examination and awards in any other University or institution. Furthermore, it represents my own scientific thoughts and opinions and not necessarily those of the Cape Peninsula University of Technology, Cape Town, South Africa.

Signed......**Date**..... **08/03/2023**

ACKNOWLEDGEMENT

First and foremost, I sincerely thank the Almighty God for His protection in the period over which I carried out this study. To my principal supervisor and academic mentor; Prof. Mangaka Clara Matoetoe, I thank you so much for the continuous and thorough evaluation of this work as well as honouring my humble request to work in this project under your supervision. The completion of this study would not have been successful without your continuous encouragement, guidance and motivation. I also want to sincerely and graciously thank you for the patience and continuous assistance you offered me upto the very end of this project. To my co-supervisor: Dr. Fredrick Oluoch Okumu of Jaramogi Oginga Odinga University of Technology, Kenya, thank you so much for the facilitation that ensured successful commencement and completion of this study. May the Almighty God Bless you abundantly. Much appreciation also goes to the laboratory technician: Mmabatho Mobo, Department of Nature conservation, and Letlotlo Nyenye, Department of Food Science and Technology, Cape Peninsula University of Technology, for providing *Escherichia coli* and *S. typhimurium* strains, respectively which ensured successful completion of this work. To the electrochemistry Research group colleagues; your moral support and motivation are highly appreciated. To the Water Research Commission (WRC), South Africa; Thank you very much for the financial assistance and support you offered me through my principal supervisor. To Cape Peninsula University of Technology (CPUT); your support towards the completion of this study is highly appreciated. Last but not least; much appreciation goes to my dear family led by Lucy Saisi Otieno (my wife), my siblings: Benard Odhiambo Duya, Paul Onyango Duya, Barrack Okoth Miniga, Christopher Onyango Miniga, Jacob Oluoch Miniga, Stephen Okuku Miniga, Sarah Miniga, Duncan Odiwuor Miniga: my friends: Dr. Olabode, Dr. Babatunde Oladipo, Dr. Jean and Mr. Uchenna Okwuosa for the continuous love and care during the period of my study in CPUT. This is highly appreciated. Thank you so much and may the Almighty God Bless you.

DEDICATION

This work is dedicated to the Almighty God, me, my dear wife Lucy Saisi Otieno and the entire Duya and Miniga families. I would not have done it without your continuous love and moral support. To Dr. Fredrick Okumu, your tremendous effort is highly appreciated, thank you so much and may God bless you abundantly. To my late academic mentors; mother, father: Benter Akinyi Duya, Joseph Duya Omollo, and the late guardians: Phoebe Akumu Miniga and Tom Miniga Olwayo thank you very much for the support and the hard academic times we shared while alive.

RESEARCH OUTPUTS

1 Conference presentations

(i) **Duya C. O.**[a]; F.O. Okumu[b]; M. C. Matoetoe[c*](2021). Title: *Ultrasensitive electrochemical nano-collision technique for Escherichia coli* O157:H7 *detection using electrochemical impedance spectroscopy*. Annual Postgraduate Conference 2021 Cape Peninsula University of Technology, Cape Town, South Africa, 31st**,** November, 2021 (**Oral presentation**).

(ii) **Duya C. O**.[a]; F.O. Okumu[b]; M. C. Matoetoe[c*](2021). Title: *Ultrasensitive electrochemical nano-collision technique for Escherichia coli* O157:H7 *detection using electrochemical impedance spectroscopy*. 10th South African Nanotechnology Initiative (SANI) annual nano-sciences Young Researchers' Symposium, 7th and 8th, October, 2021 **(Oral presentation).**

2. Publications

(i) C.O. Duya, F.O. Okumu, M.C. Matoetoe, Impedimetric nano-collision *Escherichia coli* analysis based on Silver-Gold bimetallic nanoparticles, *Bioelectrochemistry*, Volume 151, 2023, 108403, ISSN 1567-5394, https://doi.org/10.1016/j.bioelechem.2023.108403

ABSTRACT

The main objective of this study was to optimize, develop and validate bimetallic silver (Ag) - gold (Au) interdigitated nano-array sensor for ultra-sensitive detections of *Escherichia coli* (*E. coli*) and *Salmonella typhimurium (S. typhimurium*). The bimetallic Ag-Au (1:2) nanoparticles (NPs) were successfully synthesized via chemical and electrochemical methods as confirmed by the presented spectroscopic and electrochemical data. The electrochemical properties of chemically and electrochemically synthesized NPs films formed by drop-coating and electro-deposition methods, respectively were studied via cyclic (CV) and differential pulse voltammetry (DPV). Chemically modified GCE/Ag-Au (1:2) NPs film showed enhanced electron transfer coefficient (α), heterogeneous rate constant (k_s), electrode surface coverage (Γ) and diffusion coefficient (D) of 0.02, 0.01 s^{-1}, 7.00 × 10^{-11} molescm^{-2}and 7.34 × 10^{-7} cm^2s^{-1}, respectively compared to the electro-deposited NPs films. The optical and morphological properties of chemically synthesized NPs were investigated via UV-visible, FT-IR, XRD and SEM techniques. The *zeta* potential (mV) of pure bimetallic Ag-Au (1:2) NPs, untreated bacteria and their complexes with *E. coli* and *S. typhimurium* ranged between -4.34 ± 0.71 for the bimetallic NPs and -17.30 ± 0.89 for *S. typhimurium* - bimetallic Ag-Au (1:2) NPs complex. The electrochemical interactions between chemically synthesized NPs and each of the bacterium on GCE and interdigitated array electrode (IDAE) were sequentially carried out in 0.1 M PBS (pH 7.4) for sensor fabrication. The bacterium - NPs interaction studies were investigated using UV-visible, CV, DPV and EIS techniques and found to be mainly dependent on bacterial concentrations, bacteria-NPs interaction time and NPs concentrations. The UV-visible and electrochemical experiments showed blue-and negative-shifts, respectively compared to responses from the NPs, an indicative of complex formation. The electrochemical kinetic parameters determined for GCE - bacteria - NPs interactions were D (4.90 × 10^{-15} cm^2s^{-1}) and k_s (1.55 × 10^{-11} s^{-1}) for *E. coli* and D (9.13 × 10^{-4} cm^2s^{-1}) and k_s (1.54 s^{-1}) for *S. typhimurium*. The IDAE-bacteria-NPs interactions kinetic parameters determined were D (4.71 × 10^{-15} cm^2s^{-1}) and k_s (1.53 × 10^{-11}) for *E. coli* while those for *S. typhimurium* were D (5.12 ×10^{-2} cm^2s^{-1}) and k_s (0.88). Sensor's methodology was optimized for applied potential, AC amplitude, supporting electrolyte concentration and the choice of electro-analytical technique which was based on sensitivity. The optimum conditions chosen for nano-impact detections of *E. coli* using IDAE were: NPs volume (500 µL), NPs - *E. coli* incubation period (4 minutes), PBS concentration (0.1 M), AC amplitude (5 mV) and applied

potential (+0.1 V) while those obtained for *S. typhimurium* included: NPs volume (600 µL), NPs - *E. coli* incubation period (5 minutes), PBS concentration (0.1 M), AC amplitude (10 mV) and applied potential (+0.5 V). The IDAE nano-impact sensor integrated with EIS technique showed enhanced sensitivity ($\mu L \Omega^{-1} cell^{-1}$) for detections of *E. coli* (1.64×10^{-5}) and *S. typhimurium* (1.37×10^{-5}) compared to DPV technique. The IDAE nano-impact sensors for both bacteria had significantly lower LOD (10^{1} cells μL^{-1}) and LOQ (10^{2} cells μL^{-1}) for *E. coli*, and LOD of (10^{1} cells μL^{-1}) and LOQ (10^{3} cells μL^{-1}) for *S. typhimurium*. These low LOD and LOQs coupled with higher % recoveries (95.18 ± 2.50 - 100.00 ± 0.76) and (100.60 ± 0.58 - 116.02 ± 0.15) for *E. coli* and *S. typhimurium*, respectively showed that the developed nano-impact sensors for the bacteria were accurate and precise.

Table of Contents

DECLARATION ii
ACKNOWLEDGEMENT iii
DEDICATION iv
RESEARCH OUTPUTS v
ABSTRACT vi
LIST OF FIGURES xiii
LIST OF TABLES xvii
APPENDICES xviii
GLOSSARY xix
1. CHAPTER ONE 1
BACKGROUND STUDY OF THE RESEARCH 1
1.0 Summary 1
1.1. Introduction 1
1.2. Research Problem 3
1.3. Aims and objectives of the study 4
1.4 Preface 4
1.5 References 5
2. CHAPTER TWO 9
LITERATURE REVIEW 9
2.0 Summary 9
2.1. Bacteria 9
2.1.1. *Escherichia coli and Salmonella* 10
2.2. Methods of Bacterial Detection 10
2.2.1. Conventional methods 10
2.2.2 Use of nanoparticles 11
2.3 Sensors 13
2.3.1 Electrochemical sensors 14
2.4 Conclusion 20
2.5 References 21
3. CHAPTER THREE 26
SYNTHESIS AND CHARACTERIZATION OF NANOPARTICLES 26

3.0 Summary 26
3.1 Introduction 26
3.2 Experimental 30
3.2.1 Reagents and materials 30
3.2.2 Synthesis of monometallic nanoparticles 30
3.2.3 Synthesis of bimetallic nanoparticles 31
3.3 Characterization of nanoparticles 31
3.3.1 Fourier Transform-Infra-red (FT-IR) 31
3.3.2 Ultraviolet-visible (UV-Vis) 31
3.3.3 Scanning electron microscopy (SEM) 32
3.3.4 X-ray diffraction (XRD) 32
3.4 Results and Discussion 32
3.4.1 FT-IR studies of the nanoparticles 32
3.4.2 Optical properties of nanoparticles 34
3.4.3 Scanning electron microscopy (SEM) 37
3.4.4 X-Ray diffraction (XRD) analysis 39
3.5 Conclusion 40
3.6 References 41
4. CHAPTER FOUR 47
COMPARATIVE ELECTROCHEMICAL PROPERTIES OF BIMETALLIC SILVER-GOLD FILM BY DROP-COATING AND ELECTRO-DEPOSITION 47
4.0 Summary 47
4.1 Introduction 47
4.2 Experimental 49
4.2.1 Electrode cleaning and electro-deposition of nanoparticles 49
4.2.2 Chemical modification of GCE through drop-coating 50
4.2.3 Electrochemical characterization of modified GCE nano-films 50
4.3 Results and Discussion 51
4.3.1 Electro-deposition of nanoparticles 51
4.3.2 Electrochemical properties of modified nano-films 53
4.3.3 Determination of kinetic parameters for modified GCE nano-films 57
4.4 Conclusion 62
4.5 References 63

5. CHAPTER FIVE 67
DEVELOPMENT OF AN ELECTROCHEMICAL NANO-IMPACT SENSOR FOR *Escherichia coli* USING GLASSY CARBON AND INTERDIGITATED ARRAY ELECTRODES 67
5.0 Summary 67
5.1 Introduction 67
5.2 Experimental 69
5.2.1 Reagents and materials 69
5.2.2 Culture preparation 69
5.2.3 *Zeta* potential determination 69
5.2.4 Optical interaction studies using UV-visible spectroscopy 70
5.2.5 Fabrication of GCE sensor 70
5.2.6 Fabrication of IDAE sensor 71
5.3 Results and Discussion 72
5.3.1 *Zeta* potential 72
5.3.2 Optical interaction studies using UV-visible spectroscopy 73
5.3.3 Electrochemical studies of bacteria-NPs interactions using GCE 77
5.3.4 Effect of supporting electrolyte concentration on bacteria-NPs interactions 79
5.3.5 Choice of electro-analytical technique for *E. coli* detection using GCE 80
5.3.6 Determination of electron transfer kinetics parameters 81
5.3.7 Optimization of applied potential and AC amplitude 88
5.3.8 Determination of linearity and applicability of GCE nano - impact sensor 88
5.4 Validation of GCE nano-impact sensor 89
5.4.1 Repeatability, reproducibility, stability and selectivity studies 89
5.4.2 Recovery studies 92
5.4.3 Practical application of the sensor 93
5.5 Bacteria-NPs interaction studies using IDAE 93
5.5.1 Determination of electron transfer kinetic parameters 95
5.5.2 Optimization of applied potential and AC amplitude 98
5.5.3 Determination of sensor's linearity and applicability 99
5.6 Validation of IDAE sensor 100
5.6.1 Repeatability, reproducibility, stability and selectivity studies 100
5.6.2 Recovery studies 101
5.7 Conclusion 102

5.8 References 102
6. CHAPTER SIX 109
DEVELOPMENT OF AN ELECTROCHEMICAL NANO-IMPACT SENSOR FOR *Salmonella typhimurium* USING GLASSY CARBON AND INTERDIGITATED ARRAY ELECTRODES 109
6.0 Summary 109
6.1 Introduction 109
6.2 Experimental 110
6.2.1 Reagents and Materials 110
6.2.2 Culture preparation 110
6.2.3 *Zeta* potential determination and optical interaction studies 111
6.2.4 Fabrication of GCE nano-impact sensor for *S. typhimurium* 111
6.2.5 Fabrication of IDAE nano-impact sensor for *S. typhimurium* 112
6.3 Results and Discussion 113
6.3.1 *Zeta* potential 113
6.3.2 Optical interaction studies using UV-visible spectroscopy 113
6.3.3 Electrochemical interaction studies using GCE 116
6.3.4 Effects of supporting electrolyte concentration 120
6.3.5 Choice of electro-analytical technique for detection of *S. typhimurium* 120
6.3.6 Determination of electron transfer kinetics parameters 121
6.3.7 Optimization of applied potential and AC amplitude for detection of *S. typhimurium* .125
6.3.8 Determination of linearity and applicability of the nano-impact sensor 126
6.4 Sensor validation 127
6.4.1 Repeatability, reproducibility, stability and selectivity studies 127
6.4.2 Recovery studies 129
6.4.3 Application of the nano-impact sensor to real sample analysis 130
6.5 Bacteria-NPs interaction studies using IDEA 130
6.5.1 Determination of electron transfer kinetic parameters 132
6.5.2 Optimization of NPs-bacteria incubation period and NPs concentration 134
6.5.3 Optimization of AC amplitude and applied potential for detection of *S. typhimurium* using IDAE 135
6.5.4 Determination of analytical performance parameters 136
6.6 Validation of IDAE nano-impact sensor 138

6.6.1 Reproducibility and repeatability studies 138
6.6.2 Stability studies of the sensor 138
6.6.3 Selectivity studies of the sensor 138
6.6.4 Recovery studies 139
6.7 Conclusion 139
6.8 References 140
7. CHAPTER SEVEN 144
7.1 Conclusion 144
7.2 Future work and Recommendations 145
8. Appendices 147

LIST OF FIGURES

Figure 2.1: Nanomaterials reported for (a) *E. coli* and (b) *S. typhimurium* sensing (2009-2022) ...11
Figure 2.2: Electrochemical sensors components and mechanisms; (a) Nano-film sensor (b) Nano-impact sensor 14
Figure 2.3: Analysis of bio-receptors used for (a) *E. coli* and (b) *S. typhimurium* detections in the past decade 16
Figure 2.4: Analysis of electro-analytical techniques for (a) *E. coli* and (b) *S. typhimurium* detections in the past decade (2009-2022) 18
Figure 3.1: Methods of nanoparticle synthesis 26
Figure 3.2: Main advantages of chemical method. 28
Figure 3.3: Characterization techniques for nanoparticles 29
Figure 3.4: FT-IR spectroscopy for (a) Ag NPs, (b) Au NPs and bimetallic Ag-Au (1:2) NPs 33
Figure 3.5: UV-visible absorption spectra of Ag NPs (curve a), Au NPs (curve b) and (Ag-Au (1:2) bimetallic NPs (curve c) 34
Figure 3.6: Variation of $(\alpha h\nu)^2$ with $h\nu$ for Ag NPs, Au NPs and Ag-Au (1:2) NPs as a function of wavelength (λ) at n =1/2 36
Figure 3.7: Scanning electron micrographs of (a) Ag NPs, (b) Au NPs and (c) Ag-Au (1:2) NPs with their corresponding diameter histograms. 38
Figure 3.8: XRD patterns of (a) Au NPs (b) Ag NPs and (c) bimetallic Ag-Au (1:2) NPs, respectively 39
Figure 4.1: Current-time (I-t) transient curves for electro-deposition of (a) Ag NPs, (b) Au NPs and (c) Ag-Au (1:2) NPs onto GCE versus Ag/AgCl 52
Figure 4.2: CVs and DPVs of DCT (**Red**) and corresponding EDP (**Blue**) (a) GCE/Ag NPs, (b) GCE/Au NPs and (c) GCE/Ag-Au (1:2) bimetallic NPs in 0.1 M HCl vs. Ag/AgCl: Scan rate: 30 mVs^{-1} 54
Figure 4.3: Scan rate studies of (a) DCT and (b) EDP GCE/Ag NPs, and corresponding (c) *Randle's* and (d) *Laviron's* plots; scan rate: 10-130 mVs^{-1} in 0.1 M HCl vs. Ag/AgCl 59
Figure 4.4: Scan rate studies of (a) DCT and (b) EDP GCE/Au NPs, and corresponding (c) *Randle's* and (d) *Laviron's* plots; scan rate: 10-130 mVs^{-1} in 0.1 M HCl vs. Ag/AgCl 60
Figure 4.5: Scan rate studies of (a) DCT and (b) EDP GCE/Ag-Au (1:2) NPs, and corresponding (c) *Randle's* and (d) *Laviron's* plots; scan rate: 10-130 mVs^{-1} in 0.1 M HCl vs. Ag/AgCl 61

Figure 5.1: Interdigitated array electrode (IDAE) 72
Figure 5.2: UV-visible spectra of (a) Ag NPs, (b) Au NPs (c) Ag-Au (1:2) NPs in the absence and presence of varying concentrations of *E. coli* (cellsmL^{-1}); 74
Figure 5.3: UV-visible spectra of interaction time between (a) Ag NPs, (b) Au NPs, (c) Ag-Au (1:2) NPs and same concentration of *E.coli* (8.0 ×10^{1} cellsmL^{-1}); Plots of bacteria-NPs interaction time versus absorbance (**insets**); 76
Figure 5.4: Overlays of CVs and DPVs of —— 0.1 M PBS —— *E. coli* —— NPs + 0.1 M PBS —— NPs + *E. coli* 78
Figure 5.5: Effects of (a) bacteria - bimetallic Ag-Au (1:2) NPs incubation period and (b) concentration of bimetallic Ag-Au (1:2) NPs on bacteria-bimetallic NPs interactions studied using EIS technique 79
Figure 5.6: Optimization of PBS concentration for *E. coli* - NPs interaction studies using DPV ... 80
Figure 5.7: (a) Cyclic voltammogram; (b) differential pulse voltammogram; (c) Nyquist plot; and (d) Sensitivity values for Ag-Au (1:2) NPs-*E. coli* interaction studies using CV and DPV techniques 81
Figure 5.8: (a) Effects of various CV scan rates on bacterial oxidation peak current intensity; (b) *Laviron's* plot (c) *Randle's* plot, (d) Bode plots and (e) *Randle's* equivalent circuit; R_s (Solution resistance), R_{ct} (charge transfer resistance), Z_w (Warburg impedance) 83
Figure 5.9: Proposed mechanism for the interaction between *E. coli* and Ag-Au (1:2) NPs 87
Figure 5.10: Variation of (a) AC amplitude, (b) Applied potential for Ag-Au (1:2) NPs-*E. coli* interaction studies 88
Figure 5.11: a) Nyquist plot and (b) corresponding calibration plot for interactions between Ag-Au (1:2) NPs and logarithm of *E. coli* concentrations (C). 89
Figure 5.12: Proposed sensor's (a) Repeatability; (b) Stability; and (c) Selectivity studies based on Nyquist plots 91
Figure 5.13 : Cyclic voltammograms of Ag-Au (1:2) NPs in the absence (a) and presence (b) of *E. coli* in 0.1 M PBS at pH 7.4, scan rate; 0.03 Vs^{-1} 94
Figure 5.14 : Effects of (a) *E. coli*-Ag-Au (1:2) NPs incubation period and (b) concentration of bimetallic Ag-Au (1:2) NPs on bacteria-bimetallic NPs interactions studied using EIS technique 95

Figure 5.15 : (a) CV scan rates studies of *E. coli*-Ag-Au (1:2) NPs interactions (b) *Laviron's* plot (c) *Randle's* plots (c) Bode plots (e) *Randle's* equivalent circuit for the interaction studies between *E. coli* and Ag-Au (1:2) NPs.....96
Figure 5.16 : Variation of (a) AC amplitude, (b) Applied potential for interaction studies between Ag-Au (1:2) NPs and *E. coli* using IDAE.....98
Figure 5.17: a) Nyquist plot for interactions between Ag-Au (1:2) NPs and varying concentrations of *E. coli*; b) Calibration plot for ΔR_{ct}^{-1} versus logarithm C of *E. coli*; c) corresponding *Randle's* equivalent circuit. 100
Figure 5.18 : Selectivity studies of the developed nano-impact sensor based on the Nyquist plot101
Figure 6.1: UV-visible spectra of (a) Ag NPs, (b) Au NPs (c) Ag-Au (1:2) NPs in absence and presence of varying concentrations of *S. typhimurium* (cellsmL^{-1}).....114
Figure 6.2: UV-visible spectra of interaction time between (a) Ag NPs, (b) Au NPs, (c) Ag-Au (1:2) NPs and same concentration of *S. typhimurium* (8.0 $\times 10^{1}$ cellsmL^{-1}); Plots of bacteria-NPs interaction time versus absorbance (**insets**).....116
Figure 6.3: Overlays of CVs and DPVs of **0.1 M PBS ST NPs + 0.1 M PBS NPs + ST** and **Ag NPs + ST Au NPs + ST Ag-Au (1:2) NPs + ST** , respectively in 0.1 M PBS at pH 7.4, Scan rate; 0.03 Vs^{-1}. (a) Ag NPs, (b) Au NPs, (c) Ag-Au (1:2) NPs.....118
Figure 6.4: Effects of (a) incubation period (b) concentrations of Ag-Au (1:2) NPs on interaction between *S. typhimurium* (ST) and Ag-Au (1:2) NPs in 0.1 M PBS at pH 7.4 studied using EIS technique 119
Figure 6.5: Optimization of PBS concentration for nano-impact detection of *S. typhimurium* (ST) 120
Figure 6.6: (a) CV, (b) DPV, (c) Nyquist plot (inset) and (d) determined sensitivities for Ag-Au (1:2) NPs-ST interaction studies using CV and DPV techniques 121
Figure 6.7: (a) Effects of CV scan rates on ST oxidation peak current intensity (b) *Laviron's* plots (c) *Randle's* plots (d) Bode plots (e) *Randle's* equivalent circuit (REC) for Ag-Au (1:2) NPs-ST interactions in 0.1 M PBS, pH 7.4.....122
Figure 6.8: Proposed mechanism of interaction between Ag-Au (1:2) NPs and *S. typhimurium*..124
Figure 6.9: Variation of (a) AC amplitude, (b) Applied potential for Ag-Au (1:2) NPs-ST interaction studies.....126

Figure 6.10: a) Nyquist plot (b) calibration plots for the interactions between Ag-Au (1:2) NPs and varying ST concentrations (cells mL^{-1}) 127
Figure 6.11: Nyquist plots for (a) repeatability; (b) stability; and (c) selectivity studies of the developed sensor 129
Figure 6.12: Cyclic voltammogram of Ag-Au (1:2) NPs in the absence and presence of ST in 0.1 M PBS at pH 7.4, Scan rate; 0.03 Vs^{-1} 130
Figure 6.13: (a) CV scan rates studies on ST oxidation peak current, (b) *Laviron's* plot (c) *Randle's* plot (d) Bode plots (e) *Randle's* equivalent circuit for the interactions between Ag-Au (1:2) NPs and ST. 133
Figure 6.14: Effects of (a) Ag-Au (1:2) NPs concentration, (b) Ag-Au (1:2) NPs-ST incubation period on bacteria-bimetallic Ag-Au (1:2) NPs interaction studies using IDAE.....135
Figure 6.15: Variation of (a) AC amplitude, (b) Applied potential for the interaction between *S. typhimurium* and Ag-Au (1:2) NPs in 0.1 M PBS studied using IDAE 136
Figure 6.16: (a) Nyquist plot for interactions between Ag-Au (1:2) NPs and varying concentrations (cellsμL^{-1}) of *S. typhimurium*; (b) Calibration plot of ΔR_{ct}^{-1} versus logarithm of *S. typhimurium* concentrations; (c) Corresponding Randle's equivalent circuit. 137
Figure 6.17: Selectivity studies of the sensor.....139

LIST OF TABLES

Table 2.1: Differences between nano-impact and nano-film sensors.....15
Table 4.1: Electrochemical band gaps of drop-coated and electrodeposited Ag, Au and Ag-Au (1:2) NPs.....56
Table 4.2: Electrochemical kinetic parameters of drop-coated (DCT) and electro-deposited (EDP) nano-films determined from *Randle's* and *Laviron's* equations.....58
Tabe 5.1: *Zeta* (ζ) potential of NPs, untreated bacteria and bacteria-NPs complexes (n = 3).....73
Table 5.2: Electrochemical kinetic parameters for interactions between Ag-Au (1:2) NPs and *E. coli* in 0.1 M PBS, at pH 7.4.....83
Table 5.3: Comparison of reported nano-impact electrochemical detection strategies for *E. coli* with the developed method.....92
Table 6.1: *Zeta* (ζ) potential of untreated bacteria and the complexes of NPs and bacteria.....113
Table 6.2: Electrochemical kinetic parameters for interactions between Ag-Au (1:2) NPs and *S. typhimurium* in 0.1 M PBS, at pH 7.4.....123
Table 6.3: Electrochemical kinetic parameters for interactions between Ag-Au (1:2) NPs and ST on IDAE in 0.1 M PBS, at pH 7.4.....133

APPENDICES

Appendix I: Optimization of PBS concentration for (a) *E. coli* and (b) *S. typhimurium* nano-impact detections using EIS technique……147

Appendix II: Electrochemical parameters from the circle fitting and modeling of EIS data for the interaction between Ag-Au (1:2) NPs and varying concentrations (cells mL^{-1}) of *E. coli* in 0.1 M PBS, pH 7.4 using GCE……..... …147

Appendix III: Determination of concentration of *E. coli* and *S. typhimurium* in River and Ocean water samples using standard addition method (n = 3)……148

Appendix IV: Standard calibration curve for determination of *E. coli* in Liesbeek River water samples from Kirstenbosch Botanical Garden, Cape Town, South Africa……149

Appendix V: Standard calibration curve for determination of *E. coli* in Liesbeek River water samples collected from Rondebosch, Cape Town, South Africa……150

Appendix VI: Standard calibration curve for determination of *E. coli* in water samples collected from Atlantic Ocean, Cape Town, South Africa……151

Appendix VII: Electrochemical parameters from circle fitting and simulation of EIS data for the interactions between bimetallic Ag-Au (1:2) NPs and varying concentrations of *S. typhimurium* in 0.1 M PBS, pH 7.4 using GCE…….152

Appendix VIII: Electrochemical parameters from the circle fitting and modeling of EIS data for the interaction between Ag-Au (1:2) NPs and varying concentrations of *E. coli* (cells μL^{-1}) in 0.1 M PBS, pH 7.4 using IDAE……152

Appendix IX: Electrochemical parameters from the circle fitting and modeling of EIS data for the interaction between Ag-Au (1:2) NPs and varying concentration (cellsμL^{-1}) of *S. typhimurium* in 0.1 M PBS, pH 7.4 using IDAE……152

GLOSSARY

Abbreviations/Acronyms	Definition
BHI	Brain Heart Infusion
CA	Chrono-amperometry
CV	Cyclic voltammetry
CFU	Colony Forming Unit
DAEC	Diffusely Adherent *E. coli*
DPV	Differential Pulse Voltammetry
EIS	Electrochemical Impedance Spectroscopy
EET	Extracellular Electron transfer
GCE	Glassy Carbon Electrode
HUS	Haemolytic Uremic Syndrome
IDAEs	Interdigitated Array electrodes
LPS	Lipopolysaccharides
NIE	Nano-impact Electrochemistry
NPs	Nanoparticles
PBS	Phosphate Buffer Solution
REC	*Randle's* Equivalent Circuit
RMS	Root mean square
SEM	Scanning Electron Microscopy
ST	*Salmonella typhimurium*
SWV	Square Wave voltammetry
LOD	Limit of Detection
LOQ	Limit of Quantification
XRD	X-ray diffraction
UV	Ultraviolet

CHAPTER ONE

BACKGROUND STUDY OF THE RESEARCH

1.0 Summary

This chapter presents the background information of *Escherichia coli* (*E. coli*) and *Salmonella typhimurium* (*S. typhimurium*) with a brief literature review on their economic effects and most commonly used detection methods. The chapter also gives a synopsis on the development of electrochemical nano-detection techniques for the bacteria employing nano-impact electrochemistry (NIE). The research problem, justification, aims and objectives of the study are also highlighted in this chapter.

1.1. Introduction

Pathogenic bacteria commonly exist in water and food (Barak & Schroeder, 2012). *E. coli* and *S. typhimurium* are the most commonly studied pathogenic Gram negative bacteria due to their enhanced virulence and pathogenicity (Peng *et al*., 2018). *E. coli* cells of between 10^1 to 10^2 cells mL^{-1} induce *shiga*-toxin infections in humans (Nawrocki *et al*., 2020). Various studies on infectious doses of *S. typhimurium* have also been reported (Habimana *et al.*, 2018). The infections due to these bacteria have globally led to about 1.27 million fatalities especially among children under the age of 5 years (Murray *et al*., 2022). *E. coli* is always used as an indicator of faecal contamination and its presence shows heightened risk of availability of *S. typhimurium* (Lin & Ganesh, 2013). There is no confirmed cure for *shiga*-toxin and salmonellosis infections and the use of antibiotics has been reported to increase the risk of contracting haemolytic uremic syndrome (HUS) and haemorrhagic colitis diseases due to antibiotic resistance (Freedman *et al*., 2016). The prevalence of *E. coli* and *S. typhimurium* infections, their species and serotype multiplicities as well as emergence of related opportunistic pathogens in water sources they infest make their rapid, sensitive and selective detections challenging task to researchers (Plaza *et al*., 2018). In most cases, their detection levels are lower than the detection limits of most available techniques due to the low number of cells in sample matrices analysed (Niessen *et al*., 2013). Therefore, rapid, robust, selective, multiplex and miniaturized ultra-sensitive on-site detection devices are highly needed. Culture-based techniques have continued being the ‘gold standard’ for the detections of *E.*

coli and *S. typhimurium* (Hilton *et al.*, 2016). These methods are, however, time-consuming, labour intensive and require sophisticated laboratory set-ups (Zhang & Miller, 2019).

Electrochemical sensors have significantly attracted attention of most researchers in the recent past for the detections of these bacteria due to their simplicity, rapidity, sensitivity, miniaturization capability and amenability towards integration into automated and low-cost devices using nanotechnology (Arora & Siddiqui, 2018). However, their use in the detection of bacterial cells in complex sample matrices has faced many challenges in the recent past because most of these devices require larger volumes of samples and reagents hence unable to meet the current demand of low-cost-multiplexed and simple miniaturized detections (Wongkaew *et al*., 2019). The emergence of sophisticated biotechnology and nanotechnology in research has led to the development of electrochemical sensors for specific and rapid detections of bacterial cells in complex sample matrices. These developments have focused on improvement of electrode signal amplifications, electrode designs, single-analyte detection capabilities and use of novel nanomaterials for effective signal transductions (Pashazadeh *et al*., 2017). However, the current central challenge of these sensors is that the sensitivity of commonly applied analytical detection technique does not reach individual analyte entities within the complex sample matrices under analysis.

Nano-impact electrochemistry (NIE), an electrochemical detection strategy has provided new routes for the development of bacterial detection devices targetting individual bacterial cells in complex sample matrices (Zhang & Zhou, 2020). In this method, the analytes are combined with NPs in suitable electrolyte solution under optimized conditions and randomly impact the electrode surface held at an oxidizing or reducing electrode potential exceeding the standard potential of the redox active species (Sani & Tschulik, 2021). These constant collisions with the electrode surface leads to production of transient currents associated with faradaic and non-faradaic charge transfer processes measured by chrono-amperometry (CA) (Zhang & Zhou, 2020). Most of the NIE detection strategies for bacteria currently employed in research provide limited information on individual colliding bacterial cells and their structural information due to their integration with CA which is less senstitive and selective. This is due to the pseudo-capacitive nature and effects of combination of both Faradaic and non-Faradaic electrode processes which complicate bacterial detection process. The introduction of bimetallic NPs synthesized from noble metallic elements

such as Ag and Au into NIE sensors interfaced with more sensitive electro-analytical techniques including CV, DPV and EIS can enhance sensitivity and selectivity of NIE by improving both signal generation and amplifications.

1.2. Research Problem

Microbiological water monitoring and quality control play important role in human health globally. *E. coli* and *S. typhimurium* transmit waterborne diseases to humans (Gavrilescu *et al*., 2015). Therefore, their timely and rapid detections are of great economic importance. However, the current detection methods for these bacteria are costly, labor intensive with poor ultra-miniaturization capabilities (Kumar *et al*., 2019). The integration of NPs with electrochemical sensors can help shred the size of the transducer to that of the bacterial cells. Bimetallic Ag-Au NPs possess enhanced specific surface area and bio-compatibility which are effective for bacterial sensing. This is due to the synergistic effects induced by charge transfer from one metal to another within the bimetallic NPs moiety (Boken *et al*., 2017). The design of the transducers in electrochemical nano-impact sensors can also play an important role in rapid and sensitive detection of bacterial cells and the best results are obtained when interdigitated array electrodes (IDAE) whose sizes are comparable to those of bacterial cells are employed (Couniot *et al*., 2015). The use of these electrodes can further enhance ultra-miniaturization as well as improving signal amplifications (Guo & Wang, 2011). More sensitive techniques such as EIS integrated with nano-impact sensors can also help establish electrical responses of chemical systems and kinetic parameters in a non-destructive manner (Kemp, 2021). Electrochemical impedance spectroscopy (EIS) has been widely used to analyze bulk pseudo-capacitive materials including bacterial cells due to its versatility (Bredar *et al*., 2020). Therefore, EIS measurement integrated with nano-impact sensors can simultaneously yield information on various Faradaic and non-Faradaic processes as the bacterial cells interact with the electrode surface. To the best of our knowledge, no NIE study has been reported on the use of citrate-capped bimetallic Ag-Au (1:2) NPs as signal amplifiers on glassy carbon and interdigitated array electrodes for rapid and ultra-sensitive detections of *E. coli* and *S. typhimurium* in River and Ocean water samples. This study therefore focused on the detections of *E. coli* and *S. typhimurium* by NIE where citrate-capped bimetallic Ag-Au (1:2) NPs were used as electrochemical signal amplifiers at glassy carbon and interdigitated array electrodes impact sensors. These label-free nano-impact sensors integrated

with EIS technique were investigated so as to ensure rapid and ultra-sensitive detections of the bacteria in River and Ocean water samples.

1.3. Aims and objectives of the study

The main aim of this study was to develop sensitive and selective electrochemical nano-impact sensors for *E. coli* and *S. typhimurium.* Therefore, the synthesis and characterisation of monometallic Ag NPs, Au NPs and bimetallic Ag-Au (1:2) NPs for applications in ultra-sensitive detections of these bacteria using nano-impact electrochemistry (NIE) integrated with CV, DPV and EIS techniques were pursued in this study. To achieve these, the following specific objectives were outlined for this study;

1) To synthesize monometallic Ag NPs, Au NPs and bimetallic Ag-Au (1:2) NPs using citrate reduction and electrochemical methods

2) To characterize the synthesized NPs using spectroscopic and electrochemical techniques

3) To study the interactions between the NPs, *E. coli* and *S. typhimurium* using spectroscopic and electrochemical techniques

4) To design and optimize bimetallic Ag-Au (1:2) NPs impact sensors using glassy carbon and interdigitated array electrodes

5) To validate the developed nano-impact sensors and apply them for the detections of *E. coli* and *S. typhimurium* in River and Ocean water samples using electrochemical techniques

1.4 Preface

Main objective and overview of the Thesis

This thesis mainly aimed at the synthesis of silver-gold (1:2) bimetallic nanoparticles (NPs) and their applications in nano-impact electrochemical detections of *E. coli* and *S. typhimurium* in River and Ocean water samples using glassy carbon (GCE) and interdigitated array (IDAE) electrodes as transducers.

Chapter 1: This chapter presents the introduction of the study where the background of the study, problem statement and justification, aims and objectives are outlined.

Chapter 2: This chapter reviews the current literature relevant to the study by detailing *E. coli* and *S. typhimurium* electrochemical detection strategies including nano-impact

electrochemistry. The use of various NPs in electrochemical sensor development and applications is also enumerated and discussed.

Chapter 3: This chapter provides a brief description of the method used for the synthesis, microscopic and structural characterizations of the NPs. It also presents the description of the general experimental procedures for chemical synthesis of the monometallic Ag NPs, Au NPs and bimetallic Ag-Au (1:2) NPs. The optical band gaps of the NPs are also determined, reported and discussed in this chapter.

Chapter 4: This chapter presents comparative electrochemical characterizations of chemically and electrochemically modified GCE/Ag NPs, GCE/Au NPs and bimetallic GCE/Ag-Au (1:2) bimetallic films. The general procedures for electrode modification strategies through drop-coating and electro-deposition of the monometallic and bimetallic NPs are also described. The electrochemical band gaps are also determined and compared. The electrochemical kinetic parameters for both drop-coated and electro-deposited GCE nano-films were determined, compared and discussed.

Chapter 5: This chapter examines opto-electrochemical interactions between each of the chemically synthesized NPs and *E. coli*. Optimization and development of electrochemical nano-impact sensor for the bacteria using GCE and IDAE integrated with CV, DPV and EIS techniques are presented and discussed.

Chapter 6: This chapter investigates opto-electrochemical interactions between *S. typhimurium* and each of the chemically synthesized NPs. The optimization and development of electrochemical nano-impact sensor for the bacteria using GCE and IDAE as transducers is investigated via CV, DPV and EIS techniques. Various optimization studies for ultra-sensitive detections of the bacteria are also thoroughly investigated, reported and discussed.

Chapter 7: This chapter presents the study conclusions based on the overall research findings and based on these, recommendations for further studies are highlighted.

1.5 References

Ansari, S., Sherchand, J.B., Parajuli, K., Mishra, S.K., Dahal, R.K., Shrestha, S., Tandukar, S. & Pokhrel, B.M. 2012. *Bacterial etiology of acute diarrhea in children under five years of age.* Journal of Nepal Health Research Council.

Arora, S. & Siddiqui, S. 2018. Detecting food borne pathogens using electrochemical biosensors:

An overview Value addition of makhana and its by-products View project. *Researchgate.Net*, 6(April): 1031–1039. https://www.researchgate.net/publication/324273436.

Azimzadeh Sani, M. & Tschulik, K. 2021. *Nanoparticle impact electrochemistry*. Frontiers of Nanoscience: Elsevier. http://dx.doi.org/10.1016/b978-0-12-820055-1.00007-1.

Barak, J.D. & Schroeder, B.K. 2012. Interrelationships of Food Safety and Plant Pathology: The Life Cycle of Human Pathogens on Plants. *Annual Review of Phytopathology*, 50(1): 241–266. http://dx.doi.org/10.1146/annurev-phyto-081211-172936.

Boken, J., Khurana, P., Thatai, S., Kumar, D. & Prasad, S. 2017. Plasmonic nanoparticles and their analytical applications: A review. *Applied Spectroscopy Reviews*, 52(9): 774–820. http://dx.doi.org/10.1080/05704928.2017.1312427.

Bredar, A.R.C.C., Chown, A.L., Burton, A.R. & Farnum, B.H. 2020. Electrochemical Impedance Spectroscopy of Metal Oxide Electrodes for Energy Applications. *ACS Applied Energy Materials*, 3(1): 66–98. http://dx.doi.org/10.1021/acsaem.9b01965.

Couniot, N., Afzalian, A., Van Overstraeten-Schlögel, N., Francis, L.A. & Flandre, D. 2015. Capacitive biosensing of bacterial cells: Analytical model and numerical simulations. *Sensors and Actuators, B: Chemical*, 211: 428–438. http://dx.doi.org/10.1016/j.snb.2015.01.108.

Freedman, S.B., Xie, J., Neufeld, M.S., Hamilton, W.L., Hartling, L., Tarr, P.I., (APPETITE), A.P.P.E.I.T., Nettel-Aguirre, A., Chuck, A., Lee, B., Johnson, D., Currie, G., Talbot, J., Jiang, J., Dickinson, J., Kellner, J., MacDonald, J., Svenson, L., Chui, L., Louie, M., Lavoie, M., Eltorki, M., Vanderkooi, O., Tellier, R., Ali, S., Drews, S., Graham, T. & Pang, X.-L. 2016. Shiga Toxin-Producing *Escherichia coli* Infection, Antibiotics, and Risk of Developing Hemolytic Uremic Syndrome: A Meta-analysis. *Clinical Infectious Diseases*, 62(10): 1251–1258. https://pubmed.ncbi.nlm.nih.gov/26917812.

Gavrilescu, M., Demnerová, K., Aamand, J., Agathos, S. & Fava, F. 2015. Emerging pollutants in the environment: Present and future challenges in biomonitoring, ecological risks and bioremediation. New Biotechnology, 32(1): 147–156. http://dx.doi.org/10.1016/j.nbt.2014.01.001.

Guo, S. & Wang, E. 2011. Noble metal nanomaterials: Controllable synthesis and application in fuel cells and analytical sensors. *Nano Today*, 6(3): 240–264. http://dx.doi.org/10.1016/j.nantod.2011.04.007.

Habimana, J. de D., Ji, J. & Sun, X. 2018. Minireview: Trends in Optical-Based Biosensors for Point-Of-Care Bacterial Pathogen Detection for Food Safety and Clinical Diagnostics. *Analytical Letters*, 51(18): 2933–2966. http://dx.doi.org/10.1080/00032719.2018.1458104.

Hilton, S.K., Castro-Nallar, E., Pérez-Losada, M., Toma, I., McCaffrey, T.A., Hoffman, E.P., Siegel, M.O., Simon, G.L., Johnson, W.E. & Crandall, K.A. 2016. Metataxonomic and metagenomic approaches vs. culture-based techniques for clinical pathology. *Frontiers in microbiology*, 7(APR): 484. https://pubmed.ncbi.nlm.nih.gov/27092134.

Kemp, N.T. 2021. A Tutorial on Electrochemical Impedance Spectroscopy and Nanogap Electrodes for Biosensing Applications. *IEEE Sensors Journal*, 21(20): 22232–22245. http://dx.doi.org/10.1109/jsen.2021.3084284.

Kumar, S., Nehra, M., Mehta, J., Dilbaghi, N., Marrazza, G. & Kaushik, A. 2019. Point-of-Care Strategies for Detection of Waterborne Pathogens. *Sensors (Basel, Switzerland)*, 19(20): 4476. https://pubmed.ncbi.nlm.nih.gov/31623064.

Lin, J. & Ganesh, A. 2013. Water quality indicators: Bacteria, coliphages, enteric viruses. *International Journal of Environmental Health Research*, 23(6): 484–506. http://dx.doi.org/10.1080/09603123.2013.769201.

Murray, C.J.L., Ikuta, K.S., Sharara, F., Swetschinski, L., Aguilar, G.R., Gray, A., Han, C., Bisignano, C., Rao, P. & Wool, E. 2022. Global burden of bacterial antimicrobial resistance in 2019: a systematic analysis. *The Lancet*, 399(10325): 629–655.

Nawrocki, E.M., Mosso, H.M. & Dudley, E.G. 2020. A Toxic Environment: a Growing Understanding of How Microbial Communities Affect *Escherichia coli* O157:H7 Shiga Toxin Expression. *Applied and Environmental Microbiology*, 86(24): 1–12.

Niessen, L., Luo, J., Denschlag, C. & Vogel, R.F. 2013. The application of loop-mediated isothermal amplification (LAMP) in food testing for bacterial pathogens and fungal contaminants. *Food Microbiology*, 36(2): 191–206. http://dx.doi.org/10.1016/j.fm.2013.04.017.

Peng, M., Tabashsum, Z., Patel, P., Bernhardt, C. & Biswas, D. 2018. Linoleic acids overproducing lactobacillus casei limits growth, survival, and virulence of *Salmonella typhimurium* and enterohaemorrhagic *Escherichia coli*. *Frontiers in microbiology*, 9(NOV): 2663. https://pubmed.ncbi.nlm.nih.gov/30443248.

Pashazadeh, P., Mokhtarzadeh, A., Hasanzadeh, M., Hejazi, M., Hashemi, M. & de la Guardia, M.

2017. Nano-materials for use in sensing of *Salmonella* infections: Recent advances. *Biosensors and Bioelectronics*, 87: 1050–1064. http://dx.doi.org/10.1016/j.bios.2016.08.012.

Plaza, N., Castillo, D., Pérez-Reytor, D., Higuera, G., García, K. & Bastías, R. 2018. Bacteriophages in the control of pathogenic vibrios. *Electronic Journal of Biotechnology*, 31: 24–33. http://dx.doi.org/10.1016/j.ejbt.2017.10.012.

Wongkaew, N., Simsek, M., Griesche, C. & Baeumner, A.J. 2019. Functional Nanomaterials and Nanostructures Enhancing Electrochemical Biosensors and Lab-on-a-Chip Performances: Recent Progress, Applications, and Future Perspective. *Chemical Reviews*, 119(1): 120–194. http://dx.doi.org/10.1021/acs.chemrev.8b00172.

Zhang, H. & Miller, B.L. 2019. Immunosensor-based label-free and multiplex detection of influenza viruses: State of the art. *Biosensors and Bioelectronics*, 141.

Zhang, J.-H.H. & Zhou, Y.-G.G. 2020. Nano-impact electrochemistry: Analysis of single bioentities. *TrAC - Trends in Analytical Chemistry*, 123(11576): 115768. https://doi.org/10.1016/j.trac.2019.115768.

CHAPTER TWO

LITERATURE REVIEW

2.0 Summary

This chapter gives an account of the literature content of the study with emphasis on the reported electrochemical sensors for *E. coli* and *S. typhimurium*. The chapter also focuses on the application of novel nanomaterials including Ag NPs, Au NPs and their bimetallics in the fabrication of electrochemical sensors for the bacteria. The advantages and disadvantages of using nano-impact and nano-film sensors for the bacteria are enumerated compared and briefly discussed. The benefits of integrating nano-impact electrochemistry (NIE) with more sensitive electro-analytical techniques (CV, DPV and EIS) other than chrono-amperometry (CA) are presented and discussed.

2.1. Bacteria

Most bacteria store charge in their cell membranes hence exhibiting extracellular electron transfer (EET) mechanisms which are essential in sensing applications (Schrott *et al*., 2019). Based on cell envelope structures, bacteria can be categorized into Gram negative (-ve) and positive (+ve) (Kim *et al*., 2011). Bacteria normally exhibit overall negative charge in aquatic environment at normal physiological conditions of temperature and pH (Ciumac *et al*., 2019). The -ve charge exhibited by the Gram -ve bacteria is due to the ionization of the phosphoryl and 2-keto-3-deoxyoctonate carboxylate groups located in their lipopolysaccharide (LPS) chains while in Gram +ve ones, the phosphoryl groups located in both cell wall teichoic and lipoteichoic acids are responsible for the generation of net +ve (Pajerski *et al*., 2019). Literature on EET processes in Gram -ve bacteria has been widely reported compared to Gram +ve bacteria (Paquete, 2020). This is because Gram +ve bacteria lack outer cell membrane but have thicker cell walls (20 - 80 nm), peptidoglycan, teichoic acids and glycoprotein S-layer which minimize the EET processes (Paquete, 2020). Voltammetric studies have shown that Gram -ve and +ve bacteria show oxidation peak potentials (E_{pa}) at (+0.65 - +0.69) and (+0.70 - +0.74) V, respectively (Kim *et al*., 2011). These peaks are due to the oxidation of guanine and coenzyme A (Co-A) present in cell walls of most bacteria (Zhang *et al*., 2021). A recent study conducted in *G. sulfurreducens* to measure its charge storage using open circuit potentiometry revealed higher charge density in c-type cytochrome proteins abundant in the periplasms (Paquete, 2020). In Gram +ve bacteria, the EET mechanism is mainly due to the inner membranes of c-type cytochromes which receive electrons from menaquinone pools and transfers

them to the periplasmic cytochromes (Costa *et al*., 2019). The transfer of these electrons outside the cell membranes strictly depends on hexa-and-nine heme cytochromes attached to the peptidoglycan on the thicker cell wall. Gram -ve bacteria on the other hand rely on the availability of porin-cytochrome complexes made up of β-barrel porin and c-type (Carlson *et al*., 2012).

2.1.1. *Escherichia coli and Salmonella*

Pathogenic *E. coli* strains are classified into six main groups with *E. coli* O157:H7 being the most infectious strain (Croxen *et al*., 2013). The ingestion dose of 10^1 - 10^2 cells of *E. coli* O157:H7 causes gastro-intestinal diseases and death in immune-compromised individuals (Wan *et al*., 2016). Viable cell numbers of *E. coli* ranging between (10^1 - 10^2) and (10^2 - 10^3), $CFUmL^{-1}$ indicates intermediate and higher risks of infections, respectively (Ramírez-Castillo *et al*., 2015).

Salmonella is the second most frequent bacterial genus involved in gastrointestinal outbreaks mainly through its species: *S. typhimurium*. This is due to the presence of outer cell membrane consisting largely of LPS which becomes toxic upon antigen-antibody interactions. The LPS consists of O-antigen connecting the LPS to the outer membrane, two phosphorylated glucosamines which are directly linked to the fatty acids. These phosphate groups determine the bacterial toxicity and its interactions with metallic ions in antigens. The virulence and pathogenicity in this bacterium are dependent on the reducing power of nicotinamide adenine dinucleotide phosphate hydrogen (NADPH). NADPH is usually generated through the reduction of nicotinamide adenine dinucleotide phosphate ($NADP^+$) by the enzymes transketolase via the pentose phosphate pathway (PPP) (Shaw *et al*., 2018).

2.2. Methods of Bacterial Detection

2.2.1. Conventional methods

These methods mainly include culture and colony counting, immunological (ELISA) and polymerase chain reactions (PCR) (Wei, 2020). Among these, culture- and colony-counting methods have been the ‘gold standards’ for bacterial detections mainly due to their reliability and affordability (Paniel & Noguer, 2019). However, they are costly, time consuming, lack multiplexing capability and are labor intensive (Ayrapetyan & Oliver, 2016). Even though the use of paper based assays, microfluidic platforms and lateral flow assays (Singh *et al*., 2018) have further reduced the cost, time, enhanced portability, specificity and sensitivity for bacterial detections, they still experience poor multi-analyte detection, automation and miniaturization

capabilities. Therefore, ultra-miniaturized, simple, completely automated devices with improved specificity, sensitivity and multi-analyte on-site detection capabilities are currently in high demand so as to rapidly mitigate the health problems posed by *E. coli* and *S. typhimurium.*

2.2.2 Use of nanoparticles

The application of nanoparticles (NPs) in bacterial sensing is currently a novel approach in research. Different studies incorporating NPs in bio-devices for the detection of *E. coli* and *S. typhimurium* have been reported (**Figure 2.1**).

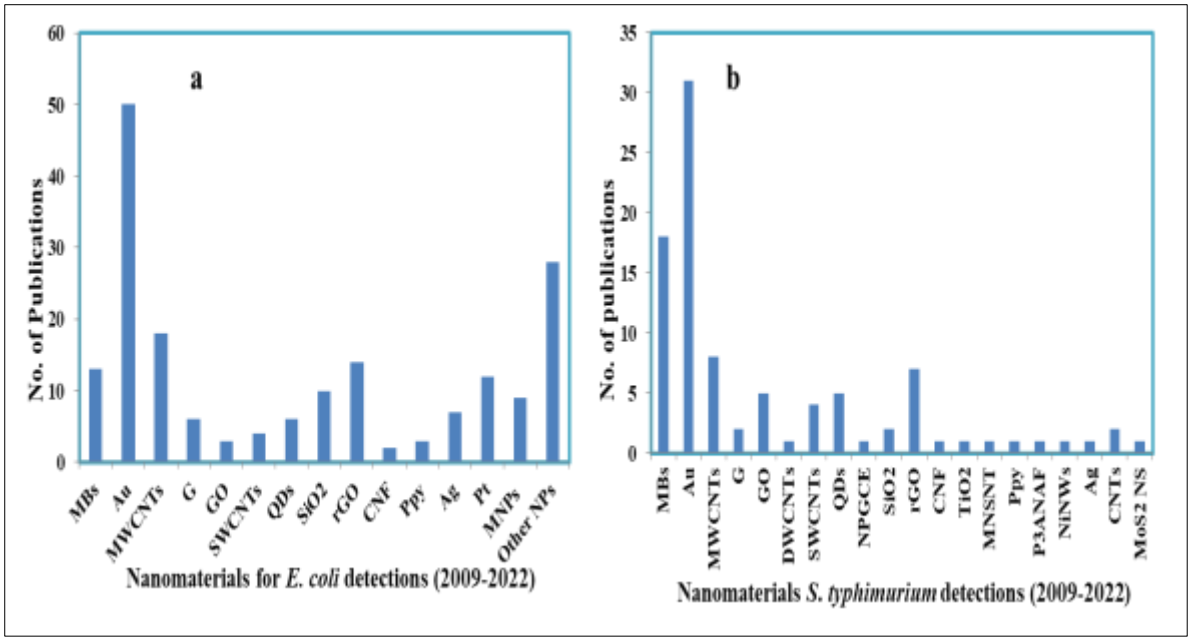

Figure 2.1: Nanomaterials reported for (a) *E. coli* and (b) *S. typhimurium* sensing (2009-2022)

Metallic NPs have been widely used due to their unique physicochemical properties. Studies have reported metallic NPs such as Zn, Cu, Ag, Au, Ti and Mg for the development of bacterial sensors (Yaqoob *et al.*, 2020). However, Au and Ag NPs have been widely reported in various studies involving the development of biosensors and chemical sensors due to their enhanced chemical reactivity, higher surface area to volume ratio and easy bio-functionalization. Literature has reported various proposed mechanisms proving the effectiveness of Ag and Au NPs as sensing agents for bacteria upon their interactions (Dizaj *et al.*, 2014). Silver (Ag) and gold (Au) NPs are positively charged and therefore can easily interact with the cell membranes of Gram -ve bacteria which are negatively charged. Silver (Ag) NPs of different sizes and shapes can attack bacterial

cells when they are attached to the surface of bacterial cell-wall. These NPs bind to the bacterial enzymes such as cytochrome C oxidase because of their surface negative charge through sulfhydryl functional groups. This in turn leads to the disruption and damage of the cell membrane as well as the interior of the bacteria causing the release of the metallic NPs ions. The interaction between the bacteria and the metallic ions leads to the production of reactive oxygen species (ROS). The metallic ions in the bacteria in turn react with the bacterial proteins thus causing protein denaturation, mitochondrial dysfunction, DNA destruction, and can finally lead to cell death.

The binding between the metallic ions and bacterial membranes occurs mainly through electrostatic interactions (Thomas & Rice, 2014). Various studies on applications of optical methods in the detection of *E. coli* and *S. typhimurium* based on their interactions with metallic ions have been reported (Kaushik *et al.*, 2019). In these methods, NPs including Au and Ag interact with the bacteria leading to changes in light intensity which is then used for bacterial detection and identification. Au and Ag NPs have been widely used in these applications attributable to their enhanced surface plasmon band localization in the visible spectrum and ease of synthesis (Elahi *et al*., 2018). The interaction between Au NPs and *E. coli* in the presence of cysteine for the detection of *E. coli* was reported (Raj *et al*., 2015). The binding affinity of the bacteria to H2 receptors on the surface of cysteine-modified Au NPs was demonstrated by the electrostatic attractions between the positively charged cysteine and negatively charged lipopolysaccharides (LPS) on the bacterial outer membrane. The negative charge on the bacteria enabled *E. coli* stabilization and hence its detection. The interaction between the bacterial membrane and Au NPs led to a clear red-to-blue shift in wavelength and hence enabled highly sensitive naked-eye detection of the bacteria.

Bacterial membranes can also bind to the NPs through non-covalent interactions as similarly described elsewhere (Hou, 2016). The size of metallic NPs employed in the interaction studies has a significant impact on anti-microbial activity. The smaller the NPs, the larger the surface area to volume ratio hence improved interaction efficiency attributed to enhanced anti-microbial properties of the NPs. Several studies have also reported the applications of novel metallic NPs such as Ag and Au in the development of sensors for *E. coli* and *S. typhimurium* (Jin *et al.*, 2017). Other methods for the detections of Gram -ve bacteria due to interactions between the bacterial

outer membranes and Au or Ag NPs and their bimetallics have also been reported (Thiramanas & Laocharoensuk, 2016). These methods are, however, tedious due to longer sample preparation and labeling.

2.3 Sensors

Sensors comprise an active sensing device directly connected to a transducer that transmits generated analytical signals from a specific analyte detected in a sample matrix onto the sensor's surface (Abdel-karim *et al.*, 2020). Sensors produce signals such as electrical, thermal or optical which are converted into digital format for further processing and display (Wang *et al.*, 2017). The main desirable qualities of a sensor include enhanced sensitivity, portability, miniaturization capability, selectivity and stability. Sensors can be classified based on the type of energy transferred, transduction mechanisms, analyte recognition principle and their areas of applications (Mahato *et al.*, 2018). They can also be generally categorized into biosensors, physical and chemical (Touhami, 2015). Biosensors detect analytes using bio-recognition elements which interact mechanistically with analytes on the transducer's surface. These interactions lead to changes in chemical properties of the analytes which are finally transformed into analytical signals and displayed onto a computer for further interpretation. Physical sensors measure variations in physical quantity of analyte such as temperature and pressure.

A chemical sensor converts a response from a specific analyte into a measurable signal through a chemical reaction. The analyte is detected and determined due to its chemical interactions with the sensor surface. The response produced is then converted into detectable signals which are finally displayed onto a computer. They are mainly categorized into electrochemical, optical, gravimetric and thermal sensors based on transduction mechanisms (Poma *et al.*, 2021). Optical and electrochemical sensors have gained popularity in the recent past for the detections of *E. coli* and *S. typhimurium* mainly due to higher sensitivity and miniaturization potential (Pebdeni *et al.*, 2022). Optical detection devices convert light rays mostly transmitted through fibre optics into detectable electrical signals. Therefore, in this case, there is no need of electrical wires and electrodes as compared to electrochemical sensors. This makes the sensing process faster and more sensitive. However, electrochemical detection devices have more stable output, higher sensitivity, rapidity, experience less interference and easy sample preparation since there is no tagging of analytes with labels as in optical sensors.

2.3.1 Electrochemical sensors

These are forms of chemical sensors that detect analytes by recording the changes in electrical parameters such as current, potential, conductance, resistance and convert the data obtained into useful analytical signals for further interpretations. These electrical properties are attributed to the interactions between the sensor surface and analyte of interest. These include: voltammetry (current), amperometry (current), EIS (impedance) and potentiometry (potential). The sensitivity of electrochemical sensors mainly depends on the electrochemical processes occurring at the transducer's surface. Therefore, proper modifications of the electrode play crucial analytical role in the development of these sensors. Surface modified electrodes are stable, have better over-redox potentials with improved electron transfer kinetics.

Based on electrode surface nano-fabrication and analytical detection strategies, electrochemical sensors can be categorized into nano-films (**a**) and nano-impact (**b**) sensors (**Figure 2.2)**.

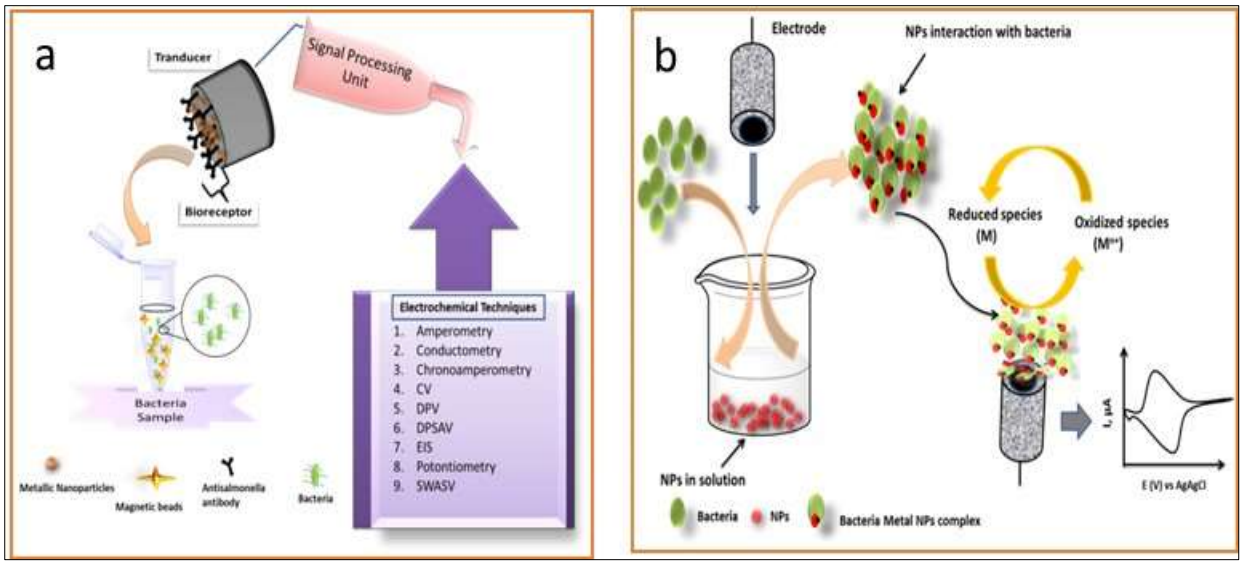

Figure 2.2: Electrochemical sensors components and mechanisms; (a) Nano-film sensor (b) Nano-impact sensor

Nano-film sensing strategies mainly involve chemical modification of transducer's surface with NPs, electrode film stabilizers and bio-receptors for selective and sensitive detections of the analyte. Nano-impact sensors detect analytes using unmodified transducers dipped into a mixture of NPs and analyte of interest dispersed in suitable electrolyte solution under oxidizing potential conditions. The main differences between these two electrochemical detection strategies are outlined in **Table 2.1.**

Table 2.1: Differences between nano-impact and nano-film sensors

Nano-impact sensor	Nano-film sensor
• Highly sensitive to single entity analytes due to the use of NIE technique	• Less sensitive due to lack of single entity analyte nature in the absence of bio-receptors
• Bio-conjugation and bio-molecular recognition events are easily realized due to ability to detect wide range of analytes simultaneously	• Specific analytes are detected at a time hence no realization of bio-conjugation and bio-molecular recognition events
• Cost-and time-effective due to its *in-situ* detection capability	• Expensive due to the fabrication materials and longer sample preparation and detection period
• Allows better understanding of biological samples' heterogeneity	• Lacks analytical information on biological samples heterogeneity due to the use of analyte specific bio-receptors
• Sample analyte detection can be attributed to both simultaneous Faradaic and non-Faradaic charge transfers	• Mainly employs Faradaic charge transfer to detect analytes
• Absolutely label-free detection strategy hence experiences reduced complexity and deleterious effects	• Can either be label-free or label dependent
• Quantification of charge passed per single current transient allows analysis and characterization of concentration and electro-catalytic properties of analytes	• Concentration and electro-catalytic properties of analytes are determined mainly by either/both oxidation or reduction peaks
• Accuracy and representativeness is a big challenge due to the adhesion and sticking of analytes onto the electrode surface hence affecting the sensor's lifetime and robustness	• Analytes rarely stick onto the electrode surface due to availability of several modified layers
• Single type of bio-analyte detection in NIE does not provide cell classification and phenotype analysis.	• Cell classification and phenotype analysis are highly possible due to the use of bio-recognition elements
• Valid signals cannot be easily distinguished from background signals	• Valid signals are easily distinguished from the background signals
• Can be used for bacterial identification and cell viability studies	• Cannot be used for bacterial cell identification and viability studies since it lacks the single analyte entity nature
• Mainly uses chrono-amperometry to collect current transients either step-like or spike-like at a given voltage hence limited analyte information on structural properties is provided	• Numerous techniques can be integrated to study the relationship between voltage applied and current produced
• Blockage principle cannot be used to distinguish between dead and live bacteria since bacteria adhere onto the electrode surface	• Dead and live bacteria in complex biological samples can be distinguished easily

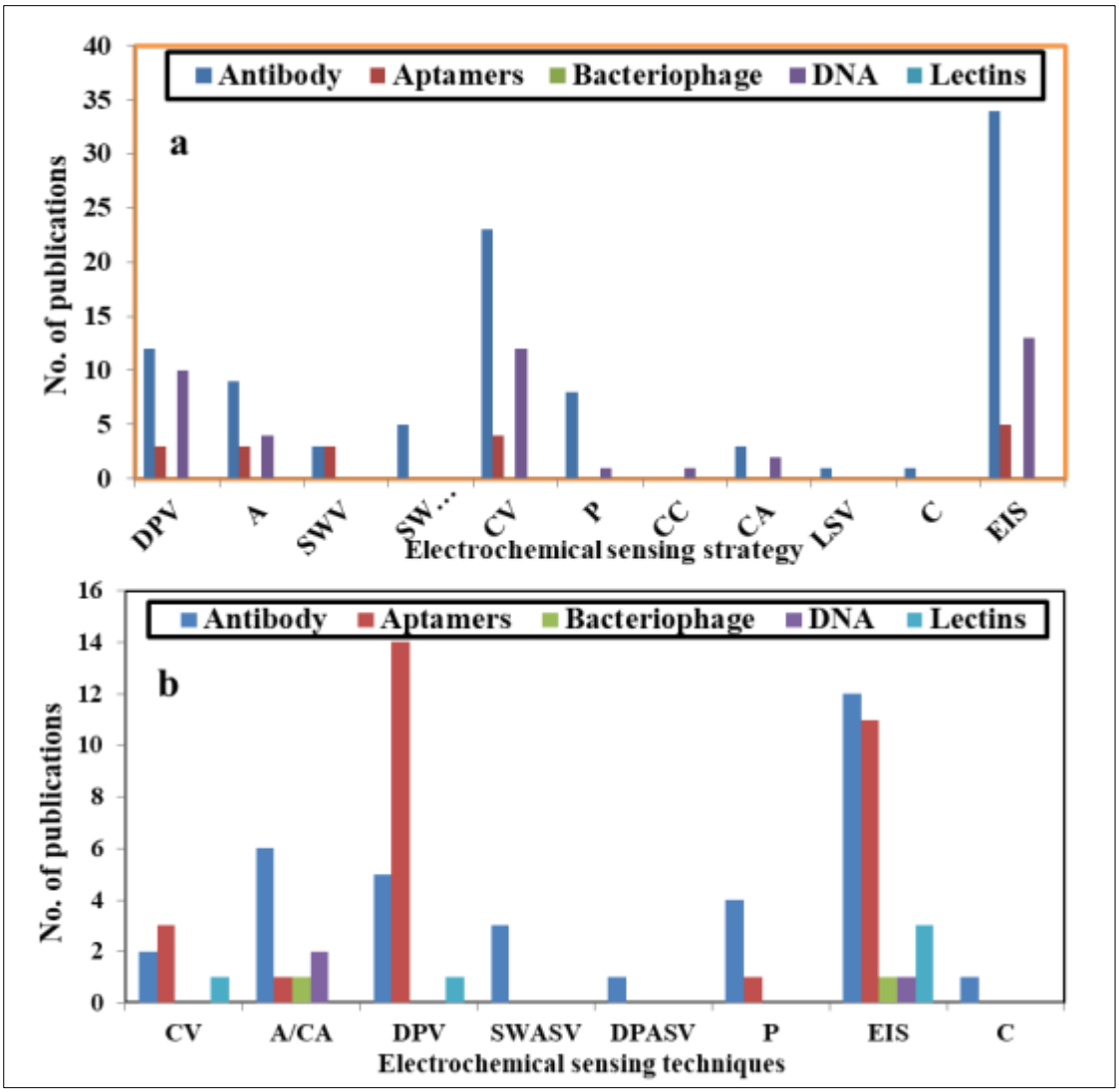

Figure 2.3: Analysis of bio-receptors used for (a) *E. coli* and (b) *S. typhimurium* detections in the past decade

Electrochemical sensors can also be categorized into label dependent-and-independent based on absence or presence of bio-receptors fabricated on the transducer. The bio-receptors enhance selectivity of the interaction between the analyte and tranducer. In the last decade, numerous studies reported the detection of *E. coli* and *S. typhimurium* using antibodies and aptamers as bio-receptors (**Figure 2.3**). This can be attributed to their higher selectivity and sensitivity which are mainly influenced by the nature and formality of sample matrices analyzed (Patris *et al.*, 2016). Most of these studies also employed label independent sensing strategies. This can be ascribed to their less labor requirements since there is no labeling of analytes and hence making detection time shorter (Ranjbar *et al.*, 2018). However, they rely on electrochemical changes caused by the direct

attachment of analytes onto the electrode for signal generation and this may not be uniform hence misleading results are obtained (Adhikary *et al*., 2020). They also show relatively higher LODs due to the absence of additional source of signal generation and amplification (Rainbow *et al*., 2020)

Electrochemical sensors are always integrated with various electro-analytical techniques for signal transductions. The choice of these techniques depends on their known limit of detection (LOD) and researcher's expertise. To improve the sensitivity and selectivity of these techniques, studies involving fabrications of transducers with NPs have been widely reported (**Figure 2.4**). Among these nano-integrated techniques, conductometry has been least used for bacterial detections (X. Zhang *et al*., 2020). In the last decade, only two studies reported the detection of *E. coli* and *S. typhimurium* using this technique (Wonsawat *et al*., 2020).

Several review articles on electrochemical sensing of *E. coli* and *Salmonella* using different labels, transducers and NPs were also published between 2015 and 2022 (Sheikhzadeh *et al*., 2021; Shen *et al*., 2021). The main transduction techniques for signal generation described in these studies included impedimetry, voltammetry, amperometry and potentiometry. Very few studies have been reported on nano-conductometric detections of these bacteria (Melo *et al*., 2016; Cesewski & Johnson, 2020) and nano-impact sensing strategies using the principle behind nano-impact electrochemistry (NIE) (J. H. Zhang & Zhou, 2020) for the detection of the bacteria. This can be ascribed to labour intensive sample preparation method and analysis. However, conductometry has promising applications for bacterial detection since it can be used to distinguish between Gram -ve and +ve bacteria based on the conductivity of their cell membranes. This is attributed to its ability to detect both electro-active and electro-inactive analyte species. Other advantages of this technique include practicality, specificity, sensitivity, affordability, rapidity and ultra-miniaturization capabilities.

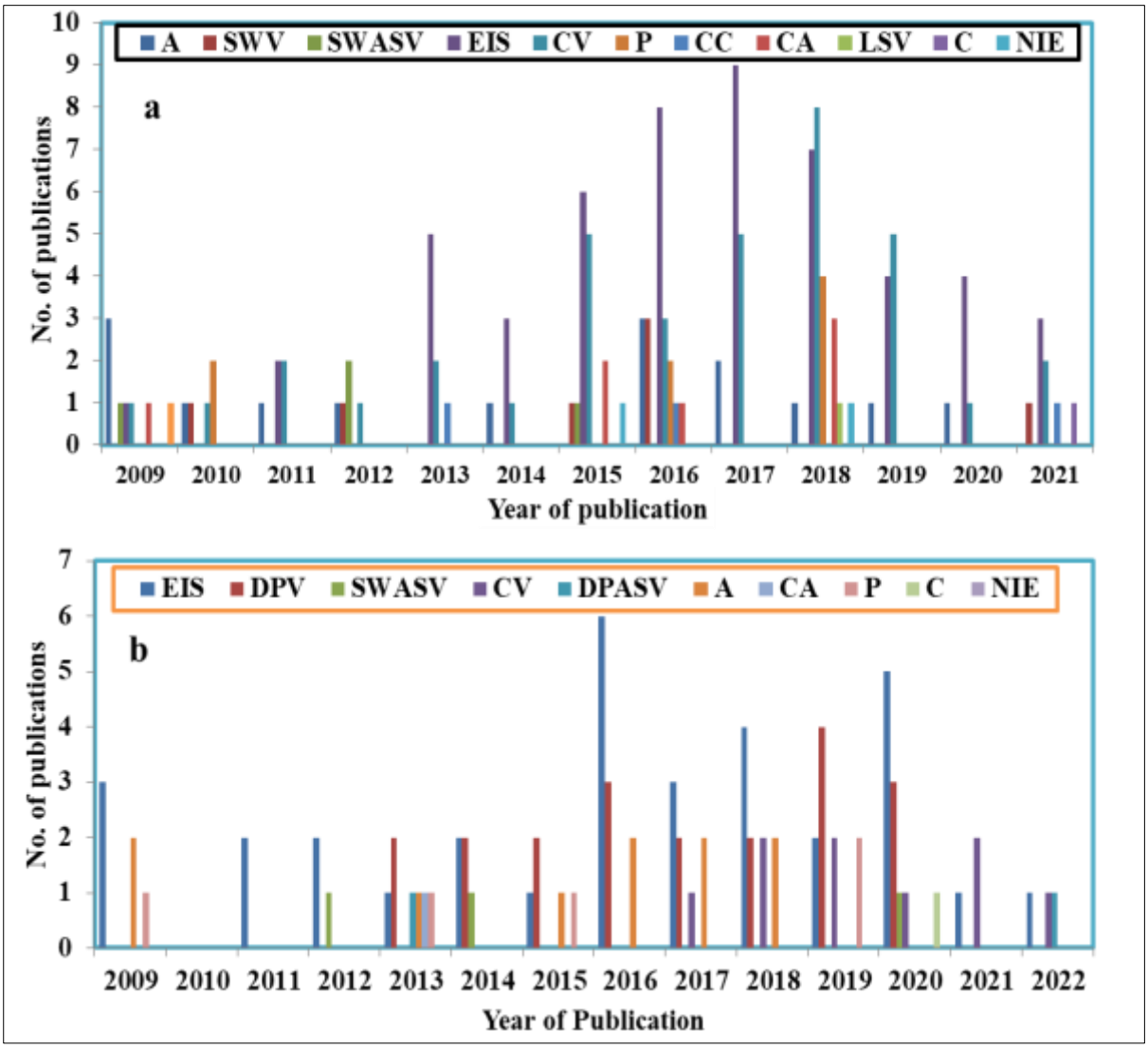

Figure 2.4: Analysis of electro-analytical techniques for (a) *E. coli* and (b) *S. typhimurium* detections in the past decade (2009-2022)

Three out of ten review articles published between 2015 and 2022 generally described the applications of different NPs in electrochemical sensing of members of the Genus *Salmonella* and *Escherichia* (Shen *et al*., 2021; Awang *et al*., 2021). Therefore, to the best of our knowledge, no study has specifically reported on electrochemical nano-impact detections of *E. coli* and *S. typhimurium* focusing on the use of novel bimetallic NPs such as Ag-Au NPs chemically or electrochemically modified on glassy carbon and interdigitated array electrodes without the use of bio-receptors. However, over the past decade, various studies have reported electrochemical sensing innovations for *S. typhimurium* and *E. coli*. The use of Au, Ag and carbon-based NPs in

designing different bacterial detection strategies for the bacteria has attracted increased attention from researchers in the last decade as evident by the large number of publications (**Figure 2.1)**. This is due to their favorable electronic properties, electro-catalytic activity and larger surface area-to-volume ratio thus enhancing signal generation and amplifications (Geagea *et al*., 2015). These NPs can also shred the signal transducer's size to that of the bacterial cell hence improving both sensitivity and selectivity of the sensors employed (Genç, 2017). Increased loading capacity for bio-receptors and their attachment onto the electrode's surface with controlled orientation in the presence of NPs can create a higher impedance response in non-faradaic sensors (Paniel & Noguer, 2019). Due to their excellent size, shape and surface structure tunability, use of these NPs in electrochemical sensing can also significantly improve analytical performances such as reaction kinetics and repeatability (Shen *et al*., 2016; Jin *et al.*, 2017). Other key performance indicators of electrochemical sensors which also directly depend on application of NPs include limit of quantification (LOQs), detection time, dynamic linear range, sample volume and concentration required for effective signal generation, geometry of transducer, reproducibility and stability (Rodriguez *et al*., 2021). The improvement on these parameters can enhance rapid and ultra-miniaturized on-site detections of the bacteria (R. Zhang *et al*., 2020).

In the past decade, several electrochemical nano-sensors reported employed potential controlled techniques especially voltammetry (**Figure 2.4**). In these techniques, the detection of the analyte (bacteria) is based on the measurement of the magnitude of current produced in response to the applied potential that drives redox reactions on the electrode. Direct measurement of current generated has made voltammetry one of the most widely used electrochemical detection technique (Silva *et al*., 2018). In addition, low LODs have also been reported in a good number of studies in the last decade (Murasova *et al*., 2020; Fathi *et al*., 2021). However, the testing of these sensors in real and complex samples for *E. coli* and *S. typhimurium* detections still remains a challenge due to interferences attributable to cross-reactions. Moreover, the detection times in most of the reported studies between the years 2009 and 2022 were also too long (Dai *et al*., 2019; Murasova *et al*., 2020) and therefore need improvement. However, shorter detection times were also reported in a number of studies (Appaturi *et al*., 2020; Fathi *et al*., 2021). Research towards simultaneous detection of *E. coli* and *S. typhimurium* in real complex sample matrices using electrochemical sensors has been a major challenge. This is due to the low concentration of the cells in some samples (Melo *et al*., 2016). Some of the interferents in these sample matrices have similar redox

potentials to the analyte hence lowering sensitivity and selectivity of the sensors (Dodevska *et al.*, 2019).

2.4 Conclusion

Rapid and sensitive bacterial sensing is essential in water industries. *E. coli* and *S. typhimurium* have caused waterborne disease outbreaks worldwide. Therefore, their appropriate and effective detection method is still a major impediment so as to avert this worrying infection trend. Even though currently used detection methods are sensitive, most of them are still time consuming and labor intensive. Therefore, there is a critical need for a faster, simpler, more sensitive, selective and cheaper method. Electrochemical sensors have outstanding qualities among the different types of bacterial detection strategies. These include; simplicity, faster response, selectivity, sensitivity, greater possibility of miniaturization and automation capabilities. Although label-free electrochemical detection methods have been widely used in the past decade due to their direct bacterial sensing nature, simplicity, relatively low detection time and greater possibility of integration into a lab-on-a chip; longer analysis time and absence of additional signal amplification are still their main limitations. These sensors cannot therefore effectively overcome cross-reactions from non-target bacteria. Due to this, label-free sensors need appropriate selection of more specific electrochemical sensing strategies. Nano-science is an emerging and growing field, and various NPs such as Au and Ag NPs have been integrated in the development of *E. coli* and *S. typhimurium* electrochemical sensors and therefore further study should be conducted so as to improve the use of these novel NPs for effective and efficient signal transductions. This will ensure overall improvement in bacterial sensing with greater simplicity. Despite higher accuracy, simplicity, cost-effectiveness and selectivity of NIE technique, no study has been reported on the detection of *E. coli* and *S. typhimurium* using novel bimetallic NPs integrated with sensitive electro-analytical techniques in the last decade. Therefore, electrochemical techniques such as (CV, DPV and EIS) other than chrono-amperometry should be integrated with NIE so as to improve the overall sensitivity and selectivity of the generated analytical information. Appropriate electrode modifications such as use of interdigitated nano-electrode arrays, appropriate sample pre-treatment and optimization of suitable experimental conditions should be incorporated into NIE so as to minimize the sticking effects of analytes onto the electrode surface hence lowering the background current.

2.5 References

Adhikary, T., Nanda, A., Thangapandi, K., Roy, S. & Jana, S.K. 2020. Trends in Biosensors and Role of Enzymes as their Sensing Element for Healthcare Applications. Microbial Fermentation and Enzyme Technology.

Appaturi, J.N., Pulingam, T., Thong, K.L., Muniandy, S., Ahmad, N. & Leo, B.F. 2020. Rapid and sensitive detection of Salmonella with reduced graphene oxide-carbon nanotube based electrochemical aptasensor. Analytical Biochemistry, 589(11348): 9. https://doi.org/10.1016/j.ab.2019.113489.

Awang, M.S., Bustami, Y., Hamzah, H.H., Zambry, N.S., Najib, M.A., Khalid, M.F., Aziah, I. & Manaf, A.A. 2021. Advancement in *Salmonella* detection methods: From conventional to electrochemical-based sensing detection. Biosensors, 11(9): 346.

Ayrapetyan, M. & Oliver, J.D. 2016. The viable but non-culturable state and its relevance in food safety. Current Opinion in Food Science, 8: 127–133.

Carlson, H.K., Iavarone, A.T., Gorur, A., Yeo, B.S., Tran, R., Melnyk, R.A., Mathies, R.A., Auer, M. & Coates, J.D. 2012. Surface multiheme c-type cytochromes from Thermincola potens and implications for respiratory metal reduction by Gram-positive bacteria. Proceedings of the National Academy of Sciences of the United States of America, 109(5): 1702–1707.

Cesewski, E. & Johnson, B.N. 2020. Electrochemical biosensors for pathogen detection. Biosensors and Bioelectronics, 159.

Ciumac, D., Gong, H., Hu, X. & Lu, J.R. 2019. Membrane targeting cationic antimicrobial peptides. Journal of Colloid and Interface Science, 537: 163–185.

Costa, N.L., Hermann, B., Fourmond, V., Faustino, M.M., Teixeira, M., Einsle, O., Paquete, C.M. & Louro, R.O. 2019. How thermophilic gram-positive organisms perform extracellular electron transfer: Characterization of the cell surface terminal reductase OcwA. mBio, 10(4): 1210–1219.

Croxen, M.A., Law, R.J., Scholz, R., Keeney, K.M., Wlodarska, M. & Finlay, B.B. 2013. Recent advances in understanding enteric pathogenic *Escherichia coli*. Clinical Microbiology Reviews, 26(4): 822–880.

Dai, G., Li, Z., Luo, F., Ai, S., Chen, B. & Wang, Q. 2019. Electrochemical determination of *Salmonella typhimurium* by using aptamer-loaded gold nanoparticles and a composite

prepared from a metal-organic framework (type UiO-67) and graphene. Microchimica Acta, 186(9): 1–9.

Dizaj, S.M., Lotfipour, F., Barzegar-Jalali, M., Zarrintan, M.H. & Adibkia, K. 2014. Antimicrobial activity of the metals and metal oxide nanoparticles. Materials Science and Engineering C, 44: 278–284.

Dodevska, T., Lazarova, Y. & Shterev, I. 2019. Amperometric biosensors for glucose and lactate with applications in food analysis: A brief review. Acta Chimica Slovenica, 66(4): 762–776.

Elahi, N., Kamali, M. & Baghersad, M.H. 2018. Recent biomedical applications of gold nanoparticles: A review. Talanta, 184: 537–556.

Fathi, S., Saber, R., Adabi, M., Rasouli, R., Douraghi, M., Morshedi, M. & Farid-Majidi, R. 2021. Novel competitive voltammetric aptasensor based on electrospun carbon nanofibers-gold nanoparticles modified graphite electrode for Salmonella enterica serovar detection. Biointerface Research in Applied Chemistry, 11(2): 8702–8715.

Geagea, R., Aubert, P.H., Banet, P. & Sanson, N. 2015. Signal enhancement of electrochemical biosensors via direct electrochemical oxidation of silver nanoparticle labels coated with zwitterionic polymers. Chemical Communications, 51(2): 402–405.

Genç, R. 2017. Nanomaterial-based sensor platforms for facile detection of food contaminants. Nanobiosensors: Elsevier.

Hou, T. 2016. Sensors based on optical interferometry. Deakin University.

Jin, B., Wang, S., Lin, M., Jin, Y., Zhang, S., Cui, X., Gong, Y., Li, A., Xu, F. & Lu, T.J. 2017. Upconversion nanoparticles based FRET aptasensor for rapid and ultrasenstive bacteria detection. Biosensors and Bioelectronics, 90: 525–533.

Kaushik, S., Tiwari, U.K., Pal, S.S. & Sinha, R.K. 2019. Rapid detection of Escherichia coli using fiber optic surface plasmon resonance immunosensor based on biofunctionalized Molybdenum disulfide (MoS_2) nanosheets. Biosensors and Bioelectronics, 126: 501–509.

Kiefer, J., Ebel, N., Schlücker, E. & Leipertz, A. 2010. Characterization of *Escherichia coli* suspensions using UV/Vis/NIR absorption spectroscopy. Analytical Methods, 2(2): 123–128.

Kim, T., Kang, J., Lee, J.H. & Yoon, J. 2011. Influence of attached bacteria and biofilm on double-layer capacitance during biofilm monitoring by electrochemical impedance spectroscopy. Water Research, 45(15): 4615–4622.

Melo, A.M.A., Alexandre, D.L., Furtado, R.F., Borges, M.F., Figueiredo, E.A.T., Biswas, A., Cheng, H.N. & Alves, C.R. 2016. Electrochemical immunosensors for Salmonella detection in food. Applied Microbiology and Biotechnology, 100(12): 5301–5312.

Murasova, P., Kovarova, A., Kasparova, J., Brozkova, I., Hamiot, A., Pekarkova, J., Dupuy, B., Drbohlavova, J., Bilkova, Z. & Korecka, L. 2020. Direct culture-free electrochemical detection of *Salmonella* cells in milk based on quantum dots-modified nanostructured dendrons. Journal of Electroanalytical Chemistry, 863(11405): 1. https://doi.org/10.1016/j.jelechem.2020.114051.

Pajerski, W., Ochonska, D., Brzychczy-Wloch, M., Indyka, P., Jarosz, M., Golda-Cepa, M., Sojka, Z. & Kotarba, A. 2019. Attachment efficiency of gold nanoparticles by Gram-positive and Gram-negative bacterial strains governed by surface charges. Journal of Nanoparticle Research, 21(8): 1–12.

Paniel, N. & Noguer, T. 2019. Detection of *Salmonella* in food matrices, from conventional methods to recent aptamer-sensing technologies. Foods, 8(9): 371.

Paquete, C.M. 2020. Electroactivity across the cell wall of Gram-positive bacteria. Computational and Structural Biotechnology Journal, 18: 3796–3802.

Patris, S., Vandeput, M. & Kauffmann, J.M. 2016. Antibodies as target for affinity biosensors. TrAC - Trends in Analytical Chemistry, 79: 239–246.

Rainbow, J., Sedlackova, E., Jiang, S., Maxted, G., Moschou, D., Richtera, L. & Estrela, P. 2020. Integrated electrochemical biosensors for detection of waterborne pathogens in low-resource settings. Biosensors, 10(4): 36. https://pubmed.ncbi.nlm.nih.gov/32294961.

Raj, V., Vijayan, A.N. & Joseph, K. 2015. Cysteine capped gold nanoparticles for naked eye detection of E. coli bacteria in UTI patients. Sensing and Bio-Sensing Research, 5: 33–36.

Ramírez-Castillo, F.Y., Loera-Muro, A., Jacques, M., Garneau, P., Avelar-González, F.J., Harel, J. & Guerrero-Barrera, A.L. 2015. Waterborne pathogens: Detection methods and challenges. Pathogens, 4(2): 307–334.

Ranjbar, S., Shahrokhian, S. & Nurmohammadi, F. 2018. Nanoporous gold as a suitable substrate for preparation of a new sensitive electrochemical aptasensor for detection of *Salmonella*

typhimurium. Sensors and Actuators, B: Chemical, 255: 1536–1544. https://doi.org/10.1016/j.snb.2017.08.160.

Rodriguez, R.S., O'Keefe, T.L., Froehlich, C., Lewis, R.E., Sheldon, T.R. & Haynes, C.L. 2021. Sensing Food Contaminants: Advances in Analytical Methods and Techniques. Analytical Chemistry, 93(1): 23–40.

Schrott, G.D., Bonanni, P.S. & Busalmen, J.P. 2019. Open circuit potentiometry reports on internal redox states of cells in G. Sulfurreducens biofilms. Electrochimica Acta, 303: 176–182.

Shaw, J.A., Henard, C.A., Liu, L., Dieckman, L.M., Vázquez-Torres, A. & Bourret, T.J. 2018. Salmonella enterica serovar Typhimurium has three transketolase enzymes contributing to the pentose phosphate pathway. Journal of Biological Chemistry, 293(29): 11271–11282.

Sheikhzadeh, E., Beni, V. & Zourob, M. 2021. Nanomaterial application in bio/sensors for the detection of infectious diseases. Talanta, 230(12202): 6. https://doi.org/10.1016/j.talanta.2020.122026.

Shen, H., Wang, J., Liu, H., Li, Z., Jiang, F., Wang, F.B. & Yuan, Q. 2016. Rapid and Selective Detection of Pathogenic Bacteria in Bloodstream Infections with Aptamer-Based Recognition. ACS Applied Materials and Interfaces, 8(30): 19371–19378.

Shen, Y., Xu, L. & Li, Y. 2021. Biosensors for rapid detection of Salmonella in food: A review. Comprehensive Reviews in Food Science and Food Safety, 20(1): 149–197.

Silva, N.F.D., Magalhães, J.M.C.S., Freire, C. & Delerue-Matos, C. 2018. Electrochemical biosensors for *Salmonella*: State of the art and challenges in food safety assessment. Biosensors and Bioelectronics, 99: 667–682.

Singh, D.P., Herrera, C.E., Singh, B., Singh, S., Singh, R.K. & Kumar, R. 2018. Graphene oxide: An efficient material and recent approach for biotechnological and biomedical applications. Materials Science and Engineering C, 86: 173–197.

Thiramanas, R. & Laocharoensuk, R. 2016. Competitive binding of polyethyleneimine-coated gold nanoparticles to enzymes and bacteria: a key mechanism for low-level colorimetric detection of gram-positive and gram-negative bacteria. Microchimica Acta, 183(1): 389–396.

Thomas, K.J. & Rice, C. V. 2014. Revised model of calcium and magnesium binding to the bacterial cell wall. BioMetals, 27(6): 1361–1370.

Wan, J., Ai, J., Zhang, Y., Geng, X., Gao, Q. & Cheng, Z. 2016. Signal-off impedimetric immunosensor for the detection of *Escherichia coli* O157:H7. Scientific Reports, 6: 1–6.

Wei, J. 2020. Approaches to Detect Foodborne Pathogenic Microorganisms. In ACM International Conference Proceeding Series. 1–7.

Wonsawat, W., Limvongjaroen, S., Supromma, S., Panphut, W., Ruecha, N., Ratnarathorn, N. & Dungchai, W. 2020. A paper-based conductive immunosensor for the determination of *Salmonella typhimurium*. Analyst, 145(13): 4637–4645.

Yaqoob, A.A., Ahmad, H., Parveen, T., Ahmad, A., Oves, M., Ismail, I.M.I., Qari, H.A., Umar, K. & Mohamad Ibrahim, M.N. 2020. Recent Advances in Metal Decorated Nanomaterials and Their Various Biological Applications: A Review. Frontiers in Chemistry, 8: 341.

Yoshida, C., Lingohr, E.J., Trognitz, F., MacLaren, N., Rosano, A., Murphy, S.A., Villegas, A., Polt, M., Franklin, K., Kostic, T., Kropinski, A.M. & Card, R.M. 2014. Multi-laboratory evaluation of the rapid genoserotyping array (SGSA) for the identification of *Salmonella* serovars. Diagnostic Microbiology and Infectious Disease, 80(3): 185–190.

Zhang, J., Sun, Q., Tang, H., Qian, Y., Chen, Y., Shan, X., Liu, X. & Gu, H. 2021. The direct electrochemistry of viable *Escherichia coli*. Journal of Electroanalytical Chemistry, 895(11542): 6.

Zhang, J.H. & Zhou, Y.G. 2020. Nano-impact electrochemistry: Analysis of single bioentities. TrAC - Trends in Analytical Chemistry, 123: 115768. https://doi.org/10.1016/j.trac.2019.115768.

Zhang, R., Belwal, T., Li, L., Lin, X., Xu, Y. & Luo, Z. 2020. Nanomaterial-based biosensors for sensing key foodborne pathogens: Advances from recent decades. Comprehensive Reviews in Food Science and Food Safety, 19(4): 1465–1487.

Zhang, X., Wang, X., Yang, Q., Jiang, X., Li, Y., Zhao, J. & Qu, K. 2020. Conductometric sensor for viable *Escherichia coli* and *Staphylococcus aureus* based on magnetic analyte separation via aptamer. Microchimica Acta, 187(1): 1–10.

CHAPTER THREE

SYNTHESIS AND CHARACTERIZATION OF NANOPARTICLES

3.0 Summary

This chapter mainly focusses on the synthesis of Ag, Au and bimetallic Ag-Au nanoparticles (NPs) using chemical reduction method. The chapter also describes briefly other general methods of NPs synthesis as well as NPs characterizations using various techniques including FT-IR, UV-visible, SEM and XRD. The brief description of the materials and procedure of NPs synthesis are also outlined in this chapter.

3.1 Introduction

The synthesis of metallic nanoparticles (NPs) has received progressively growing scientific attention in the recent past and as a result, numerous techniques have been developed based on the physico-chemical properties of the required NPs. These techniques are majorly categorized into bottom-up and top-down approaches as enlisted in **Figure 3.1**.

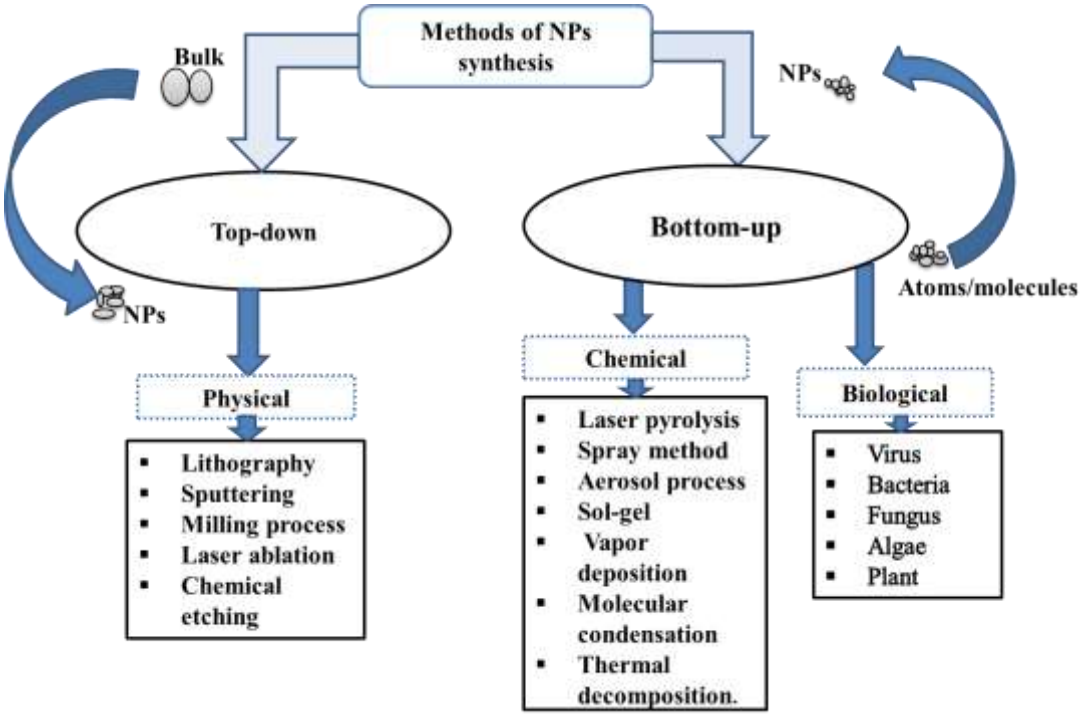

Figure 3.1: Methods of nanoparticle synthesis

The main difference between these methods is the starting materials for the NPs synthesis. In top-down methods, bulk materials are used as starting materials and the particle size reduced to form NPs through physical, biological, chemical and mechanical processes; whereas in bottom-up methods, atoms or molecules are used as the starting materials. The most commonly used strategy is the bottom-up approach with the chemical methods such as electrochemical techniques, chemical and photo-chemical reductions dominating since they offer control over the physico-chemical properties of the NPs synthesized (Jamkhande *et al*., 2019; Gutiérrez-Cruz *et al*., 2022).

Various studies reported have shown that size, stability, morphology and physico-chemical properties of the synthesized NPs are significantly influenced by experimental techniques and conditions, kinetics of interactions between the metallic ions and reducing agents as well as the adsorption processes of stabilizing agents with the NPs (Jamkhande *et al*., 2019). Therefore, the design of the method employed for NPs synthesis in which the aforementioned properties are optimized has in the recent past elicited a lot of interest in studies involving metallic NPs syntheses and applications. Chemical synthesis has been widely reported due to its enhanced tunability of the particle size, morphology, stability, composition and obtain new materials that cannot be found in the bulk state (Habibullah *et al*., 2021). These methods mainly employ reducing agents such as ascorbic acid, tri-sodium citrate, formaldehyde, hydroxylamine hydrochloride and borohydride to facilitate the formation of the NPs (De Oliveira *et al*., 2020).

Specifically, citrate reduction method enhances the formation of NPs with numerous advantages outlined in **Figure 3.2**. This method also provide vital information on systematic steps for the formation and structural design of multi-atomic nanostructures such as bimetallic NPs (McDarby *et al*., 2020). Bimetallic NPs are made up of two monometallic NPs resulting into enhanced electro-catalytic properties compared to the individual monometallic counterparts. The study of bimetallic NPs synthesis from noble metals such as Ag, Au and Pt, and their applications have received particular scientific interest from various researchers due to their higher property tunability and superior features compared to those of other metals (Ahemad *et al.*, 2022). The main types of bimetallic NPs are the alloy and core@shell nanostructures which differ based on their mode of preparation and atomic arrangements (Zaleska-Medynska *et al*., 2016). The alloy bimetallic NPs are prepared by simultaneous reduction of the metallic salt precursors to NPs while

core@shell NPs are synthesized through progressive reduction of the more noble metallic salt precursors accompanied by the reduction of the salt precursors of the less noble metal.

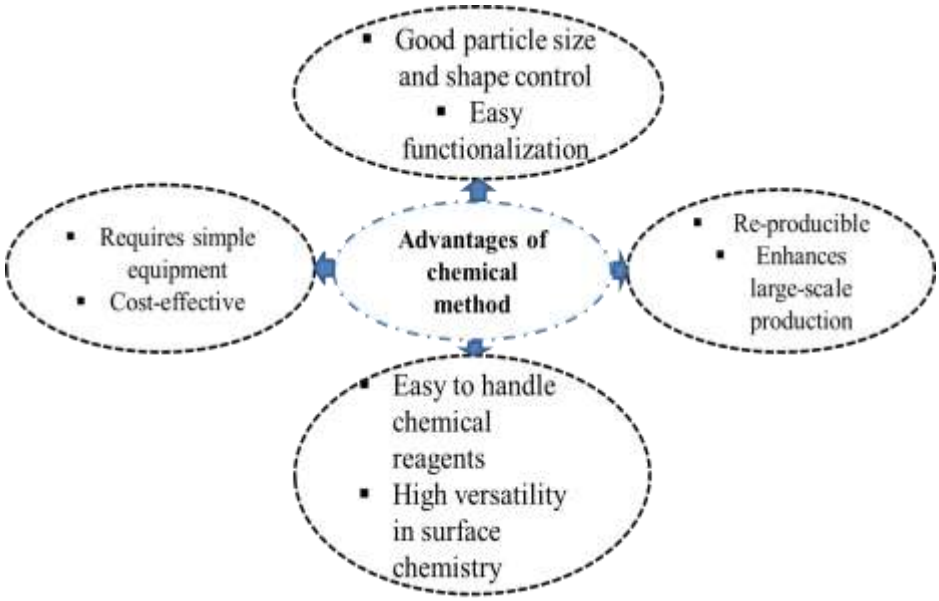

Figure 3.2: Main advantages of chemical method.

The order of metallic arrangements in these nanostructures is mainly affected by the differences in the reduction potentials of the metals making up the bimetallic NPs and it becomes pronounced as the reduction potential differences between the metals increases (Zaleska-Medynska *et al*., 2016). In the synthesis of bimetallic Ag-Au NPs, Ag is less noble than Au and therefore it is reduced faster than Au hence forming the core layer while the Au forms the shell leading to Ag (core)-Au (shell) bimetallic NPs structural configuration. The structure, size, morphology and the composition of Ag-Au bimetallic NPs formed can be studied using the techniques outlined in **Figure 3.3**. The synthesis of Ag-Au bimetallic NPs and its applications in electro-analysis studies have been widely reported compared to other bimetallic NPs due to the similar lattice parameters of the monometallic counterparts with face-centred cubic crystal structures (Das *et al*., 2021). However, proper optimization of the bimetallic NPs properties such as structure, size, shape and morphology requires suitable control of the concentrations of Ag and Au metallic salt precursors (Darabdhara *et al*., 2019). Studies have shown that the shape, structure, composition and design of Ag-Au NPs significantly influence their electro-catalytic activities (Li *et al*., 2017 ; Xue *et al.*, 2019). Au-Ag NPs with different geometries such as truncated cubes, nanocubes, octahedral,

truncated octahedral and cuboctahedral have been synthesized and shown to have varying properties (Sundarapandi *et al*., 2018).

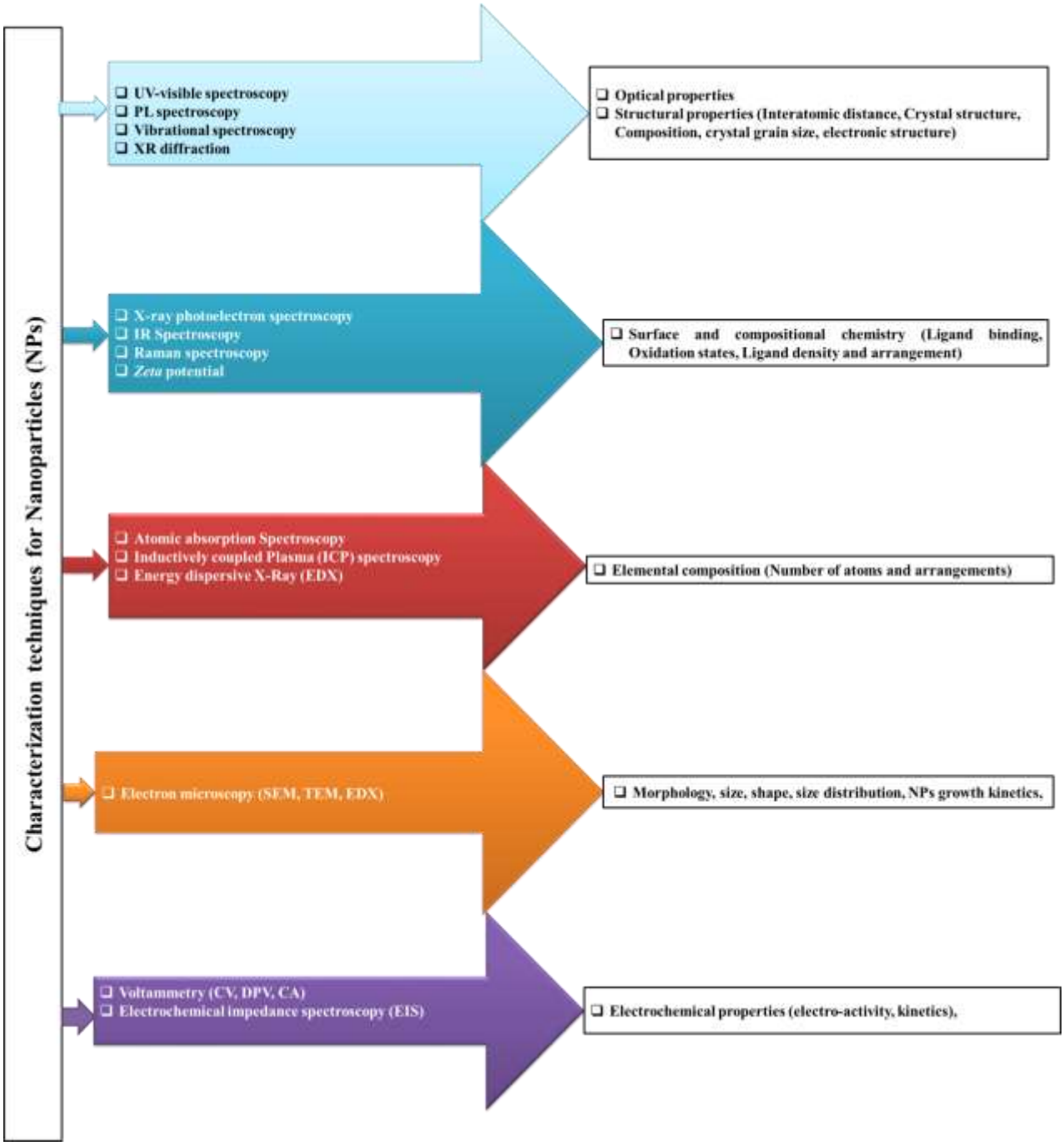

Figure 3.3: Characterization techniques for nanoparticles

Studies have also shown that differing methods and metallic compositions produce bimetallic Ag-Au NPs with varying electro-catalytic activities (Masibi *et al*., 2020). Bimetallic Ag-Au NPs of

similar size but varying Au: Ag ratios of 3:1 have shown higher catalytic activity compared to those with Au: Ag ratio of 1:1 or 1:3 (Holden *et al*., 2014). Therefore, in this study, the synthesis of only one molar of Ag: Au (1:2) NPs with relatively higher content of Au was mainly motivated by its enhanced electro-catalytic activity as supported by the literature (Holden *et al*., 2014). The systematic synthesis of the monometallic Ag NPs, Au NPs and bimetallic Ag-Au NPs synthesis was pursued in this study via citrate reduction method. The bimetallic Ag-Au NPs was synthesized via co-reduction of the corresponding monometallic precursors in a-one-pot synthesis approach. UV-visible spectroscopy was used to investigate the optical properties and appearance of the synthesized NPs. The FT-IR spectra were used to ascertain the capping and reducing action of tri-sodium citrate (TSC) in the synthesis of the NPs and also to have an idea on the existence of IR active chemical bonds between the synthesized NPs and TSC. The morphology of the synthesized NPs was investigated using SEM while the XRD technique was used to determine the crystallinity of the NPs.

3.2 Experimental

3.2.1 Reagents and materials

Silver nitrate ($AgNO_3$, 99.9 %), chloroauric acid ($HAuCl_4$. $3H_2O$, 99.9 %), tri-sodium citrate ($Na_3C_6H_5O_7$, 99.0 %), hydrochloric acid (HCl, 99.9 %) and nitric acid (HNO_3, 68.0 %) were purchased from *Sigma-Aldrich*. Deionised distilled water purified by a Milli-QTM system (18.2 MΩ.cm) was used throughout the experiment to wash and rinse the apparatus as well as a solvent. All the glasswares and magnetic stirrers were cleaned using aqua-regia (3 HCl: 1 HNO_3) and rinsed thoroughly with the de-ionized distilled water before use.

3.2.2 Synthesis of monometallic nanoparticles

Silver nanoparticles (Ag NPs) were synthesized by the reduction of silver nitrate using tri-sodium citrate (TSC). A solution of 2.5 mM $AgNO_3$ was heated to a temperature of 240 °C on a hot plate and left to boil for 15 minutes. To this solution, 10.0 mM TSC solution was added drop-wise with vigorous stirring and heating for 1 hour until a pale yellow colour was observed. The mixture was then removed from the hot plate and cooled to room temperature with continuous stirring. In the case of Au NPs, Erlenmeyer flask containing 5.0 mM $HAuCl_4.3H_2O$ solution was covered with a watch glass and heated on a hot-plate with constant and vigorous stirring to a temperature of 240 °C for 15 minutes. To this solution, 10.0 mM TSC solution was added drop-wise with vigorous

stirring and heating for 1 hour until a pale-purple colour was observed. The solution was then cooled to room temperature with continuous stirring to prevent agglomeration of the NPs.

3.2.3 Synthesis of bimetallic nanoparticles

The synthesis of Ag-Au (1:2) bimetallic NPs was carried out through the co-reduction of the metallic Ag and Au precursors using TSC as both reducing and capping agents. To 100 mL Erlenmeyer flask, 20 mL of $AgNO_3$ (2.5×10^{-3} M) and 40 mL of $HAuCl_4$ (5.0×10^{-3} M) was heated to boiling at a constant temperature of 240 ℃ under vigorous stirring followed by addition of 2 mL of TSC. The reaction mixture was then heated under reflux for another one hour with continuous and vigorous stirring and the appearance of brown colour indicated the formation of Ag-Au (1:2) bimetallic NPs. The solution was then allowed to cool under vigorous stirring to minimise agglomeration of the NPs.

3.3 Characterization of nanoparticles

3.3.1 Fourier Transform-Infra-red (FT-IR)

The FT-IR measurements were performed using FT-IR spectrometer Spectrum Two (PerkinElmer, USA) in the spectral range of 4000-400 cm^{-1}. The sample compartment was cleaned with isopropanol followed by a background scan to minimize the effects of noise and interference. Approximately 1 mL of each of the NPs was placed on the cleaned sample compartment and scanned sequentially in the aforementioned spectral range.

3.3.2 Ultraviolet-visible (UV-Vis)

The synthesized NPs sample solutions were centrifuged and placed in quartz cuvettes for the measurement of characteristic absorbance peaks using 1800-Shimadzu UV-visible dual-beam spectrophotometer, Advanced African Technology, serial number: 127471, operated at a resolution of 1 nm in the wavelength range of 200 - 800 nm. Approximately 2 mL of each of the synthesized NPs placed in a clean cuvette was inserted into the sample compartment together with another cuvette containing Milli-QTM water used as a blank. The blank was used for baseline correction and background check so as to minimize the effects of interference on the NPs wavelength of interest. The optical band gaps for each NP was determined by analyzing UV-visible spectra obtained using Tauc's model (Haq *et al*., 2021).

3.3.3 Scanning electron microscopy (SEM)

The size distribution and morphology of the synthesized NPs in powdered form were determined by spreading the NPs onto adhesive tapes covered by electro-active gold film and the images of each of the NPs were finally obtained using field emission scanning electron microscopy (Hitachi FE-SEMSU6600). The images of each of the NPs were recorded at a magnification of 1 µm and operating voltage of 5 kV. The micrographs obtained were analysed by Image J software.

3.3.4 X-ray diffraction (XRD)

The diffraction patterns of the nanoparticles were obtained using Bruker AXS (Germany) D_8 Advanced High-Resolution diffractometer (tube voltage = 40 kV; tube current = 40 mA). The XRD spectra were recorded in the range of 10° - 90° using an X-ray source of Cu-Kα (λ = 0.15406 nm) monochromatic radiation.). The NPs were first centrifuged and dried to a powdered form at room temperature (298 K). The size of each of the NPs was calculated using Debye-Scherrer equation (William Carry *et al*., 2021).

3.4 Results and Discussion

3.4.1 FT-IR studies of the nanoparticles

The FT-IR spectra of the synthesized NPs are as shown in **Figure 3.4**. As shown in the figure, the spectra of TSC without the NPs showed absorption bands at 1068, 1645 and 3320 cm^{-1}.

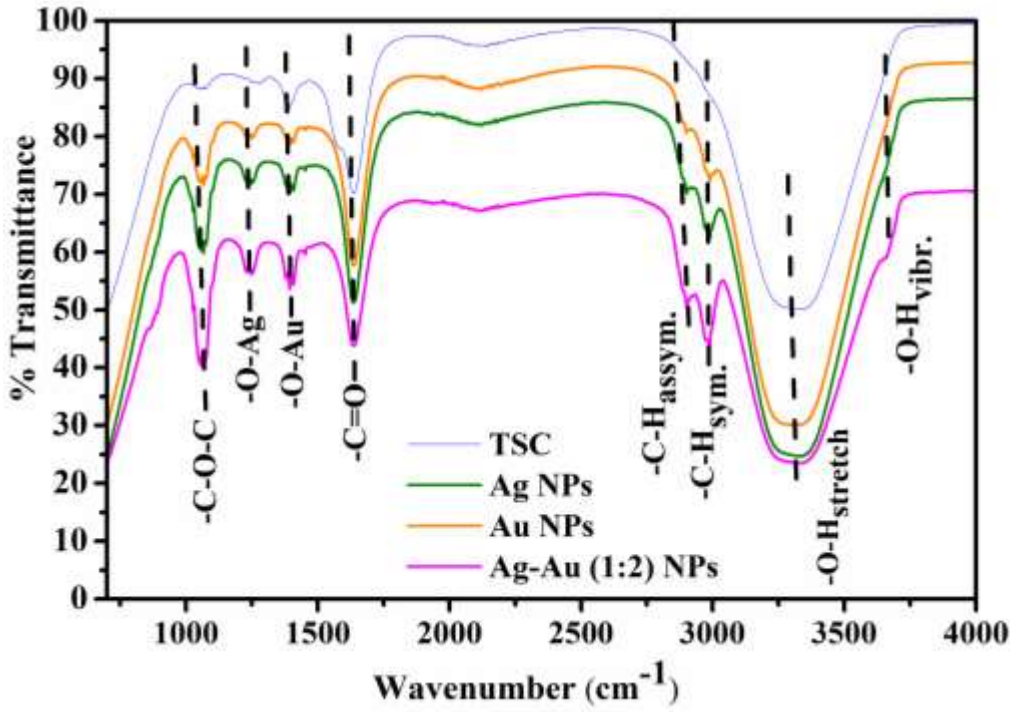

Figure 3.4: FT-IR spectroscopy for (a) Ag NPs, (b) Au NPs and bimetallic Ag-Au (1:2) NPs

The distinct sharp and broad bands at 1645 and 3320 cm^{-1} signified -C=O and -O-H bond stretches, respectively. The broadness of the absorption band at 3320 cm^{-1} was attributed to hydrogen bonding between the water molecules. The characteristic absorption band at 1068 cm^{-1} clearly indicated -C-O-C- bond stretching vibrations within the citrate ion capping the NPs. This peak also corroborated the presence of TSC (Ojea-Jiménez *et al*., 2011). In the presence of synthesized Ag, Au and Ag-Au (1:2) NPs within the TSC, it was observed that the intensity of the aforementioned bands increased relative to their original positions. This clearly indicated the existence of intimate interactions between the synthesized NPs and TSC.

The bands with significant increase in the absorbance and intensity at 1068, 1259 and 1420 cm^{-1} can be ascribed to ligand-metallic interactions between TSC and metallic ions (Ag^{+} and Au^{3+}) in the synthesized NPs. This is in agreement with a study described elsewhere (Gopinath *et al*., 2016). The variation in intensity of these peaks indicated the involvement of TSC in the reduction and stabilization of Ag, Au monometallic and Ag-Au bimetallic NPs.

3.4.2 Optical properties of nanoparticles

The formation of Ag NPs, Au NPs and bimetallic Ag-Au (1:2) NPs was also confirmed by UV-visible absorption spectroscopy through the observed colour changes (**section 3.3.2**) and localized surface plasmon resonance (LSPR) of the NPs shown in the spectra (**Figure 3.5)**.

The spectra of the NPs showed broad and narrow absorption bands for both Ag and Au NPs in the monometallic and bimetallic compositions. The pure Ag and Au NPs showed weaker and broader absorption bands centred at 497 and 580 nm, respectively. However, the LSPR of pure Au NPs was extremely broader with lower intensity than Ag NPs. This suggested that the synthesized Au NPs were of larger particle sizes than Ag NPs. This was theoretically determined to be 98 nm according to an equation proposed by Khlebtsov (Lomelí-Marroquín *et al*., 2019).

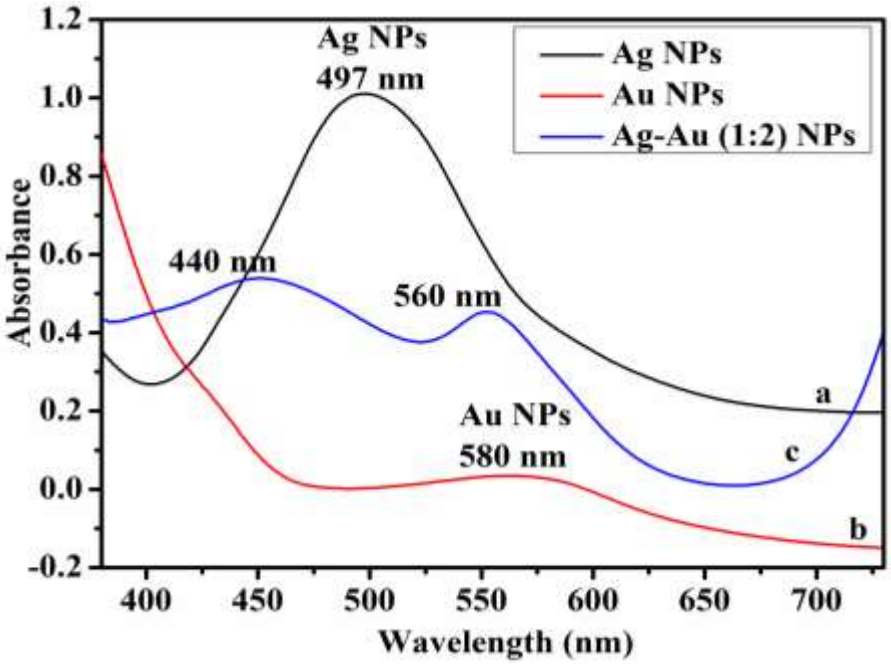

Figure 3.5: UV-visible absorption spectra of Ag NPs (curve a), Au NPs (curve b) and (Ag-Au (1:2) bimetallic NPs (curve c)

The large size of the NPs can be attributed to enhanced agglomeration due to the higher synthetic temperature employed (Aritonang *et al*., 2019). The frequency and width of LSPR in synthesized NPs are mainly affected by their size, shape, metallic dielectric constants and surrounding medium (George *et al*., 2020). The broad and weaker absorption bands observed can be ascribed to enhanced polydispersity and wider size distribution of the synthesized NPs (Piñero *et al.*, 2017).

The spectrum of Ag-Au (1:2) bimetallic NPs did not show a single absorption band lying between the LSPR bands of Ag and Au NPs on the spectra as would be expected with Ag, Au and the bimetallic NPs of comparable sizes. This was due to almost similar lattice constants of 0.408 and 0.409 nm for Au and Ag, respectively as well as their similar face-centred crystal structure (Godfrey *et al*., 2017). This is in agreement with a study reported elsewhere (Zhang *et al*., 2011). However, in this study, two distinct and well separated absorption bands centred at 410 and 508 nm for Ag and Au NPs, respectively within the bimetallic NPs were observed. This agrees with a study reported elsewhere (Elemike *et al*., 2019). Both LSPR bands of the NPs blue-shifted with respect to their monometallic counterparts signifying the formation of Ag-Au (1:2) bimetallic NPs of relatively smaller-sized particles (Lomelí-Marroquín *et al*., 2019). The Ag and Au NPs showed broad and narrow LSPR bands, respectively within the bimetallic NPs. This indicated that the synthesized Ag-Au bimetallic NPs comprised Au NPs of smaller-sizes and spherically-shaped particles as compared to Ag NPs (Duan & Wang, 2013).

The optical band gaps for each of the NPs determined using Tauc's model (Singh et al., 2016) based on the allowed direct (n = 1/2) electron transition and **Equation 3.1** are presented in **Figure 3.6**

$$(\propto hv)^{\frac{1}{n}} = B(hv - Eg) \ldots\ldots\ldots\ldots\ldots\ldots\ldots\ldots\ldots\ldots\ldots\ldots\ldots\ldots\ldots\ldots\ldots\ldots (\mathbf{3.1})$$

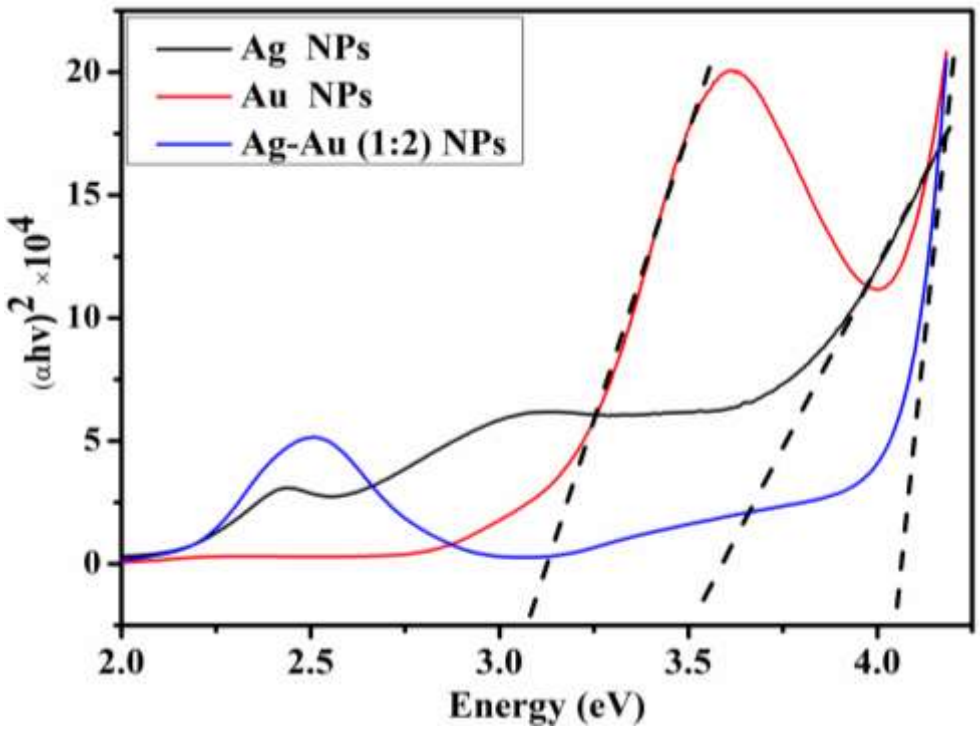

Figure 3.6: Variation of $(\alpha hv)^2$ with hν for Ag NPs, Au NPs and Ag-Au (1:2) NPs as a function of wavelength (λ) at n =1/2

The band gap energies were obtained by extrapolating the linear portions of $(\alpha hv)^2$ versus *hv* plots to the x-axis where $(\alpha hv)^2 = 0$. The band gaps (eV) for Ag, Au and the bimetallic NPs were 3.50, 3.10 and 4.05, respectively. These values were in close agreement with those already reported in the literature for monometallics, bimetallics and doped NPs (Larquet et al., 2019). The band gap energies showed an increase from 3.10 eV for Au NPs to 4.05 eV for Ag-Au (1:2) NPs. This is in agreement with the observed variations in UV-visible absorption spectrum where Ag (in the bimetallic) and Au (monometallic) NPs showed broad absorption bands (**Figure 3.5**). However, Au NPs had a broader and weaker absorption band centred at a higher wavelength (560 nm) than Ag NPs. This significantly influenced the band gap energy of the Au NPs due to larger particle-size effect. The relatively lower band gap energy of Au NPs can also be ascribed to a strong influence of the structure and morphology of the NPs since smaller Au NPs have wider optical band gaps (Alluhaybi *et al*., 2019). This observation clearly revealed that there was no remarkable change in the conduction band density of Au NPs states since continuous density states of bulk materials are known to transform to a set of discrete energy states as the optical band gap of a NP

increases. The values of band gap energy obtained for Au NPs were, however, in close agreement with those reported in the literature (Jagannath *et al*., 2018).

The relatively higher band gap energy for Ag NPs can be attributed to smaller-sized and monodispersed Ag NPs as shown by the relatively narrower absorption band centred at 497 nm (**Figure 3.5**). This value was higher than those already reported for bulk Ag (0.0 eV) and Ag dimer (2.6 eV) NPs (Gad & Hegazy, 2019). This is in agreeement with studies described elswhere (Taleshi, 2015). These results were also in agreement with theoretical calculations (Costa *et al.*, 2016).

3.4.3 Scanning electron microscopy (SEM)

The SEM images (**Figures 3.7**) indicated that the synthesized Ag, Au and bimetallic Ag-Au (1:2) NPs were generally of higher dispersity. From the SEM images of Ag NPs (**Figure 3.7 a**), it was observed that the NPs comprised semi-spherical, cuboidal-hexagonal agglomerated particles with wider size distribution of 10 - 50 nm. The particles were also polydispersed with smaller particles coalescing around larger ones forming polyp-shaped clusters. This was supported by the larger particle size determined statistically as 21.79 ± 0.79 nm. This can be attributed to the effects of agglomeration of the NPs on the glass substrate during the deposition process (Akram *et al.*, 2021).

The Au NPs SEM micrograph (**Figure 3.7 b**) showed mixtures of larger cuboidal-hexagonal and relatively smaller spherical particles with rugged edges randomly distributed within the sample holder. The numerous smaller spherical particles coalesced in a web-like structure forming cloudy-shaped clusters of particles. The NPs also had a wider size distribution (0 - 55 nm) with an average particle size of 19.18 ± 0.83 nm attributable to the numerous smaller spherical particles distantly located from the larger and agglomerated ones. The agglomeration of the particles on the holder during deposition could have led to the increase in the particle size observed. The SEM image of the bimetallic NPs (**Figure 3.7 c**) indicated that the particles were of higher dispersity with smaller-sized ones closely intertwined with relatively larger ones in chain like arrangements leading to cauliflower morphology.

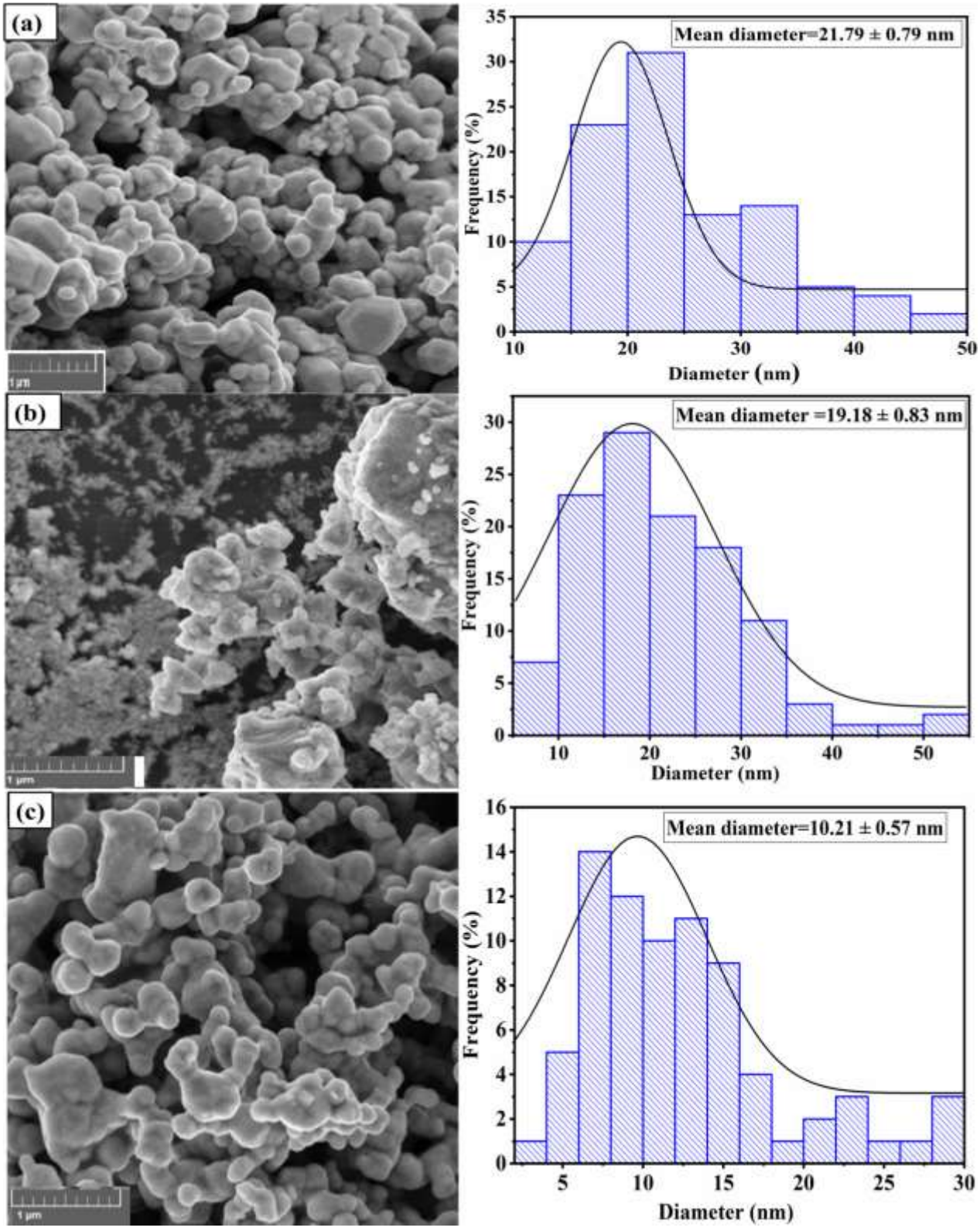

Figure 3.7: Scanning electron micrographs of (a) Ag NPs, (b) Au NPs and (c) Ag-Au (1:2) NPs with their corresponding diameter histograms.

The mean diameter of the particles was estimated as 10.21 ± 0.57 nm with narrow size distribution (0 - 30 nm) compared to the monometallic counterparts indicating that most of the particles were of smaller sizes as evident in the UV-visible data discussed earlier. This can be ascribed to higher content of Au NPs in the bimetallic NPs. Au NPs in the bimetallic had enhanced LSPR band indicating reduced NPs sizes thus narrowing of the band gap as earlier described.

3.4.4 X-Ray diffraction (XRD) analysis

The XRD patterns of Ag NPs (**Figure 3.8 b**) showed four distinct and sharp peaks of characteristic face centred cubic (FCC) planes at 38.26° (111), 46.36° (200), 64.54° (220) and 77.55° (311) according to the JCPDS File No. 04-0783. This confirmed the crystalline nature of Ag NPs (Gogoi *et al*., 2015).

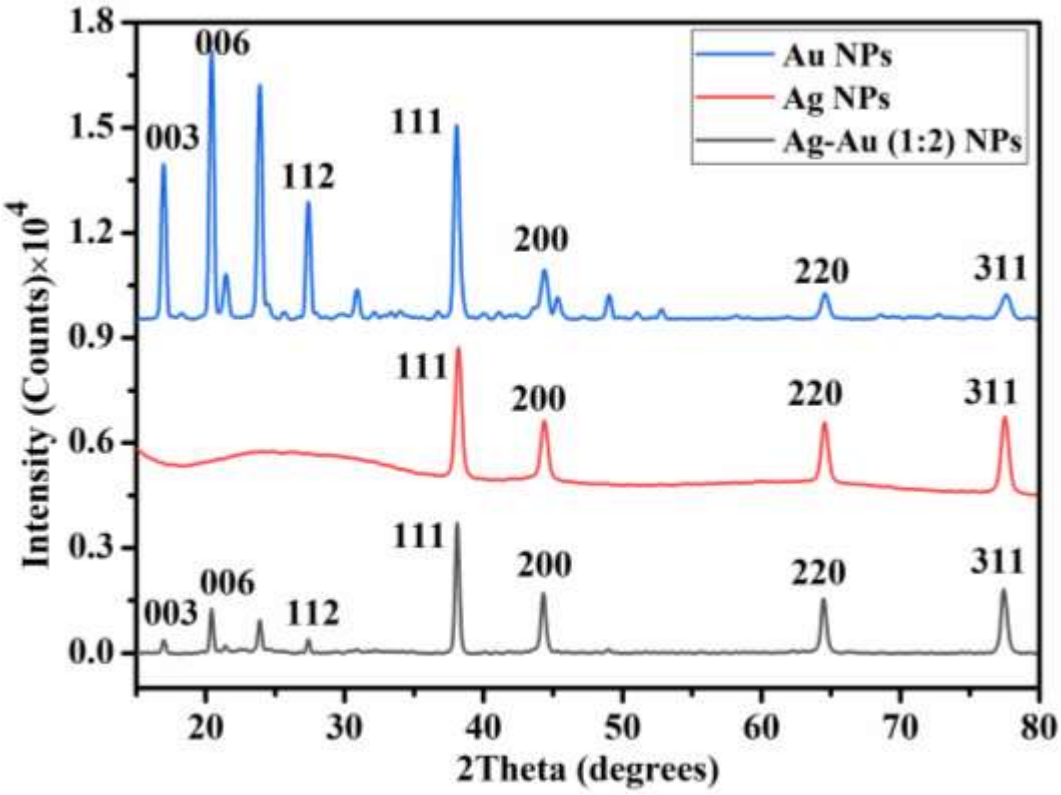

Figure 3.8: XRD patterns of (a) Au NPs (b) Ag NPs and (c) bimetallic Ag-Au (1:2) NPs, respectively

The most intense peak at 2θ = 38.26° was attributed to the diffraction of crystalline spherical Ag NPs in the FCC structures with the typical basal (111) crystallographic lattice plane. This is in

concordance with a study reported elsewhere (Raza *et al*., 2016). The XRD spectrum of Au NPs (**Figure 3.8 a**) showed all single peaks which were clearly distinguished except the ones located at (006) and (200) crystallographic planes which possessed double peaks. This suggested close packing of the Au NPs crystals. These peaks, however, shifted towards less 2 θ values with enhanced intensity indicating good Au NPs crystallinity. The shift in the 2 θ values can be attributed to enhanced d-spacing hence increased lattice volume of Au NPs.

The comparison between the XRD patterns of the monometallic NPs and bimetallic Ag-Au (1:2) NPs (**Figure 3.8 c**) showed that the bimetallic NPs were heterogeneous mixture of Ag and highly crystallined Au NPs. The bimetallic NPs had highly distinguishable diffraction peaks at 2 θ = 38.26° (111), 46.36° (200), 64.54° (220) and 77.55° (311) which were also clearly observed in the monometallic NPs especially Ag NPs. This can be attributed to the presence of bulk Ag and Au with closely similar lattice parameters (Ag-0.409, Au-0.408 nm) according to JCPDS 04-0783 and 04-0784, respectively (Verma *et al*., 2017). Closely similar results for the bimetallic NPs have also been reported (Bonigala *et al*., 2018). The average particle size of the bimetallic NPs was also determined to be 14 nm based on the full-width half maximum (FWHM) data using Scherer equation (Lomelí-Marroquín *et al*., 2019). This was found to be lower than those of the monometallic Ag (23 nm) and Au (16 nm) NPs. The lattice plane of (111) was the most intense just like in the monometallics and this was ascribed to its higher free energy and faster growth rate brought about by the synergy between the two metals. This also suggested the spherical nature of the bimetallic NPs with enhanced atomic-density (111) facets which can provide suitable active sites for appropriate electro-catalytic applications (Da *et al*., 2020). Enhanced atomic-density (111) facets have been reported to increase NPs surface area to volume ratio hence improving the NPs electro-catalytic properties (Carnovale *et al*., 2016).

3.5 Conclusion

The synthesis of the bimetallic Ag-Au (1:2) NPs was successfully achieved through appropriate variation of the concentrations of silver nitrate and tetra-chloroaurate (III) salt pre-cursors thereby yielding bimetallic Ag-Au (1:2) NPs. The variation of the concentrations of the metallic precursors used in this study was mainly based on the enhanced electro-catalytic activity of the bimetallic NPs produced when the content of Au is relatively higher than Ag as supported by studies reported in the literature. Ag-Au (1:2) bimetallic NPs were chemically synthesized through citrate reduction

method and confirmed by optical spectroscopic techniques. The optical band gap of the bimetallic NPs was found to be 4.05 eV which was higher than those of the corresponding monometallic NPs indicating the existence of stronger quantum confinement effects attributable to smaller-sized nature of the NPs as supported by the SEM analysis. This was also evident in the UV-visible results which showed enhanced LSPR for the metals in the bimetallic NPs compared to the monometallic counterparts. These were also in concordance with the XRD results which also affirmed the formation of Ag-Au (1:2) NPs coupled with enhanced crystallinity and FCC metallic structures. The dependence of optical band gaps on NPs size has been widely employed in numerous industrial applications such as the development of sensor technologies. The enhanced atomic-density (111) crystallographic plane described in the bimetallic NPs due to higher concentrations of Au atoms can lead to faster rate of NPs growth coupled with the formation of bimetallic NPs with enhanced surface area to volume ratio hence can be highly applied in electro-catalysis.

3.6 References

Ahemad, M.J., Le, T.D., Kim, D.S. & Yu, Y.T. 2022. Bimetallic AgAualloy@ZnO core-shell nanoparticles for ultra-high detection of ethanol: Potential impact of alloy composition on sensing performance. *Sensors and Actuators B: Chemical*, 359: 131595.

Akram, S., Castellon, J., Agnel, S., Zhou, K., Habas, J.P. & Nazir, M.T. 2021. Multilayer polyimide nanocomposite films synthesis process optimization impact on nanoparticles dispersion and their dielectric performance. *Journal of Applied Polymer Science*, 138(4): 49715.

Alluhaybi, H.A., Ghoshal, S.K., Shamsuri, W.N.W., Alsobhi, B.O., Salim, A.A. & Krishnan, G. 2019. Pulsed laser ablation in liquid assisted growth of gold nanoparticles: Evaluation of structural and optical features. *Nano-Structures and Nano-Objects*, 19(10035): 5.

Aritonang, H.F., Koleangan, H. & Wuntu, A.D. 2019. Synthesis of silver nanoparticles using aqueous extract of medicinal plants' (impatiens balsamina and lantana camara) fresh leaves and analysis of antimicrobial activity. *International Journal of Microbiology*, 2019.

Bonigala, B., Kasukurthi, B., Konduri, V.V., Mangamuri, U.K., Gorrepati, R. & Poda, S. 2018. Green synthesis of silver and gold nanoparticles using Stemona tuberosa Lour and screening

for their catalytic activity in the degradation of toxic chemicals. *Environmental Science and Pollution Research*, 25(32): 32540–32548.

Carnovale, C., Bryant, G., Shukla, R. & Bansal, V. 2016. Size, shape and surface chemistry of nano-gold dictate its cellular interactions, uptake and toxicity. *Progress in Materials Science*, 83: 152–190.

Costa, J.C.S., Taveira, R.J.S., Lima, C.F.R.A.C., Mendes, A. & Santos, L.M.N.B.F. 2016. Optical band gaps of organic semiconductor materials. *Optical Materials*, 58: 51–60.

Da, Y., Li, X., Zhong, C., Deng, Y., Han, X. & Hu, W. 2020. Advanced Characterization Techniques for Identifying the Key Active Sites of Gas-Involved Electrocatalysts. *Advanced Functional Materials*, 30(35): 4.

Darabdhara, G., Das, M.R., Singh, S.P., Rengan, A.K., Szunerits, S. & Boukherroub, R. 2019. Ag and Au nanoparticles/reduced graphene oxide composite materials: Synthesis and application in diagnostics and therapeutics. *Advances in Colloid and Interface Science*, 271(10199): 1.

Das, G.M., William, R. V., Dantham, V.R. & Laha, R. 2021. Study on SERS activity of Au-Ag bimetallic nanostructures synthesized using different reducing agents. *Physica E: Low-Dimensional Systems and Nanostructures*, 129(11465): 6.

Duan, S. & Wang, R. 2013. Bimetallic nanostructures with magnetic and noble metals and their physicochemical applications. *Progress in Natural Science: Materials International*, 23(2): 113–126. http://dx.doi.org/10.1016/j.pnsc.2013.02.001.

Elemike, E.E., Onwudiwe, D.C., Fayemi, O.E. & Botha, T.L. 2019. Green synthesis and electrochemistry of Ag, Au, and Ag–Au bimetallic nanoparticles using golden rod (Solidago canadensis) leaf extract. *Applied Physics A: Materials Science and Processing*, 125(1): 42.

Gad, G.M.A. & Hegazy, M.A. 2019. Optoelectronic properties of gold nanoparticles synthesized by using wet chemical method. *Materials Research Express*, 6(8): 85024.

George, J.M., Priyanka, R.N. & Mathew, B. 2020. Bimetallic Ag–Au nanoparticles as pH dependent dual sensing probe for Mn(II) ion and ciprofloxacin. *Microchemical Journal*, 155(10468): 6.

Godfrey, I.J., Dent, A.J., Parkin, I.P., Maenosono, S. & Sankar, G. 2017. Structure of gold--silver nanoparticles. *The Journal of Physical Chemistry C*, 121: 1957–1963.

Gogoi, P., Saikia, B.J. & Dolui, S.K. 2015. Effects of nickel oxide (NiO) nanoparticles on the performance characteristics of the jatropha oil based alkyd and epoxy blends. *Journal of Applied Polymer Science,* 132(8).

Gopinath, K., Kumaraguru, S., Bhakyaraj, K., Mohan, S., Venkatesh, K.S., Esakkirajan, M., Kaleeswarran, P., Alharbi, N.S., Kadaikunnan, S., Govindarajan, M., Benelli, G. & Arumugam, A. 2016. Green synthesis of silver, gold and silver/gold bimetallic nanoparticles using the Gloriosa superba leaf extract and their antibacterial and antibiofilm activities. *Microbial Pathogenesis*, 101: 1–11.

Gutiérrez-Cruz, A., Ruiz-Hernández, A.R., Vega-Clemente, J.F., Luna-Gazcón, D.G. & Campos-Delgado, J. 2022. A review of top-down and bottom-up synthesis methods for the production of graphene, graphene oxide and reduced graphene oxide. *Journal of Materials Science,* 57(31): 14543–14578.

Habibullah, G., Viktorova, J. & Ruml, T. 2021. Current Strategies for Noble Metal Nanoparticle Synthesis. *Nanoscale Research Letters,* 16(1): 1–12.

Haq, S., Ahmad, P., Khandaker, M.U., Faruque, M.R.I., Rehman, W., Waseem, M. & Din, S.U. 2021. Antibacterial, antioxidant and physicochemical investigations of tin dioxide nanoparticles synthesized via microemulsion method. *Materials Research Express*, 8(3): 35013.

Holden, M.S., Nick, K.E., Hall, M., Milligan, J.R., Chen, Q. & Perry, C.C. 2014. Synthesis and catalytic activity of pluronic stabilized silver-gold bimetallic nanoparticles. *RSC Advances*, 4(94): 52279–52288.

Jagannath, G., Eraiah, B., NagaKrishnakanth, K. & Venugopal Rao, S. 2018. Linear and nonlinear optical properties of gold nanoparticles doped borate glasses. *Journal of Non-Crystalline Solids,* 482: 160–169.

Jamkhande, P.G., Ghule, N.W., Bamer, A.H. & Kalaskar, M.G. 2019. Metal nanoparticles synthesis: An overview on methods of preparation, advantages and disadvantages, and

applications. *Journal of Drug Delivery Science and Technology*, 53: 101174.

Karkare, M.M. 2015. The Direct transition and not Indirect transition, is more favourable for Band Gap calculation of Anatase TiO2 nanoparticles. *International journal of Scientific & Engineering Research*, 6(12): 48–53.

Khalaji, A.D. & Das, D. 2014. Synthesis and characterizations of NiO nanoparticles via solid-state thermal decomposition of nickel(II) Schiff base complexes. *International Nano Letters*, 4(3): 1–5.

Larquet, C., Nguyen, A.M., Glais, E., Paulatto, L., Sassoye, C., Selmane, M., Lecante, P., Maheu, C., Geantet, C., Cardenas, L., Chanéac, C., Gauzzi, A., Sanchez, C. & Carenco, S. 2019. Band Gap Engineering from Cation Balance: The Case of Lanthanide Oxysulfide Nanoparticles. *Chemistry of Materials*, 31(14): 5014–5023.

Li, Y., Zhang, W., Zheng, Y., Chen, J., Yu, B., Chen, Y. & Liu, M. 2017. Controlling cation segregation in perovskite-based electrodes for high electro-catalytic activity and durability. *Chemical Society Reviews*, 46(20): 6345–6378.

Lomelí-Marroquín, D., Cruz, D.M., Nieto-Argüello, A., Crua, A.V., Chen, J., Torres-Castro, A., Webster, T.J. & Cholula-Díaz, J.L. 2019. Starch-mediated synthesis of mono- and bimetallic silver/gold nanoparticles as antimicrobial and anticancer agents. *International Journal of Nanomedicine*, 14: 2171–2190.

Masibi, K.K., Fayemi, O.E., Adekunle, A.S., Sherif, E.S.M. & Ebenso, E.E. 2020. Electrochemical Determination of Caffeine Using Bimetallic Au−Ag Nanoparticles Obtained from Low-cost Green Synthesis. *Electroanalysis*, 32(12): 2745–2755.

McDarby, S.P., Wang, C.J., King, M.E. & Personick, M.L. 2020. An Integrated Electrochemistry Approach to the Design and Synthesis of Polyhedral Noble Metal Nanoparticles. *Journal of the American Chemical Society*, 142(51): 21322–21335.

Ojea-Jiménez, I., Bastús, N.G. & Puntes, V. 2011. Influence of the sequence of the reagents addition in the citrate-mediated synthesis of gold nanoparticles. *Journal of Physical Chemistry C*, 115(32): 15752–15757.

De Oliveira, P.F.M., Michalchuk, A.A.L., Marquardt, J., Feiler, T., Prinz, C., Torresi, R.M.,

Camargo, P.H.C. & Emmerling, F. 2020. Investigating the role of reducing agents on mechanosynthesis of Au nanoparticles. *CrystEngComm*, 22(38): 6261–6267.

Piñero, S., Camero, S. & Blanco, S. 2017. Silver nanoparticles: Influence of the temperature synthesis on the particles' morphology. In *Journal of Physics: Conference Series*. IOP Publishing: 12020.

Raza, M.A., Kanwal, Z., Rauf, A., Sabri, A.N., Riaz, S. & Naseem, S. 2016. Size- and shape-dependent antibacterial studies of silver nanoparticles synthesized by wet chemical routes. *Nanomaterials*, 6(4): 74.

Singh, J., Pandey, J., Gupta, R., Kaurav, N. & Tripathi, J. 2016. Structural and optical properties of nanostructured nickel. *AIP Conference Proceedings*, 1728(6).

Sundarapandi, M., Viswanathan, P., Sivakumar, S. & Ramaraj, R. 2018. Catalytic Activities of Mono- and Bimetallic (Gold/Silver) Nanoshell-Coated Gold Nanocubes toward Catalytic Reduction of Nitroaromatics. *Langmuir*, 34(46): 13897–13904.

Taleshi, F. 2015. Study of morphology and band gap energy of TiO2-carbon nanotube nanocomposite. *Journal of Materials Science: Materials in Electronics*, 26(5): 3262–3267.

Verma, M., Newmai, M.B. & Senthil Kumar, P. 2017. Synergistic effect of Au-Ag nano-alloying: Intense SEIRA and enhanced catalysis. *Dalton Transactions*, 46(29): 9664–9677.

William Carry, M., Vinoth Rathan, S., Raja, A., Senthil Pandian, M. & Ramasamy, P. 2021. Non-Debye relaxation of AgBiSe2 single crystal featuring flip-flop jumps in Bi valence state. *Materials Letters*, 300: 130179.

Xue, Y., Li, H., Ye, X., Yang, S., Zheng, Z., Han, X., Zhang, X., Chen, L., Xie, Z., Kuang, Q. & Zheng, L. 2019. N-doped carbon shell encapsulated PtZn intermetallic nanoparticles as highly efficient catalysts for fuel cells. *Nano Research*, 12(10): 2490–2497.

Yathisha, R.O. & Arthoba Nayaka, Y. 2018. Structural, optical and electrical properties of zinc incorporated copper oxide nanoparticles: doping effect of Zn. *Journal of Materials Science*, 53(1): 678–691.

Zaleska-Medynska, A., Marchelek, M., Diak, M. & Grabowska, E. 2016. Noble metal-based

bimetallic nanoparticles: The effect of the structure on the optical, catalytic and photocatalytic properties. *Advances in Colloid and Interface Science*, 229: 80–107.

Zhang, H., Okuni, J. & Toshima, N. 2011. One-pot synthesis of Ag-Au bimetallic nanoparticles with Au shell and their high catalytic activity for aerobic glucose oxidation. *Journal of Colloid and Interface Science*, 354(1): 131–138.

CHAPTER FOUR

COMPARATIVE ELECTROCHEMICAL PROPERTIES OF BIMETALLIC SILVER-GOLD FILM BY DROP-COATING AND ELECTRO-DEPOSITION

4.0 Summary

This chapter mainly describes comparative electrochemical characterizations of chemically and electrochemically modified glassy carbon electrodes (GCE). The GCE was modified through drop-coating and electro-deposition methods, and the electrochemical properties of the nano-films formed studied via CV and DPV techniques in 0.1 M HCl versus Ag/AgCl, reference electrode. The results obtained have been presented and reported based on the determined electrochemical properties and electron transfer kinetic parameters.

4.1 Introduction

Modified electrodes provide important analytical information on the nature of electrochemical processes taking place on them as well as identification of their suitability in various scientific applications (Sun *et al.*, 2020). The development of a good modified electrode requires the knowledge on the fundamental electrochemistry of the electrode such as thermodynamics, mass transfer, kinetics of electron transfer, electrode surface properties and type of electrode materials used (Adarakatti & Kempahanumakkagari, 2019). These properties can be enhanced by using suitable electrode and appropriate electrode modification techniques. The electrodes commonly used in electro-analysis are made of C, Hg, Ag and Pt (Gao *et al*., 2014). Among these, carbon based electrodes such as glassy carbon (GCE) are widely used due to their broader potential window, affordability, low background current, stability and suitability in various electrochemical applications (Pandikumar & Devi, 2021). However, they are susceptible to fouling and non-specific redox behaviors. In order to overcome these challenges, appropriate electrode modifications using NPs to improve stability and sensitivity of the GCE as conductive surfaces are currently undertaken in various electro-analysis studies. The main electrode modification routes which have been widely reported are the chemical and electrochemical methods (Adarakatti & Kempahanumakkagari, 2019).

Chemical method is commonly used due to its ability to ensure control over the electrode surface structures (Adarakatti & Kempahanumakkagari, 2019). Most of the electrode reactions in chemically modified electrodes occur at the electrode/electrolyte interfaces and due to this, the

surface chemistry and structure of the electrode play vital roles in enhancing electrode kinetics. Chemical electrode modification method involves introduction of NPs solution onto electrode surface mainly through drop-coating or ink mixing methods (Silpa, 2022). Ink mixing methods depend on the optimized curing temperature and recipe mixture so as to ensure NPs batch reproducibility which dictates stability and sensitivity of modified electriodes (Chu *et al*., 2017). Drop coating method enhances electrode stability due to the placement of specified concentrations of NPs drops onto the electrode surface (Mercante *et al*., 2017). Therefore, the final concentration of NPs drop-coated can be optimized by altering the size and concentration of NPs drop-coated and dispersed in the solution. However, drop-coating is costly and susceptible to NPs aggregation hence control of NPs size and morphology becomes a challenge. Several studies involving chemical modifications of electrodes using NPs such as Bi, Pt, Rh, Au, Ag, Cu and Ni have been reported (Shabalina *et al*., 2017).

Electrochemical deposition involves reduction of metallic ions typically from NPs precursors at a fixed potential or current, electrolysis time and precursor concentration so as to obtain tailor-made NPs uniformly grown on electrode surface (Suresh *et al*., 2021). This process is carried out in one potentiostatic or galvanostatic step by adjusting the applied potential or current to systematically reduce the metallic ions into zero-valence state thus controlling both nucleation and growth rates simultaneously (Sadeghi *et al*., 2013). This leads to the formation of NPs with improved homogeneity and sensitivity (Jiao *et al*., 2021). The control of NPs size and morphology can improve NPs desired attributes such as electro-catalytic properties. The method is also cost-effective because small quantities of precursors are required. It also ensures roughening of the electrode surface thus permitting better NPs adhesion on the electrode surface which in turn enhances signal generation and amplification. Electrochemical method has been widely applied in modifications of electrodes with bimetallic NPs using various electro-analytical techniques such as cyclic voltammetry (CV), potential step and double-pulsed chrono-amperometry (DCPA) (Tonelli *et al*., 2019). Bimetallic NPs have combinations of advantages from different metallic elements involved with minimum disadvantages of each of the metals (Yadav *et al*., 2021).

The selection of metals electro-deposited, their order of deposition and metallic molar ratio are crucial in electrochemical synthesis of bimetallic NPs since they dictate the properties of the resultant bimetallic NPs. Simultaneous electro-deposition of Au and Ag with improved sensitivity

has been reported (Chen *et al*., 2016). Electrodes modified using bimetallic NPs synthesized from Ag, Au, Pd, Ir and Pt have been widely reported due to their improved electro-catalytic activities towards different analytes with enhanced electrode kinetics (Alam *et al*., 2019). However, the applications of bimetallic Ag-Au NPs modified electrodes in electro-analysis studies are dominating (Li & Jin, 2021). This is due to their unique physico-chemical properties, optimal conductivity, biological compatability and reduced over-potentials for electro-analytical reactions (Murtada & Moreno, 2020). Therefore, in this study, Ag NPs, Au NPs and bimetallic Ag-Au (1:2) NPs were synthesized via chemical reduction and electrochemical methods. The GCE was modified with each of the NPs by drop-coating and electro-deposition methods. Successful electro-deposition of each of the NPs onto GCE was confirmed via double-pulsed chrono-amperometry (DPCA) technique. The electrochemical properties of the GCE nano-films formed were studied via CV and DPV techniques in 0.1 M HCl versus Ag/Ag Cl. The data obtained from the CV studies were used to determine electrochemical parameters such as electron transfer coefficient (α), heterogeneous rate constant (k_s), electrode surface coverage (Γ), NPs charge contribution (Q) and diffusion coefficient (D). These parameters gave insights into the fundamentals of electron transfer kinetics in chemically and electrochemically modified electrodes and their applicability as sensing devices.

4.2 Experimental

4.2.1 Electrode cleaning and electro-deposition of nanoparticles

The GCE was first cleaned sequentially using alumina micro-powder (1.0, 0.3, 0.05 µm) and polishing pads, sonicated for 10 minutes in ethanol / water (1:1, v/v) followed by air-drying under room temperature and finally activated in 0.5 M H_2SO_4 by running CV within the potential range of -0.2 to -1.5 V for 5 cycles.

Ag NPs were electro-deposited onto GCE in aqueous mixture of 2.5 mM $AgNO_3$/0.1 M $NaNO_3$ using DPCA. The pulse parameters applied included; the first pulse at E_1 = -0.13 V for Ag nuclei formation within 3 s followed by second pulse for growth at E_2 = -0.26 V, for 2 s (vs. Ag/AgCl). The electro-deposition of Au NPs was done by dipping the polished GCE into a mixture of 5.0 mM $HAuCl_4$/0.5 M H_2SO_4 followed by application of deposition potential at $E_{dep.}$ = -0.8 V for 3 s. Bimetallic Ag-Au (1:2) NPs were electro-deposited from aqueous mixture of 1.0 mL of 2.5 mM $AgNO_3$/0.1 M $NaNO_3$ and 2.0 mL of 5.0 mM $HAuCl_4$/0.5 M H_2SO_4 using DPCA under the

following described conditions: the first pulse: was applied at E_1 = -0.4 V, for time 2 s; and the second pulse: E_2 = -0.7 V, for 3 s. The surfaces of each of the modified GCE nano-films were carefully cleaned with doubly-distilled water and dried under room temperature for 15 minutes to ensure stable nano-films.

4.2.2 Chemical modification of GCE through drop-coating

Before drop-coating, the GCE was first thoroughly polished as described above. The polished GCE was drop-coated with each of the NPs suspensions and left to dry for 2.5 hours yielding stable GCE/Ag NPs, GCE/Au NPs and GCE/ Ag-Au (1:2) NPs films.

4.2.3 Electrochemical characterization of modified GCE nano-films

The entire electrochemical experiment was conducted using µStat-i 400s potentiostat: IS4091096A, serial No: 176437 (Metrohm, Spain) connected to a conventional three-electrode system; GCE with a diameter of 0.3 cm (A = 0.071 cm^2), Ag/Ag Cl (3.0 M KCl) and Pt wire were used as working, reference and counter electrodes, respectively. All the experiments were performed at room temperature (298 K). Double-pulsed chrono-amperometry (DPCA) was used to investigate the nucleation and growth processes of each of the electro-deposited NPs while both CV and DPV techniques were employed to evaluate the electroactivities of each of the nano-films formed in 0.1 M HCl (vs. Ag/AgCl). The data on CV and DPV were obtained at same scan rate but varying potential ranges (vs. Ag/AgCl) based on the electro-redox reactions of each of the investigated nano-films.

Electrochemical band gap studies were done by running the CVs of each of the modified nano-films in 0.1 M HCl (vs. Ag/AgCl) and the voltammograms obtained analysed using Breda's equation (Brédas *et al*., 1983). The kinetic studies for each of the nano-films obtained were also done using CV at scan rate ranges of (10-130) mVs^{-1}. The *Laviron's* and *Randle's* plots obtained from the scan rate studies were used to determine various electron transfer kinetic parameters including electron transfer coefficient (α), heterogeneous rate constant (k_s), NPs electrode surface coverage (Γ), NPs charge contributions (Q) and diffusion coefficient (D).

4.3 Results and Discussion

4.3.1 Electro-deposition of nanoparticles

The current-time (I-t) transient curves for the systematic electro-depositions of Ag NPs, Au NPs and bimetallic Ag-Au (1:2) NPs onto GCE are as shown in **Figure 4.1 a-c**. The main regions in the curves labeled as **1**, **2** and **3** represent nucleation and growth processes for each of the NPs. The nucleation rates for each of the NPs depended on concentration of metallic ions diffusing towards the electrode surface as evident in the electrochemical changes in regions **1**, **2** and **3.** As shown in regions **1** and **2,** the nucleation rates increased with time between t = 1.0 and t = 2.0 s for both Ag and bimetallic NPs.

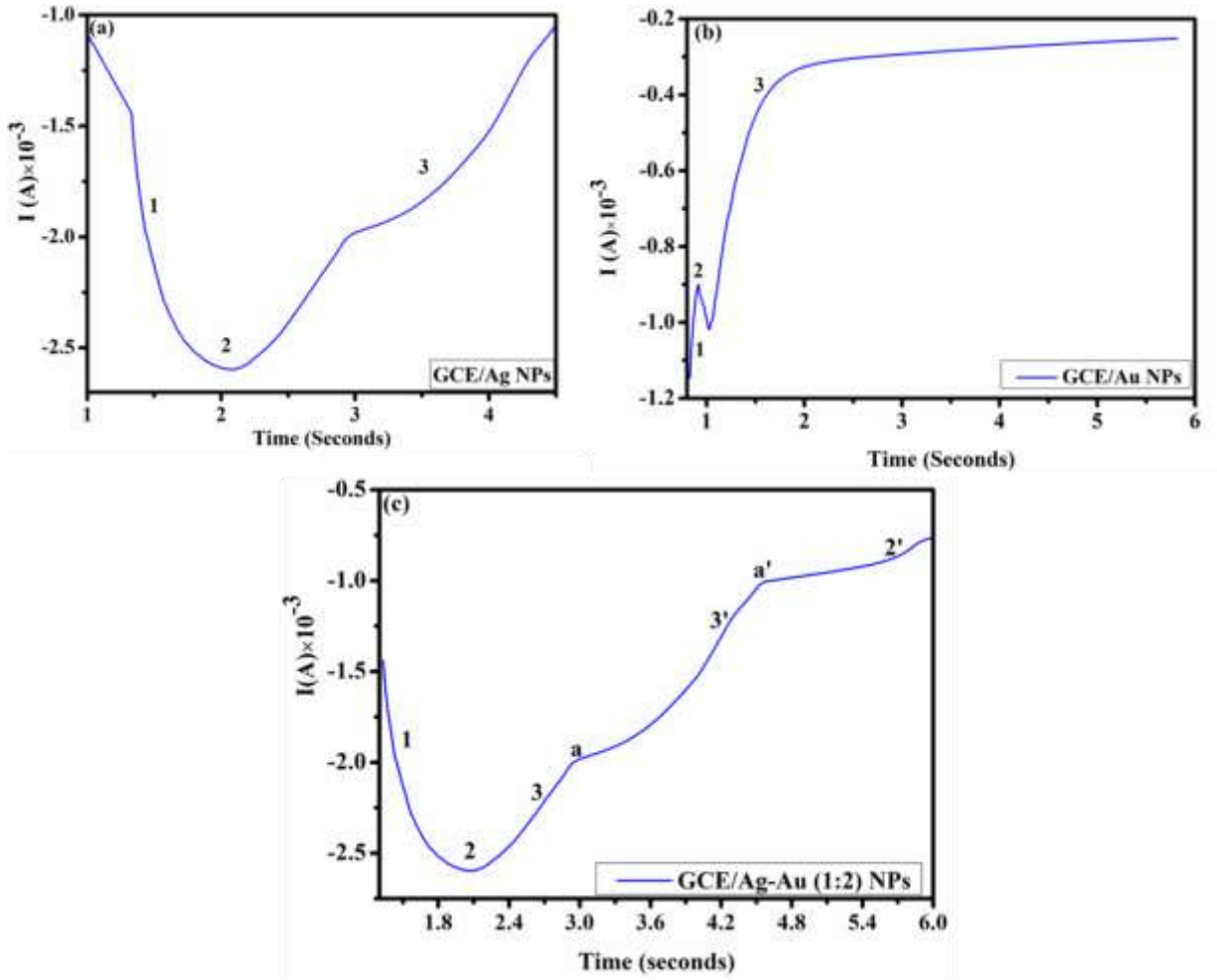

Figure 4.1: Current-time (I-t) transient curves for electro-deposition of (a) Ag NPs, (b) Au NPs and (c) Ag-Au (1:2) NPs onto GCE versus Ag/AgCl

This is depicted by the significant increase in cathodic over-voltage with time. However, the nucleation rate for Au NPs was much more rapid than that of Ag NPs leading to rapid formation of unstable Au nuclei as depicted by the slight decrease in cathodic current immediately after region **2**. This indicates that the nucleic growth for Au NPs was much slower than in Ag NPs as supported by the sharp increase in peak current for Ag NPs. Therefore, Ag nuclei were formed and deposited much earlier than Au NPs. This is in agreement with the theory of nucleation (Staikov, 2016). Earlier deposition of Ag is also supported by the small wave evident between regions **2-3** which is absent in the Au NPs curve but visible in the growth phase of the bimetallic NPs in the same region**.** The increase in peak current in both Ag and Au NPs curves indicated the growth of their nuclei. The increase was sharper and longer in Au NPs compared to Ag NPs leading to the formation of monodispersed NPs with narrow size distribution (Zhang & Tang, 2017). These

indicated increased concentrations of Au^{3+}, their exposure onto the electrode surface and close inter-particle distance between the deposited Au atoms. This is in agreement with a study reported elsewhere (Crespo-Yapur *et al.*, 2019). The final flattening of the current after **region 3** can possibly be ascribed to the depletion of Au salt precursors in the interfacial region resulting into linear diffusional conditions (Sharma *et al*., 2017).

As evident in **Figure 4.1 c**, immediately after **region 3**, the growth rate of Au increased exponentially. This was to prevent the system from exceeding the applied deposition potential for Au. In region **3'**, the current slightly remained stable accompanied by a small wave, **a**, which was replicated as **a'**. These can possibly be ascribed to the formation of Au nuclei which in turn grew over the Ag atoms as shown by the slight increase in current in region **2'** (Crespo-Yapur *et al.*, 2019). This growth process, however, did not conform to the theoretical predictions as advanced elsewhere (Isaev & Grishenkova, 2013).

4.3.2 Electrochemical properties of modified nano-films

The voltammograms of drop-coated (DCT) and electro-deposited (EDP) GCE nano-films as determined by CV and DPV techniques are as shown in **Figure 4.2**. The voltammograms of the bare GCEs showed no peaks indicating that they were non-electroactive. However, the CVs for all the modified nano-films generally showed typical anodic and cathodic peaks at the indicated potentials. These were in agreement with the corresponding DPV results.

The CV of both DCT and EDP GCE/Ag NPs film had characteristic one oxidation and reduction peaks attributable to Ag^0/Ag^+ couples as illustratred in **equation 4.10**.

$$\mathrm{Ag^0} \leftrightarrow \mathrm{Ag^+} + \mathrm{e^-} \ldots\ldots\ldots\ldots\ldots\ldots\ldots\ldots\ldots\ldots\ldots\ldots\ldots\ldots\ldots\ldots\ldots\ldots\ldots\ldots\ldots\ldots\ldots\ldots\ldots (4.10)$$

However, EDP nano-film had broader anodic and cathodic peaks appearing at higher peak potentials compared to DCT. Similar trend was also observed in the DPV results. This suggested that all the electro-deposited Ag NPs on the electrode surface were not stripped off during the anodic scan leading to higher over-potentials. This can also be attributed to diffusion-limited transport of Ag^+ ions towards the electrode surface due to a thicker film of electro-deposited Ag NPs formed on the electrode surface. This reduced the rate of reduction of Ag^+ to Ag^0 hence the observed higher peak potentials.

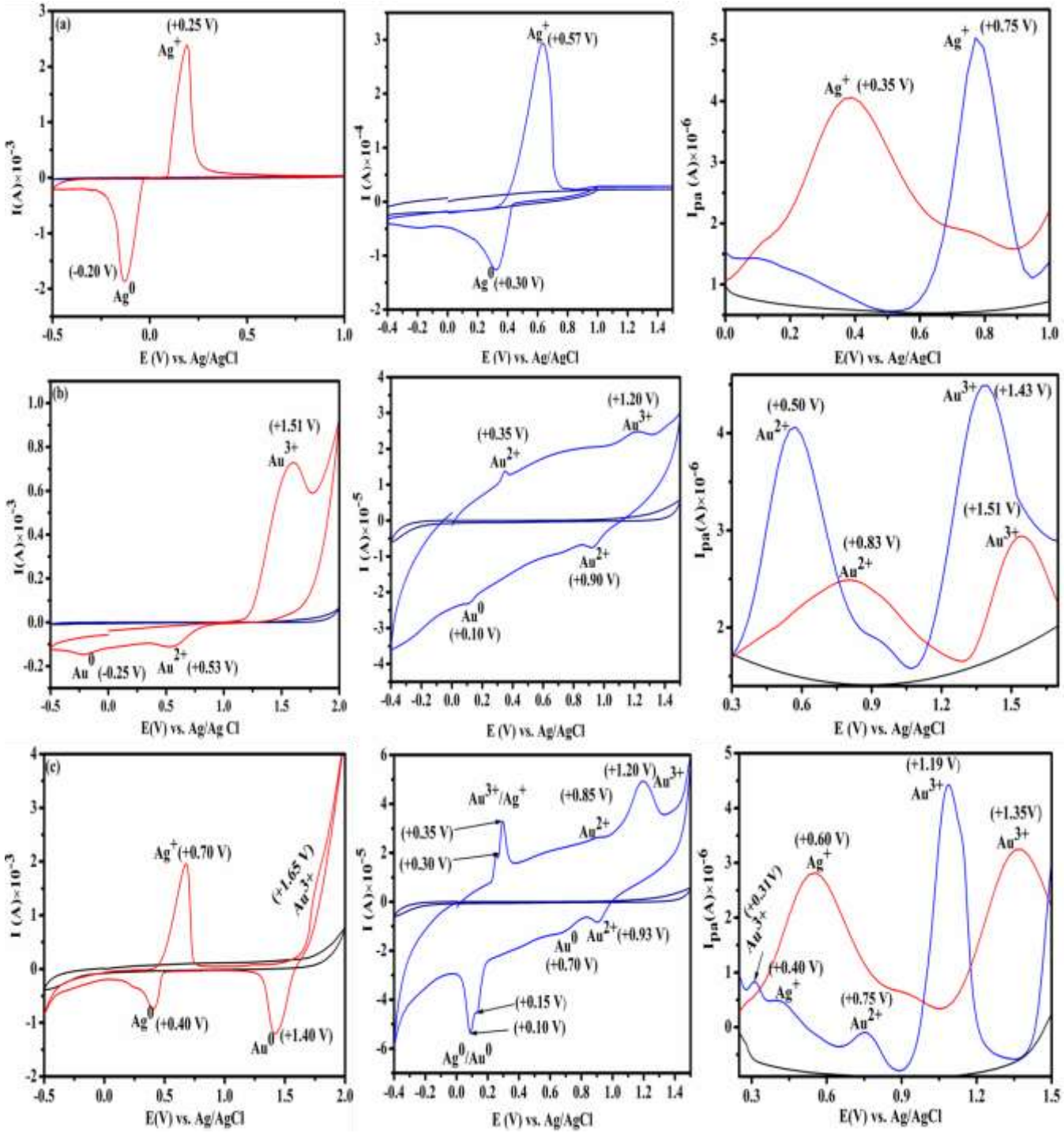

Figure 4.2: CVs and DPVs of DCT (**Red**) and corresponding EDP (**Blue**) (a) GCE/Ag NPs, (b) GCE/Au NPs and (c) GCE/Ag-Au (1:2) bimetallic NPs in 0.1 M HCl vs. Ag/AgCl: Scan rate: 30 mVs^{-1}

The DCT GCE/Au NPs film had one oxidation and two reduction peaks while EDP GCE/Au NP film had two oxidation and two reduction peaks at slightly lower peak potentials. These were in agreement with the DPV results which also showed two anodic peaks with the DCT peaks being broader than those of EDP nano-films. The appearance of two anodic peaks can be ascribed to surface oxidation of Au NPs to form a mixture of Au_2O and Au_2O_3 during the anodic scan (Jeyabharathi *et al*., 2016; Steven, 2017). This is in close agreement with a study reported elsewhere (Hassan *et al.*, 2015). According to thermodynamics, gold is always oxidized to hydrated gold oxide, Au $(OH)_3$ or Au_2O_3. $3H_2O$ at +1.458 V and to anhydrous gold oxide at + 1.511 V (**Equations 4.11** and **4.14**). These values also closely agree with what this study found out. The anodic peak at +1.51 V can be due to the oxidation of Au to Au $(OH)_3$ (**Equation 4.14**) which was in turn reduced to Au^{2+} at +0.53 V as shown by equations **4.12 and 4.13** (Oko, 2014)**.** However, these results were not in concordance with studies reported elsewhere (Scanlon *et al*., 2012, Diaz-morales *et al*., 2013).

$$2\,Au^0 + 3H_2O \rightarrow Au_2O_3 + 6\,H^+ + 6\,e^- \quad \ldots\ldots\ldots\ldots\ldots\ldots\ldots\ldots\ldots\ldots\ldots\ldots\ldots\ldots\ldots\ldots (4.11)$$

$$Au_2\,(OH)_9^{3-} + 9\,H^+ + 6\,e^- \rightarrow 2\,Au^{2+} + 9\,H_2O \quad \ldots\ldots\ldots\ldots\ldots\ldots\ldots\ldots\ldots\ldots\ldots\ldots\ldots\ldots (4.12)$$

$$Au^{2+} + 2\,e^- \rightarrow Au^0 \quad \ldots\ldots\ldots\ldots\ldots\ldots\ldots\ldots\ldots\ldots\ldots\ldots\ldots\ldots\ldots\ldots\ldots\ldots\ldots\ldots\ldots\ldots\ldots\ldots (4.13)$$

$$Au_4(OH)_2 + H_2O \rightarrow Au(OH)_3 + 3\,Au^0 + H^+ + e^- \quad \ldots\ldots\ldots\ldots\ldots\ldots\ldots\ldots\ldots\ldots\ldots\ldots (4.14)$$

The slight difference can possibly be attributed to the nature of the electrode modification employed in our study which experienced enhanced quantum confinement effects due to the nano-scale size of Au NPs hence the decreased cathodic peak potentials observed. In both GCE/Au NPs films**,** the peak potential separations (ΔE_p) were the greatest (E_p >0.059 V) indicating that the redox reaction of Au NPs was of quasi-reversible type (Modiba *et al*., 2012; Wanjau *et al*., 2015).

The CV of DCT GCE/Ag-Au (1:2) NPs showed two anodic and two cathodic peaks while those of EDP nano-films had three distinct anodic and cathodic peaks with two similar humps at both anodic and cathodic sides. Both anodic and cathodic peaks of different shapes with significantly low peak current intensities for Au appeared distinctly at different potentials. The Ag peak in the hump was more enhanced in peak current intensity compared to the Au peak. The appearance of the hump indicated the formation of Ag-Au alloy as similarly reported elsewhere (Arvinte *et al*., 2018; Ning, 2019).

The DPV of the bimetallic NPs also showed two anodic peaks closely similar to those observed in CVs with the Au^{3+} peak experiencing the highest peak currents. The appearance of the anodic hump observed in the CV was also evident in the DPV at approximately same potentials. This confirmed the sensitivity of DPV technique. The Au^{3+} peak for the DCT nano-film shifted towards more positive potentials. The shapes of the voltammograms in the bimetallic NPs also showed that the redox reaction of Ag NPs was relatively faster than Au NPs with enhanced cathodic and anodic peak currents relative to the EDP nano-film. This is attributed to faster electron transfer rates as depicted by the sharper anodic peaks of DCT GCE/Ag NPs film compared to those of DCT GCE/Au NPs film. These electrochemical properties confirmed the major electrical contribution of Ag in the GCE/Ag-Au (1:2) NPs film.

The electrochemical band gaps for DCT and EDP nano-films as determined using Breda's equation (Brédas *et al*., 1983) are as shown in **Table 4.1.**

Table 4.1: Electrochemical band gaps of drop-coated and electrodeposited Ag, Au and Ag-Au (1:2) NPs

GCE/NPs	E_g^{CV} **(eV)**	
	DCT	**EDP**
Ag	1.34	1.40
Au	1.20	2.05
Ag-Au (1:2)	1.65	2.40

The band gap energies (E_g) for DCT and EDP nano-films were in the order: GCE/Au NPs>GCE/Ag NPs> GCE/Ag-Au (1:2) NPs and GCE/Ag NPs> GCE/Au NPs> GCE/Ag-Au (1:2) NPs, respectively. The general trend for EDP E_g was in agreement with the nanoparticle sizes determined using SEM technique as discussed in **section 3.4.3**. The increase in E_g can be attributed to the decrease in particle size from Ag NPs to bimetallic Ag-Au (1:2) NPs (Andrade *et al*., 2017). The E_g for all DCT nano-films were generally lower than those of corresponding EDP films with the EDP bimetallic nano-film having the largest E_g. This can be ascribed to enhanced quantum confinement effects due to smaller-sized nature of the EDP bimetallic NPs (Movlarooy, 2018).

4.3.3 Determination of kinetic parameters for modified GCE nano-films

The CVs for each of the DCT and EDP GCE nano-films showed both anodic and cathodic peaks at different scan rates (**Figures 4.3-4.5**). The different scan rates were studied using *Randle's* and *Laviron's* plots. This was done so as to determine the electron transfer kinetic parameters including standard heterogenous rate constant (k_s), electron transfer coefficient (α), diffusion coefficient (D), NPs charge contribution and electrode surface coverage (Γ) for each of the modified nano-films using equations **4.1-4.6**. The values obtained were tabulated as shown in **Table 4.2**.

$$\mathrm{E_{pa}} = \mathrm{E^0} \ + \frac{2.3\mathrm{RT}}{(1-\alpha)\mathrm{nF}}\log \mathrm{V} \ldots\ldots\ldots\ldots\ldots\ldots\ldots\ldots\ldots\ldots\ldots\ldots\ldots\ldots\ldots\ldots\ldots\ldots\ldots\ldots\ldots.. (4.1)$$

$$\mathrm{E_{pc}} = \mathrm{E^0} - \frac{2.3\mathrm{RT}}{\alpha\mathrm{nF}}\log \mathrm{V} \ldots\ldots\ldots\ldots\ldots\ldots\ldots\ldots\ldots\ldots\ldots\ldots\ldots\ldots\ldots\ldots\ldots\ldots\ldots\ldots\ldots\ldots\ldots\ldots.. (4.2)$$

$$\log \mathrm{k_s} \ = \alpha \log(1-\alpha) + (1-\alpha)\log\alpha - \log\left(\frac{\mathrm{RT}}{\mathrm{nF}}\right) - (1-\alpha)\alpha\mathrm{nF}\frac{\Delta \mathrm{E_p}}{2.3\mathrm{RT}} \ldots\ldots (\ 4.3)$$

$$\Gamma = \frac{\mathrm{Q}}{\mathrm{nFA}} \ldots\ldots\ldots\ldots\ldots\ldots\ldots\ldots\ldots\ldots\ldots\ldots\ldots\ldots\ldots\ldots\ldots\ldots\ldots\ldots\ldots\ldots\ldots\ldots\ldots\ldots\ldots\ldots\ldots\ldots.. (4.4)$$

$$\mathrm{I_p} = \frac{\mathrm{A\Gamma V n^2 F^2}}{4\mathrm{RT}} \ldots\ldots\ldots\ldots\ldots\ldots\ldots\ldots\ldots\ldots\ldots\ldots\ldots\ldots\ldots\ldots\ldots\ldots\ldots\ldots\ldots\ldots\ldots\ldots\ldots\ldots.. (4.5)$$

$$I_{pa} = (2.99 \times 10^5) nAC_o\sqrt{\alpha D\upsilon} \ldots\ldots\ldots\ldots\ldots\ldots\ldots\ldots\ldots\ldots\ldots\ldots\ldots\ldots\ldots\ldots\ldots\ldots\ldots\ldots\ldots. (4.6)$$

Where E_{pa}, E_{pc}, R, F and T represent anodic peak potential, cathodic peak potential, universal gas constant (8.314 J mol^{-1} K $^{-1}$), Faraday constant (1 mole of e$^-$ = 96,500 C) and absolute temperature (298 K), respectively. Other electrochemical symbols used in the above equations have their usual meanings.

Table 4.2: Electrochemical kinetic parameters of drop-coated (DCT) and electro-deposited (EDP) nano-films determined from *Randle's* and *Laviron's* equations

GCE nano-films	**Ag**		**Au**		**Ag-Au (1:2)**			
Electrode modifications	**DCT**	**EDP**	**DCT**	**EDP**	**DCT**	**Ag (Au)**	**EDP**	**Ag (Au)**
E_{pa} (V)	+0.25	+0.57	+1.51	+1.20	+0.70	(+1.65)	+0.35	(+1.20)
E_{pc} (V)	-0.20	+0.30	+0.53	+0.90	+0.40	(+1.40)	+0.10	(+0.93)
E^{O}	+0.23	+0.44	+1.02	+1.05	+0.55	(+1.53)	+0.23	(+1.07)
ΔE_p (V)	0.05	0.27	0.98	0.30	0.30	(0.25)	0.25	(0.27)
α	1.16	1.38	0.88	0.82	0.02	(1.64)	0.84	(2.29)
αn	0.12	0.07	0.22	0.47	1.04	(0.39)	0.19	(0.50)
k_s (s^{-1})	0.43	0.26	0.12	0.41	0.01	(0.60)	0.82	(0.59)
Q (C)× (10^{-7})	3.37	2.13	1.90	2.00	4.00	(0.13)	1.00	(9.80)
Γ (molescm^{-2})× (10^{-11})	4.92	3.11	1.40	1.00	5.00	(7.00)	1.00	(6.55)
D (cm^{2}s^{-1}) × (10^{-7})	2.10	2.70	7.00	7.00	1.31	(7.34)	0.50	(4.87)
Randle's Plot (R^2)	0.999	0.987	0.998	0.976	0.995	(0.998)	0.996	(0.999)
Laviron's Plot (R^2)	0.983	0.996	0.989	0.992	0.989	(0.986)	0.985	(0.998)

The anodic peak currents (I_{pa}) of both DCT and EDP GCE/Ag NPs films increased exponentially with increase in square root of the scan rates ($V^{1/2}$) and perfect linear correlations between I_{pa} and $V^{1/2}$, were obtained (**Figure 4.3)**. As shown in **Table 4.2**, the *Randle's* plot for DCT had significantly higher R^2 compared to EDP suggesting enhanced diffusion rates of Ag^+ in DCT nano-films compared to EDP. The plots of log V versus anodic peak potentials (E_{pa}) for both films also showed perfect linear correlations. However, the E_{pa} for the EDP nano-film shifted towards more positive side with increasing scan rates relative to the DCT film. The *Laviron's* plot for EDP film also had higher R^2 than DCT.

The determined values of k_s, Q and Γ for DCT GCE/Ag NPs films were greater than those of EDP except for α and D. The low value of α for DCT film can be attributed to faster electron transfer rates compared to the EDP nano-films. This is supported by the well-defined shape and symmetry of the DCT Ag NPs CV peaks relative to the broad EDP CV peaks. These values obtained were however greater than those reported in the literature for ideal charge transfer kinetics at typically modified nano-films (Guidelli *et al*., 2014). The α values less than 0.5 indicate steeper slope for anodic peaks (Sisay, 2021). This was not in agreement with what this study found out.

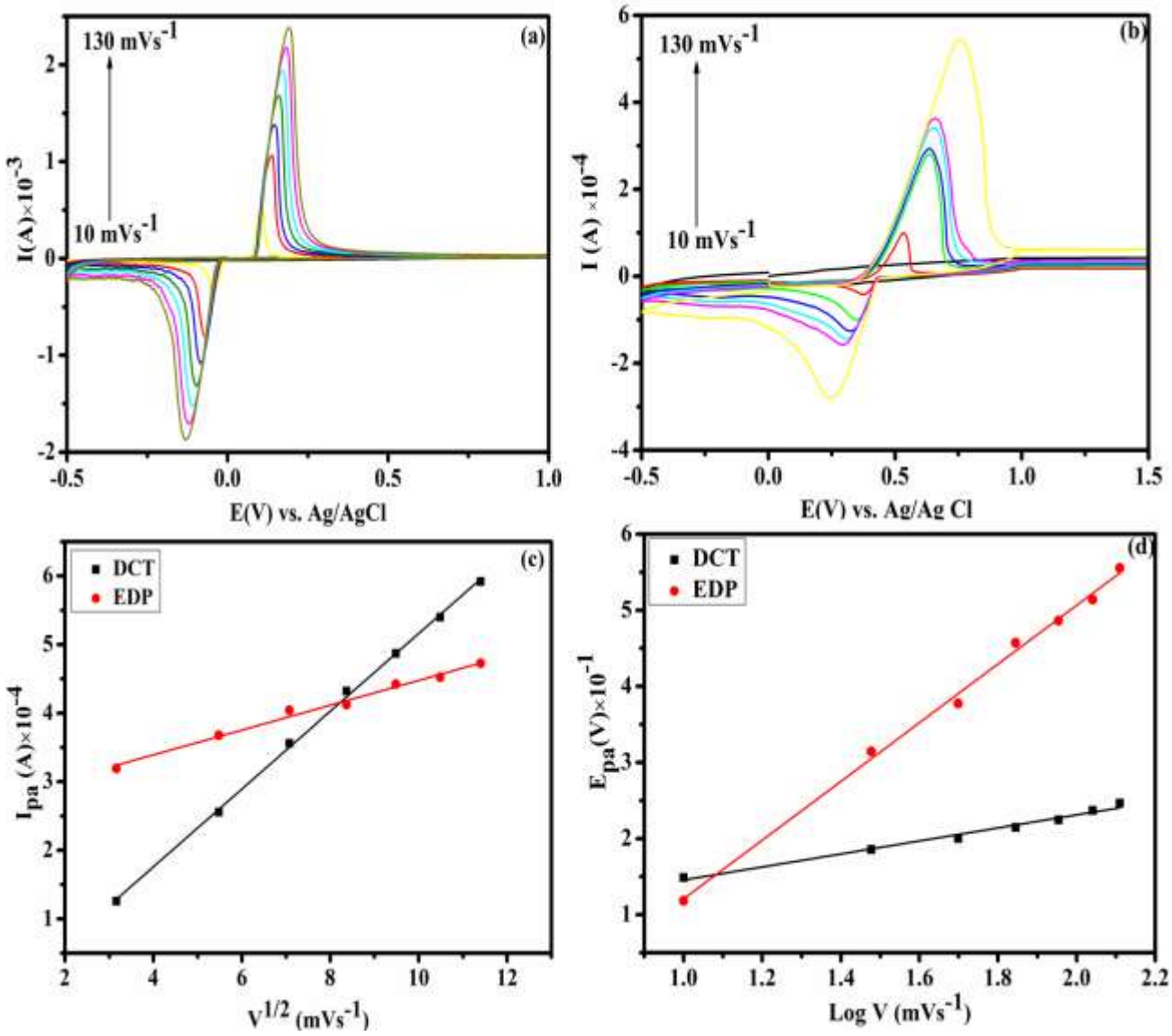

Figure 4.3: Scan rate studies of (a) DCT and (b) EDP GCE/Ag NPs, and corresponding (c) *Randle's* and (d) *Laviron's* plots; scan rate: 10-130 mVs^{-1} in 0.1 M HCl vs. Ag/AgCl

The I_{pa} for both DCT and EDP GCE/Au NPs films increased linearly with $V^{1/2}$ and significantly higher R^2 values were obtained. However, the R^2 value for the DCT nano-film was greater than EDP. This suggested that the rate of diffusion of Au^{3+} was faster in DCT film relative to the EDP. The E_{pa} for the DCT nano-film also shifted significantly to higher positive values with increasing scan rate compared to EDP. This indicated that the oxidation of Au^0 to Au^{3+} involved more than one step. The Au^0 was first oxidized to Au^{2+} which was finally oxidized to Au^{3+}. This electrochemical behavior of Au is supported by its existence in various oxidation states of +1, +2

and +3 as similarly described elsewhere (Bellia *et al*., 2017). The formation of mixtures of Au oxides during its oxidation to Au^{3+} could have led to slow electron transfer kinetics, uncompensated solution resistance and non-linear diffusion of Au^{3+} towards electrode surface hence the observed shift in potentials to more positive values (Nkunu *et al*., 2017).

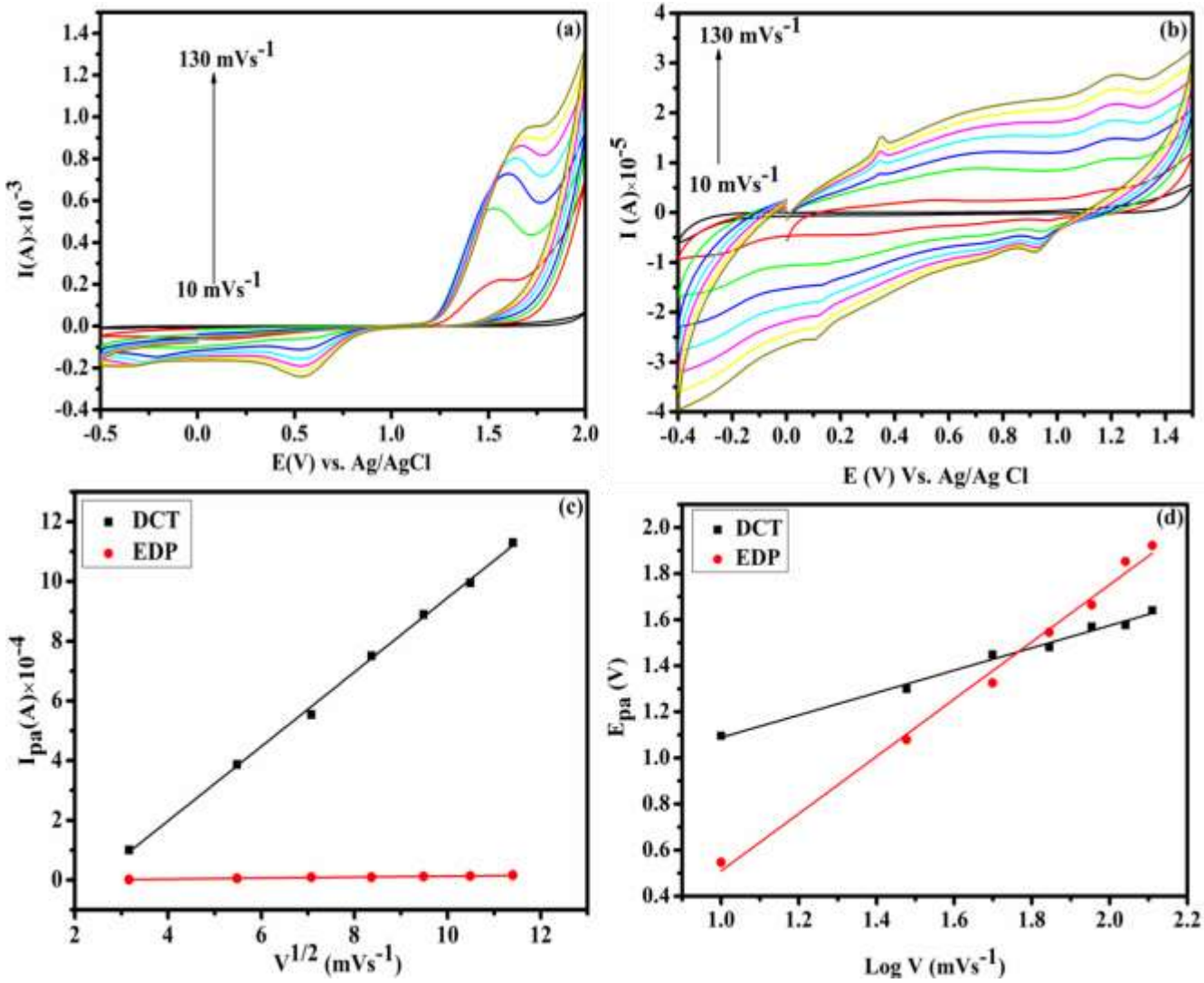

Figure 4.4: Scan rate studies of (a) DCT and (b) EDP GCE/Au NPs, and corresponding (c) *Randle's* and (d) *Laviron's* plots; scan rate: 10-130 mVs^{-1} in 0.1 M HCl vs. Ag/AgCl

The calculated values of α, k_s, Q, Γ and D for both DCT and EDP nano-films varied with EDP film having higher values of k_s and Q while DCT had higher values of α and Γ. Both films had same value for D. However, the values of Q were found to be higher than -2.0×10^{-3} C for colloidal

GCE/Au NPs (Kumal *et al*., 2015). The lower and higher values of k_s and α, respectively for DCT suggested enhanced electron transfer rates as supported by higher Γ. The low value of Γ in EDP film might be attributed to agglomeration of Au NPs on the electrode surface due to its incomplete coverage during the voltammetric scans as similarly described elsewhere (Han *et al*., 2015; Kraikaew *et al*., 2016). The determined value of D for both films can be attributed to their almost equal charge contributions.

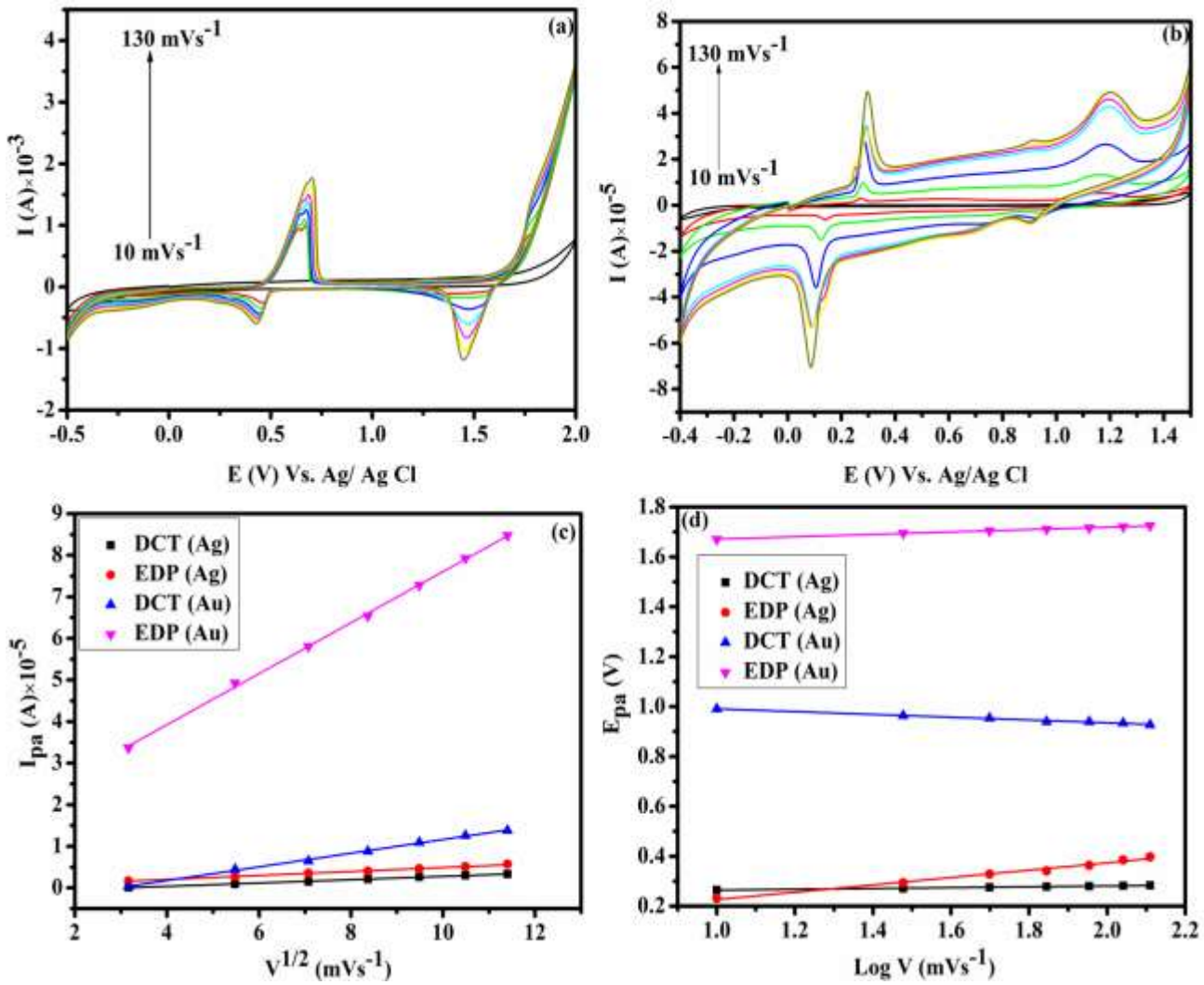

Figure 4.5: Scan rate studies of (a) DCT and (b) EDP GCE/Ag-Au (1:2) NPs, and corresponding (c) *Randle's* and (d) *Laviron's* plots; scan rate: 10-130 mVs^{-1} in 0.1 M HCl vs. Ag/AgCl

The I_{pa} for both DCT and EDP GCE/Ag-Au (1:2) films increased exponentially with $V^{1/2}$ and significantly higher values of R^2 were obtained. The R^2 value due to the effects of Au in EDP nano-film was the greatest compared to Ag in both nano-films. This suggested that higher content of Au in the EDP film enhanced faster rates of diffusion of Au^{3+} relative to its effects in the DCT nano-films. The E_{pa} of both nano-films increased with scan rates. However, the increase was much more distinct and significant in the EDP nano-film with slight positive shift in peak potentials due to the oxidation of Au^{2+} to Au^{3+} compared to DCT film. This is supported by the higher value of R^2 obtained due to the influence of Au in the bimetallic EDP nano-film.

The calculated values of α, k_s, Q, Γ and D for both bimetallic nano-films varied significantly with EDP nano-film due to Au content having the highest values of α and Q . The DCT film due to Au content had higher values of Γ and D. The values of k_s determined were found to be within the expected range for normal electrode kinetic processes (Fayemi *et al*., 2018). The smallest value of k_s due to Ag in the DCT nano-film suggested the availability of electroactive species largely dissolved in the bulk electrolyte (Sakthivel *et al.*, 2018; Shen *et al*., 2018). The values obtained for k_s and Q due to Ag and Au contents, respectively in the EDP nano-film indicated faster electron transfer rates relative to the DCT nano-film as similarly described elsewhere (Brown, 2015; Fayemi *et al*., 2018). This suggested that the electronic structure and surface physicochemistry of the EDP bimetallic nano-film experienced enhanced electron transfer rates (Baig *et al*., 2019).

However, its Γ and D values were lower than those of DCT nano-film due to Au content hence significantly experienced slow rates of diffusion of electro-active species towards the electrode surface. The DCT nano-film due to Au content also had higher value of k_s compared to EDP nano-film. The D value of the DCT nano-film was also found to be higher than those reported in the literature (Guo & Yarger, 2018).

4.4 Conclusion

Based on the results discussed above, there were successful chemical and electrochemical modifications of GCE with bimetallic Ag-Au (1:2) NPs. However, chemically modified GCE/Ag-Au (1:2) NPs film had more electrochemical attributes as determined by its CV analyses compared to electrochemically modified nano-film. The chemically modified GCE nano-film generally showed enhanced values of k_s, Γ and D determined from the experimental data compared to those of electrochemically modified GCE film. This suggested higher possibility of their applications in

various electro-analysis studies. The electrochemical modifications of GCE with NPs can also experience limitations on the appropriate NPs dimensions and morphologies. This makes it require accurate and thorough optimization of NPs synthesis steps and conditions which are labour intensive and time consuming.

4.5 References

Adarakatti, P.S. & Kempahanumakkagari, S.K. 2019. Modified electrodes for sensing. *Electrochemistry*.

Alam, M.S., Shabik, M.F., Rahman, M.M. & Valle, D. 2019. M. & Hasnat, M. A Enhanced electrocatalytic effects of Pd particles immobilized on GC surface on the nitrite oxidation reactions, 839: 1–8.

Andrade, A.B., Ferreira, N.S. & Valerio, M.E.G. 2017. Particle size effects on structural and optical properties of BaF2 nanoparticles. *RSC Advances*, 7(43): 26839–26848.

Arvinte, A., Crudu, I.A., Doroftei, F., Timpu, D. & Pinteala, M. 2018. Electrochemical codeposition of silver-gold nanoparticles on CNT-based electrode and their performance in electrocatalysis of dopamine. *Journal of Electroanalytical Chemistry*, 829: 184–193.

Baig, N., Sajid, M. & Saleh, T.A. 2019. Recent trends in nanomaterial-modified electrodes for electroanalytical applications. TrAC - *Trends in Analytical Chemistry*, 111: 47–61.

Bellia, G.F., Corrall, H., Baron, M.G., Croxton, R. & Gonzalez-Rodriguez, J. 2017. An investigation of digoxin by cyclic voltammetry using gold and silver solid electrodes and chemometric analysis. *International Journal of Electrochemical Science*, 12(4): 3050–3062.

Brédas, J.L., Silbey, R., Boudreaux, D.S. & Chance, R.R. 1983. Chain-Length Dependence of Electronic and Electrochemical Properties of Conjugated Systems: Polyacetylene, Polyphenylene, Polythiophene, and Polypyrrole. *Journal of the American Chemical Society*, 105(22): 6555–6559.

Brown, J.H. 2015. Development and Use of a Cyclic Voltammetry Simulator To Introduce Undergraduate Students to Electrochemical Simulations. *Journal of Chemical Education*, 92(9): 1490–1496.

Chen, Y.H., Kirankumar, R., Kao, C.L. & Chen, P.Y. 2016. Electrodeposited Ag, Au, and AuAg nanoparticles on graphene oxide-modified screen-printed carbon electrodes for the voltammetric determination of free sulfide in alkaline solutions. *Electrochimica Acta*, 205: 124–131.

Chu, Z., Peng, J. & Jin, W. 2017. Advanced nanomaterial inks for screen-printed chemical sensors. *Sensors and Actuators*, B: Chemical, 243: 919–926.

Crespo-Yapur, D.A., Elizondo, A.S., Herrera, D. & Videa, M. 2019. Galvanostatic electrodeposition of silver nanoparticles: Nucleation and growth studies. *Materials Today*: Proceedings.

Diaz-morales, O., Calle-vallejo, F. & Munck, D. 2013. C. & KOPER, M. T Electrochemical water splitting by gold: evidence for an oxide decomposition mechanism, 4: 2334–2343.

Fayemi, O.E., Adekunle, A.S., Kumara Swamy, B.E. & Ebenso, E.E. 2018. Electrochemical sensor for the detection of dopamine in real samples using polyaniline/NiO, ZnO, and Fe_3O_4 nanocomposites on glassy carbon electrode. *Journal of Electroanalytical Chemistry*, 818: 236–249.

Gao, C., Hu, Y., Wang, M., Chi, M. & Yin, Y. 2014. Fully alloyed Ag/Au nanospheres: Combining the plasmonic property of Ag with the stability of Au. *Journal of the American Chemical Society*, 136(20): 7474–7479.

Guidelli, R., Compton, R.G., Feliu, J.M., Gileadi, E., Lipkowski, J., Schmickler, W. & Trasatti, S. 2014. Defining the transfer coefficient in electrochemistry: An assessment (IUPAC Technical Report).

Guo, C. & Yarger, J.L. 2018. Characterizing gold nanoparticles by NMR spectroscopy. Magnetic Resonance in Chemistry, 56(11): 1074–1082.

Hassan, A., Ali, S. & Muhammad, M. 2015. Cyclic Voltammetric Study of Clarithromycin Using Gold Electrode. *International Research Journal of Pure and Applied Chemistry*, 8(4): 221–228.

Isaev, V.A. & Grishenkova, O. V. 2013. Galvanostatic nucleation and growth under diffusion control. *Journal of Solid State Electrochemistry*, 17(6): 1505–1508.

Jeyabharathi, C., Ahrens, P., Hasse, U. & Scholz, F. 2016. Identification of low-index crystal planes of polycrystalline gold on the basis of electrochemical oxide layer formation. Journal of Solid State Electrochemistry, 20(11): 3025–3031.

Jiao, L., Xu, W., Wu, Y., Yan, H., Gu, W., Du, D., Lin, Y. & Zhu, C. 2021. Single-Atom catalysts boost signal amplification for biosensing. *Chemical Society Reviews*.

Kraikaew, P., Tanner, E.E.L., Sokolov, S. V., Batchelor-McAuley, C., Holter, J., Young, N.P. & Compton, R.G. 2016. Nanoparticle Surface Coverage Controls the Speciation of Electrochemically Generated Chlorine. *ChemElectroChem*, 3(11): 1794–1798.

Kumal, R.R., Karam, T.E. & Haber, L.H. 2015. Determination of the surface charge density of colloidal gold nanoparticles using second harmonic generation. *Journal of Physical Chemistry C*, 119(28): 16200–16207.

Li, C. & Jin, Y. 2021. Shell-Isolated Plasmonic Nanostructures for Biosensing, Catalysis, and Advanced Nanoelectronics. *Advanced Functional Materials*, 31(7): 31.

Mercante, L.A., Facure, M.H.M., Sanfelice, R.C., Migliorini, F.L., Mattoso, L.H.C. & Correa, D.S. 2017. One-pot preparation of PEDOT:PSS-reduced graphene decorated with Au

nanoparticles for enzymatic electrochemical sensing of H_2O_2. *Applied Surface Science*, 407: 162–170.

Modiba, P., Matoetoe, M. & Crouch, A.M. 2012. Electrochemical impedance spectroscopy study of Ce(IV) with aminopolycarboxylate ligands for redox flow batteries applications. *Journal of Power Sources*, 205: 1–9. http://dx.doi.org/10.1016/j.jpowsour.2012.01.004.

Movlarooy, T. 2018. Study of quantum confinement effects in ZnO nanostructures. *Materials Research Express*, 5(3): 35032.

Murtada, K. & Moreno, V. 2020. Nanomaterials-based electrochemical sensors for the detection of aroma compounds - towards analytical approach. *Journal of Electroanalytical Chemistry*, 861: 113988.

Muya, C.N., Guto, P.M., Wangui, T.W. & Kamau, G.N. 2015. Electrocatalytic Decomposition Of (3ar. , 4(7): 417–425.

Nkunu, Kamau, Kithure, G.N. & Muya, J.G. 2017. Electrochemical Studies of Potassium Ferricyanide in Acetonitrile-Water Media (1:1) using Cyclic Voltammetry Method. International *Journal of Scientific Research and Innovative Technology*, 4(5): 2313–3759.

Oko, D.N. 2014. Electrocatalytic Activity of Small Organic Molecules at PtAu Alloy Nanoparticles for Fuel Cells and Electrochemical Biosensing Applications. I*nstitut national de la recherche scientifique*: Université du Québec. http://espace.inrs.ca/id/eprint/2626.

Pandikumar, A.. & DEVI, K.S. 2021. Disposable Electrochemical Sensors for Healthcare Monitoring. *Royal Society of Chemistry*. http://ebook.rsc.org/?DOI=10.1039/9781839163364.

Sadeghi, S., Hemmati, M. & Garmroodi, A. 2013. Preparation of Ag-Nanoparticles/Ionic-Liquid Modified Screen-Printed Electrode and Its Application in the Determination of Metronidazole. *Electroanalysis*, 25(1): 316–322.

Sakthivel, M., Ramaraj, S., Chen, S.M., Dinesh, B. & Chen, K.H. 2018. A highly conducting flower like Au nanoparticles interconnected functionalized CNFs and its enhanced electrocatalytic activity towards hydrazine through direct electron transfer. *Journal of the Taiwan Institute of Chemical Engineers*, 82: 64–74.

Shabalina, A. V., Svetlichnyi, V.A., Ryzhinskaya, K.A. & Lapin, I.N. 2017. Copper nanoparticles for ascorbic acid sensing in water on carbon screen-printed electrodes. *Analytical Sciences*, 33(12): 1415–1419.

Sharma, D., Lee, J., Seo, J. & Shin, H. 2017. Development of a sensitive electrochemical enzymatic reaction-based cholesterol biosensor using Nano-sized carbon interdigitated electrodes decorated with gold nanoparticles. *Sensors* (Switzerland), 17(9): 2128.

Shen, B., Wen, X. & Korshin, G. V. 2018. Electrochemical oxidation of ciprofloxacin in two different processes: The electron transfer process on the anode surface and the indirect oxidation process in bulk solutions. *Environmental Science: Processes and Impacts*, 20(6): 943–955.

Silpa, P.A. 2022. Modification of screen printed biosensors using nanomaterials. In Advanced Nanomaterials for Point of Care Diagnosis and Therapy. *Elsevier:* 249–274.

Sisay, M. 2021. Voltammetric Determination Of Gallic Acid In Groundnut Using Glycine Modified Carbon Paste Electrode.

Staikov, G. 2016. Nanoscale electrodeposition of low-dimensional metal phases and clusters. *Nanoscale*, 8(29): 13880–13892.

Sun, J., Liu, L. & Yang, F. 2020. A WO3/PPy/ACF modified electrode in electrochemical system for simultaneous removal of heavy metal ion Cu2+ and organic acid. J*ournal of Hazardous Materials*, 394(12253): 4.

Suresh, R.R., Lakshmanakumar, M., Arockia Jayalatha, J.B.B., Rajan, K.S., Sethuraman, S., Krishnan, U.M. & Rayappan, J.B.B. 2021. Fabrication of screen-printed electrodes: opportunities and challenges. *Journal of Materials Science*, 56(15): 8951–9006.

Tonelli, D., Scavetta, E. & Gualandi, I. 2019. Electrochemical deposition of nanomaterials for electrochemical sensing. *Sensors* (Switzerland), 19(5).

Wanjau, T.W., Kamau, G.N., Mwaniki, S.N. & Muya, C.N. 2015. Electrocatalytic reduction of 2. , 2: 2.

Yadav, H.K.S., Usman, S., Ghanem, K.A.F. & Beevi, R. 2021. Synthesis of Nanomaterials for Drug Delivery. *Functionalized Nanomaterials* II, 23: 23–44.

Zhang, D. & Tang, Y. 2017. Enhancing light reflective properties on ITO glass by plasmonic effect of silver nanoparticles. *Results in Physics*, 7: 2874–2877.

CHAPTER FIVE

DEVELOPMENT OF AN ELECTROCHEMICAL NANO-IMPACT SENSOR FOR *Escherichia coli* USING GLASSY CARBON AND INTERDIGITATED ARRAY ELECTRODES

5.0 Summary

This chapter mainly deals with the study of the optimum conditions for opto-electrochemical interactions between *Escherichia coli* (*E. coli*) and bimetallic Ag-Au (1:2) NPs in 0.1 M PBS (pH 7.4). The optimum conditions obtained were used to develop electrochemical nano-impact sensor for the bacteria employing both glassy carbon and interdigitated array electrodes (IDAE) as transducers. The practical applicability of the developed sensor was investigated by detecting the bacteria in River and Ocean water samples.

5.1 Introduction

Electrode materials are important in the design and optimization of electrochemical sensors. Effective electrochemical sensing requires electrodes that are efficient in electron transport, highly portable and electrochemically interference-free (Idris *et al*., 2022). The use of macro-electrodes made of Au, Ag, Pt and C especially glassy carbon electrode (GCE) has been dominating the field of bacterial sensing due to their chemical inertness, lower background currents and wider potential window (Seymour, 2020). However, these electrodes require larger sample volumes, are prone to fouling and have poor miniaturization potentials.

Therefore, electrode miniaturization from macro-to-micro has been an important aspect in bacterial sensing applications in the recent past (Parlak & Richter-Dahlfors, 2020). Micro-electrodes are electrodes that have at least one dimension smaller than 100 μm with special characteristics which are directly related to their size. Reduction of electrode size leads to lower capacitive currents with convergent diffusion compared to the planar diffusion in macro-electrodes. This allows for rapid attainment of steady-state currents. Scaling down the electrode size also lowers the cost of mass production of sensors with improved analytical performance and enhanced capability of using smaller sample volumes. The effect of electrode size in bacterial sensing has been a subject of research interest in the applications of electrochemical detection strategies especially nano-impact electrochemistry (NIE). This is because this technique detects analytes due to intimate interactions between electrode and analyte, and the collisions between the

bacteria and electrode increase with decrease in electrode size due to increased electrode surface area to volume ratio. This technique is also sensitive to other experimental conditions including electrolyte composition, concentration and the chemistry at the detecting electrode. These factors are directly linked to the electrode size since the electrode must be in contact with them during the analysis (Sekretareva, 2021). Several studies involving nano-impact detections of *E. coli* using ultra-micro-electrodes (UME) as transducers have been reported (Lee *et al*., 2016; Gao *et al*., 2018; Ronspees & Thorgaard, 2018). However, the main disadvantage of these sensors has been the applications of higher electrode potentials unfavorable to most bacteria due to the larger electrode size. This increases the cost and lowers sensitivity, and selectivity of the bacterial detection process. Therefore, the advancements from the micro-to-nano-electrode systems can reduce the electrode size and spacing between electrodes to match the dimensions of the bacterial cells and maintaining the production of higher quality signal at the same time. However, as the size of the electrode decreases signal quality drops due to an increase in the electrical resistance at the electrode/electrolyte interface. This effect can be attributed to a decrease in the interfacial capacitance which in turn directly correlates with the area of the electrode. For this reason, interdigitated array electrodes (IDAEs) with higher surface area to volume ratio have been the subject of intensive research in the recent past. The adjustment of electroactive surface area of electrodes to the size of a bacterium provides an explicit advantage for direct sensing of bacteria. The IDAE also presents other promising advantages including low ohmic drop, faster establishment of steady-state, rapid reaction kinetics and increased signal-to-noise ratio compared to UMEs (Brosel-Oliu *et al*., 2019). To the best of our knowledge, no study has been reported on the applications of NIE technique integrated with CV, DPV and EIS techniques for the detections of *E. coli* using both GCE and IDAE as transducers.

Therefore, in this chapter, a simple, label-free and rapid Ag-Au (1:2) bimetallic NPs impact sensor integrated with EIS technique was designed, optimized and applied for ultra-sensitive detections of *E. coli* in River and Ocean water samples using GCE and IDAE as transducers. The potential usage of the developed nano-impact sensors in detecting the bacteria in spiked fruit juice and tap water samples was also pursued in this chapter. The effects of various parameters such as concentration of bacteria, bacteria-NPs incubation period, AC amplitude, electrode geometry and size, and applied potential on bacteria-NPs interactions were investigated.

5.2 Experimental

5.2.1 Reagents and materials

All the reagents were of analytical grade and were used as received. Brain Heart Infusion (BHI) and Nutrient Agars were obtained from *Sigma-Aldrich* and their solutions freshly prepared before use. 0.1 M phosphate buffer solution (PBS) pH 7.4 was prepared by mixing standard stock solutions (8 gL^{-1} NaCl, 0.2 gL^{-1} KCl, 1.44 gL^{-1} Na_2HPO_4, 0.24gL^{-1} KH_2PO_4) from *Sigma-Aldrich*. Gold interdigitated array electrodes (IDAEs) with reference No. G-MEA222 were purchased from Metrohm (South Africa) and used according to the manufacturer's instructions. Absolute ethanol was used to clean IDAE. All other solutions used were prepared in ultra-pure water (18 M Ω.cm) Milli-Q, Millipore.

5.2.2 Culture preparation

E. coli ATCC 25922 bacteria were stored as frozen stocks at -10 °C before cultivation. The bacteria were cultivated using BHI broth containing 17.5 gL^{-1} porcine, 10.0 gL^{-1} tryptose, 2.0 gL^{-1} glucose, 5.0 gL^{-1} NaCl and 2.5 gL^{-1} Na_2HPO_4 at a pH of 7.4. The bacteria were cultured at 37 °C in a rotation shaker for 18 hrs and harvested by centrifugation at 6000 revolutions per minute (rpm) for 20 minutes to remove the culture medium. The cells were washed twice using 0.1 M PBS solution (pH 7.4) and suspended in sterile 0.1 M PBS so as to obtain bacterial suspensions. The relationship between *E. coli* concentrations and OD_{600nm} was established based on spectrophotometric method (OD_{600nm} of 1.0 = 8×10^8 cellsmL^{-1}). The cell suspensions obtained were immediately used for subsequent optical and electrochemical interaction studies. All the sample cultures were prepared on the day of the tests.

5.2.3 *Zeta* potential determination

The *zeta* potentials (ζ) of the investigated bacteria and NPs in water suspensions were determined via electrophoretic light scattering using *Zetasizer* Nano ZS (Malvern Instruments, Malvern) equipment under the same conditions of temperature (298 K), preparation time (10 minutes) and pH (7.4). The ζ-potential of the bacterial suspensions, synthesized NPs and NPs-bacteria mixtures (1:1 v/v) were determined before bacteria-NPs opto-electrochemical interaction studies following protocols described elsewhere (Pajerski *et al*., 2019).

5.2.4 Optical interaction studies using UV-visible spectroscopy

Serial dilutions of bacterial cells were prepared in Milli-QTM water. UV-visible spectroscopy was used to investigate the effects of bacteria-NPs interaction time and bacterial cell concentrations on the wavelegths of each of the NPs in the range of 200 - 800 nm. The effects of bacterial cell concentrations on each of the NPs plasmonic band positions was done by placing 1 mL of each of the NPs into a clean quartz cuvette placed along side another cuvette with a blank solution (de-ionized water) in the sample compartments and their wavelengths determined. This was then followed by three consecutive additions of 1 mL of the bacterial suspensions to each of the NPs and uniformly mixing the two, and recording the changes in wavelength after each addition relative to same volume of bacterial growth medium used as blank instead of de-ionized water. The effects of interaction time were done by taking aliquots of each of the bacteria-NPs mixtures (1:1 v/v) kept in stoppered glass test tubes at specific time intervals of 0, 5, 10 and 15 minutes and determining their absorbance and wavelengths in the aforementioned wavelength range.

5.2.5 Fabrication of GCE sensor

The GCE was first polished as described in **section 4.2.1** and activated by sweeping it to higher anodic potential from + 0.6 to +1.3 V in 0.5 M H_2SO_4 (vs. Ag/AgCl), thoroughly rinsed with doubly-distilled water to completely remove the acid and dried under a stream of nitrogen gas for 1 hour so as to activate the NPs for effective NPs-bacterial interactions. Nano-impact electrochemistry was used to investigate the electro-activity of bacteria-NPs mixture (1:1, v/v) in 0.1 M PBS (pH 7.4) vs. Ag/AgCl, reference electrode. The CV and DPV data were obtained at same scan rate and potential ranges (vs. Ag/AgCl) based on the electro-oxidation reactions of the bacterial cells. The source of the signals due to electro-oxidation reactions of the bacteria were confirmed by 3 consecutive additions of 1 mL (8×10^1 cellsmL^{-1}) of bacterial solution to same volume of the NPs and determining their effects on the peak current intensity using (CV and DPVs) and magnitude of charge transfer resistance using Nyquist plots in the frequency range of 10^5 - 10^{-1} Hz.

The sensor method development involved determination of the analytical parameters using calibration graphs. This was followed by method validation and application of the sensor to real samples using recovery studies of spiked samples and standard addition method.

The repeatability and reproducibility of the developed sensor were evaluated with repeated EIS responses to 2.4×10^3 cellsmL^{-1} of *E. coli* and recording ΔR_{ct} obtained in six repetitive assays (n = 6) using one and three similarly developed sensors, respectively under the same optimized conditions. The % RSD value of the sensor for the six successive measurements of ΔR_{ct} was determined by comparing the values obtained using $\frac{\Delta R_{ct}{}^{\text{Ag–Au (1:2)NPs+}E.coli}}{\Delta R_{ct}{}^{\text{Ag–Au (1:2)NPs}}}$ for the six measurements.

The precision of the method was also investigated by measuring ΔR_{ct} for four replicate measurements (n = 4) using same bacterial concentration under the same optimized conditions followed by determination of % RSD.

The stability of the sensor was determined by storing the same bimetallic NPs in 0.1 M PBS, pH 7.4 at 4 °C for 4 days and determining ΔR_{ct} relative to the initial EIS responses after repeated additions of same concentrations of *E. coli* to the NPs solution.

The selectivity of the sensor was investigated by determining ΔR_{ct} of same concentration (2.4×10^3 cellsmL^{-1}) of *E. coli* added to the bimetallic NPs in the absence and presence of *S. typhimurium* using EIS technique.

For the standard addition analyses of River and Ocean water samples for the bacteria, 10 mL of each of the samples was filtered using 0.45 µm Whatman filter paper Grade 1 and then the filter paper dipped into 10 mL of 0.1 M PBS (pH 7.4). 1 mL aliquots of each of the samples were spiked with desired concentrations (cellsmL^{-1}) of 8×10^1, 1.6×10^2 and 2.4×10^3 *E. coli* cells. The samples were then subsequently analysed for *E. coli* exploiting the same proposed strategy under the same optimized conditions.

5.2.6 Fabrication of IDAE sensor

The gold interdigitated array electrode (IDAE) with specifications shown in **Figure 5.1** was also used as transducer. The electrode was cleaned, dried under a stream of nitrogen gas and activated following a protocol described elsewhere (Borchers *et al*., 2021). The cleaning protocol was used successfully for all the devices over the entire experiment.

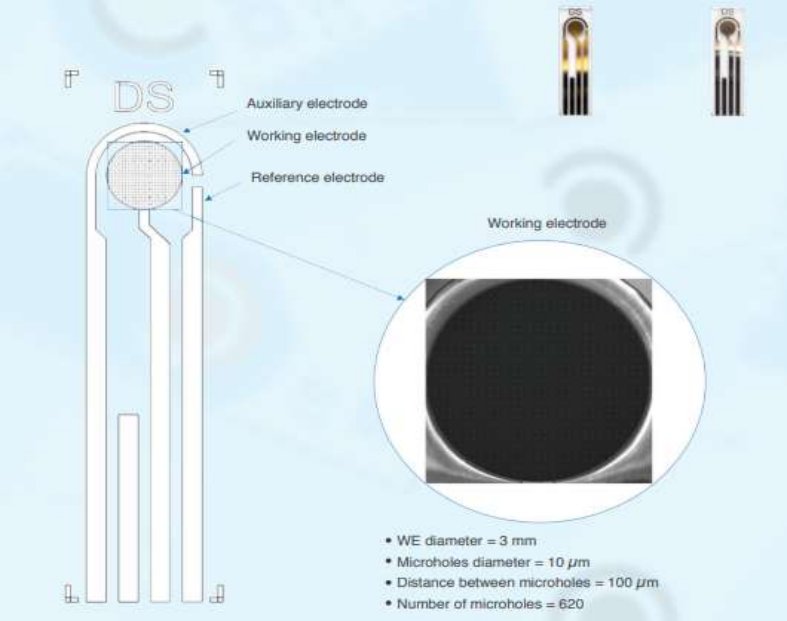

Figure 5.1: Interdigitated array electrode (IDAE)

The impedance measurements for the bacteria-NPs interactions were performed using μStat-i-400s potentiostat described in **section 4.2.3** interfaced with Drop-view 8400 software. The IDAE was connected to the potentiostat according to the manufacturer's instructions followed by impedance measurements under optimized conditions in the frequency range of (10^{5}-10^{-1}) Hz at room temperature (298 K). Wider frequency range (10^{-1} - 10^{5} Hz) was chosen for this study so as to allow the measurement of impedance for both sluggish and faster electrode processes associated with bacteria-NPs complexes.

5.3 Results and Discussion

5.3.1 *Zeta* potential

The *zeta* potentials of pure NPs, untreated bacteria and bacteria-NPs mixtures (1:1, v/v) are as shown in **Table 5.1**.

Tabe 5.1: *Zeta* (ζ) potential of NPs, untreated bacteria and bacteria-NPs complexes (n = 3)

NPs/NPs-bacteria complex	**ζ (mV)**
Ag	-6.29 ± 0.50
Au	-10.50 ± 0.20
Ag-Au (1:2)	-4.34 ± 0.71
E. coli	-15.50 ± 0.92
Ag + *E. coli*	-8.43 ± 0.10
Au + *E. coli*	-12.70 ± 0.23
Ag-Au (1:2) + *E. coli*	-11.30 ± 0.75

The measured average (n = 3) values of the *zeta* potential (mV) for the NPs were -6.29 ± 0.50 (Ag NPs), -10.50 ± 0.20 (Au NPs) and -4.34 ± 0.71 (Ag-Au 1:2 NPs). The bacteria significantly showed higher negative *zeta* potential (-15.50 ± 0.92 mV) than those of pure NPs. This can be due to the presence of higher density of anionic functional groups and O-antigen in the bacterial lipopolysaccharide (LPS) membranes (Tavares et al., 2020). This is in agreement with studies reported elsewhere (Hua *et al*., 2017; Saeed *et al*., 2021). The observed differences in the *zeta* potential values between the untreated bacteria and NPs had a strong impact on the bacterial adhesive properties towards the NPs. The significant decrease in the negative surface charge of the bacteria in the complex formed indicated the occurrence of effective bacteria-NPs interactions (Ahmad *et al*., 2017). The obtained negative surface charge for the synthesized NPs indicated that they were less toxic to the bacteria hence ensured effective interactions between live bacterial cells and NPs (El Badawy *et al*., 2011).

5.3.2 Optical interaction studies using UV-visible spectroscopy

The UV - visible spectra of the NPs before and after interactions with varying concentrations of *E. coli* are as shown in **Figure 5.2.** As shown in the figure, Ag NPs in the absence of the bacteria showed an SPR band at 430 nm. In the presence of increased concentration of the bacteria, significant increase in peak intensity coupled with distinct bathochromic shift from an SPR band of 430 to 460 nm was observed. The increase in peak intensity with increasing bacterial concentration (**Shown by the arrows**) can be attributed to the development of resistance of the bacteria towards the NPs due to the production of flagellin which triggers the aggregation of the NPs hence preventing maximum interactions between NPs and bacteria (Joshi *et al*., 2020). As shown in **Figure 5.2 b**, equilibrium was reached between Au NPs and bacteria interactions with

the Au NPs plasmon band peaked at 550 nm with increasing bacterial concentrations followed by a slight blue-shift.

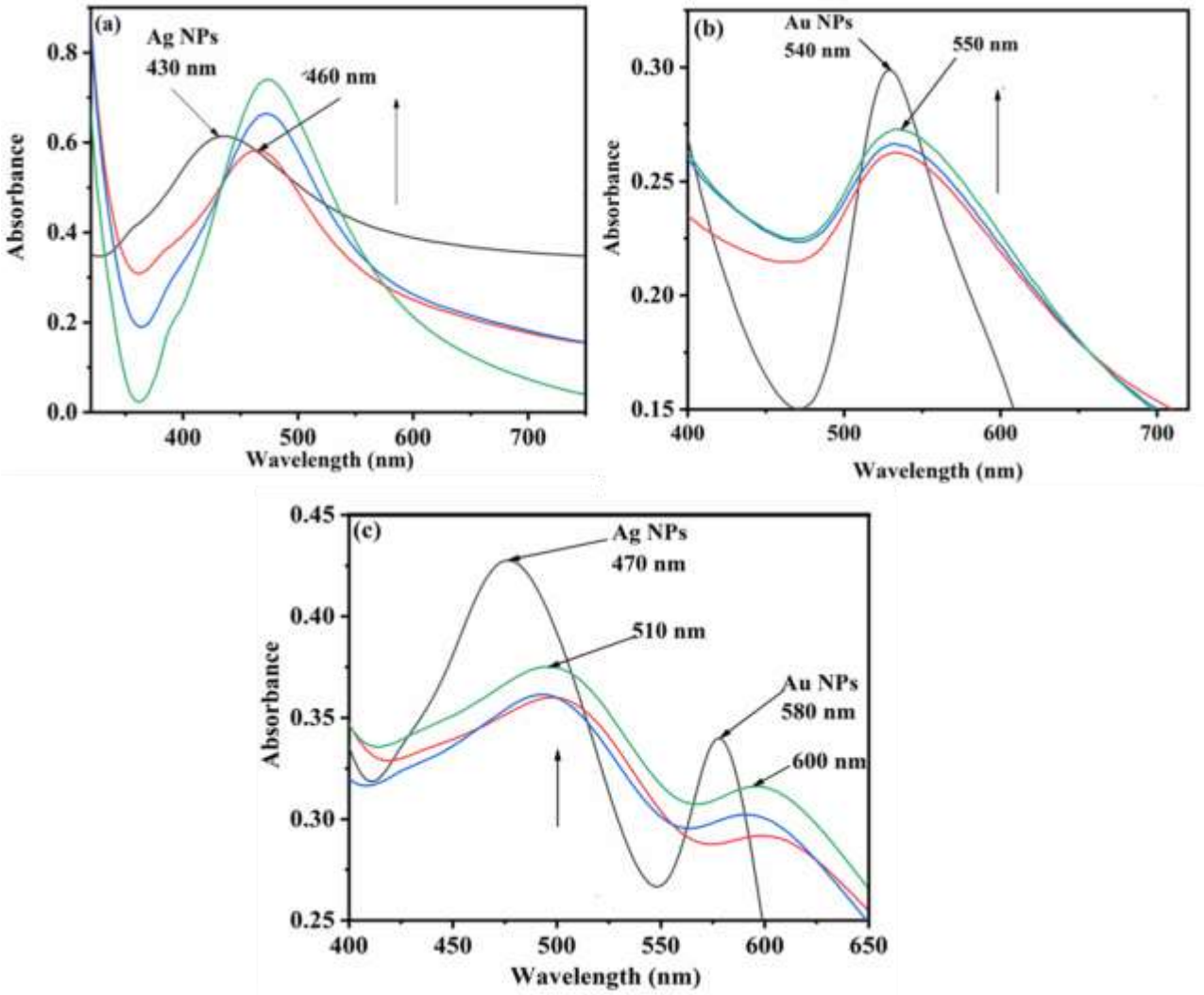

Figure 5.2: UV-visible spectra of (a) Ag NPs, (b) Au NPs (c) Ag-Au (1:2) NPs in the absence and presence of varying concentrations of *E. coli* (cellsmL^{-1});

Key: — NPs — NPs + 8.0×10^1 — NPs+1.6×10^2 — NPs +2.4×10^3

This can be attributed to the formation of significantly smaller and scattered aggregates coupled with decreased inter-particle coupling rate between NPs and bacteria (Hayden *et al*., 2012). The biocompatibility nature of Au NPs leads to stronger electrostatic interactions with the bacterial thiol (-SH) containing protein molecules hence the observed decrease in peak intensity relative to the pure Au NPs (Jena *et al*., 2020). Au NPs and their ions can also preferentially interact with

amino acids in the bacterial membrane due their biocompatibility nature forming strong bonds in the ligand-metallic interaction fashions (Taran *et al.*, 2017). The bimetallic NPs–*E. coli* interactions exhibited significant decrease in peak intensity coupled with enhanced red-shift relative to the pure NPs. The SPR bands of Ag and Au NPs in the bimetallic NPs shifted from 470 to 510 nm and 580 to 600 nm, respectively. This indicated significant aggregation between Ag and Au NPs, and the bacterial cells.

The Ag NPs experienced enhanced aggregation as shown by the larger red-shift compared to Au NPs. Au NPs peak intensity was also lower than those of Ag NPs. This showed that Ag NPs actively involved in the interactions compared to Au NPs. This is also supported by the exponential increase in absorbance of Ag NPs with increasing interaction time (**Figure 5.2 a**). The red-shift of the Au NPs plasmon bands with concomitant slight broadening of the spectra also occurred in a concentration dependent manner. The shift and broadening attained maximum value at the highest concentration of the bacteria. There was also a general increase in absorbance with bacterial concentration and this was found to be generally lower than that of Au NPs plasmon bands in the pure bimetallic NPs even at the highest concentration (**Figure 5.2 c**). This can be due to the induction of aggregation of Au NPs by the *E. coli* cells through electrostatic interactions (Raj *et al.*, 2015). The aggregation of the NPs around the bacterial cells can also be caused by the presence of LPS and phospholipids in bacterial membranes (Verma *et al*., 2014; Khorsandi *et al*., 2021).

The effects of bacteria-NPs interaction time on the plasmon band positions of Ag NPs, Au NPs and bimetallic Ag-A (1:2) NPs are as shown in **Figure 5.3**. From the figures, it can be observed that the plasmonic bands of the NPs generally displayed red-shift with increase in bacteria-NPs interaction time. In the monometallic NPs, the interaction between Au NPs and the bacteria showed significant red-shift with increasing interaction time (**Figure 5.3 b**). This can be ascribed to plasmon coupling of the NPs as they approach each other (Xu *et al*., 2021). The formation of larger Au NPs - *E. coli* complexes adhered to membrane surfaces as supported by significant increase in *zeta* potential (**Table 5.1**) of the bacteria. This has been similarly described elsewhere (Abadeer *et al*., 2015).

After 5 minutes of NPs - bacteria interactions, a slight increase in absorbance was observed up to the 15th minute (**Figure 5.3 d**) in both the monometallic Ag and Au NPs complexes indicating

effective binding between the facets in each of the NPs, bacterial membranes and LPS. Significant increase in absorbance indicates poor binding between metallic ions and LPS of the bacteria. Therefore, this increase in absorbance indicated poor sensitivity of monometallic Ag and Au NPs towards *E. coli* cells. The surface plasmons generated due to enhanced binding between the metallic surfaces of the NPs and LPS are sensitive to smaller changes in local refractive indices of monometallic Au and Ag NPs (Liu *et al*., 2021).

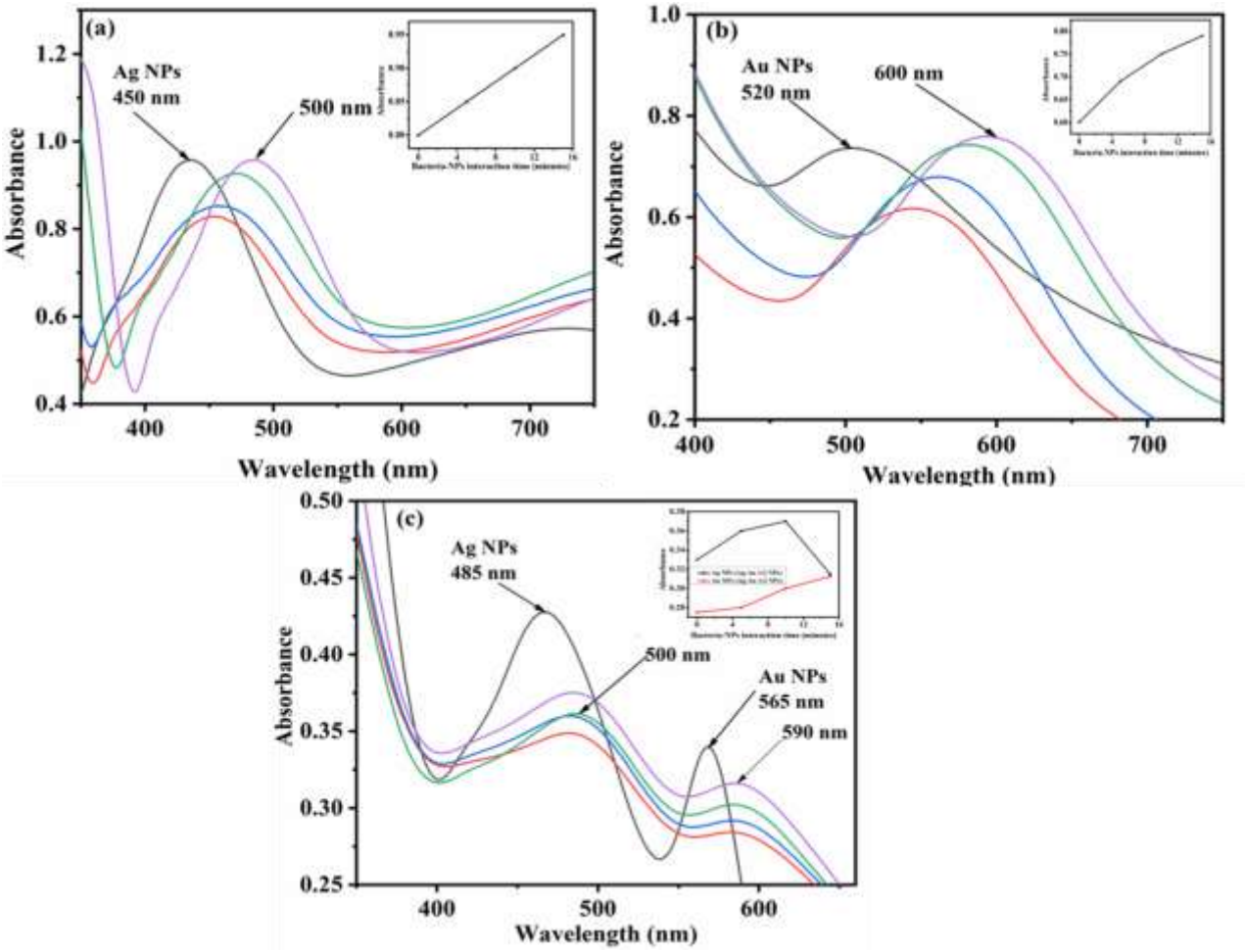

Figure 5.3: UV-visible spectra of interaction time between (a) Ag NPs, (b) Au NPs, (c) Ag-Au (1:2) NPs and same concentration of *E.coli* (8.0×10^1 cellsmL^{-1}); Plots of bacteria-NPs interaction time versus absorbance (**insets**);

Key NPs 0 minute 5 minutes 10 minutes 15 minutes

Significant red-shift and increasing absorbance with interaction time was evident in the bimetallic Ag-Au (1:2) NPs (**Figure 5.3 c**). There was also a general increase in absorbance with interaction

time for both metals in the bimetallic NPs upto the 15th minute when a convergence in their absorbances was noted (**Figure 5.3 c, inset**). This indicated complete saturation of the bacterial membranes with both Ag NPs and Au NPs in the bimetallic NPs. The increased red-shifting observed in the bimetallic NPs - bacteria interactions indicated that a large number of the NPs coagulated around the bacterial cells with increasing interaction time. The plasmon bands due to these interactions became stable at 15 minutes followed by dissipation attributable due to the complete coverage of the bacterial membrane with the bimetallic NPs. This is supported by the observed significant increase in *zeta* potential of the membrane from -15.50 ± 0.92 to -11.30 ± 0.75 mV (**Table 5.1**).

5.3.3 Electrochemical studies of bacteria-NPs interactions using GCE

The CVs and DPV for the interactions between *E. coli* and each of the NPs in 0.1 M PBS, pH 7.4 are as shown in **Figure 5.4**. The overlay of the CVs of each of the NPs in absence and presence of the bacteria showed an additional irreversible oxidation peak labelled as *E. coli* at the indicated potentials in the presence of *E coli*. The peak was, however, absent in the CVs of the pure NPs indicating that it was due to the presence of the bacteria. No corresponding signal reduction wave was observed in the reverse scans confirming that the electrochemical interactions between the bacteria and NPs was irreversible. In addition, a noticeable negative shift of the peak potentials of Ag and Au were also observed in the bimetallic NPs in the presence of *E. coli*. The signal can possibly be attributed to the oxidation of the bacterial membrane proteins such as cytochrome C oxidase abundant in the bacterial metabolic pathways (Hamidi-Asl *et al*., 2016; R. Zhang *et al*., 2020). The oxidation of quinone to hydroquinone derivatives in *E. coli* cells due to electrochemical tension on electrode surface has also been reported (Tonelli *et al*., 2015; Hamidi-Asl *et al*., 2016). The significant shift in peak potentials of Ag and Au NPs confirmed the formation of the bimetallic Ag-Au (1:2) NPs - *E. coli* complex (Sepunaru *et al*., 2015). The gold oxidation in the bimetallic NPs also took place closer to the *E. coli* oxidation potential indicating that it significantly played a synergistic role in the bacterial detection. Similar argument has been advanced elsewhere (Hamidi-Asl *et al*., 2016; Zhang *et al.*, 2021).

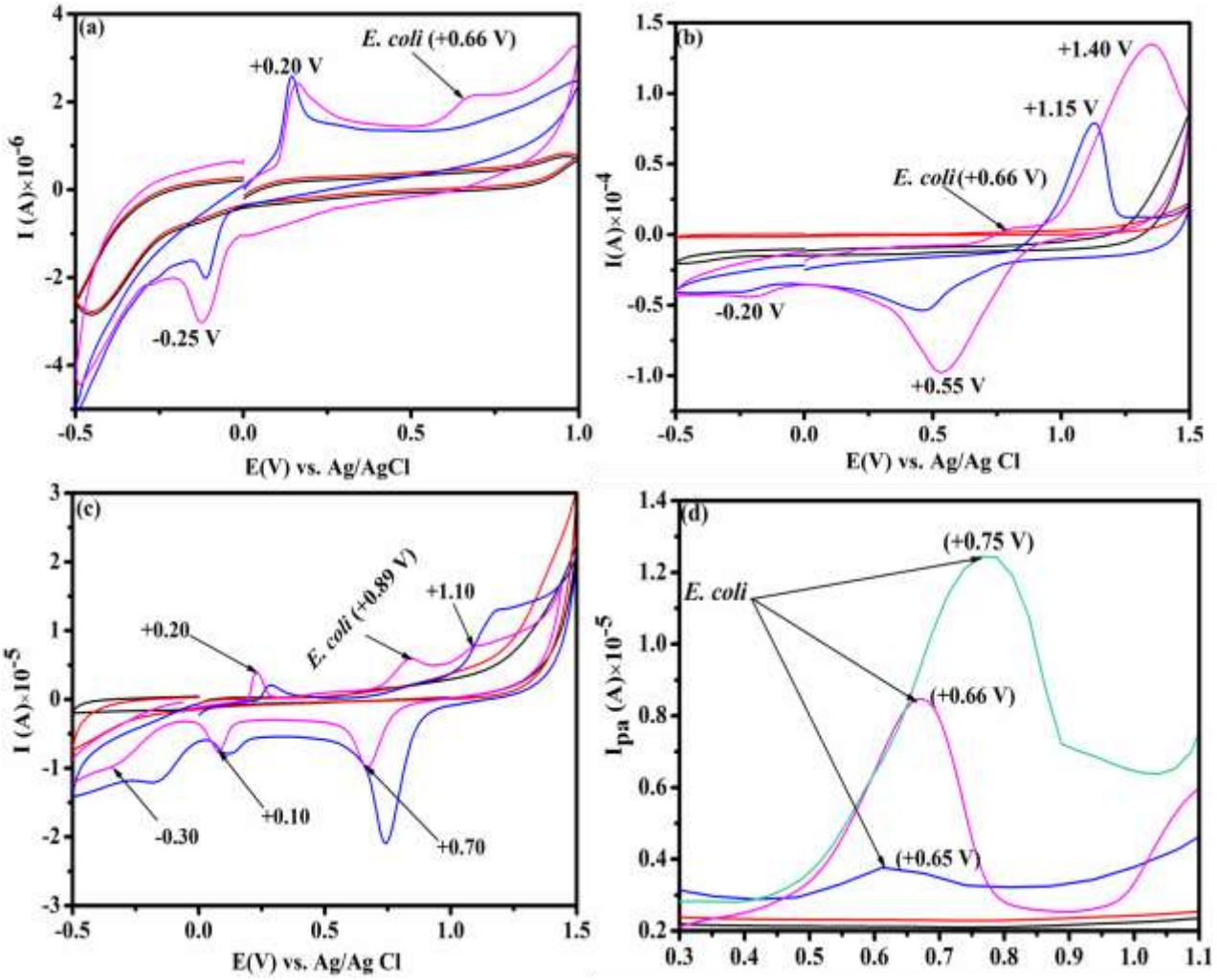

Figure 5.4: Overlays of CVs and DPVs of —— 0.1 M PBS —— *E. coli* —— NPs + 0.1 M PBS —— NPs + *E. coli* and —— Ag NPs+*E. coli* —— Au NPs+*E. coli* —— Ag-Au (1:2) NPs+*E. coli*, respectively in 0.1 M PBS, pH 7.4; Scan rate: 30 mVs^{-1}; (a) Ag NPs, (b) Au NPs (c) Ag-Au (1:2) NPs;

The overlay of the DPVs for the interactions between each of the NPs and *E. coli* also showed more distinct and resolved oxidation peaks labeled as *E. coli*. The oxidation peak current intensity and peak resolution were more enhanced in the bimetallic NPs compared to the monometallic NPs. This can be attributed to the improved electron transfer reactions between the electro-active centers of the bacterial cells and bimetallic NPs due to its biocompatibility nature (Kus-liśkiewicz *et al*., 2021). This increases the rate of electron exchange reactions between the bimetallic NPs and electro-active centres of bacterial cells (Ramesh *et al*., 2020). The slight shift in peak potential of the bimetallic NPs towards more positive side can possibly be attributed to spanned wider range of

the applied potentials which exposed numerous bacterial electro-active centres to the bimetallic NPs as similarly reported elsewhere (Harnisch & Freguia, 2012).

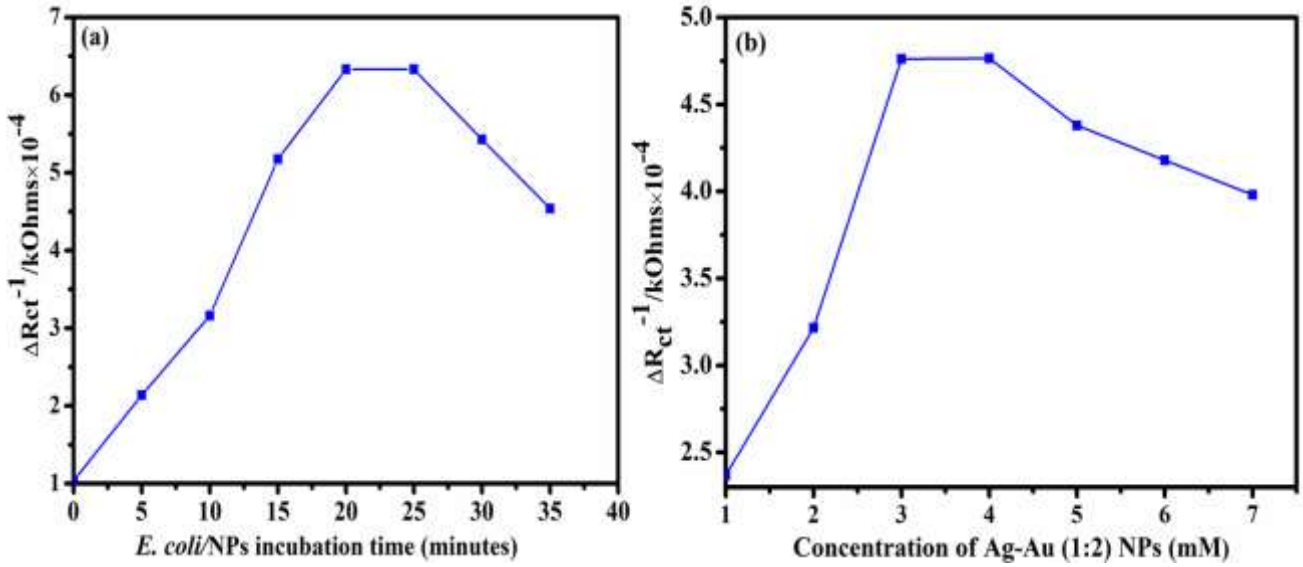

Figure 5.5: Effects of (a) bacteria - bimetallic Ag-Au (1:2) NPs incubation period and (b) concentration of bimetallic Ag-Au (1:2) NPs on bacteria-bimetallic NPs interactions studied using EIS technique

The effect of incubation period and NPs concentration (**Figure 5.5**) indicated an initial increase in the *E. coli* oxidation peak current intensity for both, then a plateau followed by a decrease. These changes can be attributed to increased rate of collisions between the bacterial cells and bimetallic NPs as concentration increases. The rate of bacteria-NPs interactions significantly decreased due to maximum saturation of the bacterial membranes with the NPs (Gammoudi *et al*., 2013). From the data obtained above, the optimum bacteria-bimetallic NPs interaction incubation period and concentration of 20 minutes and 3 mM, respectively were employed for further interaction studies.

5.3.4 Effect of supporting electrolyte concentration on bacteria-NPs interactions

The results (**Figure 5.6**) obtained for the optimization of supporting electrolyte concentration showed that 0.1 M PBS had enhanced peak current intensity indicating good electrical conductivity. The oxidation peak due to the bacterium at pH 7.4 was also well resolved with minimum background currents. This was also in agreement with the EIS results (**Appendix I**). Therefore, 0.1 M PBS at pH 7.4 was chosen for further electrochemical interaction studies.

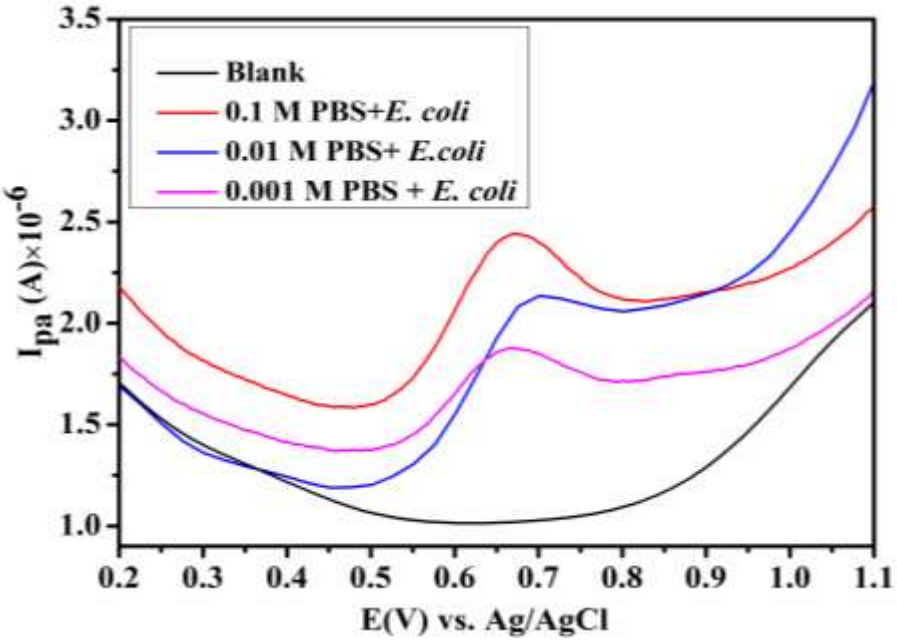

Figure 5.6: Optimization of PBS concentration for *E. coli* - NPs interaction studies using DPV

5.3.5 Choice of electro-analytical technique for *E. coli* detection using GCE

The sensitivities of the electro-analytical techinques were compared and the signals obtained represented as shown in **Figure 5.7**. In **Figures 5.7 (a - b)**, the electro-analytical techniques employed showed increased current intensity with increasing bacterial concentrations. The data obtained also showed that all the techniques investigated could be used for the development of the sensor. However, based on enhanced sensitivity determined and the known exclusive frequency dependent nature, EIS was chosen as the main electro-analytical technique for further Ag-Au (1:2) NPs- *E. coli* sensing studies.

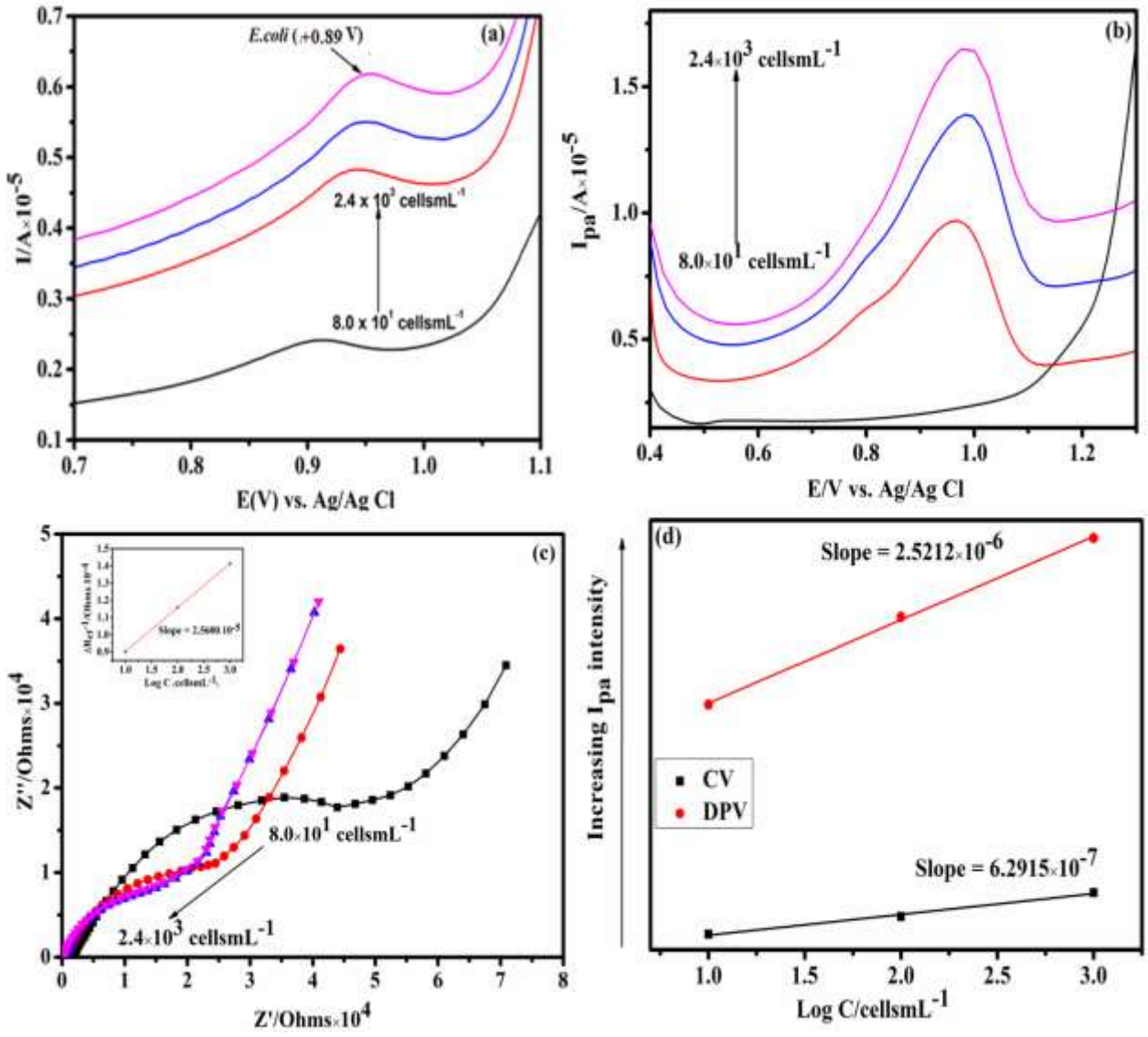

Figure 5.7: (a) Cyclic voltammogram; (b) differential pulse voltammogram; (c) Nyquist plot; and (d) Sensitivity values for Ag-Au (1:2) NPs-*E. coli* interaction studies using CV and DPV techniques

5.3.6 Determination of electron transfer kinetics parameters

The kinetics for the interactions between bacteria and Ag-Au (1:2) NPs were investigated using Bode plots and CV scan rate studies (**Figure 5.8)**. The effects of scan rates on electro-oxidation of the bacterial membrane proteins showed that the oxidation peak current intensity increased linearly with scan rates and the best scan rate chosen was 0.03 Vs^{-1} due to its enhanced and stable signal response. The oxidation peak current also linearly increased with the square root of scan rate

according to the linear equation: I_{pa}= 8.914E-07$V^{1/2}$ - 2.667; (R^2 = 0.9966). This showed that the electron transfer processes during the bacterium-NPs interactions were mainly diffusion-controlled.

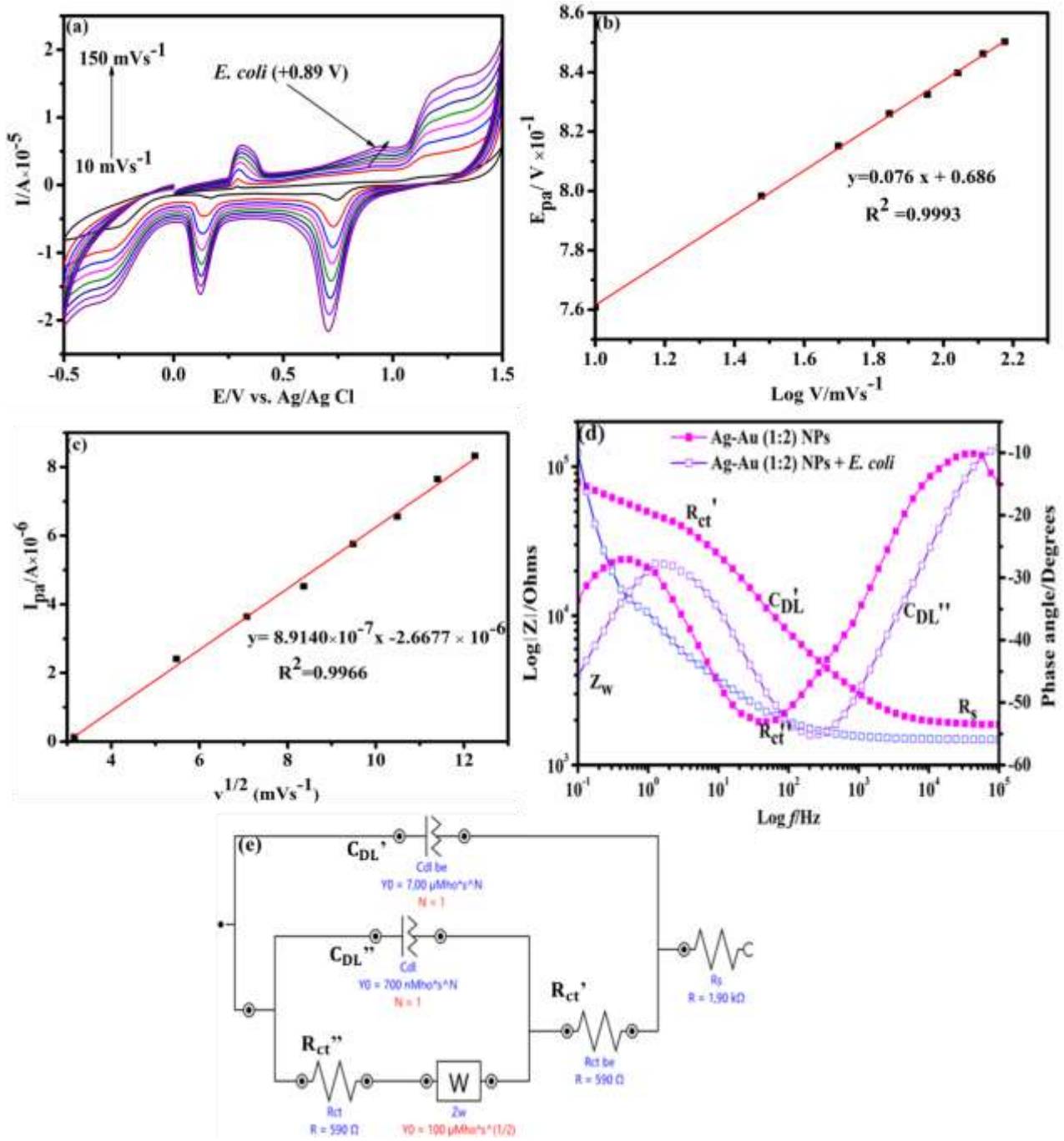

Figure 5.8: (a) Effects of various CV scan rates on bacterial oxidation peak current intensity; (b) *Laviron's* plot (c) *Randle's* plot, (d) Bode plots and (e) *Randle's* equivalent circuit; R_s (Solution resistance), R_{ct} (charge transfer resistance), Z_w (Warburg impedance)

Laviron's equation (**5.1**) was used to validate the linearity between the oxidation peak potentials and applied scan rates.

$$E_{pa} = E^{\theta} + \left(\frac{RT}{\alpha nF}\right) \ln\left(\frac{RTk_s}{\alpha nF}\right) + \left(\frac{RT}{\alpha nF}\right) \ln V \ldots\ldots\ldots\ldots\ldots\ldots\ldots\ldots\ldots\ldots\ldots\ldots\ldots\ldots\ldots\ldots (5.1)$$

Where $\alpha, k, n, V \; and \; E^{\theta}$ represented electron transfer coefficient, heterogeneous rate constant, number of electrons transferred (n), scan rate applied and formal standard oxidation peak potential, respectively.

The *Laviron's* equation was used to determine various electrochemical parameters including electron transfer coefficients (α), heterogeneous rate constants (k_s) and diffusion coefficient (D) and the values obtained tabulated (**Table 5.2)**.

Table 5.2: Electrochemical kinetic parameters for interactions between Ag-Au (1:2) NPs and *E. coli* in 0.1 M PBS, at pH 7.4

Electrochemical parameters	**CV**	**EIS**
D (cm^2s^{-1}) $\times 10^{-15}$	4.90	4.71
$\alpha \times 10^{-1}$	1.20	-
Redox activity (moles/bacterial cell)$\times 10^{-8}$	-	1.69
k_s (s^{-1}) $\times 10^{-11}$	1.55	1.53
n (number of electrons transferred)	7	6.5

The relationships between scan rates and peak potentials indicated that the anodic peak potentials shifted towards more positive side with increasing scan rate. This suggested that the electron transfer rates between the bacterial proteins in the bacterial metabolic pathway and Ag-Au (1:2) NPs was irreversible and mass transfer dependent (Gowda & Nandibewoor, 2014). Linear relationships were also obtained between the plots of log V versus E_{pa} with linear equation: E_{pa} (A) = 0.076logV + 0.686; (R^2 = 0.9993). The value of E_{pa} for irreversible electrode processes was determined using equation (**5.1**). The slope of plots of log V versus E_{pa} was used to determine the

values of αn. For the reaction between the bacterial cells and NPs, the slopes were determined from the linear equation (**Figure 5.8 b**) and obtained to be 0.076.

Taking F = 96,500 $\mathrm{Cmole^{-1}}$, R = 8.314 $\mathrm{JK^{-1}mole^{-1}}$ and T = 298 K, the value of αn was calculated to be 0.598. According to Bard and Faulkner equation (Mohamed et al., 2017), the value of α was determined to be 0.1195. This indicated more homogeneous electrode surface coupled with efficient electro-catalytic processes during bacteria-Ag-Au (1:2) NPs interactions. The number of electrons (n) transferred during these reactions was calculated to be 6.598 ~ 7. The heterogeneous rate constant was determined from the intercepts of the plots of log V versus E_{pa} using the values of E^{θ} obtained from the intercept by extrapolating to the vertical axes at $\upsilon = 0$. The value of E^{θ} was determined as 0.765. The value of k_s was calculated to be $1.545 \times 10^{11}\ \mathrm{s^{-1}}$ indicating that the NPs-bacterial interactions had excellent reversibility. The diffusion coefficient (D) was also determined using the *Randle's-Sevcik* equation **(5.2)** and tabulated (**Table 5.2)**. Higher values of D were obtained suggesting faster rate of electron transfer towards the electrode surface.

$$\mathrm{I_{pa}} = (2.99 \times 10^5)\mathrm{nAC_o}\sqrt{\alpha \mathrm{D}\upsilon} \ldots\ldots\ldots\ldots\ldots\ldots (5.2)$$

$$\mathrm{K_{et}} = \frac{\mathrm{RT}}{\mathrm{n^2F^2A\Delta R_{ct}C_o}} \ldots\ldots\ldots\ldots\ldots\ldots (5.3)$$

$$\mathrm{R_{ct}} = \frac{\mathrm{RT}}{\mathrm{n^2F^2AK_{et}}} \cdot \frac{1}{\mathrm{C_0}} \ldots\ldots\ldots\ldots\ldots\ldots (5.4)$$

$$\mathrm{D} = \frac{\mathrm{R^2T^2}}{\mathrm{2n^4F^4A^2C^2}\delta^2} \ldots\ldots\ldots\ldots\ldots\ldots (5.5)$$

$$\mathrm{Z'} = \mathrm{R_s} + \mathrm{R_{ct}} + \delta \mathrm{w}^{0.5} \ldots\ldots\ldots\ldots\ldots\ldots (5.6)$$

For comparison purposes, EIS technique was also used to determine the kinetic parameters for the interactions between the bacteria and Ag-Au (1:2) NPs using **Equations 5.2-5.6** and the values obtained tabulated as (**Table 5.2)**.

The Bode plots (**Figure 5.8 d**) showed that the interactions between the NPs and bacteria significantly influenced the magnitude of impedance at lower frequencies. In order to interpret the physical significance of the difference in the magnitudes of impedance observed and to quantify the electrochemical parameters of the interface, theoretical Randles equivalent circuits (RECs) whose impedance exhibited the same behavior as the experimental impedance were constructed. The RECs for the bacteria - NPs interactions mainly consisted of solution resistance (R_s), charge transfer resistance (R_{ct}), double layer capacitance (C_{DL}) and Warburg impedance (Z_w). Due to the

inhomogeneity and defects on the electrode surfaces, the constant phase element (CPE) was used instead of an ideal capacitor for the curve fitting and modeling. The CPE represented the C_{DL} accounting for the distribution of currents in the inhomogeneous electrode surface.

The fitting and modelling data obtained showed that the REC fitted the measured data points with average errors less than 1 % and acceptable *chi* square (X^2) values (**Appendix II**). The values of the electrical elements determined for the interactions between the bimetallic NPs and GCE were; 22.32 ± 0.34 kΩ (R_{ct}), 1.91 ± 1.05 kΩ (R_s), 7.96×10^{-5} F (C_{DL}), 0.996 (α), 2.64×10^{-5} µF (Z_w). These values significantly decreased to 9.99 ± 0.08 kΩ, 0.59 ± 0.53 kΩ, 8.70×10^{-7} F, 0.994 and 2.09×10^{-5} µF, respectively in the presence of the bacteria. The significant decrease in R_{ct} compared to R_s in the presence of *E. coli* showed that the change in R_s was not enormously affected by the chemical transformations on the electrode surface as the bacterial cells interacted with the NPs. This also indicated that the intrinsic conducting and dielectric properties of the bacterial cells decreased the R_{ct} and increased the C_{DL} hence led to a consequent decrease in impedance magnitude. This can also be ascribed to the attachment of the bacterial cells to the electrode surface which in turn enhanced the exchange of electrons between the bimetallic NPs and electrode surface. The interactions between the bimetallic NPs and bacteria increased the number of ionic charges in the C_{DL} due to the formation of bacterial cell layer charges which in turn enhanced the dielectric constant and decreased the double layer thickness. Comparing the R_{ct} and C_{DL} for the complex formed before and after bacteria-NPs interactions, the presence of the bacterial cells enhanced more charge transfer and consequently increased the C_{DL}. This showed that the more the bacterial cells in close contact with the electrode surface, the smaller the distance between the two interacting surfaces and hence the larger the value of C_{DL} obtained Simeon & Freitag, 2022).

The value of α; the indicator of the electrode surface roughness decreased from 0.996 to 0.994 after bacteria-NPs interactions. This was attributed to the smaller-size nature of the bacterial cells which formed a sheath on the electrode surface. This in turn increased the electrode surface roughness hence enhanced the charge transfer processes between the NPs and bacterial cells. The observed increase in charge transfer between the bacterial cells and NPs enhanced the reduction of the monometallic ions (Ag^+, Au^{3+}) in the bimetallic NPs. In bacterial cells, free electrons from the cytochrome C oxidase abundant on the bacterial cell membrane give rise to short-range electron

exchange reactions mainly through their carboxylate ions (Herrero-Hernandez *et al*., 2019; Chinnaraj & Priya Ponnaiah, 2021). To confirm the flow of electrons from the bacterial cells towards the metallic ions (Ag^{+}, Au^{3+}) on the electrode surface, the value of D (diffusion coefficient) for a totally irreversible electrode process was determined using equation **5.2** and found to be to be 4.901×10^{-15} cm^2s^{-1} (**Table 5.2**) and this suggested an enhanced mass transport of bacterial cells towards the electrode surface. The EIS technique was also used to determine the kinetic parameters (k_s, D, n) employing equations **5.3-5.6** and the values obtained tabulated in **Table 5.2**. The values obtained with both CV and EIS techniques were found to correlate well. These values suggested an irreversible reaction, homogeneous electrode surface interaction and efficient electro-catalytic reactions between the bacterial cells and bimetallic NPs.

The results described above provided some insights into the potential mechanism (**Figure 5.9**) associated with effective interactions between the bacteria and the bimetallic NPs. The hypothesis is that the redox activity of the bacteria to the NPs is based on the transfer of electrons from the bacterial metabolic pathway to the NPs. Bacterial surface is known to be negatively charged while the NPs are positively charged. Electrons therefore moved from the bacterial surface to the NPs which in turn became reduced hence leading to the formation bacteria-NPs complex. Upon collision of the complex with the active electrode surface, the NPs became re-oxidized thus generating electrical signals at applied electrical potential of +0.5 V. The more the NPs re-oxidized, the greater the redox activity of the bacteria to the NPs hence rapid signal generation and amplifications. Therefore, the proposed mechanism for the electro-oxidation reaction between the NPs and bacteria conformed to a 7-electron transfer process. This was attributed to the presence of 2 moles of Au^0 and 1 mole of Ag^0 in the bimetallic NPs requiring a total of 7 electrons for complete electro-oxidation process. This is accompanied by the pumping of 8 H^+ from the matrix of the mitochondrion within the enzyme (cytochrome C oxidase) of the bacteria. 4 H^+ out of the 8 H^+ were then pumped into the inner matrix of the enzyme's mitochondrion so as to create a steeper proton gradient for faster synthesis of ATP which in turn enhanced the stabilization of the bacteria-NPs complex formed.

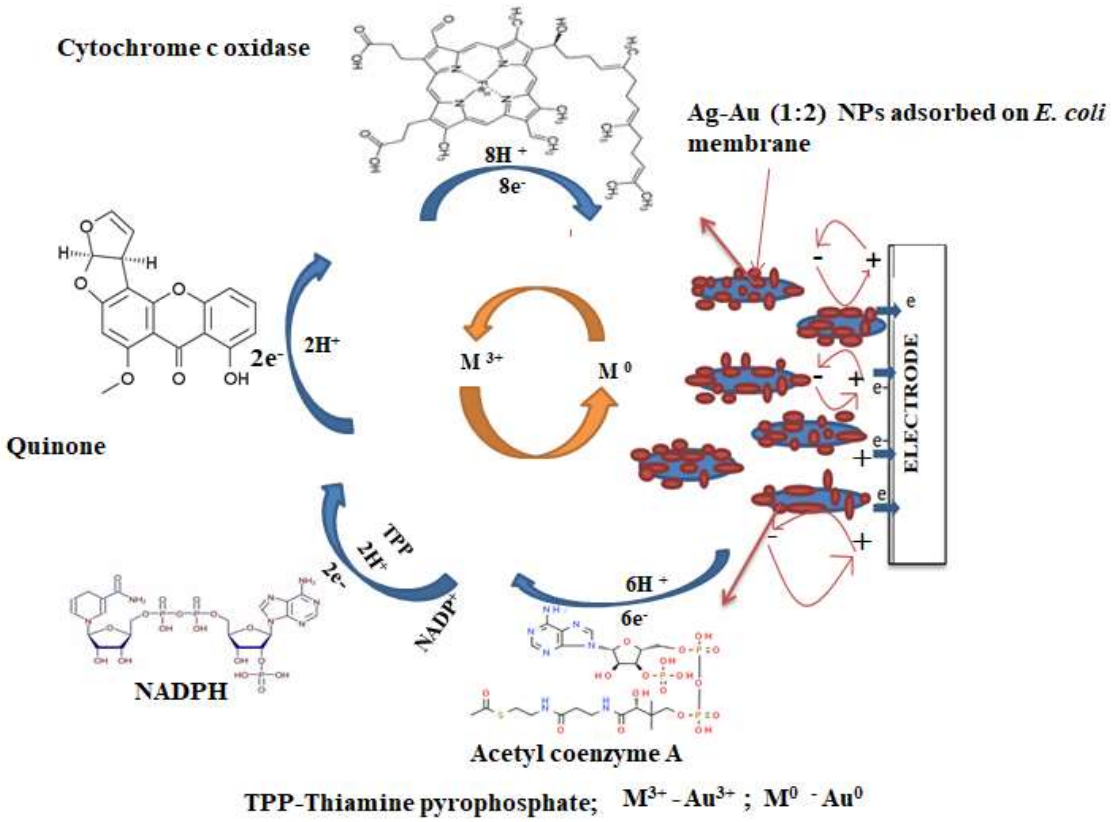

Figure 5.9: Proposed mechanism for the interaction between *E. coli* and Ag-Au (1:2) NPs

The concentration of NPs re-oxidized on the electrode surface can be equated to the redox activity of 1 mole of cytochrome C oxidase. This is directly proportional to the quantity of electric charge (Q) accompanying the electro-oxidation reactions. This was determined using the Faraday's Law (**Equation 5.7**) and obtained as 1.688×10^{-8} molescell^{-1}.

$$Q = nFm \ldots\ldots\ldots\ldots\ldots\ldots\ldots\ldots\ldots\ldots\ldots\ldots\ldots\ldots\ldots\ldots\ldots\ldots\ldots\ldots\ldots\ldots\ldots\ldots\ldots . (5.7)$$

Where n is the number of electrons transferred, F, Faraday's constant = 96,500 Cmole^{-1}; M is the concentration of the NPs re-oxidized. The obtained value was found greater than what was reported elsewhere (Chen *et al*., 2019). This indicated that the electrostatic adsorption between the bimetallic NPs and bacterial surface was successful thus enhanced the electro-oxidation reactions between the bacteria and NPs. The *zeta* potential (mV) of *E. coli* was also determined to be -15.50 ± 0.92 and upon adsorption of the positively charged Ag-Au (1:2) NPs with a potential of -4.34 ± 0.71, the *zeta* potential of the complex slightly decreased to -11.30 ± 0.75. These results indicated

successful complex formation due to the strong electrostatic interactions between the bacteria and bimetallic NPs (Smith *et al*., 2017).

5.3.7 Optimization of applied potential and AC amplitude

Based on the oxidation peak potential for the bacteria determined using CV, the applied potential and AC amplitude were each optimized by varying them between (0.0 to +1.0 V) and (1-15 mV), respectively (F**igure 5.10)** for the bacteria-bimetallic NPs interaction studies using EIS technique. The ΔR_{ct} significantly decreased with increase in applied potential and AC amplitude. The ΔR_{ct} was significantly lowest at applied potential and AC amplitude of +0.5 V and 10 mV, respectively. Closely similar observations have been reported elsewhere (Kanokkanchana *et al*., 2018). Therefore, these optimum conditions were chosen for further electrochemical interaction studies using EIS techniques.

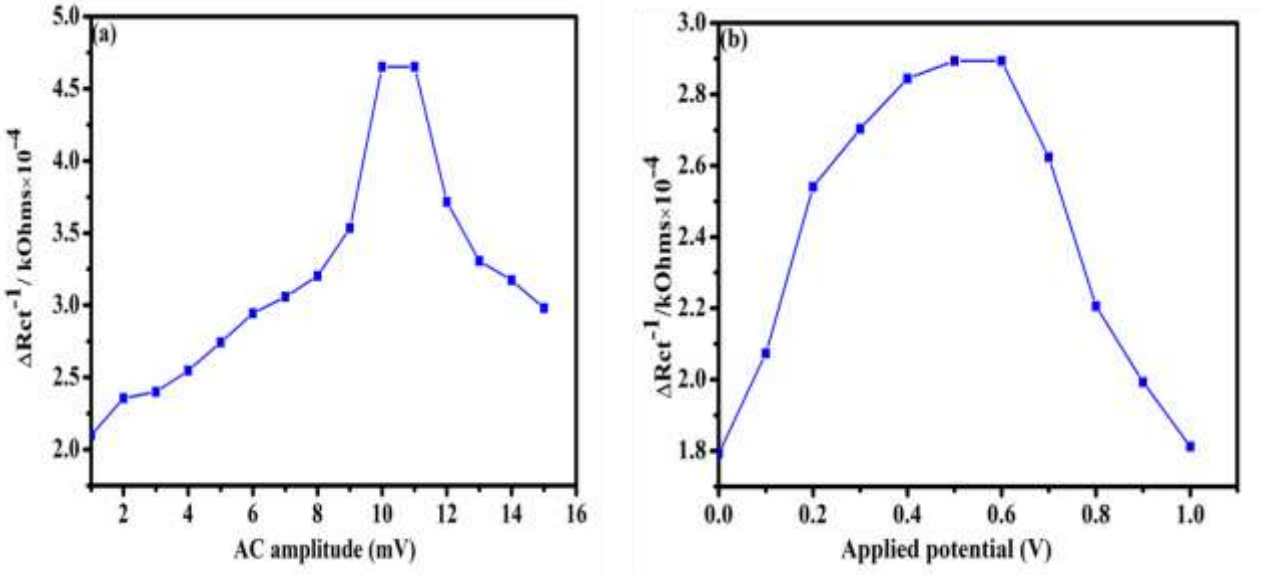

Figure 5.10: Variation of (a) AC amplitude, (b) Applied potential for Ag-Au (1:2) NPs-*E. coli* interaction studies

5.3.8 Determination of linearity and applicability of GCE nano - impact sensor

An overlay of various standard Nyquist plots (**Fig. 5.11**) showed that the addition of *E. coli* in increasing concentration (10^1-10^7) cellsmL^{-1} into the bimetallic NPs led to an exponential decrease in R_{ct}. This indicated an inverse relationship between R_{ct} and increasing *E. coli* concentrations. This inverse relationship has been reported elsewhere (Randviir, 2018) and was used in plotting a

calibration graph of logarithm of bacterial concentrations (C) versus ΔR_{ct}^{-1} as shown in **Figure 5.11**. The plot was used to determine the analytical parameters for the sensor.

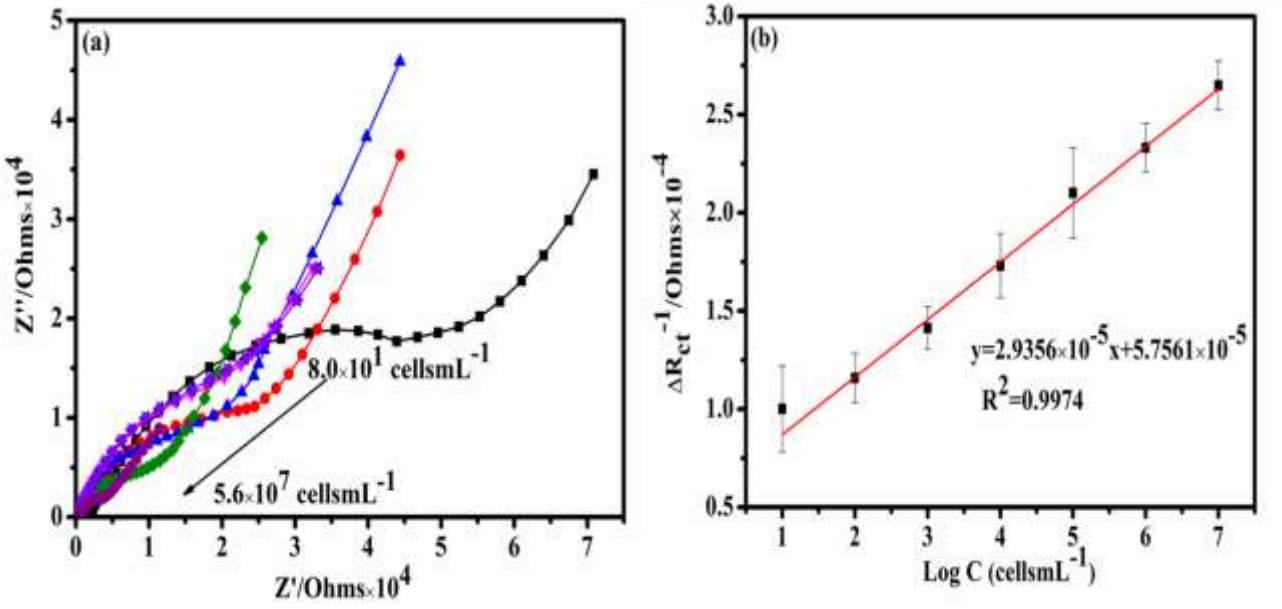

Figure 5.11: a) Nyquist plot and (b) corresponding calibration plot for interactions between Ag-Au (1:2) NPs and logarithm of *E. coli* concentrations (C).

A perfect linear relationship between ΔR_{ct}^{-1} and log C was established (**Figure 5.11 b)** with an R^2 of 0.999. LOD and LOQs of 1.8×10^1 and 2.3×10^2 cellsmL^{-1}, respectively were also determined using equations **5.8 and 5.9**.

$$\mathrm{LOD} = 3\left(\frac{\mathrm{s}}{\mathrm{m}}\right) \ldots\ldots\ldots\ldots\ldots\ldots\ldots\ldots\ldots\ldots\ldots\ldots\ldots\ldots\ldots\ldots\ldots\ldots\ldots\ldots\ldots\ldots\ldots\ldots\ldots\ldots\ldots\ldots (5.8)$$

$$\mathrm{LOQ} = 10\left(\frac{\mathrm{s}}{\mathrm{m}}\right) \ldots\ldots\ldots\ldots\ldots\ldots\ldots\ldots\ldots\ldots\ldots\ldots\ldots\ldots\ldots\ldots\ldots\ldots\ldots\ldots\ldots\ldots\ldots\ldots\ldots\ldots\ldots\ldots (5.9)$$

This response was attributed to the excellent electro-catalytic activity of Ag-Au (1:2) NPs coupled with higher sensitivity of EIS technique.

5.4 Validation of GCE nano-impact sensor

5.4.1 Repeatability, reproducibility, stability and selectivity studies

Repeatability and reproducibility studies (**Figure 5.12**) of the developed sensor gave percentage relative standard deviations (% RSD) of 2.3 and 3.18 %, respectively indicating good and acceptable repeatability and reproducibility for the sensor.

The results for stability studies (**Figure 5.12 b**) showed that the ΔR_{ct} of the NPs was maintained at 88 % even after the NPs were stored at 4 °C in 0.1 M PBS, pH 7.4 for 4 days. The performance of the old NPs also showed no significant reduction in sensing capabilities compared to the detection of the bacteria using freshly prepared NPs.

Selectivity studies of the sensor showed that the magnitude of ΔR_{ct} for *E. coli* assay was unaffected even in the presence of higher concentrations of the non-target bacteria: *E. coli*: *salmonella typhimurium* ratio of 1:2 (**Figure 5.12 c**). The ΔR_{ct} for *E. coli* alone (55 kΩ) was also significantly lower compared to that of *S. typhimurium* (60 kΩ) indicating enhanced charge transfer due to the presence of *E. coli*. This proved that the sensor was selective to *E. coli*.

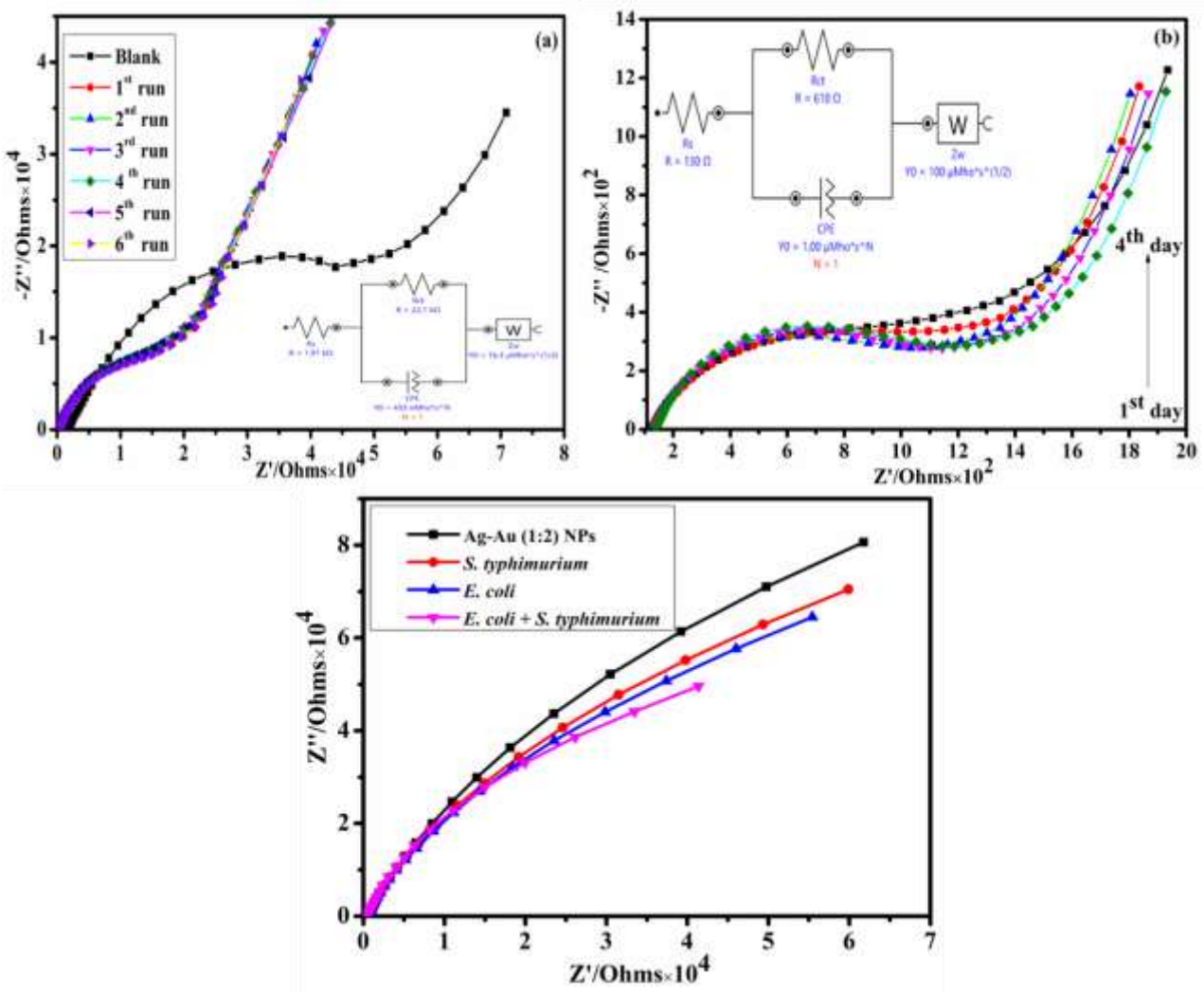

Figure 5.12: Proposed sensor's (a) Repeatability; (b) Stability; and (c) Selectivity studies based on Nyquist plots

The analytical performance of the sensor in both qualitative and quantitative determinations of *E. coli* assays was also compared with those of previously reported methods (**Table 5.3**). It was found that our proposed nano-impact sensor integrated with EIS technique displayed improved sensitivity and wider dynamic linear range compared to other methods (Sepunaru *et al*., 2015; Lee *et al*., 2016; Couto *et al*., 2018; Ronspees & Thorgaard, 2018; Frkonja-Kuczin *et al*., 2018; Gao *et al*., 2018; Y. Chen *et al*., 2021). Therefore, our developed nano-impact sensor might satisfy the requirements for effective profiling of low abundance *E. coli* in water due its lower LOD.

Table 5.3: Comparison of reported nano-impact electrochemical detection strategies for *E. coli* with the developed method

Electrochemical technique	**Detection platform**	**Electrolyte composition**	**LOD (cellsmL^{-1})**	**Linear range (cellsmL^{-1})**	**References**
EIS	GCE	0.1 M PBS/Ag-Au (1:2) NPs	1.8×10^{1}	10^{1}-10^{8}	This work
CV	GCE/PI-5-CA/C-SWCNTs/Ab	0.1 M PBS (pH 6)	-	10^{1}-10^{7}	(Wang *et al*., 2022)
CA	Carbon- UME	0.1 M KCl	-	-	(Chen *et al*., 2021)
CA	Au electrode	2.1 mM TMPD-BF_4/ 0.1 M PBS (pH 7.4)	5.0×10^{6}	10^{6}-10^{7}	(Couto *et al*., 2018)
CA	Pt-UME	1 mM KCl/ 2 mM FcM	8.4×10^{5}	10^{5}-10^{6}	(Ronspees & Thorgaard, 2018)
CA	Pt-UME	0.1 M, $Fe(CN)_6^{4-}$	-	-	(Gao *et al*., 2018)
DPV	Pt electrode	PAPG/ PBS (pH 7.2)	5.0×10^{3}	10^{3}-10^{6}	(Wang *et al*., 2017)
CA	UME	0.02 M $Fe(CN)_6^{4-}$	-	-	(Lee *et al*., 2016)
CA	GCE	0.1 M KCl/ Ag NPs	-	10^{5}-10^{9}	(Sepunaru *et al*., 2015)

Ab: Antibody, CA: chronoamperometry, EIS: electrochemical impedance spectroscopy, UME: Ultra-microelectrode, FcM: Ferrocene methanol, PI-5-CA: poly-5-carboxyindole, C-SWCNTs: carboxylated single-walled carbon nanotubes, PAPG: 4-Aminophenyl-β-galactopyranoside)

5.4.2 Recovery studies

The concentrations of the bacteria in the spiked fruit juice (FJ) and tap water (TW) samples evaluated from the calibration graph showed that the recovery studies were in the range of (122.12 ± 0.10-161.86 ± 0.12) % for TW and (98.79 ± 0.14-124.25 ± 0.15) % FJ with significantly lower % RSD (1.8-2.4) and (1.82 - 3.5) % for TW (n = 3) and FJ (n = 3) samples, respectively. The obtained recovery percentages and low % RSD indicated that the proposed method was accurate and precise with a possibility of application in water and fruit juice samples with minimum interferences. The reported values were within ranges reported for closely similar studies (Okumu *et al*., 2020)

5.4.3 Practical application of the sensor

In order to demonstrate the practical applicability of the developed nano-impact sensor for *E. coli*, standard addition method of analysis of River and Ocean water samples for the bacterial cells was undertaken (**Appendices III, IV, V and VI**). It was found out that the concentrations of the bacterial cells detected were in the range of (1200 ± 327)-($9.3 \times 10^8 \pm 54800$) and ($3.60 \times 10^4$-$4.17 \times 10^9$) cells$mL^{-1}$ for River (n = 6) and Ocean (n = 6) water samples, respectively. The results obtained also revealed that the spiked concentration of *E. coli* cells was significantly consistent with the concentration detected by the sensor. This showed that the proposed electrochemical nano-impact strategy can be applied in real samples analyses and has greater potential in practical applications for early and sensitive detection of *E. coli* in complex samples.

5.5 Bacteria-NPs interaction studies using IDAE

The CVs of IDAE and Ag-Au (1:2) NPs in the absence and presence of the bacteria are as shown in **Figure 5.13**. It was observed that the interactions between the electrode and bimetallic NPs showed two anodic and two cathodic peaks centred at -0.33 (Au^{2+} to Au^0), +0.17 (Ag^0 to Ag^+), +1.10 (Au^0 to Au^{3+}) and +1.30 V (Au^{3+} to Au^{2+}). The peaks shifted to less positive potentials from -0.33 to -0.43 and +1.03 to +1.20 V relative to those observed in GCE except the oxidation of Ag^0 to Ag^+ (+0.17 to +0.25 V) and reduction of Au^{3+} to Au^0 (+1.10 to +1.25 V) which slighltly shifted to more positive potentials. This can possibly be attributed to rapid formation of mixtures of hydrous and anhydrous Au oxides nearly at the same potential. This reduced the rate of electron exchange reactions due to temporary electron transfer hindrance imposed by the mixture of Au oxides on the electrode surface as similarly reported elsewhere (Hassan *et al*., 2015; Testolin *et al*., 2019). Correct orientation of electro-active species on electrode surface has been reported to enhance electron transfer rates since the distances between electrochemically active centres in the bacterial cells and electrode surfaces are minimized (Scanlon *et al*., 2012).

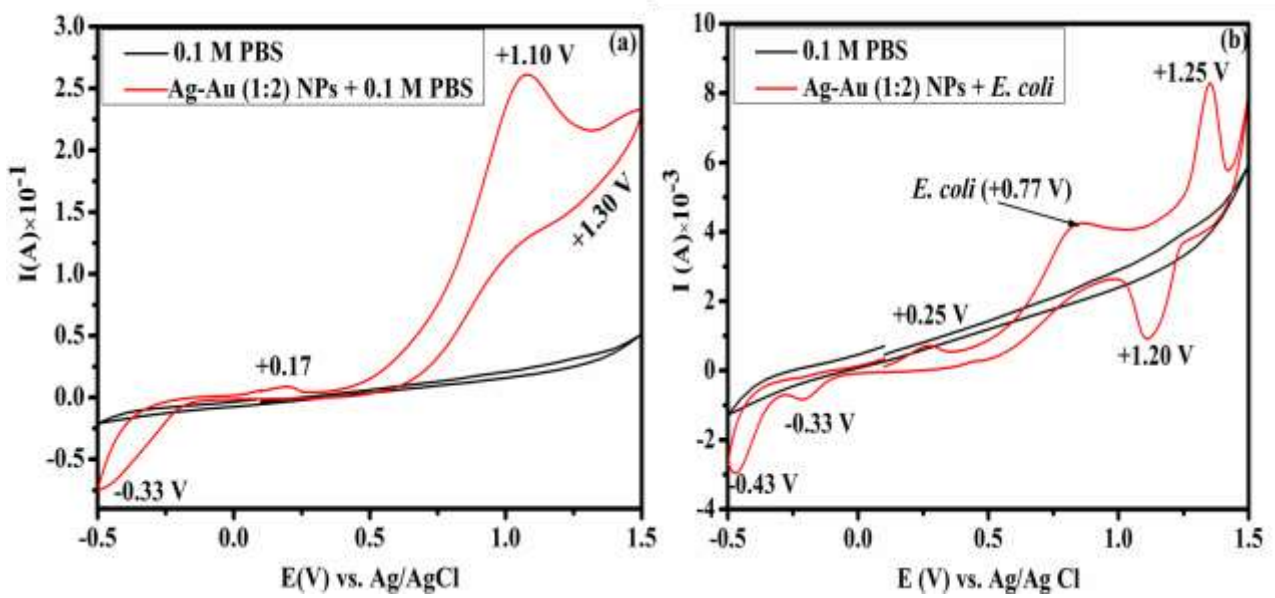

Figure 5.13 : Cyclic voltammograms of Ag-Au (1:2) NPs in the absence (a) and presence (b) of *E. coli* in 0.1 M PBS at pH 7.4, scan rate; 0.03 Vs^{-1}

The peak potentials due to the interactions between the bacteria and bimetallic NPs shifted to less positive values in (Au^0 to Au^{3+}), (Au^{2+} to Au^0), (Ag^0 to Ag^+) and (Ag^+ to Ag^0) reactions with enhanced peak current intensities relative to those observed in GCE. This can possibly be due to the larger surface area to volume ratio of IDAE hence faster bacterial-NPs interactions. This reaction also led to the formation of a broad and distinct irreversible oxidation peak centred at +0.77 V signifying the presence of the bacteria. This peak, however, shifted slightly to less positive potential compared to the one observed in GCE. This can be attributed to enhanced interactions between the bacterial membrane proteins and electrode surface due to the small size nature of the bacteria (1.0 × 2.0 × 0.5 µm) which made the cells to fit into the smaller micro-holes (10 µm) of the IDAE. The arrays of the interdigitated electrodes in turn yielded higher currents due to the faster electrode kinetic reactions due to the close contact between the complex and electrode surface. The current intensity due to bacteria-NPs interactions also increased with bacteria-NPs incubation period and concentrations of the NPs as shown in **Figure 5.14**. To the best of our knowledge, no study in the literature has reported this electrochemical phenomenon.

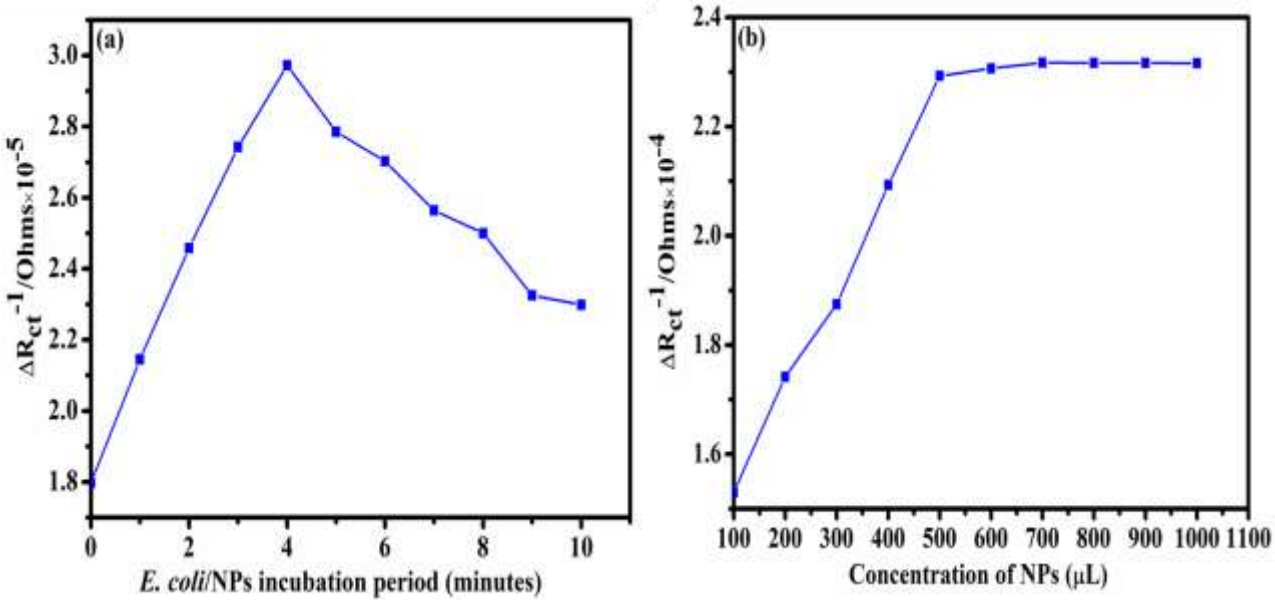

Figure 5.14 : Effects of (a) *E. coli*-Ag-Au (1:2) NPs incubation period and (b) concentration of bimetallic Ag-Au (1:2) NPs on bacteria-bimetallic NPs interactions studied using EIS technique

5.5.1 Determination of electron transfer kinetic parameters

The CV results obtained showed that the oxidation peak current increased proportionally with $V^{1/2}$ as represented by the linear equation: I_{pa} (A) = 3.8902E-04 V (Vs^{-1})-0.0252; (R^2 = 0.9977) shown in **Figure 5.15**. This showed that the electro-catalytic processes between the bacterium and bimetallic NPs on the IDAE were mainly irreversible and diffusion-controlled due to the significantly higher value of R^2 obtained. *Laviron's* equation (**5.1**) for irreversible electrode processes was used to determine the values of n and k_s. The value of α was assumed to be 0.5 for irreversible electrode processes (Hegde *et al*., 2011). The results obtained were tabulated as shown in **Table 5.2**.

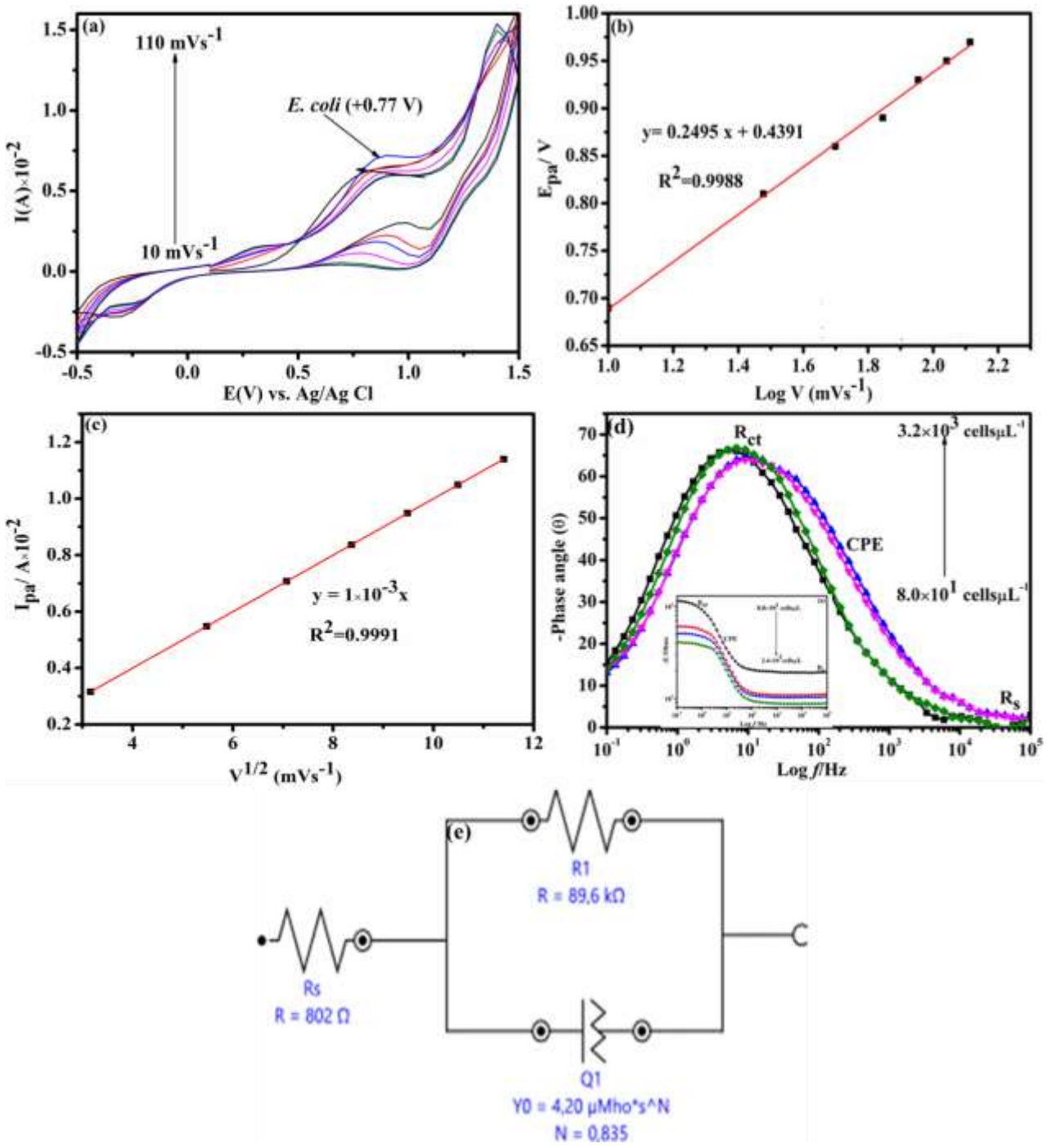

Figure 5.15 : (a) CV scan rates studies of *E. coli*-Ag-Au (1:2) NPs interactions (b) *Laviron's* plot (c) *Randle's* plots (c) Bode plots (e) *Randle's* equivalent circuit for the interaction studies between *E. coli* and Ag-Au (1:2) NPs

The relationship between scan rates and peak potentials indicated that the anodic peak potentials shifted towards less positive values with increasing scan rate compared to the ones observed in GCE. This suggested that the electron transfer rates between the bacterial proteins in the bacterial metabolic pathways and Ag-Au (1:2) NPs were irreversible, mass transfer and electrode surface area to volume ratio dependent. Linear relationships were also obtained between the plots of log V versus E_{pa} with linear equation: E_{pa} (V) = 0.2495 log V (Vs^{-1}) + 0.4391; (R^2 = 0.9988).

Figure 5.15 d shows the fitted curve of the magnitude and phase angle of the impedance measurements with the generated equivalent circuit (**Figure 5.15 e**) representing the electrochemical system established as the bimetallic NPs interacted with varying bacterial concentrations. From the figure, three main regions were identified in the spectra. These included; constant phase element, CPE (Q_1) representing the double layer capacitance (C_{DL}) generated by the ionic species in the bacteria-bimetallic NPs complex overlaid near the electrode surface, solution electrolyte resistance (R_s) and charge transfer (R_{ct}) resistance. The fitting and modeling data obtained showed that both R_s and R_{ct} significantly decreased in the presence of the bacteria. The values (kΩ) of R_s and R_{ct} due to the interactions between electrode and bimetallic NPs were 1.02 ± 0.04 and 10.51 ± 1.25, respectively.

Comparing the values of the parameters determined before and after *E. coli*-NPs interactions, it was observed that the R_s and R_{ct} significantly decreased to 0.50 ± 0.74 and 89.62 ± 1.63 kΩ, respectively in the presence of the bacteria (**Appendix VII**). This indicated that the rate of formation of the complex, electrode size, concentration of the bacteria and bacteria-NPs complex thickness greatly influenced the impedance magnitude of the entire electrochemical system. The decrease in impedance magnitude can also be ascribed to the release of ionic metabolites from the live bacterial cells as well as through the exchange of ions such as K^+ and Na^+ via the bacterial membrane as the bacterial cells interact with the bimetallic NPs (Mallén-Alberdi *et al.*, 2016). The increase in conductivity can also be due to the capturing of *E. coli* cells by IDAE surface leading to enhanced release of intracellular ions such as K^+ and Na^+ through electropermeabilization. Bacterial cells contain numerous dissolved charged molecules making them highly conductive (1 Sm^{-1}) (Xu *et al.*, 2016). This enhances the detection of biological cells by impedance due to the lysis of cells or release of intracellular ions into the electrolyte.

5.5.2 Optimization of applied potential and AC amplitude

The intracellular components of bacterial cells are highly conductive and show impedimetric properties (Brosel-Oliu *et al*., 2019). Therefore, AC amplitude was also optimized for the nano-impact impedimetric detection of the bacteria using IDAE. Increasing the AC amplitude from 1 to 15 mV led to a decrease in ΔR_{ct} upto 5 mV (**Figure 5.16 a**). Above this, the ΔR_{ct} increased with increasing AC amplitude upto 15 mV. The response of bacterial cells to an electric field is an intrinsic feature related to the bacterial cell shape and size, bacterial cell internal structure, electrical conductivity, electrode size and permittivity of different components of bacterial cells (Zhang *et al*., 2021). Therefore, increase in AC amplitude can possibly be attributed to the attachment of the bacterial cells to the electrode surface hence causing resitance to electron flow (Couniot *et al*., 2015).

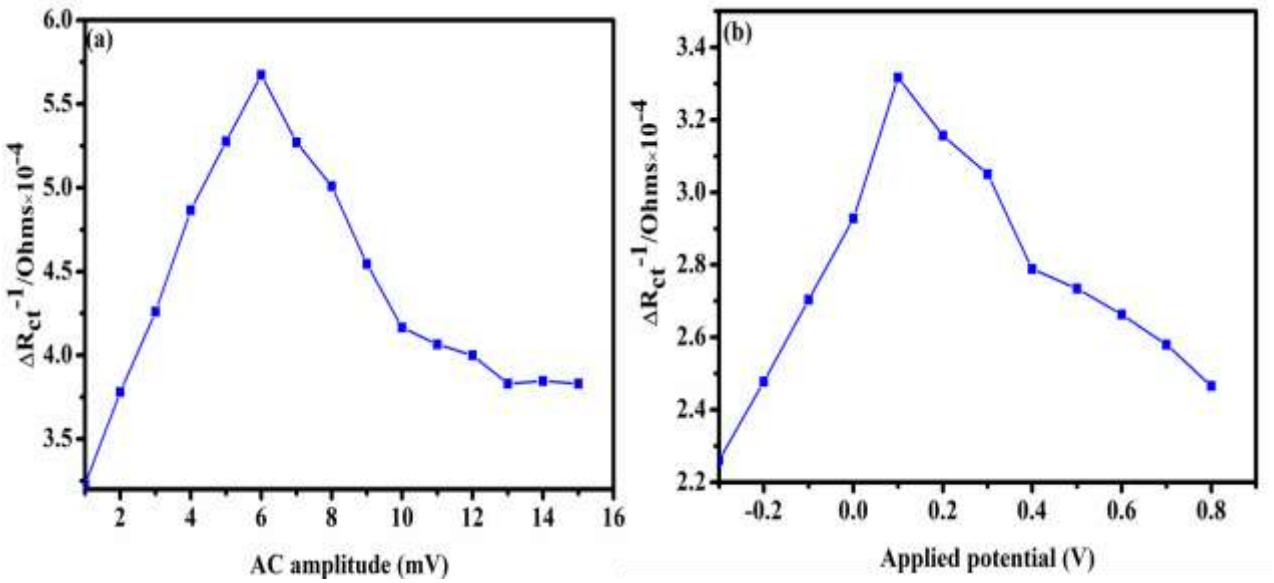

Figure 5.16 : Variation of (a) AC amplitude, (b) Applied potential for interaction studies between Ag-Au (1:2) NPs and *E. coli* using IDAE.

Based on the oxidation peak potential for the bacterial cells determined from the CV studies (**Figure 5.13**) and the reported oxidation peak potential ranges for Gram-ve and+ve bacteria in the literature (Wang *et al*., 2021), the applied potentials for the detection of the bacteria was varied between - 0.3 to +1.0 V (**Figure 5.16 b**). Increasing the potential from -0.3 to +0.8 V, led to proportional decrease in ΔR_{ct} upto +0.1 and +0.5 V. The ΔR_{ct}^{-1} significantly decreased with applied potential upto +1.0 V. This indicated that an increase in applied potential impaired the bacterial cell membranes due to shock waves (Estifaee *et al*., 2019). The application of external

electric field in the presence of bacterial cells affects their overall impedance. At low frequency, electrical fields permeate bacterial cells due to the isolating properties of cell membranes while at higher frequencies the field lines partially penetrate the membrane giving information of the cytoplasmic properties (Güler & Oruç, 2021).

Based on the above optimization studies, the following optimum conditions were chosen for further bacteria-bimetallic NPs interaction studies using IDAE as a transducer. These included; *E. coli*: Ag-Au (1:2) NPs volume (500 µL), Ag-Au (1:2) NPs-*E. coli* incubation period (4 minutes), PBS concentration (0.1 M), modulation amplitude (5 mV) and applied potential (+0.1 V).

5.5.3 Determination of sensor's linearity and applicability

The developed *E. coli* nano-impact sensor was used to determine the impedance responses of varying concentrations of the bacterial cells under the above optimized conditions. **Figure 5.17** shows the Nyquist impedance spectra of varying concentrations (10^1 -10^7) cellsμL^{-1} of *E. coli* in 0.1 M PBS at pH 7.4. It can be observed that the charge transfer resistance (R_{ct}) under the optimized conditions significantly decreased with increasing cell concentrations in the frequency range of 10^5-10^{-1} Hz. A perfect linear relationship between ΔR_{ct}^{-1} and logarithm of bacterial cell concentration was also established in the concentration range of 10^1-10^7 cellsμL^{-1} and the LOD and LOQ were calculated to be 10^1 and 10^2 cells μL^{-1}, respectively. The equation of the calibration curve was established as $\Delta R_{ct}^{-1}\ (\Omega) = \log 1.6432 \times 10^{-5} x + 8.6205 \times 10^{-6}$ ($R^2 = 0.9975$). This decrease in R_{ct} with increasing bacterial cell concentrations indicated that the bacterial cells with higher concentrations are more conductive than those with lower concentrations (Mashkour *et al*., 2017). Electrical nature and ion release from bacterial cells coupled with the reduced size of the electrode used might have enhanced the conductivity of bacteria-bimetallic NPs suspension hence the observed decrease in impedance with increasing bacterial concentrations.

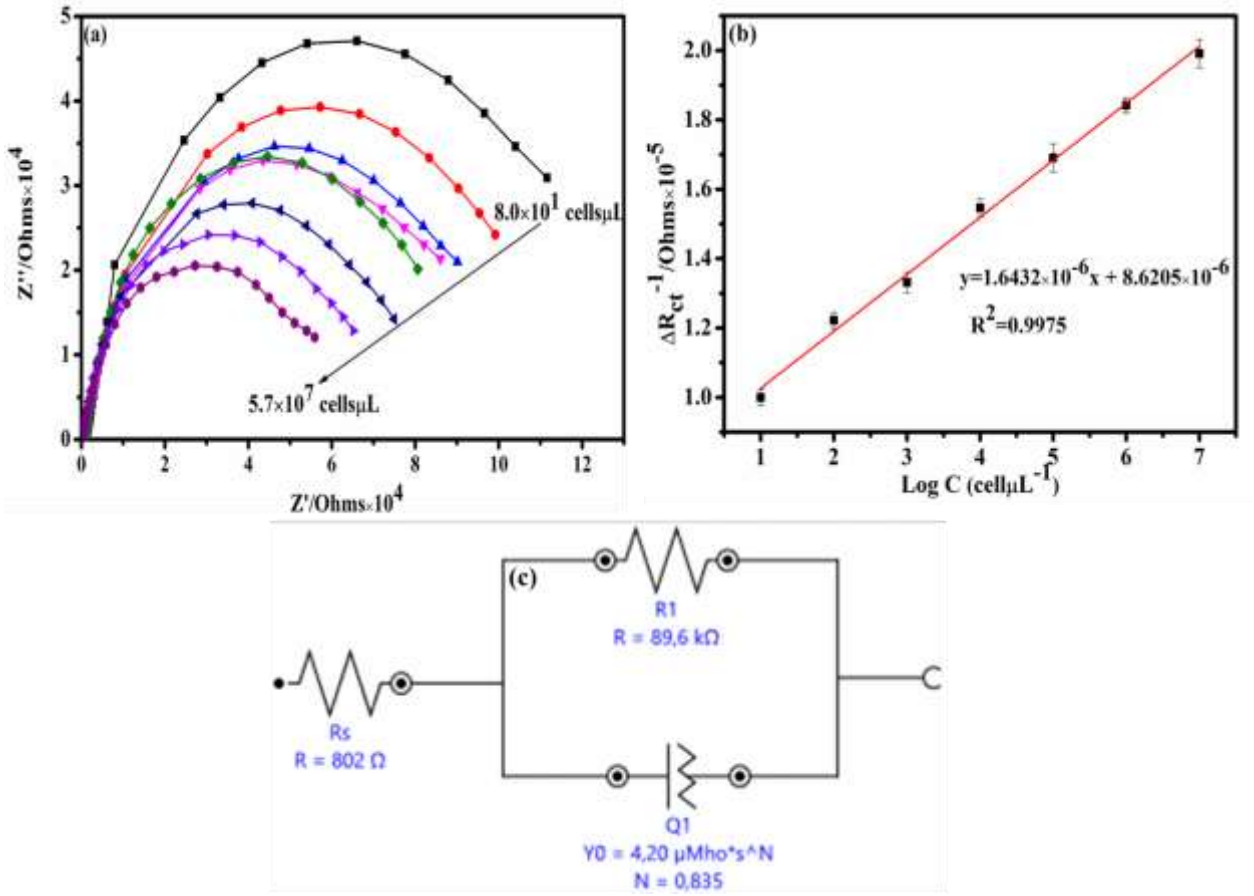

Figure 5.17: a) Nyquist plot for interactions between Ag-Au (1:2) NPs and varying concentrations of *E. coli*; b) Calibration plot for ΔR_{ct}^{-1} versus logarithm C of *E. coli*; c) corresponding *Randle's* equivalent circuit.

5.6 Validation of IDAE sensor

5.6.1 Repeatability, reproducibility, stability and selectivity studies

Repeatability and reproducibility of the proposed nano-impact sensor were tested. The reproducibility studies of the proposed nano-impact sensor (n = 3) gave % RSD of 2.08 % at concentration of 10^2 cellsµL^{-1}. Repeatability studies gave % RSD of 2.11 (n = 6). These results indicated that the proposed interdigitated nano-impact sensor for the bacteria represented good and acceptable repeatability and reproducibility.

Three different but same samples of Ag-Au (1:2) NPs stored at 4 °C in 0.1 M PBS (pH 7.4) were separately prepared on the same day and used to detect the bacteria daily for 4 days under the optimized conditions. There was no significant loss in activity of all the NPs after the 4 days. After

the 4th day of storage, the (n = 3) NPs retained 95.20 ± 0.40 % of their initial impedimetric responses. This can be ascribed to the stability of the Ag-Au (1:2) NPs used.

S. typhimurium strain was used to investigate the specificity of the developed *E. coli* nano-impact sensor (**Figure 5.18**). Solutions containing 10^2 cells of *S. typhimurium*, equal mixture (1:1, v/v) of *E. coli* and *S. typhimurium*, and *E. coli* alone were incubated with the NPs and ΔR_{ct} determined under the optimized conditions. The ΔR_{ct} (kΩ) for the *S. typhimurium* alone was significantly higher (0.43 ± 0.10) than for *E. coli* (0.39 ± 0.57) and a mixture of *E. coli* and *S. typhimurium* (0.29 ± 0.10). This confirmed the selectivitiy of the nano-impact sensor towards *E. coli*.

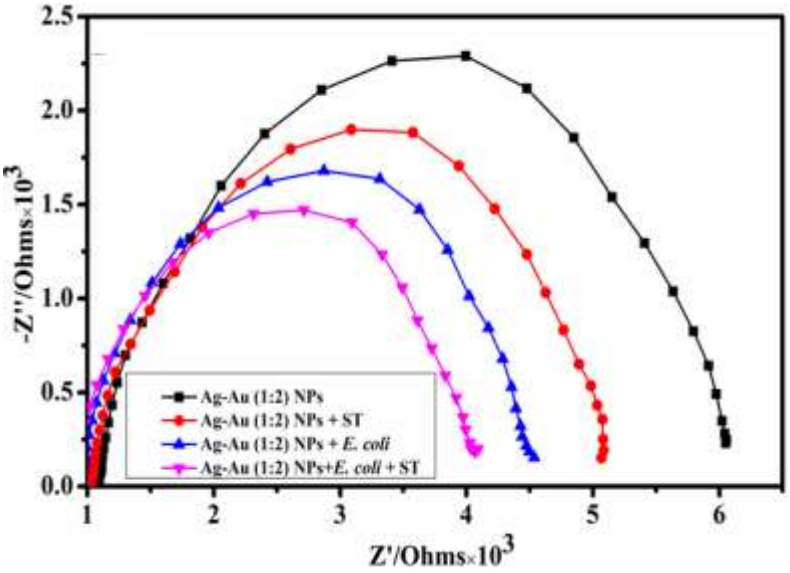

Figure 5.18 : Selectivity studies of the developed nano-impact sensor based on the Nyquist plot

5.6.2 Recovery studies

To demonstrate the practical applicability of the proposed interdigitated nano-impact sensor to real sample analyses, recovery studies on spiked tap water (TW) and fruit juice (FJ) samples were performed. The percentage recoveries for the bacteria ranged between (95.18 ± 2.50 - 105.01 ± 0.58) and (95.94 ± 010 - 100.00 ± 0.76) % in TW (n = 3) and FJ (n = 3), respectively. The % RSD determined for *E. coli* were also significantly low and ranged between (2.4 - 3.5) % and (1.03 - 2.53) % for TW and FJ, respectively.

These results showed that the developed interdigitated nano-impact sensor for *E. coli* was precise and accurate. To the best of our knowledge, no study has reported these higher percentage

recoveries for *E. coli* in tap water and fruit juice samples determined using a simple and label-free interdigitated Ag-Au (1:2) NPs array impact sensor.

5.7 Conclusion

From the above discussed results, it was noted that the optical interactions between the bacteria and each of the NPs were mainly affected by bacterial cell concentrations, incubation period, surface charge and NPs-type. This was evident in the variation of absorbance which generally decreased with bacterial cell concentrations and interaction time relative to the pure NPs. The intensities of the plasmon bands were pronounced in the bimetallic NPs compared to the corresponding monometallic counterparts. Electrochemical interactions showed the appearance of new irreversible oxidation peaks in the CV results obtained using both GCE and IDAE as transducers. These peaks were, however, absent in the CVs of pure NPs in both electrodes confirming the presence of the bacteria. The peaks were more resolved and enhanced in the DPV results. The peak position and intensity were also NPs-and electrode type dependent with the bacteria-bimetallic NPs interactions on IDAE showing more visible and resolved oxidation peak with enhanced currents and a shift in potential to slightly less positive value relative to GCE. These were also supported by the EIS results which showed significant decrease in charge transfer resistance with increasing bacterial cell concentrations. The intensity of the signals in DPV and EIS techniques were mainly influenced by interaction time, bacterial cell concentrations, applied potential, AC amplitude, supporting electrolyte concentration and NPs-type. The EIS results were more sensitive than DPV and therefore, two impedimetric nano-impact sensors based on GCE and IDAE were developed and evaluated for rapid detections of *E. coli* in River and Ocean water samples using EIS technique through recovery studies. In both sensors, different bacterial cell concentrations resulted into different electrochemical impedance spectral responses and the impedance of the bacterial cells significantly decreased with increasing bacterial concentrations. Both nano-impact sensors developed showed higher potentials for detections of the bacteria in a rapid and very simple manner. However, IDAE sensor showed significantly higher % recoveries of between (100.60 ± 0.58 - 116.02 ± 0.15) % in spiked fruit juice and tap water samples with lower % RSD indicating that the sensor was accurate and precise.

5.8 References

Abadeer, N.S., Fülöp, G., Chen, S., Käll, M. & Murphy, C.J. 2015. Interactions of Bacterial

Lipopolysaccharides with Gold Nanorod Surfaces Investigated by Refractometric Sensing. *ACS Applied Materials and Interfaces*, 7(44): 24915–24925.

Ahmad, A., Wei, Y., Syed, F., Tahir, K., Rehman, A.U., Khan, A., Ullah, S. & Yuan, Q. 2017. The effects of bacteria-nanoparticles interface on the antibacterial activity of green synthesized silver nanoparticles. *Microbial Pathogenesis*, 102: 133–142.

El Badawy, A.M., Silva, R.G., Morris, B., Scheckel, K.G., Suidan, M.T. & Tolaymat, T.M. 2011. Surface charge-dependent toxicity of silver nanoparticles. *Environmental science & technology*, 45(1): 283–287.

Borchers, J.S., Campbell, C.R., Van Scoy, S.B., Clark, M.J. & Anand, R.K. 2021. Redox Cycling at an Array of Interdigitated Bipolar Electrodes for Enhanced Sensitivity in Biosensing**. *ChemElectroChem*, 8(18): 3482–3491.

Brosel-Oliu, S., Abramova, N., Uria, N. & Bratov, A. 2019. Impedimetric transducers based on interdigitated electrode arrays for bacterial detection – A review. *Analytica Chimica Acta*, 1088: 1–19.

Chen, X., Shen, Y., Zhou, P., Zhong, X., Li, G., Han, C., Wei, D. & Li, S. 2019. Bimetallic Au/Pd nanoparticles decorated ZnO nanowires for NO2 detection. *Sensors and Actuators, B: Chemical*, 289: 160–168.

Chen, Y., Wang, D., Liu, Y., Gao, G. & Zhi, J. 2021. Redox activity of single bacteria revealed by electrochemical collision technique. *Biosensors and Bioelectronics*, 176(11291): 4.

Chinnaraj, G. & Priya Ponnaiah, G. 2021. Sustainable Electricity Generation from Continuous Microbial Fuel Cells. *Chemical Engineering and Technology*, 44(5): 884–891.

Couniot, N., Afzalian, A., Van Overstraeten-Schlögel, N., Francis, L.A. & Flandre, D. 2015. Capacitive biosensing of bacterial cells: Analytical model and numerical simulations. *Sensors and Actuators, B: Chemical*, 211: 428–438. http://dx.doi.org/10.1016/j.snb.2015.01.108.

Couto, R.A.S., Chen, L., Kuss, S. & Compton, R.G. 2018. Detection of *Escherichia coli* bacteria by impact electrochemistry. *Analyst*, 143(20): 4840–4843.

Estifaee, P., Su, X., Yannam, S.K., Rogers, S. & Thagard, S.M. 2019. Mechanism of *E. coli*

Inactivation by Direct-in-liquid Electrical Discharge Plasma in Low Conductivity Solutions. *Scientific Reports*, 9(1): 1–12.

Frkonja-Kuczin, A., Ray, L., Zhao, Z., Konopka, M.C. & Boika, A. 2018. Electrokinetic preconcentration and electrochemical detection of Escherichia coli at a microelectrode. *Electrochimica Acta*, 280: 191–196.

Gammoudi, I., Faye, N.R., Moroté, F., Moynet, D. & Grauby-heywang, C. 2013. Characterization of Silica Nanoparticles in Interaction with Escherichia coli Bacteria. *Proceedings of World Academy of Science, Engineering and Technology*, 7(79): 658–664.

Gao, G., Wang, D., Brocenschi, R., Zhi, J. & Mirkin, M. V. 2018. Toward the Detection and Identification of Single Bacteria by Electrochemical Collision Technique. *Analytical Chemistry*, 90(20): 12123–12130. http://dx.doi.org/10.1021/acs.analchem.8b03043.

Gowda, J.I. & Nandibewoor, S.T. 2014. Electrochemical behavior of paclitaxel and its determination at glassy carbon electrode. *Asian Journal of Pharmaceutical Sciences*, 9(1): 42–49.

Güler, S. & Oruç, Ç. 2021. Controlling the movements of E. faecalis bacteria that carry a negative electric charge with an electric field. *Journal of Electrostatics*, 112(July).

Hamidi-Asl, E., Dardenne, F., Pilehvar, S., Blust, R. & De Wael, K. 2016. Unique properties of core shell Ag@Au nanoparticles for the aptasensing of bacterial cells. *Chemosensors*, 4(3): 16.

Harnisch, F. & Freguia, S. 2012. A basic tutorial on cyclic voltammetry for the investigation of electroactive microbial biofilms. *Chemistry - An Asian Journal*, 7(3): 466–475.

Hassan, A., Ali, S. & Muhammad, M. 2015. Cyclic Voltammetric Study of Clarithromycin Using Gold Electrode. *International Research Journal of Pure and Applied Chemistry*, 8(4): 221–228.

Hayden, S.C., Zhao, G., Saha, K., Phillips, R.L., Li, X., Miranda, O.R., Rotello, V.M., El-Sayed, M.A., Schmidt-Krey, I. & Bunz, U.H.F. 2012. Aggregation and interaction of cationic nanoparticles on bacterial surfaces. *Journal of the American Chemical Society*, 134(16): 6920–6923.

Hegde, R.N., Chandra, P. & Nandibewoo, S.T. 2011. Sensitive voltammetric determination of atenolol at multi-walled carbon nanotubes modified glassy carbon electrode. *Research Journal of Nanoscience and Nanotechnology*, 1: 75–86.

Herrero-Hernandez, E., Greenfield, D., Smith, T.J. & Akid, R. 2019. Evaluation of the Performance of a Mediatorless Microbial Fuel Cell by Electrochemical Impedance Spectroscopy. *Electroanalysis*, 31(6): 1189–1194.

Hua, X.W., Bao, Y.W., Wang, H.Y., Chen, Z. & Wu, F.G. 2017. Bacteria-derived fluorescent carbon dots for microbial live/dead differentiation. *Nanoscale*, 9(6): 2150–2161.

Jena, P., Bhattacharya, M., Bhattacharjee, G., Satpati, B., Mukherjee, P., Senapati, D. & Srinivasan, R. 2020. Bimetallic gold-silver nanoparticles mediate bacterial killing by disrupting the actin cytoskeleton MreB. *Nanoscale*, 12(6): 3731–3749.

Joshi, A.S., Singh, P. & Mijakovic, I. 2020. Interactions of gold and silver nanoparticles with bacterial biofilms: Molecular interactions behind inhibition and resistance. *International Journal of Molecular Sciences*, 21(20): 1–24.

Kanokkanchana, K., Saw, E.N. & Tschulik, K. 2018. Nano-Impact Electrochemistry: Effects of Electronic Filtering on Peak Height, Duration, and Area. *ChemElectroChem*, 5(20): 2917.

Kim, D.M., Park, J.S., Jung, S.W., Yeom, J. & Yoo, S.M. 2021. =Biosensing Applications Using Nanostructure-Based Localized Surface Plasmon Resonance Sensors. *Sensors*, 21(9): 3191.

Kus-liśkiewicz, M., Fickers, P. & Ben Tahar, I. 2021. Biocompatibility and cytotoxicity of gold nanoparticles: Recent advances in methodologies and regulations. *International Journal of Molecular Sciences*, 22(20): 10952.

Lee, J.Y., Kim, B.K., Kang, M. & Park, J.H. 2016. Label-Free Detection of Single Living Bacteria via Electrochemical Collision Event. *Scientific Reports*, 6: 1–6.

Liu, J., Lan, L., Liu, X., Yang, X. & Wu, X. 2021. Facile synthesis of agglomerated Ag–Pd bimetallic dendrites with performance for hydrogen generation from formic acid. *International Journal of Hydrogen Energy*, 46(9): 6395–6403.

Mashkour, Mehrdad, Rahimnejad, M., Mashkour, Mahdi, Bakeri, G., Luque, R. & Oh, S.E. 2017.

Application of Wet Nanostructured Bacterial Cellulose as a Novel Hydrogel Bioanode for Microbial Fuel Cells. *ChemElectroChem*, 4(3): 648–654.

Mohamed, M.A., Yehia, A.M., Banks, C.E. & Allam, N.K. 2017. Novel MWCNTs/graphene oxide/pyrogallol composite with enhanced sensitivity for biosensing applications. *Biosensors and Bioelectronics*, 89: 1034–1041.

Okumu, F.O., Silwana, B. & Matoetoe, M.C. 2020. Application of MWCNT/Ag-Pt Nanocomposite Modified GCE for the Detection of Nevirapine in Pharmaceutical Formulation and Biological Samples. *Electroanalysis*, 32(12): 3000–3008.

Pajerski, W., Ochonska, D., Brzychczy-Wloch, M., Indyka, P., Jarosz, M., Golda-Cepa, M., Sojka, Z. & Kotarba, A. 2019. Attachment efficiency of gold nanoparticles by Gram-positive and Gram-negative bacterial strains governed by surface charges. *Journal of Nanoparticle Research*, 21(8): 1–12.

Parlak, O. & Richter-Dahlfors, A. 2020. Bacterial Sensing and Biofilm Monitoring for Infection Diagnostics. *Macromolecular Bioscience*, 20(11): 2000129.

Raj, V., Vijayan, A.N. & Joseph, K. 2015. Cysteine capped gold nanoparticles for naked eye detection of *E. coli* bacteria in UTI patients. *Sensing and Bio-Sensing Research*, 5: 33–36.

Ramesh, M., Balakrishnan, P., Dhanaprabhu, S.S., Ravanan, A. & Maniraj, J. 2020. Enzyme-modified electrodes for biofuel cells: A comprehensive review. *Materials Today: Proceedings*, 46: 3495–3501.

Randviir, E.P. 2018. A cross examination of electron transfer rate constants for carbon screen-printed electrodes using Electrochemical Impedance Spectroscopy and cyclic voltammetry. *Electrochimica Acta*, 286: 179–186.

Ronspees, A.T. & Thorgaard, S.N. 2018. Blocking electrochemical collisions of single *E. coli* and *B. subtilis* bacteria at ultramicroelectrodes elucidated using simultaneous fluorescence microscopy. *Electrochimica Acta*, 278: 412–420.

Saeed, W., Abbasi, Z., Majeed, S., Shahzad, S.A., Khan, A.F. & Shaikh, A.J. 2021. An insight into the binding behavior of graphene oxide and noble metal nanoparticles. *Journal of Applied Physics*, 129(12): 2.

Scanlon, M.D., Salaj-Kosla, U., Belochapkine, S., MacAodha, D., Leech, D., Ding, Y. & Magner, E. 2012. Characterization of nanoporous gold electrodes for bioelectrochemical applications. *Langmuir*, 28(4): 2251–2261.

Sepunaru, L., Tschulik, K., Batchelor-McAuley, C., Gavish, R. & Compton, R.G. 2015. Electrochemical detection of single *E. coli* bacteria labeled with silver nanoparticles. *Biomaterials Science*, 3(6): 816–820. http://dx.doi.org/10.1039/c5bm00114e.

Seymour, I.P. 2020. Nanowire and microband arrays for enhanced electrochemical sensing.

Simeon, M.I. & Freitag, R. 2022. Influence of electrode spacing and fed-batch operation on the maximum performance trend of a soil microbial fuel cell. *International Journal of Hydrogen Energy*, 47(24): 12304–12316.

Smith, M.C., Crist, R.M., Clogston, J.D. & McNeil, S.E. 2017. Zeta potential: a case study of cationic, anionic, and neutral liposomes. *Analytical and Bioanalytical Chemistry*, 409(24): 5779–5787.

Taran, N., Storozhenko, V., Svietlova, N., Batsmanova, L., Shvartau, V. & Kovalenko, M. 2017. Effect of Zinc and Copper Nanoparticles on Drought Resistance of Wheat Seedlings. *Nanoscale Research Letters*, 12(1): 1–6.

Tavares, T.D., Antunes, J.C., Padrão, J., Ribeiro, A.I., Zille, A., Amorim, M.T.P., Ferreira, F. & Felgueiras, H.P. 2020. Activity of specialized biomolecules against gram-positive and gram-negative bacteria. *Antibiotics*, 9(6): 1–16.

Testolin, A., Cattaneo, S., Wang, W., Wang, D., Pifferi, V., Prati, L., Falciola, L. & Villa, A. 2019. Cyclic Voltammetry Characterization of Au, Pd, and AuPd Nanoparticles Supported on Different Carbon Nanofibers. *Surfaces*, 2(1): 205–215.

Tonelli, F.M., Goulart, V.A., Gomes, K.N., Ladeira, M.S., Santos, A.K., Lorençon, E., Ladeira, L.O. & Resende, R.R. 2015. Graphene-based nanomaterials: Biological and medical applications and toxicity. *Nanomedicine*, 10(15): 2423–2450.

Verma, M.S., Chen, P.Z., Jones, L. & Gu, F.X. 2014. Chemical nose. *for the visual identification of emerging ocular pathogens using gold nanostars. Biosensors and Bioelectronics*, 61: 386–390.

Wang, D., Chen, J. & Nugen, S.R. 2017. Electrochemical Detection of *Escherichia coli* from Aqueous Samples Using Engineered Phages. *Analytical Chemistry*, 89(3): 1650–1657.

Wang, H., Fan, Y., Yang, Q., Sun, X., Liu, H., Chen, W., Aziz, A. & Wang, S. 2022. Boosting the Electrochemical Performance of PI-5-CA/C-SWCNT Nanohybrid for Sensitive Detection of *E. coli* O157:H7 From the Real Sample. *Frontiers in Chemistry*, 10.

Wang, Z., Gao, H., Cui, J., Zhou, S., Zhao, Y., Ye, C., Li, J. & Wu, D. 2021. Two-signal electrochemical detection system for evaluation viability of *Staphylococcus aureus.* *Electrochimica Acta*, 367: 137258.

Xu, M., Wang, R. & Li, Y. 2016. Rapid detection of *Escherichia coli* O157:H7 and *Salmonella typhimurium* in foods using an electrochemical immunosensor based on screen-printed interdigitated microelectrode and immunomagnetic separation. *Talanta*, 148: 200–208. http://dx.doi.org/10.1016/j.talanta.2015.10.082.

Xu, Y., Wang, H., Zhang, M., Zhang, J. & Yan, W. 2021. Plasmon-enhanced antibacterial activity of chiral gold nanoparticles and in vivo therapeutic effect. *Nanomaterials*, 11(6): 1621.

Zhang, F., Wang, S., Yang, Y., Jiang, J. & Tao, N. 2021. Imaging Single Bacterial Cells with Electro-optical Impedance Microscopy. *ACS Sensors*, 6(2): 348–354.

Zhang, J., Sun, Q., Tang, H., Qian, Y., Chen, Y., Shan, X., Liu, X. & Gu, H. 2021. The direct electrochemistry of viable Escherichia coli. *Journal of Electroanalytical Chemistry*, 895(11542): 6.

Zhang, R., Belwal, T., Li, L., Lin, X., Xu, Y. & Luo, Z. 2020. Nanomaterial-based biosensors for sensing key foodborne pathogens: Advances from recent decades. *Comprehensive Reviews in Food Science and Food Safety*, 19(4): 1465–1487.

CHAPTER SIX

DEVELOPMENT OF AN ELECTROCHEMICAL NANO-IMPACT SENSOR FOR *Salmonella typhimurium* USING GLASSY CARBON AND INTERDIGITATED ARRAY ELECTRODES

6.0 Summary

This chapter mainly focuses on the optimization and development of nano-impact sensor for *S. typhimurium* using glassy carbon (GCE) and interdigitated array (IDAE) electrodes. The effects of bacterial cell concentrations and bacteria-NPs interaction time on opto-electrochemical properties of Ag NPs, Au NPs and bimetallic Ag-Au (1:2) NPs are also investigated and reported. The developed nano-impact sensor was applied for practical analysis of the bacteria in River and Ocean water samples using electrochemical impedance spectroscopy (EIS) as a transduction technique.

6.1 Introduction

Electro-analytical techniques are effective tools in bacterial sensing since they determine the analytical characteristics of bacteria as the electrode interacts with the bacterial cells. The effective interactions between the electrode and bacteria lead to signal generation. The quality of the signal produced is mainly influenced by the sensitivity of the technique, electrode size, interaction time and concentration of bacteria. In the recent past, electrochemical sensors for *S. typhimurium* employing different electro-analytical techniques have been reported (Awang *et al*., 2021). Voltammetric and impedimetric techniques have been dominating (Leva-Bueno *et al*., 2020; Magar *et al*., 2021). This is due to their affordability, simplicity and enhanced sensitivity. However, impedimetric techniques have received considerable attention from researchers compared to voltammetric methods due to their ability to perform label-free sensing with enhanced miniaturization potentials (Wang *et al*., 2022). The impedimetric techniques, especially electrochemical impedance spectroscopy (EIS) can accurately monitor changes in the electrical properties of bacteria during bacteria-electrode interactions without the use mediators such as bio-recognition elements thus improving the overall sensitivity of the detection process. Electrochemical sensors for *S. typhimurium* using EIS as a transduction technique are currently common compared to the use of direct current techniques such as cyclic voltammetry and differential pulse voltammetry (Patra *et al*., 2022). This is due to the ability of EIS to analyze electrode double layer formation and diffusion processes associated with complex formation on

electrode surface during bacterial analysis (Wang *et al*., 2022). However, most of the reported studies employ modified electrodes which lack single entity nature for faster detection of bacteria in complex samples. Single entity electrochemistry has recently emerged as a way of studying individual analytes one by one so as to build a bottom-up model for better understanding of the heterogeneity of electrode processes as analytes interact with electrode. This has been achieved through nano-impact electrochemistry (NIE) which involves stochastic collisions of the bacterial cells with the electrode surface leading to production of both Faradaic and non-Faradaic currents that can be used to monitor concentration and electro-catalytic properties of the bacteria. These properties cannot be distinguished easily using chrono-amperometry (CA), CV and DPV techniques due to their lower sensitivity compared to EIS (Matoetoe *et al*., 2022).

Therefore, in this chapter, an electrochemical nano-impact sensor for the bacteria was designed, developed and applied for the detection of the bacteria in River and Ocean water samples using glassy carbon (GCE) and interdigitated array electrodes (IDAE). Opto-electrochemical interaction studies between Ag NPs, Au NPs, bimetallic Ag-Au (1:2) NPs and the bacteria were investigated and used to obtain the optimum conditions for the sensor development. The nano-impact interactions between the bacteria and bimetallic Ag-Au (1:2) NPs on the electrode surface were also studied mechanistically using CV and EIS results.

6.2 Experimental

6.2.1 Reagents and Materials

Luria Bertani (LB) and Nutrient Agars were obtained from *Sigma-Aldrich* and their solutions freshly prepared before use. Phosphate buffer solution (PBS), 0.1 M, pH 7.4 was prepared as earlier described in **section 5.2.1**.

6.2.2 Culture preparation

S. typhimurium were cultivated in LB broth at 37 °C for 18 hours. The enriched bacteria were centrifuged at 4000 rpm for 5 minutes at room temperature so as to remove the bacterial growth medium. The supernatant was discarded and the bacterial pellets formed re-suspended in 0.1 M PBS, pH 7.4. The cells were washed twice using 0.1 M PBS solution at pH 7.4 to remove the undesired metabolites and lysed bacterial cells accumulated in the nutrient medium during the bacterial growth. The final concentration of the bacterial cells was adjusted spectrophotometrically

at the wavelength of 600 nm ($OD_{600\ nm}$) using UV-visible spectrophotometer to OD of 1.0. The relationship between the cell concentrations and OD_{600nm} values was established using spectrophotometric method (Couto *et al*., 2018). All the tubes used were autoclaved at 121 °C and stored in a clean bench while the cell suspensions were kept in sealed tubes before use. To avoid cell contamination due to unfavourable environmental factors, the suspensions obtained were immediately used for subsequent optical and electrochemical interaction experiments. All the sample cultures for this bacterium were prepared on the day of the test.

6.2.3 *Zeta* potential determination and optical interaction studies

The ζ of the untreated bacteria, NPs and NPs-bacteria mixtures (1:1, v/v) in water were determined as described in **section 5.2.3**. The bacteria-nanoparticle optical interaction experiments were also investigated as described in section **5.2.4.**

6.2.4 Fabrication of GCE nano-impact sensor for *S. typhimurium*

The GCE was first polished and activated as described in **sections 4.2.1 and 5.2.4**. The source of the signals due to interactions between the bacteria and NPs were confirmed by three concecutive additions of 1 mL (8×10^1 cellsmL^{-1}) of bacterial cells to the same volume of NPs and determining the variations in oxidation peak current intensities due to the bacteria and charge transfer resistance (ΔR_{ct}) using CV, DPV and EIS techniques. The slopes of the plots of logarithm of bacterial concentrations versus peak current intensities for CV and DPV, and ΔR_{ct}^{-1} for EIS were used to obtain the most sensitive technique for sensor development.

The parameters including supporting electrolyte concentrations (0.1, 0.01, 0.001 M), Ag-Au (1:2) NPs concentration, Ag-Au (1:2) NPs-bacteria incubation period, applied potential and AC amplitude were optimized and the optimum conditions obtained employed in sensor development. This was done by varying one parameter at a time while keeping all others constant followed by determination of the sensor's linearity and applicability.

The repeatability and reproducibility studies of the developed sensor were evaluated with repeated responses to 1.6×10^2 cells mL^{-1} of *S. typhimurium* cells and recording the changes in ΔR_{ct} obtained during the repetitive assays using the same sensor under the same optimized conditions.

The reproducibility and repeatability of the sensor were determined using the expresion: $\frac{\Delta R_{ct}^{(Ag-Au\ (1:2)NPs+S.typhimurium)}}{\Delta R_{ct}^{Ag-Au\ (1:2)NPs}}$.

The stability of the bimetallic NPs towards effective interactions with the bacteria was also investigated by storing the NPs at a temperature of 4 °C for 4 days and comparing the initial and final ΔR_{ct} for the bacteria-NPs interactions using old bimetallic Ag-Au (1:2) NPs and freshly prepared bimetallic NPs.

Selectivity of the sensor was investigated by determining ΔR_{ct} of same concentration of *E. coli* (1.6×10^2 cellsmL^{-1}) added to the same bimetallic NPs in the absence and presence of *S. typhimurium* using EIS technique.

Different concentrations (cells mL^{-1}) of *S. typhimurium*; 8×10^1, 1.2×10^2 and 1.6×10^2 were spiked into each of the filtered tap water (TW) and fruit juice (FJ) samples and their ΔR_{ct} measured directly using EIS technique under the same optimized conditions without any other extensive pre-treatments except the filtration and dilution of the samples with 0.1 M PBS (pH 7.4).

The feasibility of the developed electrochemical detection strategy for practical analysis of *S. typhimurium* in River and Ocean water samples was undertaken using standard addition method. River and Ocean water samples were prepared as described in **section 5.2.5** followed by spiking each sample with known concentrations (cells mL^{-1}) of the bacteria: 8×10^1, 1.6×10^2 and 2.4×10^3. The samples were then subsequently analysed using the same proposed electrochemical strategy under the same optimized conditions.

6.2.5 Fabrication of IDAE nano-impact sensor for *S. typhimurium*

The electrode was cleaned and activated following the same procedure described in **section 5.2.5**.

The *S. typhimurium* and bimetallic Ag-Au (1:2) NPs interaction studies were investigated using CV and EIS techniques. This was followed by optimization of various parameters including volume of the bimetallic NPs, bacteria-NPs incubation period, applied potential and AC amplitude by varying one parameter while keeping all others constant. The optimum conditions obtained were used for calibration and validation studies. The repeatability, reproducibility, stability and selectivity studies of the developed nano-impact sensor were done following the same procedure described in section **5.2.6** except for the optimum conditions employed for the bacterial detections.

6.3 Results and Discussion

6.3.1 *Zeta* potential

The *zeta* potentials (mV) for untreated bacteria, pure NPs and bacteria-NPs mixtures (1:1, v/v) are as shown in **Table 6.1**.

Table 6.1: *Zeta* (ζ) potential of untreated bacteria and the complexes of NPs and bacteria

NPs/NPs-bacteria complex	**ζ (mV)**
S. typhimurium	-16.60 ± 0.32
Ag + *S. typhimurium*	-14.50 ± 0.67
Au + *S. typhimurium*	-12.60 ± 0.25
Ag-Au (1:2) + *S. typhimurium*	-17.30 ± 0.89

The average values of the *zeta* potentials (mV) for the synthesized NPs are as shown in **Table 6.1**. The bacteria showed significantly higher negative *zeta* potential of -16.60 ± 0.32 compared to those of pure NPs. This can be attributed to the presence of higher density anionic groups attached to the bacterial cell membrane. The *zeta* potential of the bacteria increased from -16.60 ± 0.32 to -17.30 ± 0.89 mV after bacteria-NPs interactions. The significant difference in the *zeta* potential between the bimetallic NPs (-4.34 ± 0.71) and bacteria (-16.60 ± 0.32) had a significant impact on the bacterial adhesive properties towards the NPs. This increase in *zeta* potentials indicated effective bacteria-NPs interactions (Ahmad *et al.*, 2017).

6.3.2 Optical interaction studies using UV-visible spectroscopy

The UV-visible spectra for the interactions between Ag NPs, Au NPs, bimetallic Ag-Au (1:2) NPs and varying concentrations of *S. typhimurium* are presented in **Figure 6.1.** As shown in the figures, both interaction between the bacteria and Ag, and Au NPs showed distinct red-shifts with increase in bacterial concentration (**shown by the arrows**). However, the red-shift in case of Au NPs was more significant and concentration dependent (**Figure 6.1 b**). This is due to the rapid formation of larger complexes due to the interactions between Au NPs and the bacteria. This can also be due to the enhanced repulsion between the citrate ions capping the Au NPs and a mosaic of anionic surfaces covering the cell wall of the bacteria (Fanoro & Oluwafemi, 2020). Studies on interactions between Au NPs and *S. typhimurium* have also reported that Au NPs adsorb more readily onto the bacterial membrane surfaces but do not easily penetrate into cell contents leading to the formation of larger complexes (Shuguang Wang *et al.*, 2011). *S. typhimurium* can also

undergo rapid conformational changes and acetylation reactions upon interacting with Au NPs due to the presence of O-antigen (Sargo *et al.*, 2015; Wang-Kan *et al.*, 2021).

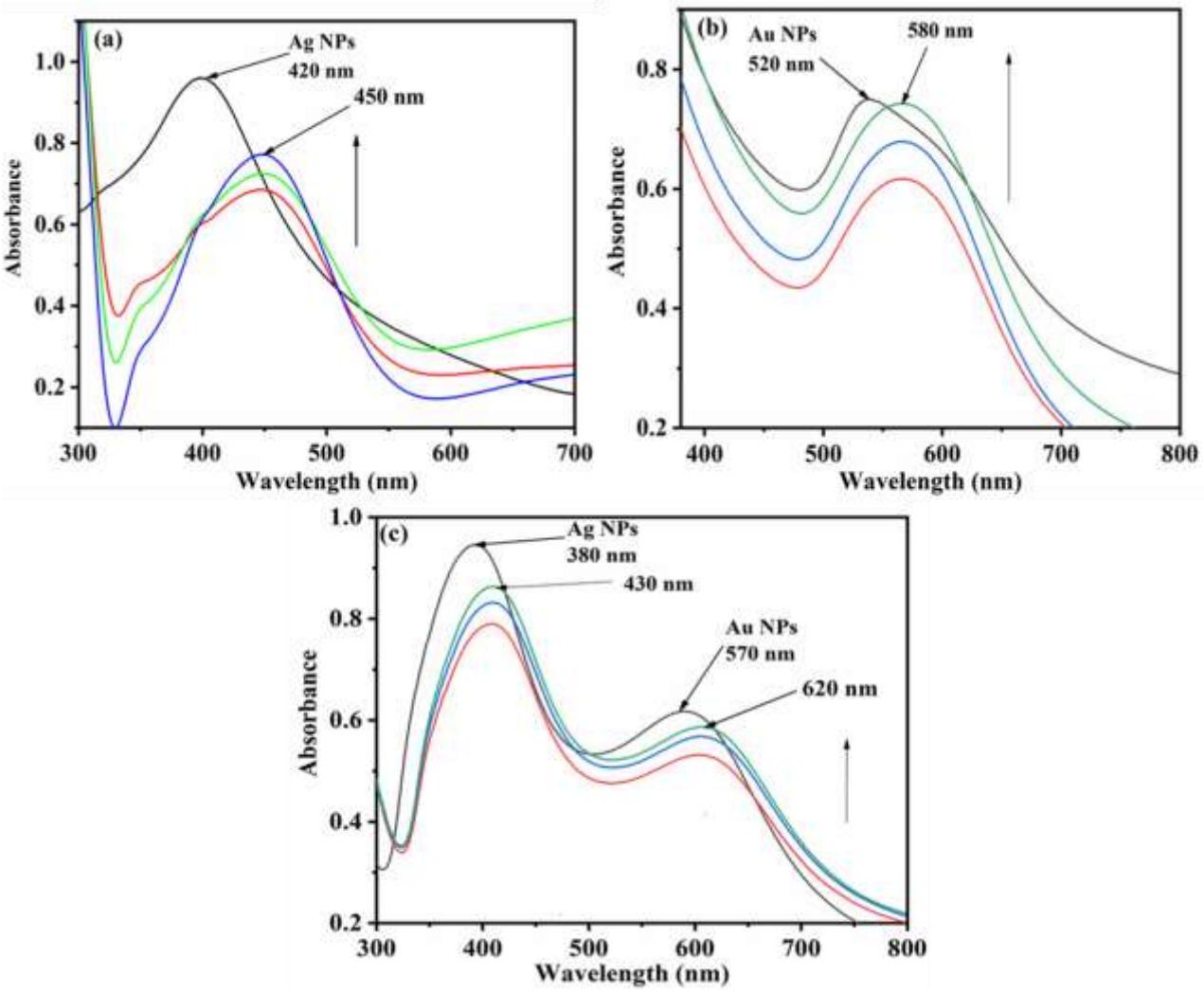

Figure 6.1: UV-visible spectra of (a) Ag NPs, (b) Au NPs (c) Ag-Au (1:2) NPs in absence and presence of varying concentrations of *S. typhimurium* (cellsmL^{-1})

Key: — NPs — NPs + 8.0×10^1 — NPs+1.6×10^2 — NPs +2.4×10^3

The peak intensities for both nanoparticles were also higher and increased exponentially with bacterial concentrations. The SPR peak intensity due to the interaction between the bacteria and Au NPs was lower than those of Ag NPs (Francesco Montesi, 2015). This is due to the presence of thicker layers of lipopolysaccharides covering the bacterial membrane. This minimizes the passage of Ag^+ into the bacterial cells hence leading to reduced rate of oxidative reactions with the cell

contents such as DNA (Edis *et al*., 2020). The interactions between *S. typhimurium* and bimetallic Ag-Au (1:2) NPs showed larger red-shifts which were enhanced on the Au NPs within the bimetallic NPs as compared to those observed in the corresponding monometallic NPs. This increase in wavelength was also bacterial concentration dependent. This can be due to greater rigidity and complexity of the *S. typhimurium* bacterial lipopolysaccharide layer. This enhances the aggregation of the Au NPs on the membrane surface of the bacteria instead of NPs dissolution hence leading to the formation of larger complexes which shifted the plasmon bands to longer wavelengths. This is in agreement with mathematical calculations on electrophoretic mobility studies reported elsewhere (Slavin *et al*., 2017).

Apart from the effects of bacterial concentration on bacteria-nanoparticle interactions, the rate of aggregation between the nanoparticles and bacteria with time (minutes) was also investigated and the results obtained presented as shown in **Figure 6.2**. This was done so as to obtain optimum bacteria-nanoparticle interactions time and its relevance in designing rapid, simple, cost-effective and stable nano-impact sensors for *S. typhimurium.*

There was a general significant increase in absorbance with bacteria-NPs interaction time for each of the NPs (Ag, Au, Ag-Au (1:2) NPs) (**Figure 6.2 insets**). The interactions between the bacteria and Ag NPs and Ag NPs in the bimetallic NPs showed the greatest increase in absorbance indicating enhanced interactions with increasing times. This can be due to the presence of double thicker peptidoglycan layers in the bacterial membrane coupled with the observed decrease in the bacterial membrane *zeta* potential in the presence of Ag NPs (**Table 6.1**). Increased ionization of phosphoryl and 2-keto-3-deoxyoctonate carboxylate groups in bacterial LPS chain increases the negative charge on the bacterial membrane (French *et al*., 2013). The presence of negatively charged layer on the bacterial membrane leads to increased dispersive forces hence the observed poor bacteria-NPs interactions.

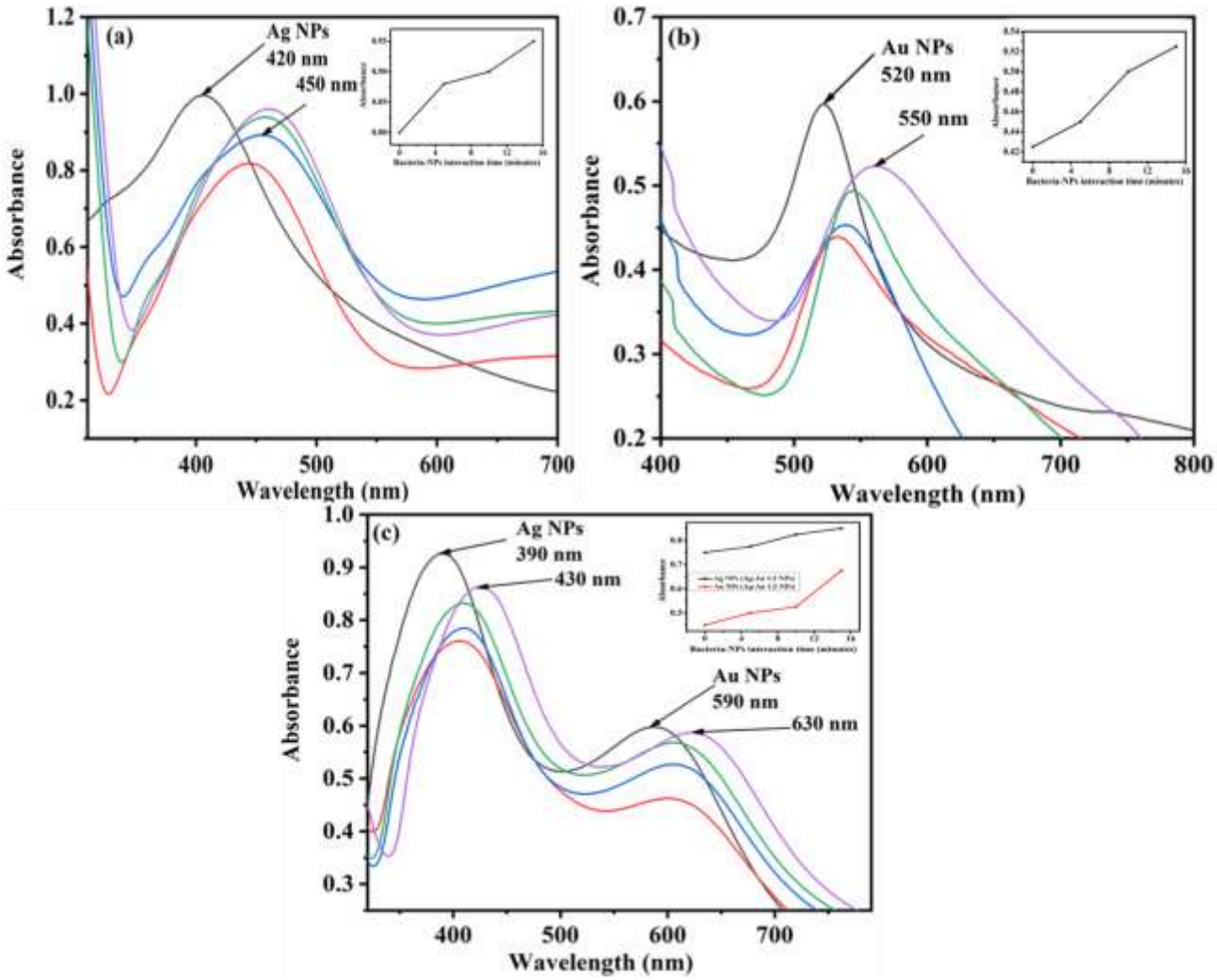

Figure 6.2: UV-visible spectra of interaction time between (a) Ag NPs, (b) Au NPs, (c) Ag-Au (1:2) NPs and same concentration of *S. typhimurium* (8.0×10^1 cellsmL^{-1}); Plots of bacteria-NPs interaction time versus absorbance (**insets**)

Key: NPs — 0 minute — 5 minutes — 10 minutes — 15 minutes

6.3.3 Electrochemical interaction studies using GCE

The CVs for the interactions between Ag NPs, Au NPs and bimetallic Ag-Au (1:2) NPs, and *S. typhimurium* (ST) in 0.1 M PBS, pH 7.4 are as shown in **Figure 6.3.**

There was no oxidation peak observed in the presence of both 0.1 M PBS and ST. The interactions between ST and each of the NPs led to the formation of oxidation peaks at the indicated potentials. The peak became more distinct and resolved in the bimetallic NPs compared to the monometallic NPs. This can possibly be due to the electrochemical synergy between Ag and Au in the bimetallic

NPs. The observed peak can be ascribed to lipo-oxidation reactions on the bacterial cell membrane due to the loss of electrons by transketolase in the bacterial metabolic pathway to the metallic ions within the bulk solution leading to complex formation. This peak, however, shifted towards more positive potential compared to those observed in the monometallic NPs. This can be attributed to the thicker cell membrane of the bacteria which limits the rate of electron transfer from the bacterial metabolic pathway towards the metallic ions on the electrode surface. This therefore, might have slowed down the rate of lipid oxidation reactions. This can also be ascribed to the formation of biofilm on the electrode surface (Kracke *et al*., 2015). Formation of biofilm is accompanied by excretion of different compounds by the cells which block the electrode surface hence limiting the transport of electrons from the electro-active centers of the bacterial cells to the electrode surface.

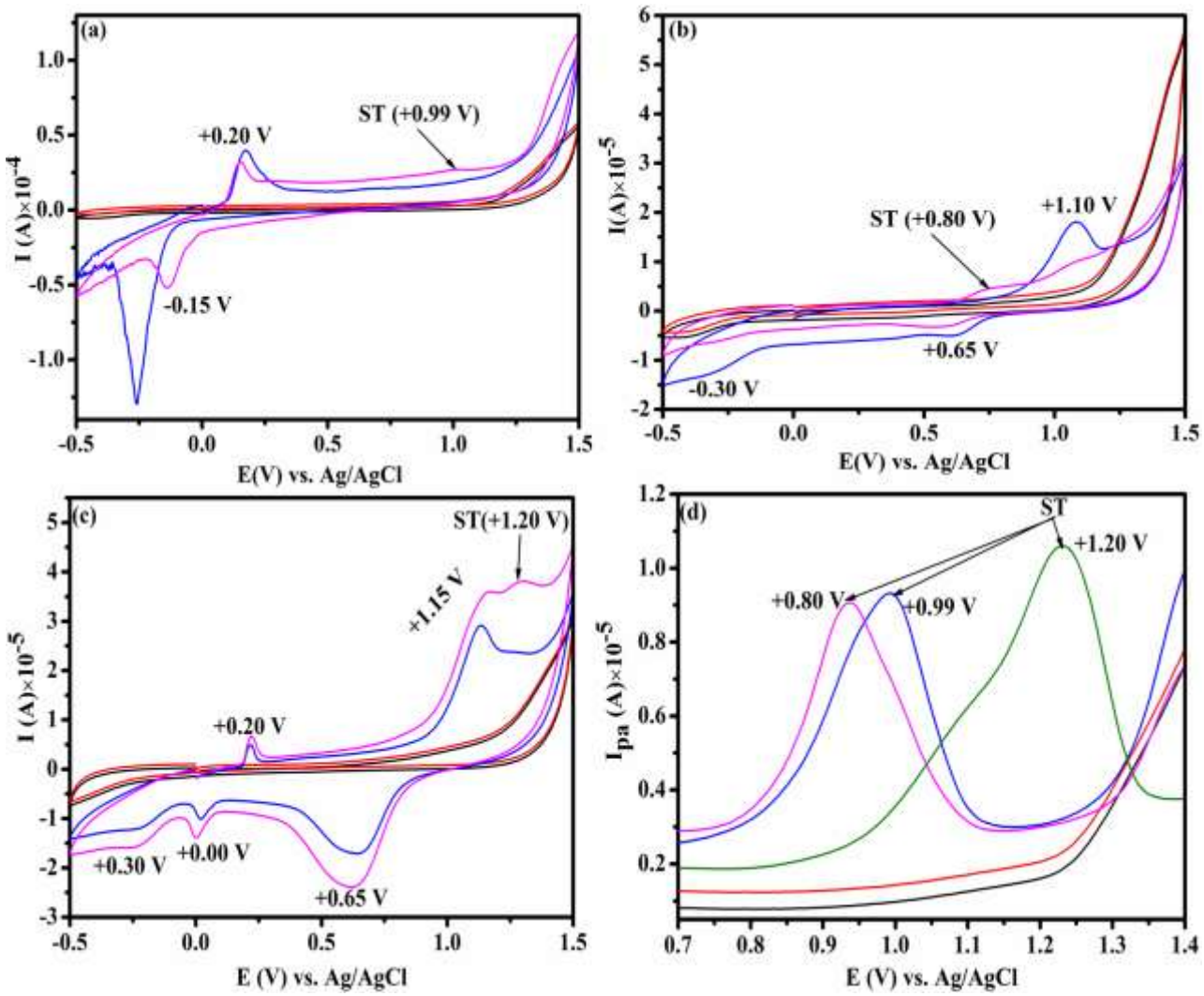

Figure 6.3: Overlays of CVs and DPVs of —— 0.1 M PBS —— ST —— NPs + 0.1 M PBS —— NPs + ST —— Ag NPs + ST —— Au NPs + ST —— Ag-Au (1:2) NPs + ST , respectively in 0.1 M PBS at pH 7.4, Scan rate; 0.03 Vs^{-1}. (a) Ag NPs, (b) Au NPs, (c) Ag-Au (1:2) NPs

The intensity of the peak current due to the oxidation of Au^0 to Au^{3+} in the complex greatly decreased compared to the pure bimetallic NPs. The peak due to the formation of Au^{3+} also shifted towards more potential potentials compared to the one observed due to the interactions between pure Ag-Au (1:2) NPs and 0.1 M PBS. This can be attributed to natural agglomeration of the bacterial cells hence influencing the diffusion rates of the NPs towards the electrode surface. This significantly influenced the current magnitude due to the shielding effects resulting from the insulating sheath of the agglomerated bacterial cells on the electrode surface (2014; Kätelhön *et al.*, 2014; Couto *et al.*, 2018).

The oxidation of Au^0 to Au^{3+} also occurred at approximately close potential as the ST signal. This confirmed that the overlap between the oxidation of thiamine pyrophosphate (TPP) abundant in the transketolase pathway and Au^0 in ST and bimetallic nanostructure respectively played a synergistic role in the bacterial detection. The DPV results showed more intense and resolved oxidation peaks centered at + 0.99, +0.80 and +1.20 V due to the interactions between ST and Ag, Au and Ag-Au (1:2) NPs, respectively (**Figure 6.3 d**).

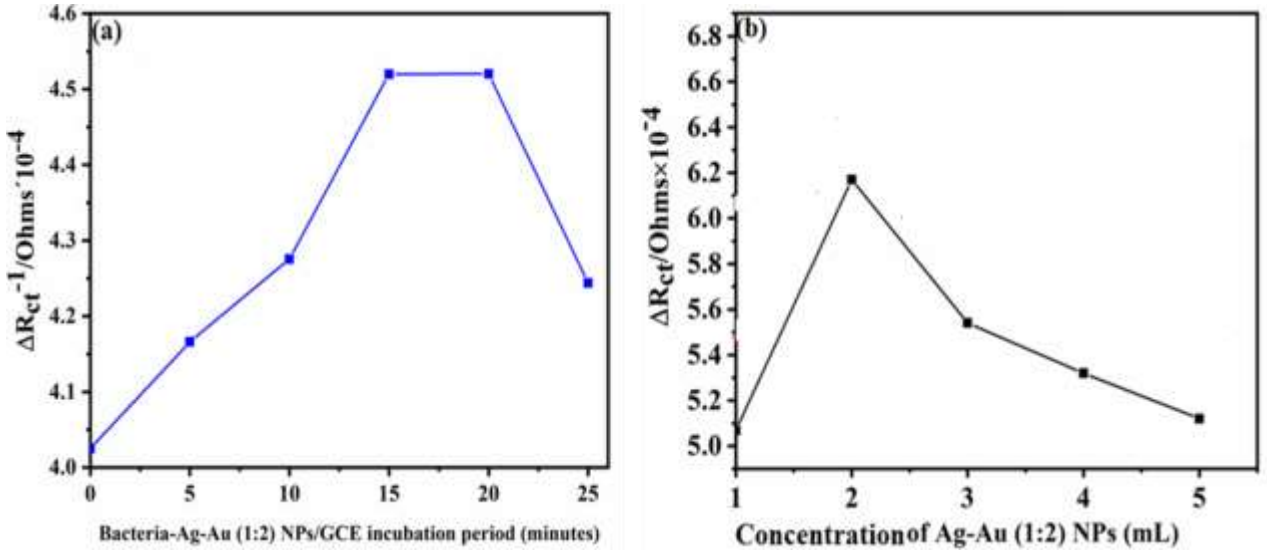

Figure 6.4: Effects of (a) incubation period (b) concentrations of Ag-Au (1:2) NPs on interaction between *S. typhimurium* (ST) and Ag-Au (1:2) NPs in 0.1 M PBS at pH 7.4 studied using EIS technique

The oxidation peak due to the bimetallic NPs shifted towards more positive potentials compared to the monometallic NPs as earlier observed in CV. The peak current intensity was also higher than those of the monometallic NPs. The shift to higher potential can be due to the influence of applied pulse electric field (PEF) on the bacterial membrane structure as the bacterial cells interact with the NPs (Yun *et al*., 2016). PEF treatment in *S. typhimurium* induces a decrease in membrane fluidity due to the alterations of fatty acid membrane structures associated with the bacterial gene expressions (Yun *et al*., 2016). This in turn leads to the death of bacterial cells hence the formation of electron transfer barriers on the electrode surface.

The current intensity of ST peak increased with Ag-Au (1:2) NPs concentrations and bacteria-bimetallic NPs incubation period (**Figure 6.4**). This suggested that diffusible mediators derived from the bacterial cells enhanced conduction of electrons hence the observed increase in peak

current intensity with increasing bacterial concentrations (Herrero-Hernandez *et al*., 2019; Kiran & Patil, 2019). This confirmed that the signals observed were due to the presence of the bacteria.

6.3.4 Effects of supporting electrolyte concentration

The peak due to the oxidation of the bacterial proteins in 0.1 M PBS was well resolved with the highest peak current intensity (**Figure 6.5**) and minimum background currents attributable to excellent electrical conductivity. Therefore, 0.1 M PBS was chosen for further Ag-Au (1:2) NPs-*S. typhimurium* interaction studies.

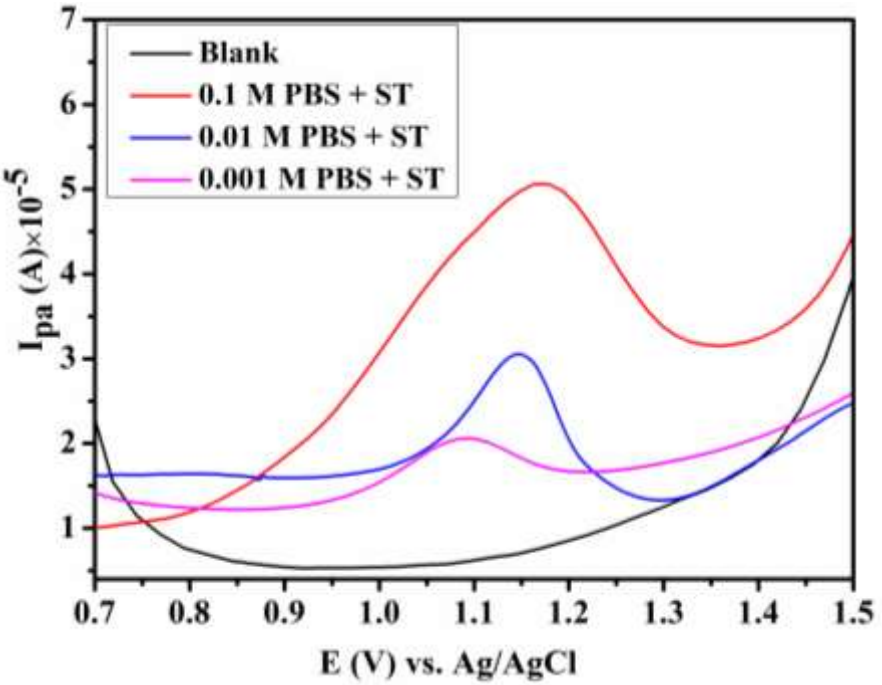

Figure 6.5: Optimization of PBS concentration for nano-impact detection of *S. typhimurium* (ST)

6.3.5 Choice of electro-analytical technique for detection of *S. typhimurium*

All the techniques investigated for nano-impact detection of the bacteria showed increased charge transfer with increasing bacterial concentrations (**Figure 6.6**). This indicated that all the electro-analytical techniques studied were suitable for the development of the nano-impact sensor for the bacteria. However, the slope obtained for EIS interaction studies was the greatest indicating that EIS had the highest sensitivity and therefore, was chosen for further bacteria-bimetallic NPs interaction studies.

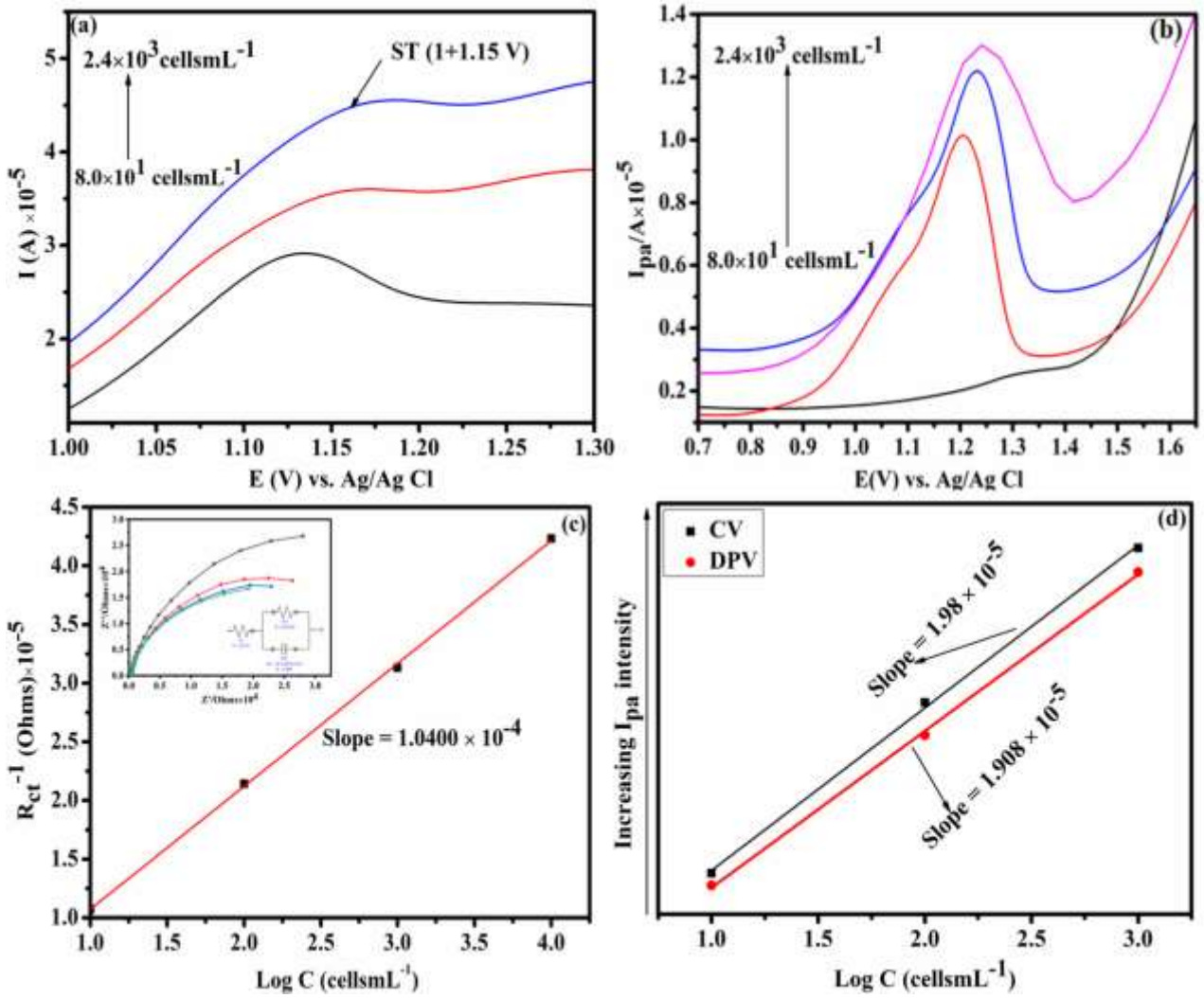

Figure 6.6: (a) CV, (b) DPV, (c) Nyquist plot (inset) and (d) determined sensitivities for Ag-Au (1:2) NPs-ST interaction studies using CV and DPV techniques

6.3.6 Determination of electron transfer kinetics parameters

Cyclic voltammetry (CV) was used to determine the effects of scan rates on electro-oxidation of the bacterial membrane proteins. The oxidation peak currents increased linearly with square root of scan rate: I_{pa}= 8.914E-07$V^{1/2}$ - 2.667; (R^2 = 0.9966). This showed that the bimetallic NPs-bacteria interaction was mainly controlled by diffusion processes. The linearity between oxidation peak potentials and scan rates was determined using *Laviron's* equation **5.1** and the values of α, k_s and n obtained tabulated (**Table 6.2**). The diffusion coefficients (D) was also determined using *Randle's Secvik* equation **5.4** and represented as shown in **Table 6.2**.

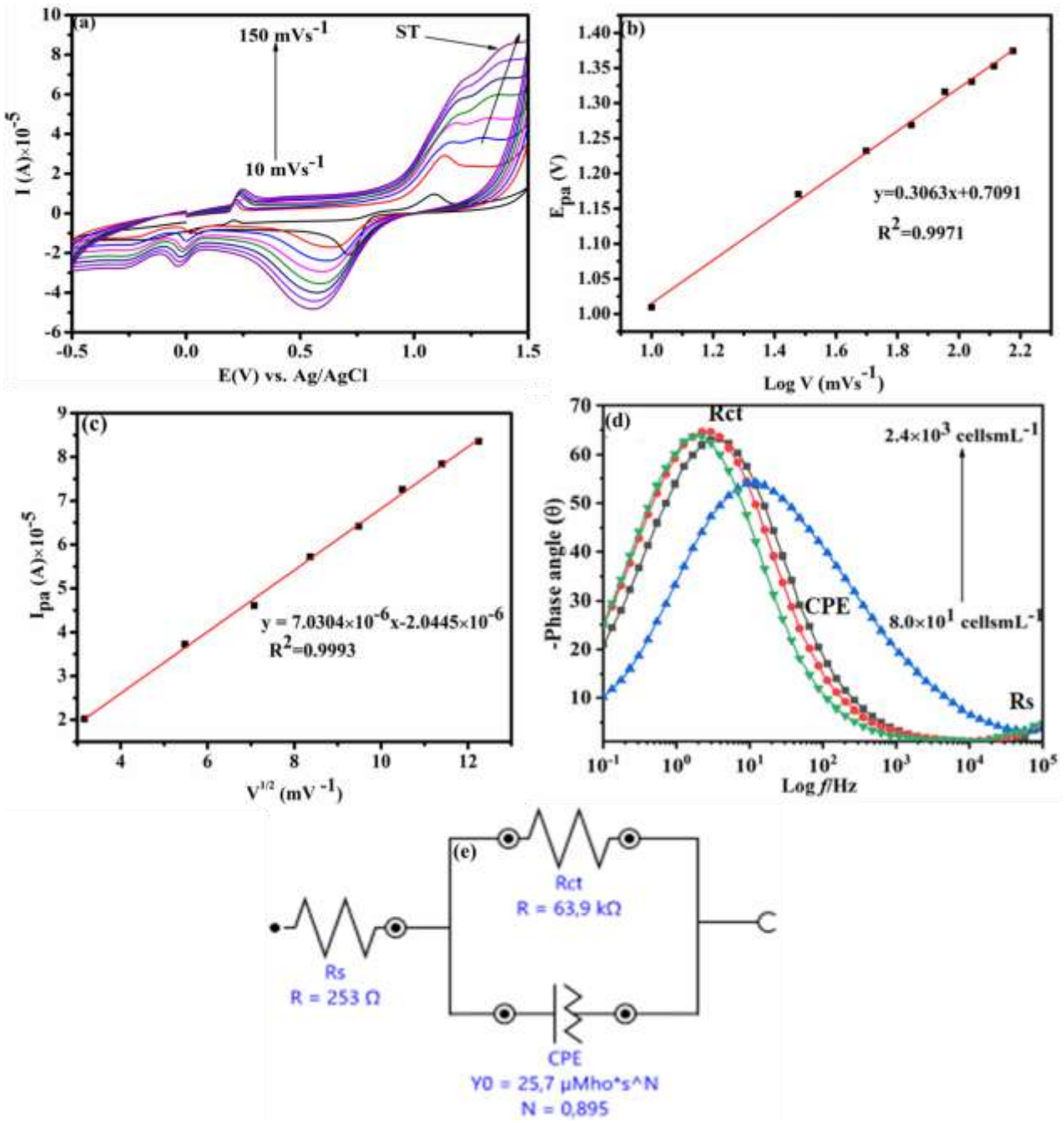

Figure 6.7: (a) Effects of CV scan rates on ST oxidation peak current intensity (b) *Laviron's* plots (c) *Randle's* plots (d) Bode plots (e) *Randle's* equivalent circuit (REC) for Ag-Au (1:2) NPs-ST interactions in 0.1 M PBS, pH 7.4

Table 6.2: Electrochemical kinetic parameters for interactions between Ag-Au (1:2) NPs and *S. typhimurium* in 0.1 M PBS, at pH 7.4

Electrochemical parameters	**CV**	**EIS**
D (cm^2s^{-1})	9.4×10^{-5}	9.13×10^{-4}
α	2.29×10^{-1}	-
Redox activity (moles/bacterial cell)	6.79×10^{-10}	-
k_s (s^{-1})	1.69×10^{-11}	1.54
n	8	7.5

Perfect linear relationship was also obtained between the plots of log V versus E_{pa} with the linear equation: $E_{pa} = 0.3063x + 0.7091$ ($R^2 = 0.9971$). The value of α was determined to be 0.0229 indicating that the electrode surface was more homogeneous thus experienced enhanced bacteria-bimetallic NPs interactions. The value of k_s was calculated to be 1.545×10^{11} s^{-1} showing that the NPs-bacterial interactions had excellent reversibility.

The Bode plots along with the corresponding REC for the interactions between each of the NPs and varying concentrations of *S. typhimurium* are as **Figure 6.7 d**. The obtained plots were analyzed using several possible models of equivalent circuits which were appropriate for the interaction studies between the NPs-bacteria. To the best of our knowledge, no possible equivalent circuit describing the mechanism of interactions between the bimetallic Ag-Au (1:2) NPs and *S. typhimurium* has been reported in the literature. After examining several possible equivalent circuit diagrams for the interaction studies, the experimental data obtained for the bimetallic Ag-Au (1:2) NPs/bacteria interactions were best fitted with the indicated REC over the frequencies ranging of 100 kHz to 0.1 Hz. The REC shown consisted mainly of one R_s in series with one R_{ct} and CPE. The CPE was used to account for the inhomogeneities and defects on the electrode surface. The obtained REC best described the system where non-Faradaic processes occurred which was found consistent with the impedance measurement conditions designed for our experiment. In the REC, R_s describes the bulk electrolyte resistance while R_{ct} represents electron-transfer resistance between bacteria-NPs complex and electrode interfaces. A fitting analysis showed that the equivalent circuit provided fitted the measured data points with an average error of less than 1 % and an acceptable *chi* square (X^2) (**Appendix VIII)** for the bimetallic NPs-bacteria interactions. The fitting and modeling data obtained showed that the values determined for the electrical elements; R_{ct}, R_s and Z_{CPE} for the bimetallic NPs/electrode interactions were: 63.93 ± 0.16 kΩ, 0.25 ± 0.24 kΩ and 2.5742×10^{-5} F, respectively.

The values of R_{ct} R_s and Z_{CPE} changed to 46.02 ± 0.63 kΩ, 0.35 ± 0.32 kΩ and 2.5904 × 10^{-5} F, respectively after the bimetallic NPs-bacteria interactions with a significant decrease in R_{ct} compared to both Z_{CPE} and R_s. The increase in CPE due to the interactions can be attributed to the decrease in Debye-length (Kadan-Jamal *et al*., 2021). The strong surface bacterial charge can also increase the ionic density within the complex formed hence the observed increase in CPE. Direct transfer of electrons from bacterial cells to electrode through membrane bound pili has been reported elsewhere (Nath *et al*., 2021). *S. typhimurium* has pronounced electro-active LPS and protruding pili within its outer membrane which anchor it easily onto the electrode surface hence facilitating electron transfer rates between the bacteria and electrode surface.

Based on the kinetic studies, the proposed mechanism of interaction between *S. typhimurium* and Ag-Au (1:2) NPs (**Figure 6.8**) involved transfer of electrons initiated by the enzyme; transketolase in the bacterial metabolic pathway to the NPs. This enzyme requires thiamine diphosphate (TPP) and a metallic ion as co-factors for the electro-catalysis process.

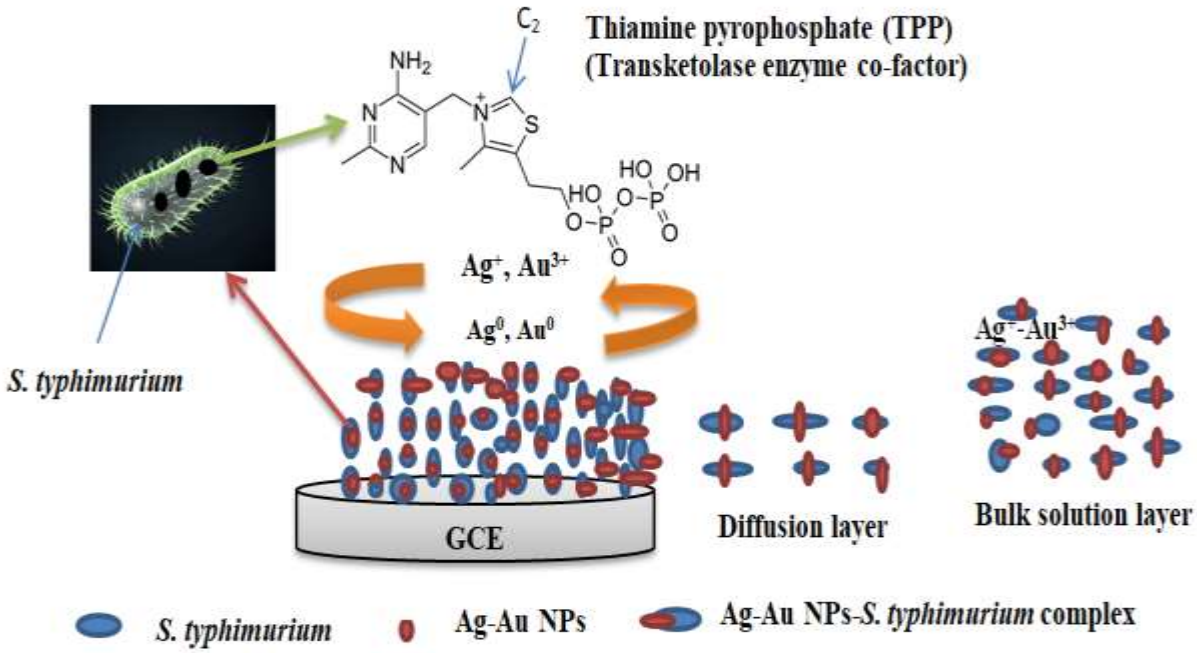

Figure 6.8: Proposed mechanism of interaction between Ag-Au (1:2) NPs and *S. typhimurium*

The interaction between the bacteria and NPs is initiated by application of an oxidizing potential at the electrode as well as the de-protonation of TPP at the thiozolium ring (C_2). The de-protonation leads to the formation of carbanion which binds to the NPs hence forming bacteria-NPs complex. The complex is then bound to the hydrophobic pocket at the interface of two thiozolium sub-units within the enzyme moeity. This reaction takes place within the bulk electrolyte followed by the reduction of the metallic ions (Ag^{+}, Au^{3+}) in the bimetallic NPs. The collision between the complex formed and electrode surface leads to the re-oxidation of the metallic atoms thus generating electrical signals that is detected and quantified. The ability of the enzyme, transketolase to supply electrons to the reduced NPs in solution creates feedback redox cycle mechanism for the metals at the electrode/bacteria-NPs interfacial diffusion layer. This consequently leads to spike in electric currents as the concentration of the bacteria increases. The intensity of the signal produced depends on the concentrations of the NPs and stability of the complex formed. Therefore, the proposed mechanism for the electro-oxidation reactions between the NPs and bacteria conformed to an 8-electron transfer process. This is attributed to the presence of 2 moles of Au^{0} and 1 mole of Ag^{0} requiring a total of 7 electrons for complete electro-oxidation process with the remaining electron neutralizing one of generated H^{+}. This is accompanied by influx of 8 moles of H^{+} ions into the cell so as to decrease the intracellular pH. The regulation of intracellular pH of *S. typhimurium* in this manner through acetylation reaction has been described elsewhere (Ren *et al*., 2015).

6.3.7 Optimization of applied potential and AC amplitude for detection of *S. typhimurium*

The applied potential and AC amplitude were varied between (0.0 to +1.0 V) and (1-15 mV), respectively (F**igure 6.9)**. The ΔR_{ct}^{-1} significantly increased with applied potential and AC amplitude. The ΔR_{ct}^{-1} was significantly highest at applied potential and AC amplitude of + 1.0 V and 5 mV, respectively. Therefore, these optimum conditions were chosen for further bimetallic NPs-bacteria interaction studies.

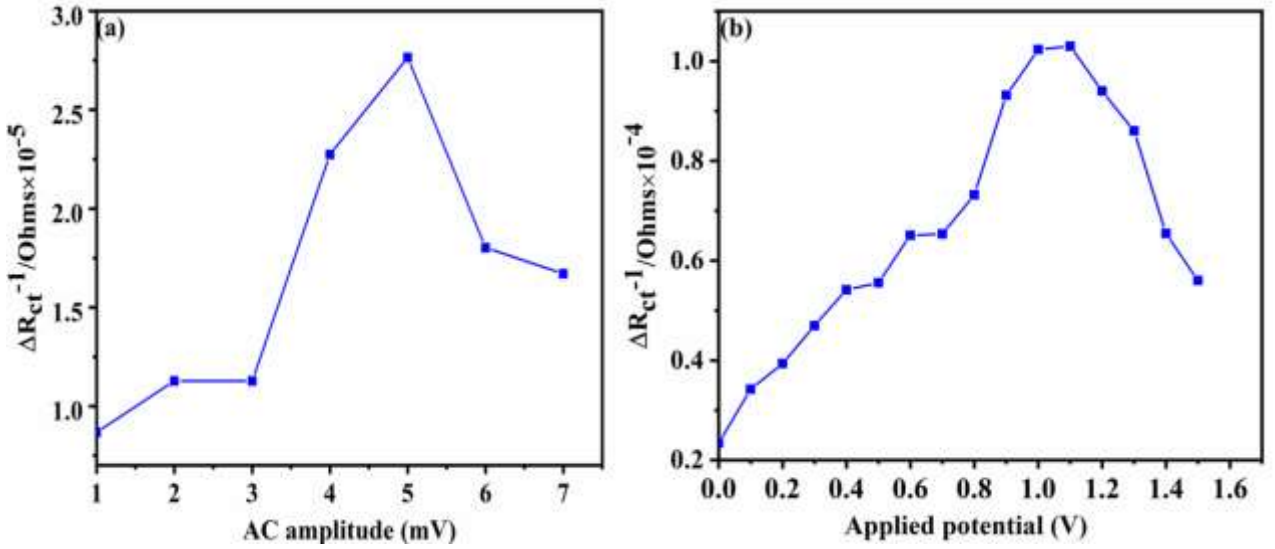

Figure 6.9: Variation of (a) AC amplitude, (b) Applied potential for Ag-Au (1:2) NPs-ST interaction studies

6.3.8 Determination of linearity and applicability of the nano-impact sensor

S. typhimurium standard culture solution (OD_{600nm} = 1.0) was diluted in 0.1 M PBS, pH 7.4 to make various concentrations of the bacterial cells (10^1-10^7). The optical densities (OD) of each of the solutions obtained were determined using spectrophotometric method at OD_{600nm} and the number of bacterial cells (cellsmL^{-1}) present in each of the solutions estimated following a procedure described elsewhere (Couto *et al*., 2018). The dilutions formed were then mixed thoroughly with the NPs and the complexes obtained analyzed using EIS technique at the above described optimum conditions. This was done so as to investigate the effects of increasing concentration of the bacterial cells on ΔR_{ct} during the bimetallic NPs-bacteria interactions.

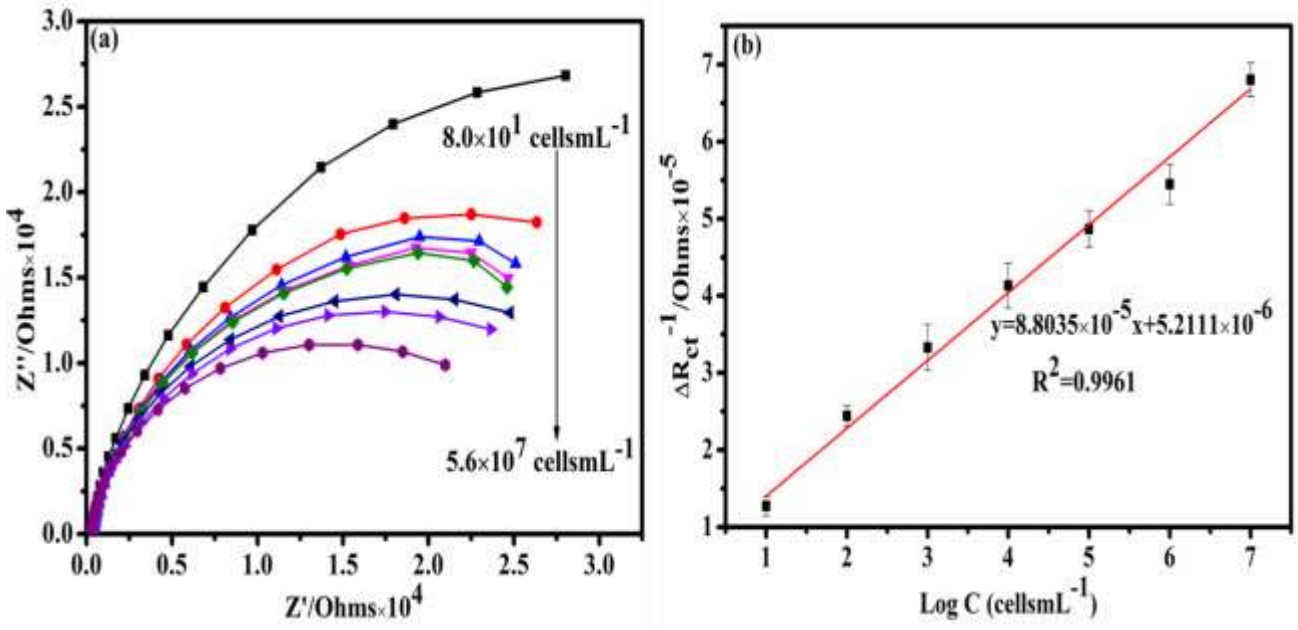

Figure 6.10: a) Nyquist plot (b) calibration plots for the interactions between Ag-Au (1:2) NPs and varying ST concentrations (cells mL^{-1})

The Nyquist plot obtained showed that consecutive additions of the bacterial cells in increasing concentration (10^1-10^7) into the NPs led to an exponential decrease in ΔR_{ct}. A perfect linear relationship between ΔR_{ct}^{-1} and logarithm of bacterial cell concentrations was established in the range of 10^1-10^7 and the limits of detection (LOD) and quantification (LOQ) determined to be 10^1 and 10^3 cells mL^{-1} , respectively using Equations (**5.8** and **5.9**). The equation of the calibration curve for EIS was expressed as $\Delta Rct^{-1}\ (\Omega) = log 8.8035 \times 10^{-6} + 5.2111 \times 10^{-5}$ ($R^2 = 0.9907$).

6.4 Sensor validation

6.4.1 Repeatability, reproducibility, stability and selectivity studies

Repeatability and reproducibility studies of the developed sensor gave % RSD of 1.3 and 3.2, indicating good and acceptable repeatability and reproducibility of the sensor. The precision of the proposed method also gave % RSD value of 2.17 % indicating an acceptable precision for the proposed sensor.

The ΔR_{ct} was maintained at 95 % even after the bimetallic NPs was stored at 4° C in 0.1 M PBS, pH 7.4 for 4 days. The performance of the NPs showed no significant reduction in detection capabilities when used to detect the bacteria in freshly prepared samples.

Under the optimized conditions, the influence of Gram-ve bacteria: *E. coli* (non-target bacteria) on the selectivity of the developed sensor showed that the magnitude of ΔR_{ct} for *S. typhimurium* assay was unaffected (**Figure 6.11 a**) even in the presence of higher concentration of the non-target bacteria.

The ΔR_{ct} for *S. typhimurium* alone (32.78 kΩ) was also significantly lower as compared to both of *E. coli* alone (39.51 kΩ) and a mixture of the two bacteria (17.50 kΩ) indicating enhanced charge transfer due to the presence of *S. typhimurium*. This can be attributed to the ability of *S. typhimurium* to move towards the nanoparticles faster and form a complex compared to *E. coli*. The interaction between the two leads to enhanced charge transfer thus the reduced charge transfer resistance observed. This proved that the developed sensor was selective to *S. typhimurium*. Another possible explanation may be due to the enhanced pathogenicity nature of the bacteria in general (Galán, 2021). This bacterium has been reported to regulate more genes than *E. coli* in a given time thus causing inflammation faster (Blais *et al*., 2015).

The dynamic movement of *S. typhimurium* towards the nanoparticles leads to current response over-powering those from *E. coli* thus the sensor turns electric current responses specific to that of *S. typhimurium* faster. The qualitative and quantitative determination of *S. typhimurium* assays using the proposed nano-impact sensor integrated with EIS technique displayed enhanced sensitivity and wider dynamic linear range. However, to the best of our knowledge, no study has been reported on nano-impact electrochemical detection of *S. typhimurium* using Ag-Au (1:2) NPs in 0.1 M PBS at pH 7.4 under the optimized experimental conditions. Therefore, our developed nano-impact sensor might satisfy the requirements for effective and sensitive detections of low concentrations of *S. typhimurium* in water due its lower LOD.

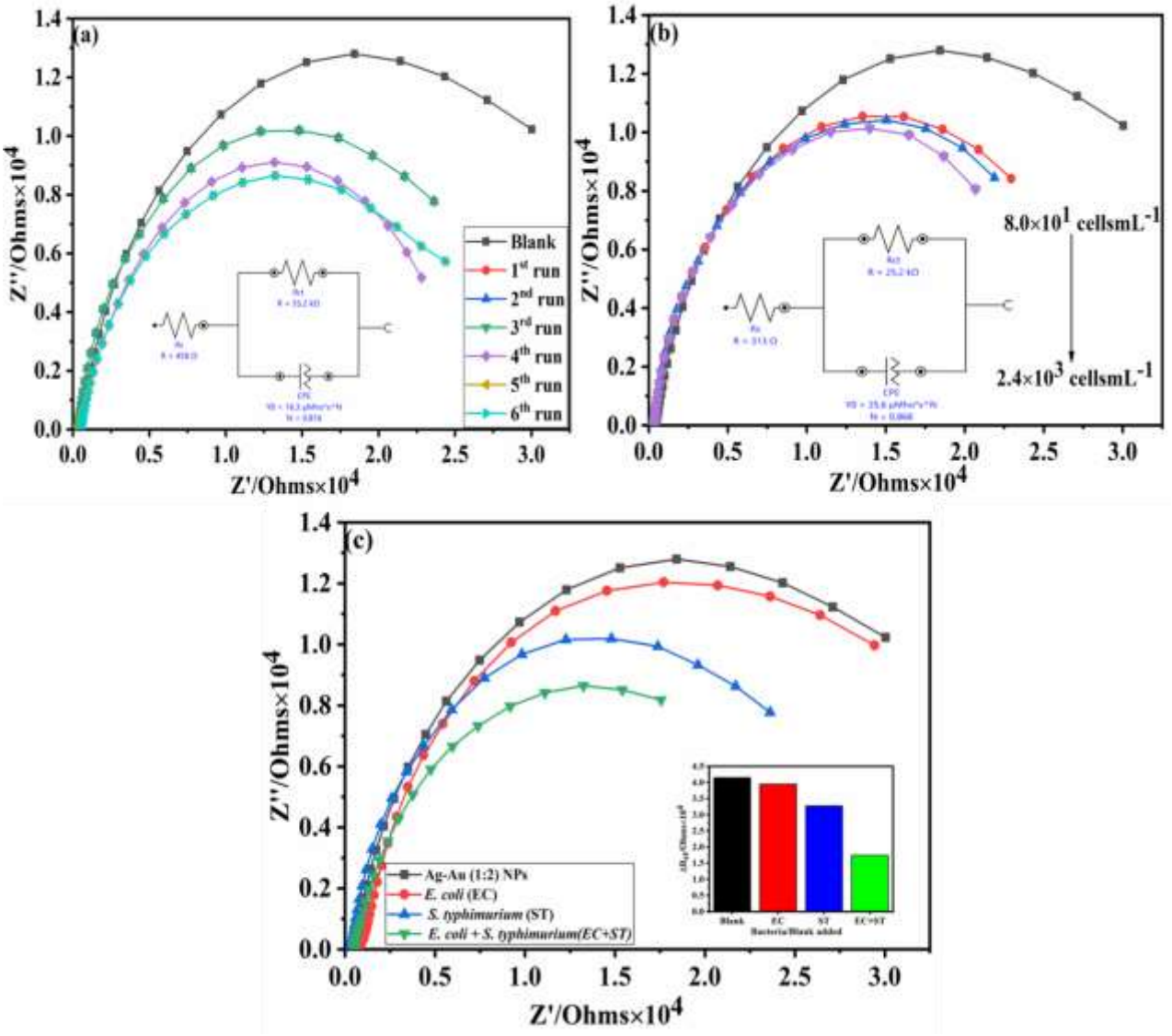

Figure 6.11: Nyquist plots for (a) repeatability; (b) stability; and (c) selectivity studies of the developed sensor

6.4.2 Recovery studies

The % recoveries of the proposed method for the detection of *S. typhimurium* were in the range of (95.28 ± 0.41 - 110.65 ± 0.11) % FJ (n = 3 and (98.20 ± 0.10 - 113.17 ± 0.29) % TW (n = 3) with significantly lower % RSD of (1.04 - 3.15) % and (1.20 - 2.32) % for FJ and TW, respectively. These higher % recoveries obtained showed that the developed electrochemical

detection strategy for the bacteria was accurate and can be applied in real sample analysis with minimum interferences.

6.4.3 Application of the nano-impact sensor to real sample analysis

The results obtained showed that the concentration of bacterial cells detected in spiked River and Ocean water samples analysed were in the range of $2.17 \times 10^6 \pm 950$ and $2.31 \times 10^7 \pm 230$ cells mL^{-1}, respectively. These results obtained indicated that the accuracy of the assay is satisfactory hence the strategy has higher potential for monitoring *S. typhimurium* in practical samples with acceptable accuracy and rapidity.

6.5 Bacteria-NPs interaction studies using IDEA

The CV of IDAE and Ag-Au (1:2) NPs in the presence and absence of *S. typhimurium* (ST) is as shown in **Figure 6.12**.

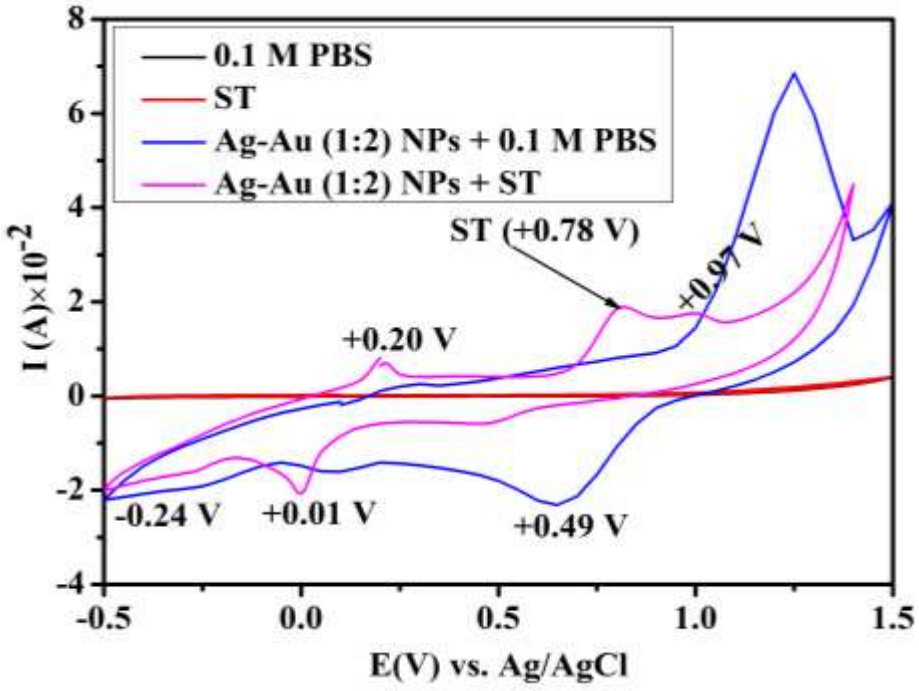

Figure 6.12: Cyclic voltammogram of Ag-Au (1:2) NPs in the absence and presence of ST in 0.1 M PBS at pH 7.4, Scan rate; 0.03 Vs^{-1}

The CV of Ag-Au (1:2) NPs in the absence of *S. typhimurium* displayed two anodic and three cathodic peaks at closely same potentials as earlier described for the nano-impact detection of the bacteria using GCE. However, in the presence of the bacteria, a more enhanced and visible irreversible oxidation peak labeled as ST was observed at +0.78 V. This peak was, however, absent in the blank (IDAE) indicating that it was due to the presence of the bacteria. The peak potential of ST significantly shifted towards less positive value with enhanced oxidation peak current intensity compared to the one observed in GCE. The reduction (E_{pc}) and oxidation (E_{pa}) peak potentials of Ag and Au within the bimetallic NPs in the presence of the bacteria were +0.20, +0.01, +0.97, +0.49 and -0.24 V. These potentials significantly shifted to less positive values relative to those observed in GCE. This can be attributed to various factors including the smaller size nature of the electrode and its micro-holes (10 µm), bacteria cells (1 - 3×0.5-0.6 µm) and Ag-Au (1:2) NPs (0.01 µm). This ensured close contact between the electrode surface and the bacteria-NPs complexes formed thus increased the surface area for the interactions leading to faster rate of electron exchange reactions. This in turn led to the prounced peak current intensity observed.

6.5.1 Determination of electron transfer kinetic parameters

The CV results for the interaction between the bacteria and bimetallic NPs showed oxidation peak currents increasing linearly with the square root of the applied scan rate (**Figure 6.13**).

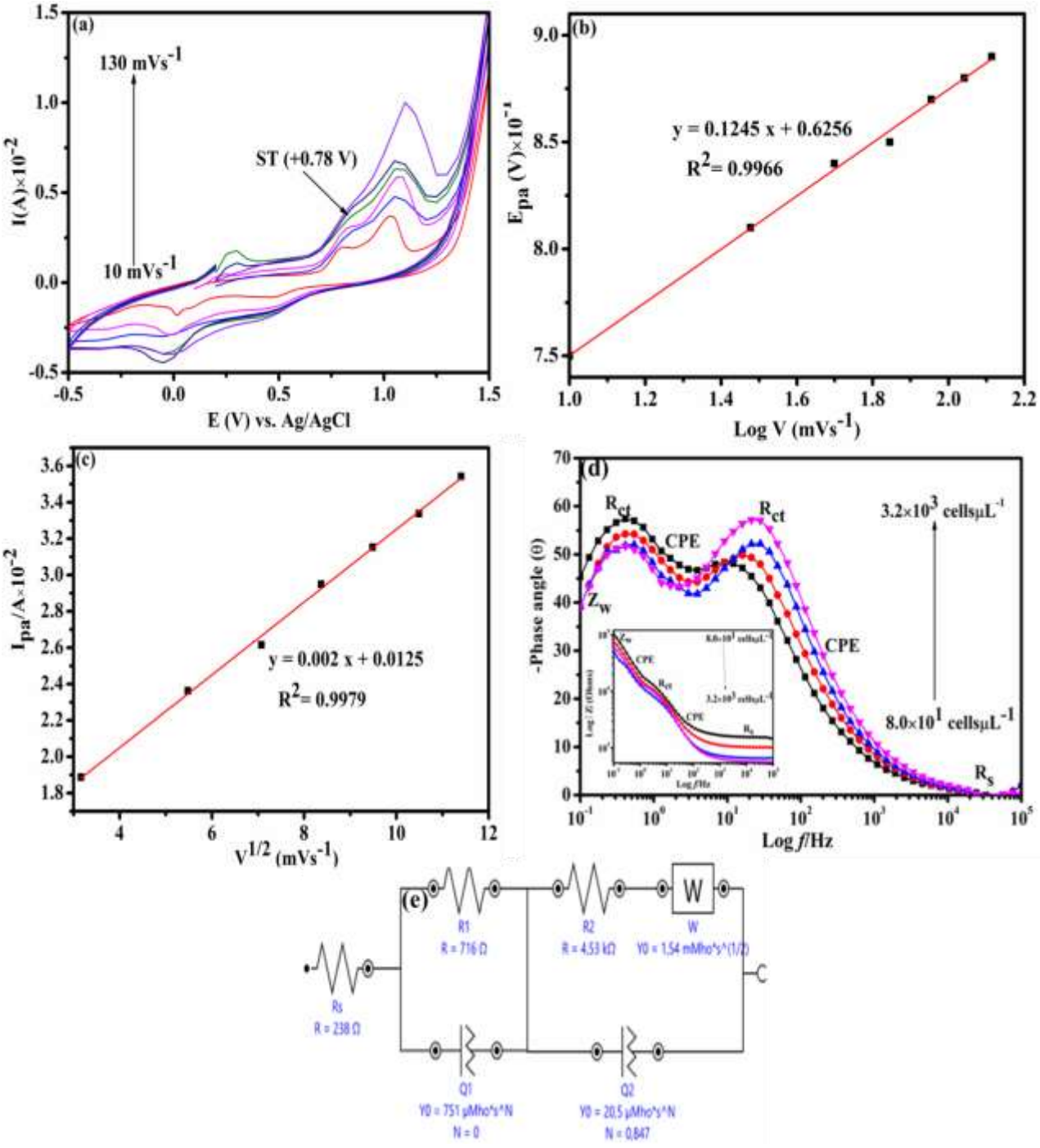

Figure 6.13: (a) CV scan rates studies on ST oxidation peak current, (b) *Laviron's* plot (c) *Randle's* plot (d) Bode plots (e) *Randle's* equivalent circuit for the interactions between Ag-Au (1:2) NPs and ST.

The linear equation for the relationship between the oxidation peak current and $V^{1/2}$ was represented as; I_{pa} (A) = 0.002 V (Vs^{-1}) + 0.0125; (R^2 = 0.9979) indicating that the reactions were largely controlled by diffusion processes.

The peak potentials at different scan rates also slightly shifted to less positive values compared to those obtained using GCE. This can possibly be attributed to increased surface area of the bacteria and IDAE due to their smaller sizes. The increased surface area enhanced the interaction rates between the bacteria and bimetallic NPs.

Laviron's equation **5.1** was used to determine the electrochemical parameters**:** α, n and k_s while the diffusion coefficient (D) was calculated using *Randle's Secvik* equation **5.2** and the values obtained tabulated (**Table 6.3**). These values were significantly enhanced relative to those obtained using GCE attributable to increased surface of IDAE. This increased the rate of bacteria-bimetallic NPs interactions.

Table 6.3: Electrochemical kinetic parameters for interactions between Ag-Au (1:2) NPs and ST on IDAE in 0.1 M PBS, at pH 7.4

Electrochemical parameters	**CV**
D ($\mu m^2 s^{-1}$) $\times 10^{-12}$	5.1204
$\alpha \times 10^{-1}$	0.5000
k_s (s^{-1})	0.8842
n	1.5

The measured EIS spectra obtained showed progressive development of an electrochemical system where electrode polarization was due to combination of diffusion and kinetic electrode processes **(Figure 6.13 d)**. Based on the general electronic equivalent model of any electrochemical system and the behavior of IDAE, REC comprising one R_s, two R_{ct}, two C_{DL} represented as CPE (Q_1) and a Warburg impedance (Z_w) was considered for the simulation of the measured spectra. The R_s represented the resistance to electron flow due to the electrolyte (0.1 M PBS, pH 7.4); the two R_{ct} were attributed to the resistance to electron flow due to the formation of two double layers of non-conductive materials formed as a result of interactions between the bacteria and bimetallic NPs.

This is in agreement with the presented Bode phase angle (**Figure 6.13 d**) which exhibited two well defined slopes in the lower frequency regions. The simulated and fitted data for the spectra showed that the values of the electrical elements due to bimetallic NPs-IDAE interactions were: 5.22 ± 0.10 kΩ (R_{ct}), 0.83 ± 0.02 kΩ (R_s), 2.0×10^{-4} F (Z_{CPE}) and 1.1×10^{12} µF (Z_w). The fitted data significantly agreed with the measured data as shown by lower value of X^2 (0.02) and the estimated error which was below 1 % (**Appendix IX)**. The values of R_{ct} and R_s decreased to 4.27 ± 0.10 and 0.78 ± 0.01 kΩ, respectively after bimetallic NPs-bacteria interactions with significantly low X^2 (0.01).

In the cicuit model, two C_{DL} and R_{ct} are in series with the R_s and Z_w. Both (Z_w and R_{ct}) and (C_{DL} and R_s) significanlty influenced the impedance changes due to bacteria-NPs interactions at lower and higher frequencies, respectively. This was found to be in agreement with the phase angle plots (**Figure 6.13 d**) which exhibited a shape that can possibly be associated with combined kinetic and diffusion dependent electrode processes. The plots also had two distinct slopes attributable to the occurrence of two C_{DL} and two R_{ct} between the bacteria-bimetallic NPs/IDAE interfaces.

Closely similar observation was reported elsewhere (Mallén-Alberdi *et al.*, 2016). This indicated that the bacteria-NPs interactions at frequency range $10^{-1} – 10^2$ was capacitive in nature and hence the appearance of the two distinct slopes. The significant decrease in the slope at frequencies > 10^2 Hz can be ascribed to the resistance from the IDAE surfaces (Kim *et al.*, 2013; Etayash *et al.*, 2014). The characterististics of the *S. typhimurium*-bimetallic NPs interactions spectra described above along with their REC clearly showed that the release of electro-active species into the suspension significantly decreased the impedance magnitude with increasing bacterial concentration as similarly described elsewhere (Nguyen *et al.*, 2014).

6.5.2 Optimization of NPs-bacteria incubation period and NPs concentration

The interaction between same concentrations of the bacteria and varying volumes of bimetallic NPs (100-1000 µL) increased the ΔR_{ct}^{-1} upto 600 µL above which there was significant decrease in ΔR_{ct}^{-1} upto 1000 µL (**Figure 6.14 a**). The increase in impedance above 600 µL suggested that the bacteria-bimetallic NPs suspension became less conductive due to the depletion of the bimetallic NPs. The bacterial cytoplasmic membrane is composed of roughly equal proportions of lipids and protein with the phospholipids as the main components (Strahl & Errington, 2017). Therefore,

increased volume of the bimetallic NPs decreases the number of negatively charged functional groups on the bacterial membrane proteins and phospholipids hence the observed increase in impedance with increasing NPs volume. Therefore, 600 µL was chosen for further bacteria-bimetallic NPs interaction studies.

ΔR_{ct}^{-1} generally increased with time upto the 5th minute (**Figure 6.14 b)**. Further increase in incubation time led to almost stable value for ΔR_{ct}^{-1} indicating increased effective interactions between the bacteria and NPs with increasing incubation period. Increased incubation time above 5 minutes led to maximum saturation of the membrane surface with the NPs hence reducing the number of active sites on the bacterial membrane. Therefore, 5 minutes was chosen as the incubation period for further bacteria-bimetallic NPs interaction studies.

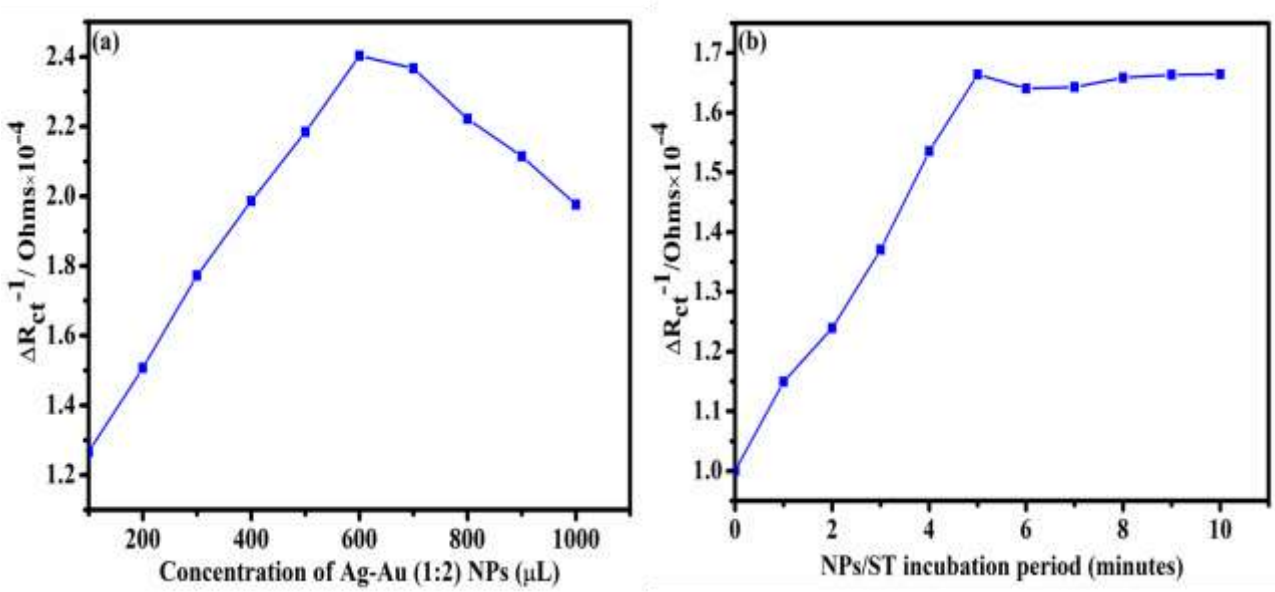

Figure 6.14: Effects of (a) Ag-Au (1:2) NPs concentration, (b) Ag-Au (1:2) NPs-ST incubation period on bacteria-bimetallic Ag-Au (1:2) NPs interaction studies using IDAE

6.5.3 Optimization of AC amplitude and applied potential for detection of *S. typhimurium* using IDAE

Increasing the AC amplitude from (1-15) mV significantly led to an increase in ΔR_{ct}^{-1} upto 10 mV above which ΔR_{ct}^{-1} became constant with increasing AC amplitude upto 15 mV (**Figure 6.15 a**). This can possibly be ascribed to equal charge distribution between the bacterial membrane and electrode surface. The applied potential was varied between - 0.3 and +1.0 V. Increasing the

potential from -0.3 to +0.8 V, led to a significant increase in ΔR_{ct}^{-1} upto +0.5 V (**Figure 6.15 b**). Above +0.5 V, ΔR_{ct}^{-1} significantly decreased upto +1.0 V. This indicated that an increase in applied potential above + 0.5 V disrupted the charge distribution on the bacterial membrane. This in turn might have led to poor electrical conductivity of the bacterial membrane (Estifaee *et al*., 2019).

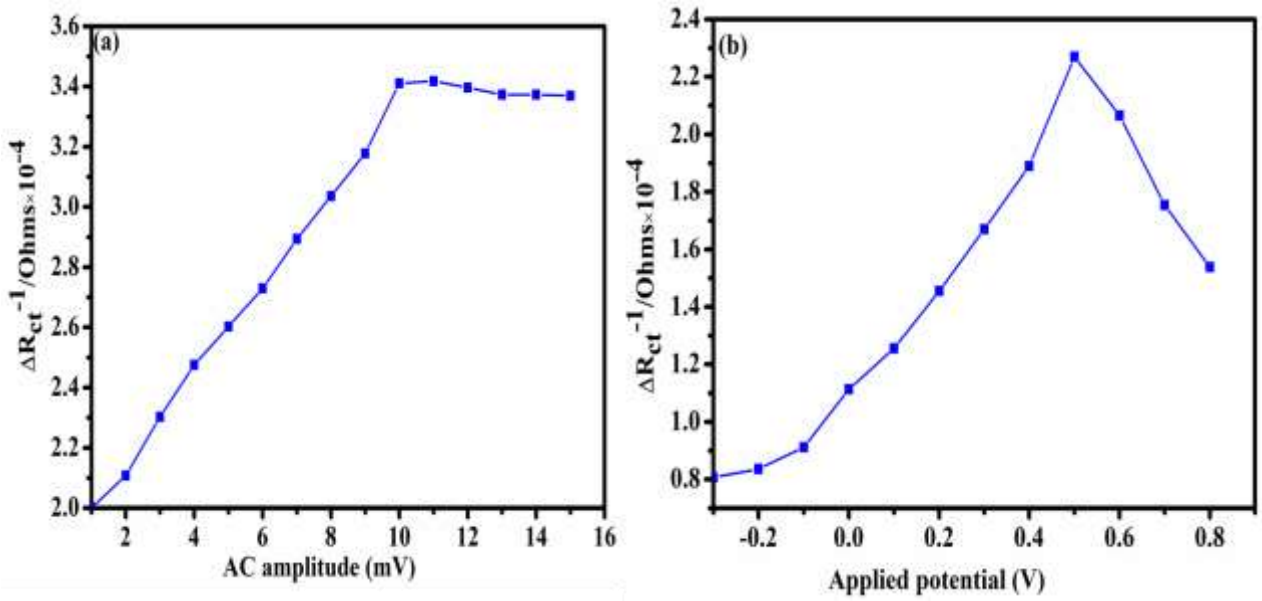

Figure 6.15: Variation of (a) AC amplitude, (b) Applied potential for the interaction between *S. typhimurium* and Ag-Au (1:2) NPs in 0.1 M PBS studied using IDAE

6.5.4 Determination of analytical performance parameters

The developed nano-impact sensor was exposed to varying concentrations of the bacteria (10^1-10^7 cellsµL^{-1}) in 0.1 M PBS (pH 7.4) so as to determine the effects of increasing the concentration of the bacterial cells on ΔR_{ct}^{-1} under the above optimum conditions. The results obtained were presented as shown in **Figure 6.16.**

The Nyquist impedance spectrum obtained showed that the addition of the bacterial cells in increasing concentration (10^1-10^7) cellsµL^{-1} to the bimetallic Ag-Au (1:2) NPs resulted into a significant increase in ΔR_{ct}^{-1} with a perfect linearity between ΔR_{ct}^{-1} and logarithm of concentration of *S. typhimurium* in the aforementioned concentration range. The calibration curve equation was determined as $\Delta Rct^{-1}\ (\Omega) = log 1.3659 \times 10^{-5} x + 1.4707 \times 10^{-4}\ (R^2 = 0.9955)$. The LOD and LOQ were calculated as $10^{1.1946}$ and 10^3 cellsµL^{-1}, respectively**.** The observed increase in ΔR_{ct}^{-}

[1] with bacterial concentration can be attributed to various factors including leakage of ions from the bacterial cells through the cytoplasmic membrane, negative adsorption of PBS electrolyte onto the bacterial cells, ion release from the bacterial cells and increased bacterial cell surface charges coupled with osmotic shock.

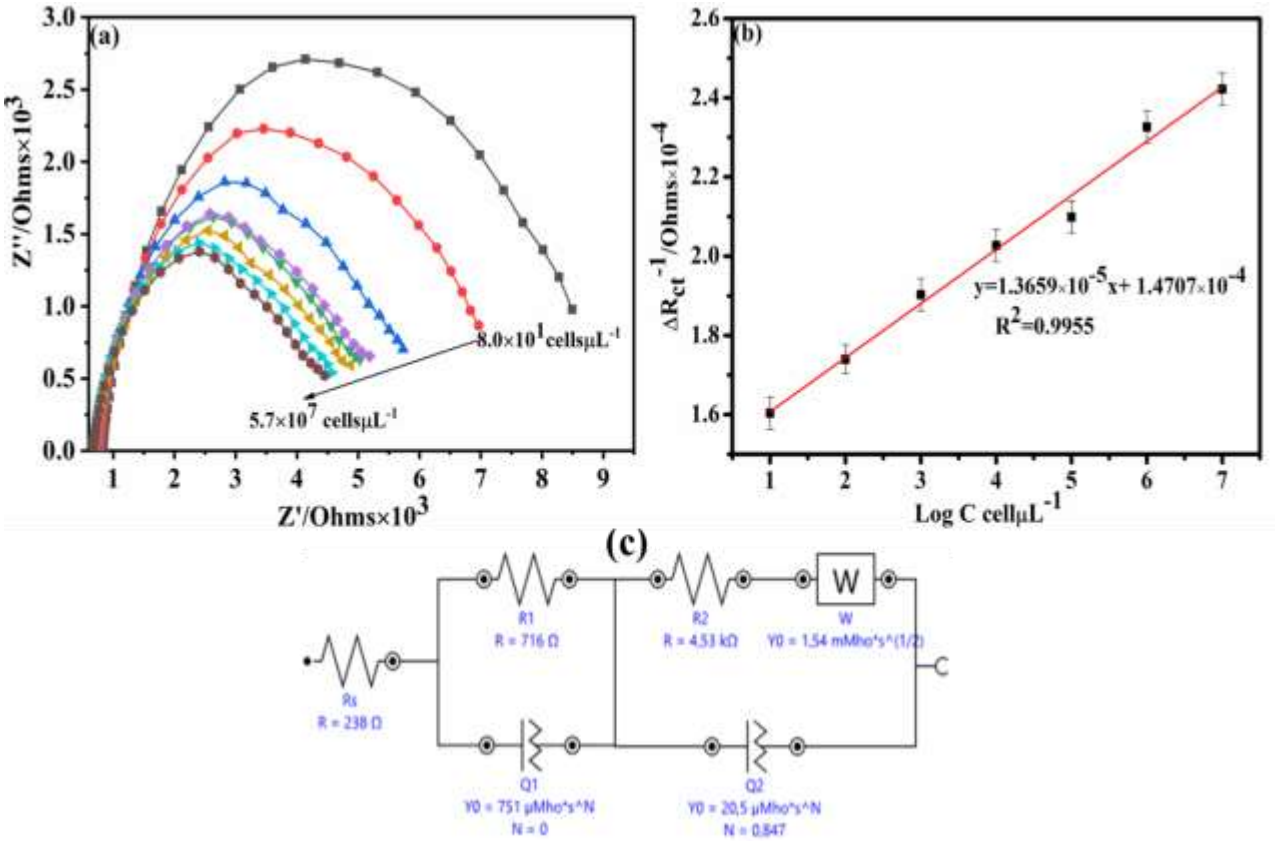

Figure 6.16: (a) Nyquist plot for interactions between Ag-Au (1:2) NPs and varying concentrations (cellsµL^{-1}) of *S. typhimurium*; (b) Calibration plot of ΔR_{ct}^{-1} versus logarithm of *S. typhimurium* concentrations; (c) Corresponding Randle's equivalent circuit.

This is supported by the presented Randle's Equivalent circuit (REC) (**Figure 6.16 c**) which showed one solution resistance (R_s) in series with two charge transfer resistances (R_{ct}), two C_{DL} represented as Q_1 and Q_2, and one Warburg impedance (Z_w). The presence of two charge transfer resistances in the REC clearly indicated the formation of two double layers comprising dead bacterial cells which inturn created electron transfer barriers on the electrode surface as the electrode interacted with the bacteria-bimetallic NPs complexes. This was also in agreement with Bode phase angle plots with two well defined slopes representing the two charge transfer resistances (R_{ct}).

6.6 Validation of IDAE nano-impact sensor

6.6.1 Reproducibility and repeatability studies

Repeatability and reproducibility are two important properties that show the analytical success of sensors. Therefore, repeatability and reproducibility of the proposed nano-impact sensor were investigated. The reproducibility studies of the proposed nano-impact sensor (n = 3) gave % RSD of 2.63 % at bacterial concentrations of 10^3 cellsμL^{-1}. Repeatability studies of the sensor gave % RSD of 1.51 % (n = 6). These results indicated that the proposed interdigitated nano-impact sensor for the bacteria represented good and acceptable repeatability and reproducibility. This indicated that the proposed interdigitated nano-impact sensor for the bacteria represented good and acceptable repeatability and reproducibility.

6.6.2 Stability studies of the sensor

Three similar samples of Ag-Au (1:2) NPs prepared on the same day and stored at 4 °C in 0.1 M PBS (pH 7.4) were used to separately detect the bacteria daily for 4 days under the optimized conditions. There was no significant loss in activity of all the NPs samples after the 4 days of storage. After the 4^{th} day of storage, the IDAE sensor retained 94.76 ± 0.07 % of their initial impedimetric responses. This can be ascribed to the stability of the bimetallic Ag-Au (1:2) NPs used.

6.6.3 Selectivity studies of the sensor

The selectivity of the sensor was investigated by separately incubating 10^3 cellsμL^{-1} of *E. coli*, a mixture of *E. coli* and *S. typhimurium* (1:1, v/v), and *S. typhimurium* alone with the developed sensor and determining the ΔR_{ct} (kΩ) under the optimized conditions. The results obtained were presented as shown in **Figure 6.17.** It was found that the ΔR_{ct} (kΩ) for *E. coli* (11.54 ± 012) alone was higher than that of *S. typhimurium* alone and their mixtures indicating enhanced specificity of the sensor towards *S. typhimurium*.

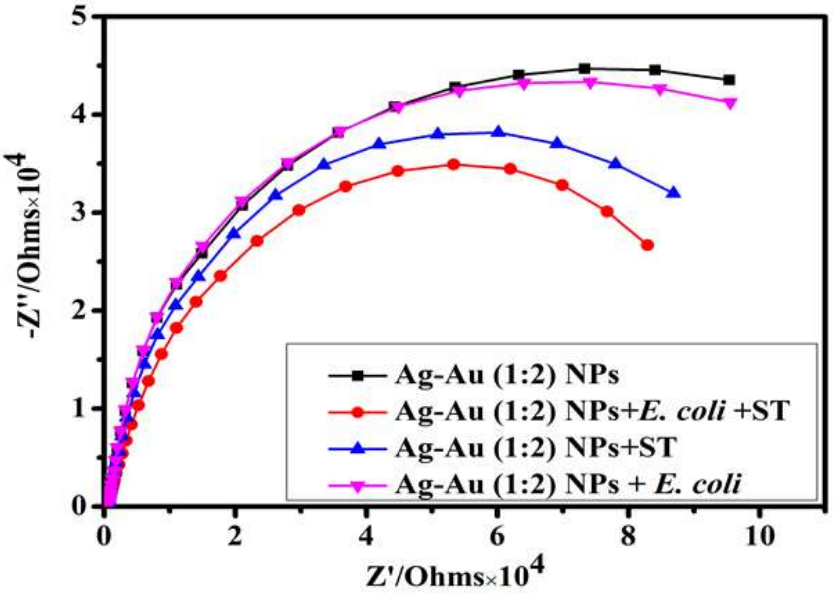

Figure 6.17: Selectivity studies of the sensor

6.6.4 Recovery studies

To demonstrate the practical applicability of the proposed interdigitated nano-impact sensor to real sample analyses, recovery studies on spiked tap water (TW) and fruit juice (FJ) samples were performed. The percentage recoveries ranged between (95.94 ± 010 - 100.00 ± 0.76) % in TW (n = 3) and FJ (n = 3). The % RSD ranging between (0.34-0.78) and (0.85 - 3.6) % for TW and FJ, respectively were also determined. These results showed that the developed interdigitated nano-impact sensor for the bacteria was precise and accurate. To the best of our knowledge, no study has reported these higher percentage recoveries for *S. typhimurium* detections in tap water (TW) and fruit juice (FJ) samples determined using simple and label-free interdigitated bimetallic Ag-Au (1:2) NPs array impact sensors.

6.7 Conclusion

The bacteria-NPs interaction studies revealed an irreversible oxidation peak whose position and intensity were mainly dependent on bacterial concentrations, bacteria-NPs interaction time, sensitivity of electro-analytical technique, electrode-type and size. The peak was more visible and resolved in the DPV with the peak current intensity more enhanced in the bimetallic NPs relative to the monometallic counterparts. This was also supported by the EIS studies which showed significant decrease in charge transfer resistance (ΔR_{ct}) with increasing bacterial concentrations in

both GCE and IDAE interactions. Therefore, highly sensitive, cost-effective and rapid nano-impact sensors integrated with EIS for ultra-sensitive detection of *S. typhimurium* was developed using GCE and IDAE as transducers. The bacteria-bimetallic NPs interactions on IDAE sensor showed excellent electro-catalytic activity coupled with desirable analytical advantages including lower LOD, LOQ, higher sensitivity, good stability and selectivity even in higher concentrations of non-target bacteria: *E. coli* compared to GCE nano-impact sensor. Moreover, the sensor was successfully applied in spiked tap water (TW) and fruit juice (FJ) samples analysis for the bacteria without major sample pre-treatments with significantly higher average % recoveries (95.94 ± 010 - 100.00 ± 0.76). The sensor also had relatively lower % RSD (0.34 - 0.78) and (0.85 - 3.6) for TW and FJ samples, respectively. Therefore, this nano-impact sensor achieved the desirable *S. typhimurium* sensing capabilities with promising applications in monitoring micro-biological qualities of water infested with other Gram-ve bacteria.

6.8 References

Ahmad, A., Wei, Y., Syed, F., Tahir, K., Rehman, A.U., Khan, A., Ullah, S. & Yuan, Q. 2017. The effects of bacteria-nanoparticles interface on the antibacterial activity of green synthesized silver nanoparticles. *Microbial Pathogenesis*, 102: 133–142.

Awang, M.S., Bustami, Y., Hamzah, H.H., Zambry, N.S., Najib, M.A., Khalid, M.F., Aziah, I. & Manaf, A.A. 2021. Advancement in *Salmonella* detection methods: From conventional to electrochemical-based sensing detection. *Biosensors*, 11(9): 346.

Blais, M., Fortier, M., Pouliot, Y., Gauthier, S.F., Boutin, Y., Asselin, C. & Lessard, M. 2015. Colostrum whey down-regulates the expression of early and late inflammatory response genes induced by *Escherichia coli* and *Salmonella enterica Typhimurium* components in intestinal epithelial cells. *British Journal of Nutrition*, 113(2): 200–211.

Couto, R.A.S., Chen, L., Kuss, S. & Compton, R.G. 2018. Detection of *Escherichia coli* bacteria by impact electrochemistry. *Analyst*, 143(20): 4840–4843.

Edis, Z., Haj Bloukh, S., Ibrahim, M.R. & Abu Sara, H. 2020. “Smart” antimicrobial nanocomplexes with potential to decrease surgical site infections (SSI). *Pharmaceutics*, 12(4): 361.

Eloul, S. & Compton, R.G. 2014. Shielding of a Microdisc Electrode Surrounded by an Adsorbing

Surface. *ChemElectroChem*, 1(5): 917–924.

Estifaee, P., Su, X., Yannam, S.K., Rogers, S. & Thagard, S.M. 2019. Mechanism of *E. coli* Inactivation by Direct-in-liquid Electrical Discharge Plasma in Low Conductivity Solutions. *Scientific Reports*, 9(1): 1–12.

Etayash, H., Jiang, K., Thundat, T. & Kaur, K. 2014. Impedimetric detection of pathogenic gram-positive bacteria using an antimicrobial peptide from class IIa bacteriocins. *Analytical chemistry*, 86(3): 1693–1700.

Fanoro, O.T. & Oluwafemi, O.S. 2020. Bactericidal antibacterial mechanism of plant synthesized silver, gold and bimetallic nanoparticles. *Pharmaceutics*, 12(11): 1–20.

Francesco Montesi, V.B. 2015. Study of the Interaction between Silver Nanoparticles and *Salmonella* as Revealed by Transmission Electron Microscopy. *Forest Research Open Access*, 03(01): 10–4172.

French, S., Puddephatt, D., Habash, M. & Glasauer, S. 2013. The dynamic nature of bacterial surfaces: Implications for metal-membrane interaction. *Critical Reviews in Microbiology*, 39(2): 196–217.

Galán, J.E. 2021. *Salmonella typhimurium* and inflammation: a pathogen-centric affair. *Nature Reviews Microbiology*, 19(11): 716–725.

Ghosh Dastider, S., Barizuddin, S., Yuksek, N.S., Dweik, M. & Almasri, M.F. 2015. Efficient and rapid detection of *Salmonella* using microfluidic impedance based sensing. *Journal of Sensors*, 2015.

Herrero-Hernandez, E., Greenfield, D., Smith, T.J. & Akid, R. 2019. Evaluation of the Performance of a Mediatorless Microbial Fuel Cell by Electrochemical Impedance Spectroscopy. *Electroanalysis*, 31(6): 1189–1194.

Kadan-Jamal, K., Sophocleous, M., Jog, A., Desagani, D., Teig-Sussholz, O., Georgiou, J., Avni, A. & Shacham-Diamand, Y. 2021. Electrical impedance spectroscopy of plant cells in aqueous buffer media over a wide frequency range of 4 Hz to 20 GHz. *MethodsX*, 8(11248): 5.

Kätelhön, E., Cheng, W., Batchelor-Mcauley, C., Tschulik, K. & Compton, R.G. 2014. Nanoparticle-Impact Experiments are Highly Sensitive to the Presence of Adsorbed Species on Electrode Surfaces. *ChemElectroChem*, 1(6): 1057–1062.

Kim, G., Moon, J.-H. & Morgan, M. 2013. Multivariate data analysis of impedimetric biosensor responses from *Salmonella typhimurium*. *Analytical Methods*, 5(16): 4074–4080.

Kiran, R. & Patil, S.A. 2019. *Microbial Electroactive Biofilms*. Introduction to Biofilm Engineering. ACS Publications.

Kracke, F., Vassilev, I. & Krömer, J.O. 2015. Microbial electron transport and energy conservation - The foundation for optimizing bioelectrochemical systems. *Frontiers in Microbiology*, 6(JUN): 575.

Leva-Bueno, J., Peyman, S.A. & Millner, P.A. 2020. A review on impedimetric immunosensors for pathogen and biomarker detection. *Medical Microbiology and Immunology*, 209(3): 343–362. https://doi.org/10.1007/s00430-020-00668-0.

Magar, H.S., Hassan, R.Y.A. & Mulchandani, A. 2021. Electrochemical impedance spectroscopy (Eis): Principles, construction, and biosensing applications. *Sensors*, 21(19): 6578.

Mallén-Alberdi, M., Vigués, N., Mas, J., Fernández-Sánchez, C. & Baldi, A. 2016. Impedance spectral fingerprint of *E. coli* cells on interdigitated electrodes: A new approach for label free and selective detection. *Sensing and Bio-Sensing Research*, 7: 100–106. https://doi.org/10.1016/j.sbsr.2016.02.001.

Matoetoe, M., Duya, C., Silwana, B., Shekede, B. & Jabe, Z. 2022. Rapid, Efficient Ag-Au NPs Interdigitated Nano Biosensor Arrays for Water Quality Analysis.

Nath, D., Das, S. & Ghangrekar, M.M. 2021. High throughput techniques for the rapid identification of electroactive microorganisms. *Chemosphere*, 285(13148): 9.

Nguyen, P.-D.D., Tran, T.B., Nguyen, D.T.X. & Min, J. 2014. Magnetic silica nanotube-assisted impedimetric immunosensor for the separation and label-free detection of *Salmonella typhimurium*. *Sensors and Actuators, B: Chemical*, 197: 314–320. http://dx.doi.org/10.1016/j.snb.2014.02.089.

Patra, I., Kadhim, M.M., Mahmood Saleh, M., Yasin, G., Abdulhussain Fadhil, A., Sabah Jabr, H. & Hameed, N.M. 2022. Aptasensor Based on Microfluidic for Foodborne Pathogenic Bacteria and Virus Detection: A Review. *Critical Reviews in Analytical Chemistry*: 1–10.

Ren, J., Sang, Y., Ni, J., Tao, J., Lu, J., Zhao, M. & Yao, Y.F. 2015. Acetylation regulates survival of *Salmonella enterica serovar typhimurium* under acid stress. *Applied and Environmental Microbiology*, 81(17): 5675–5682.

Sargo, C.R., Campani, G., Silva, G.G., Giordano, R.C., Da Silva, A.J., Zangirolami, T.C., Correia, D.M., Ferreira, E.C. & Rocha, I. 2015. *Salmonella typhimurium* and *Escherichia coli* dissimilarity: Closely related bacteria with distinct metabolic profiles. *Biotechnology Progress*, 31(5): 1217–1225.

Shuguang Wang, Lawson, R., Ray, P.C. & Hongtao Yu. 2011. Toxic effects of gold nanoparticles on Salmonella typhimurium bacteria. *Toxicology and Industrial Health*, 27(6): 547–554.

Slavin, Y.N., Asnis, J., Häfeli, U.O. & Bach, H. 2017. Metal nanoparticles: Understanding the mechanisms behind antibacterial activity. *Journal of Nanobiotechnology*, 15(1): 1–20.

Wang-Kan, X., Rodríguez-Blanco, G., Southam, A.D., Winder, C.L., Dunn, W.B., Ivens, A. & Piddock, L.J.V. 2021. Metabolomics reveal potential natural substrates of acrb in escherichia coli and *Salmonella enterica serovar typhimurium*. *mBio*, 12(2): 109–121.

Wang, Ji, Li, H., Li, C., Ding, Y., Wang, Y., Zhu, W., Wang, Jia, Shao, Y., Pan, H. & Wang, X. 2022. EIS biosensor based on a novel *Myoviridae* bacteriophage SEP37 for rapid and specific detection of Salmonella in food matrixes. *Food Research International*, 158: 111479.

Yun, O., Zeng, X.A., Brennan, C.S. & Han, Z. 2016. Effect of Pulsed electric field on membrane Lipids and Oxidative injury of *Salmonella typhimurium*. *International Journal of Molecular Sciences*, 17(8).

CHAPTER SEVEN

CONCLUSION AND RECOMMENDATIONS

7.1 Conclusion

This chapter mainly presents the conclusion of the study based on the main objective and findings. The study addressed five specific objectives. These included; chemical and electrochemical syntheses of monometallic Ag NPs, Au NPs and bimetallic Ag-Au (1:2) NPs, their spectroscopic and electrochemical characterizations which formed the first and second objectives. These objectives were sequentially accomplished and discussed together. The opto-electrochemical interaction studies between the NPs and bacteria formed the optimization steps for the development of the bacterial sensors using glassy carbon (GCE) and interdigitated array (IDAE) electrodes. The last objective entailed sensor validation and applications. Further recommendations of other electrochemical detection strategies for *E. coli* and *S. typhimurium* based on the findings are also highlighted.

The chemical and electrochemical syntheses of Ag NPs, Au NPs and bimetallic Ag-Au (1:2) NPs through citrate reduction and electro-deposition methods were successfully achieved as demonstrated by the reported and discussed spectroscopic and electrochemical data. The UV-visible, FT-IR, SEM and XRD data confirmed the optical and morphological properties while the the electrochemical studies using CV, DPCA, DPV and EIS techniques affirmed the electro-activity of the synthesized NPs.

The UV-visible absorption spectroscopy and the electrochemical techniques; CV, DPV and EIS confirmed the successful interactions between Ag NPs, Au NPs, Ag-Au (1:2) NPs and each of the bacterium as depicted by the observed changes in NPs plasmon bands, absorbance, band gaps, electrode potentials and charge transfer resistances. These interaction studies are dependent on bacterial concentrations, bacteria-NPs interaction time, applied potential, AC amplitude, NPs-type, NPs concentrations, electrode-type and size, surface charge and sensitivity of the electro-analytical techniques. The signals due to each of the bacterium significantly increased with increasing bacterial concentrations and this was more enhanced in bimetallic Ag-Au (1:2) NPs-IDAE integrated with EIS compared to DPV technique. Therefore, ultra-sensitive nano-impact sensors

for *E. coli* and *S. typhimurium* were designed optimized and developed using IDAE integrated with EIS technique.

The interdigitated Ag-Au (1:2) NPs array sensors showed the lowest LOD (10^1 cellsμL^{-1}) and LOQ (10^1 cellsμL^{-1}) for *E. coli* and LOD (10^1 cellsμL^{-1}) and LOQ (10^3 cellsμL^{-1}) for *S. typhimurium* compared to GCE/Ag-Au (1:2) nano-impact sensor. This indicated that the electrode size and geometry significantly enhanced the bacteria- bimetallic Ag-Au (1:2) NPs interactions in IDAE compared to GCE. The reduced sizes of IDAEs significantly improved the surface area for maximum bacteria-bimetallic Ag-Au (1:2) NPs interactions.

The validation of the interdigitated nano-impact array sensors for both bacteria indicated that these sensors had greater possibility of applications in trace environmental analysis of water samples for *E. coli* and *S. typhimurium.* The analysis of these bacteria in spiked tap water (TW) and fruit juice (FJ) samples was rapid with minimal sample preparation. The % recoveries of the bacteria were also significantly higher (95.18 ± 2.50 - 100.00 ± 0.76) and (100.60 ± 0.58 - 116.02 ± 0.15) % for *S. typhimurium* and *E. coli*, respectively. The developed nano-impact sensors are therefore ideal for monitoring these bacteria in real samples such as River and Ocean water.

7.2 Future work and Recommendations

Further studies of concern based on the above findings include the following;

- Integration of silver-gold bimetallic nanoparticles interdigitated array sensor with dielectrophoresis to concentrate the bacterial cells in a microfluidic detection chip. This will further improve the sensitivity of the interdigitated array nano-impact sensor.
- Fabrication and optimization of interdigitated array sensor using bimetallic Ag-Au NPs with different molar ratios of Ag and Au for detections of *E. coli* and *S. typhimurium* in food and water.
- Simultaneous detections of *E. coli* and *S. typhimurium* in water and food using bimetallic Ag-Au (1:2) NPs interdigitated array sensor.
- Application of the bimetallic Ag-Au (1:2) NPs interdigitated array sensor for detections of Gram positive bacteria.

- Validation, testing and specificity studies of the performance of bimetallic Ag-Au (1:2) NPs interdigitated array sensor under non-laboratory conditions.
- Comparative study of sensitivity of bimetallic Ag-Au (1:2) NPs modified interdigitated array sensor and interdigitated nano-impact array sensor for detection of *E. coli* and *S. typhimurium* in water.

8. Appendices

Appendix I: Optimization of PBS concentration for (a) *E. coli* and (b) *S. typhimurium* nano-impact detections using EIS technique

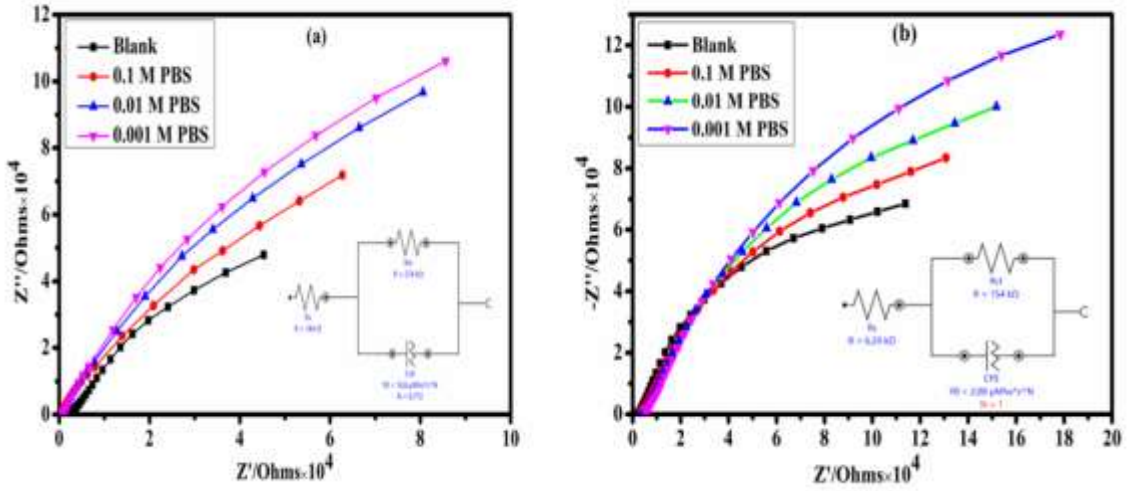

Appendix II: Electrochemical parameters from the circle fitting and modeling of EIS data for the interaction studies between bimetallic Ag-Au (1:2) NPs and varying concentrations (cells mL^{-1}) of *E. coli* in 0.1 M PBS, pH 7.4 using GCE

	R_{ct}(k'Ω)	R_s (k'Ω)	$C_{DL}(10^{-7}$ F)	α	$Z\omega/10^{-5}$ 'Ω)	X^2
Ag-Au (1:2) NPs	22.32±0.34	1.91±1.05	7.96	0.996	2.64	0.020
8.0×10^1 cellsmL^{-1}	9.99±0.08	0.59±0.53	8.70	0.994	2.09	0.093
1.6×10^2 ''	8.63±0.01	0.27±0.03	8.87	0.993	2.24	0.048
2.4×10^3 ''	7.08±0.01	0.30±0.01	8.89	0.992	2.24	0.035

Appendix III: Determination of concentration of *E. coli* and *S. typhimurium* in River and Ocean water samples using standard addition method (n = 3)

Standard solution added (mL)			0	1	1.5	2.0	V_a (mL)	ACP×10^8
BG	ST	BG_1	229.84±46.91[a]	193.45±31.68[a]	182.78±42.43[a]	166.92±43.20[a]	0.41	3.3
		BG_2	5.88±1.25[b]	4.50±0.50[b]	3.98± 0.49[b]	3.58±0.44[b]	0.15	1.2
		BG_3	17.36±4.00[c]	15.03±1.25[c]	14.02±4.71[c]	12.98±1.25[c]	0.21	1.7
	p-value		>0.05					
	EC	BG_1	28.92± 24.12[a]	24.22±23.61[a]	20.85±37.95[a]	18.59±8.18[a]	0.40	3.2
		BG_2	24.85±33.74[b]	22.73±24.06[b]	21.22±20.55[b]	19.57± 8.64[b]	0.60	4.8
		BG_3	26.33± 2.49[c]	23.65±32.29[c]	20.84±8.81[c]	19.28± 8.16[c]	0.20	1.6
	p-value		>0.05					
LR	ST	LR_1	14.88±0.82[a]	13.20±1.25[a]	12.50±0.82[a]	12.00±0.82[a]	0.30	2.4
		LR_2	17.14±0.82[b]	13.30±1.70[b]	12.01±0.82[b]	10.73± 0.82[b]	0.15	1.2
		LR_3	14.39±0.77[c]	10.43±2.49[c]	9.37±0.82[c]	8.38±1.25[c]	0.40	3.2
	p-value		>0.05					
	EC	LR_1	26.64± 28.52[a]	16.89±3.68[a]	13.39±5.89[a]	10.51± 3.27[a]	0.15	1.2
		LR_2	24.32± 2.16[b]	19.21± 2.94[b]	14.51±3.68[b]	12.32± 51.41[b]	0.65	5.2
		LR_3	18.25± 8.96[c]	13.95±4.19[c]	10.50±4.11[c]	8.71±46.42[c]	0.40	3.2
	p-value		>0.05					
SW	ST	SW_1	7.55±1.25[a]	6.36±2.05[a]	5.96±0.65[a]	5.55.20±0.59[a]	0.10	0.8
		SW_2	10.27±1.40[b]	7.90±0.71[b]	7.06±0.51[b]	6.29±1.70[b]	0.05	0.4
		SW_3	21.81±1.63[c]	16.04±1.25[c]	13.93±1.25[c]	12.51± 0.82[c]	0.05	0.4
	p-value		>0.05					
	EC	SW_1	9.52±4.08[a]	8.29±4.85[a]	7.58±1.84[a]	6.93±5.99[a]	0.49	3.9
		SW_2	14.75±4.08[b]	11.19±2.41[b]	8.89±4.78[b]	7.79±3.19[b]	0.40	3.2
		SW_3	15.59±3.17[c]	13.71±1.70[c]	12.20±1.70[c]	11.01± 2.16[c]	0.45	3.6
	p-value		>0.05					

BG-Liesbeek River in Kirstenbosch National Botanical Garden; LR-Liesbeek River in Rondebosch; SW-Seawater; ST-*Salmonella typhimurium*; EC-*Escherichia coli*; GPS-Global positioning system; ACP-Approximated cell population; V_a-Volume of analyte; Similar letters in the same column indicate no significant difference (p<0.05) and vice-versa (p>0.05).

Water sampling locations; BG, GPS: 33.984976796579424, 18.43244033375491;LR, GPS: 33°56’11’’S, 18°28’35’’E 33.936389, 18.476389

Appendix IV: Standard calibration curve for determination of *E. coli* in Liesbeek River water samples collected from Kirstenbosch Botanical Garden, Cape Town, South Africa.

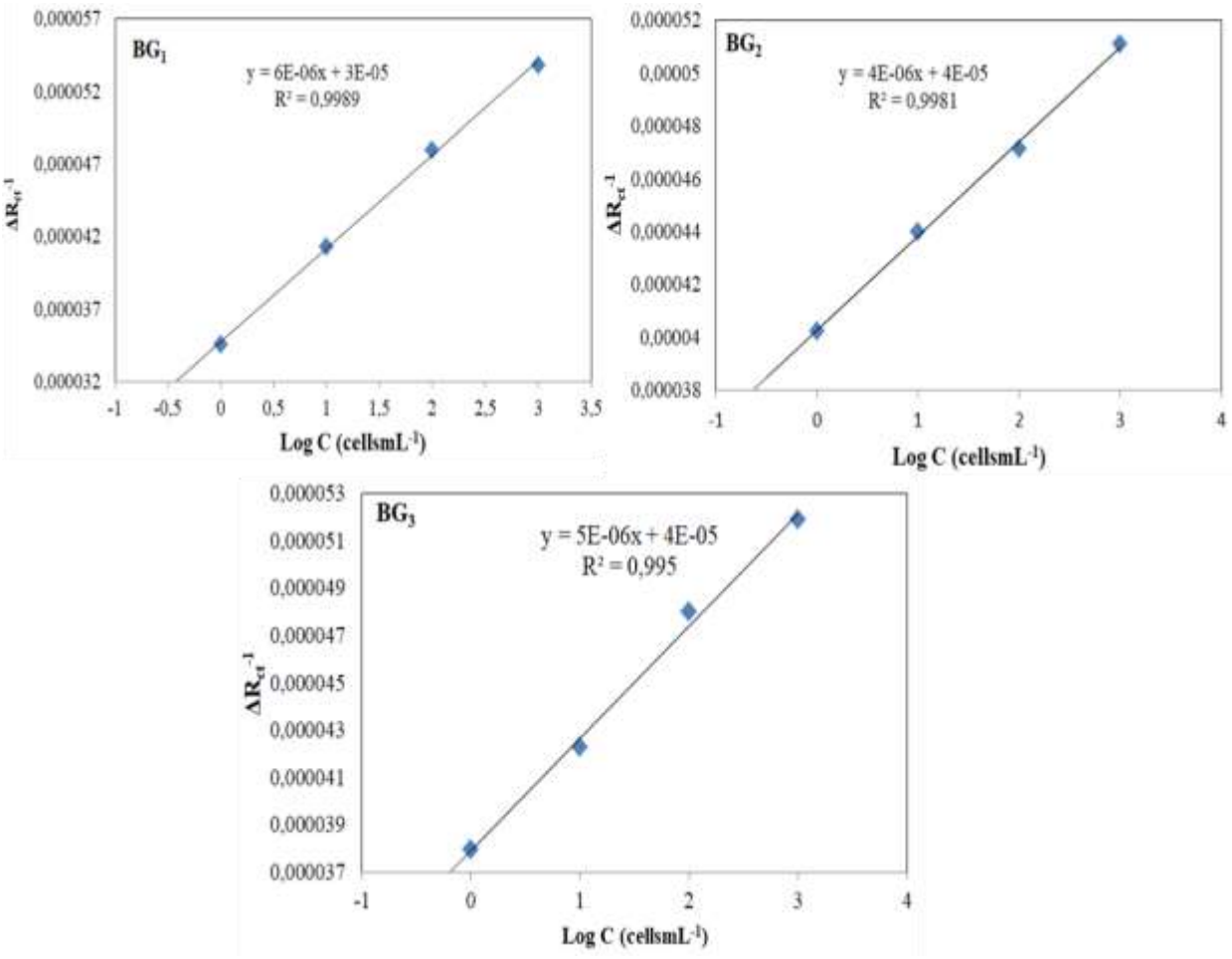

Appendix V: Standard calibration curve for determination of *E. coli* in Liesbeek River water samples collected from Rondebosch, Cape Town, South Africa.

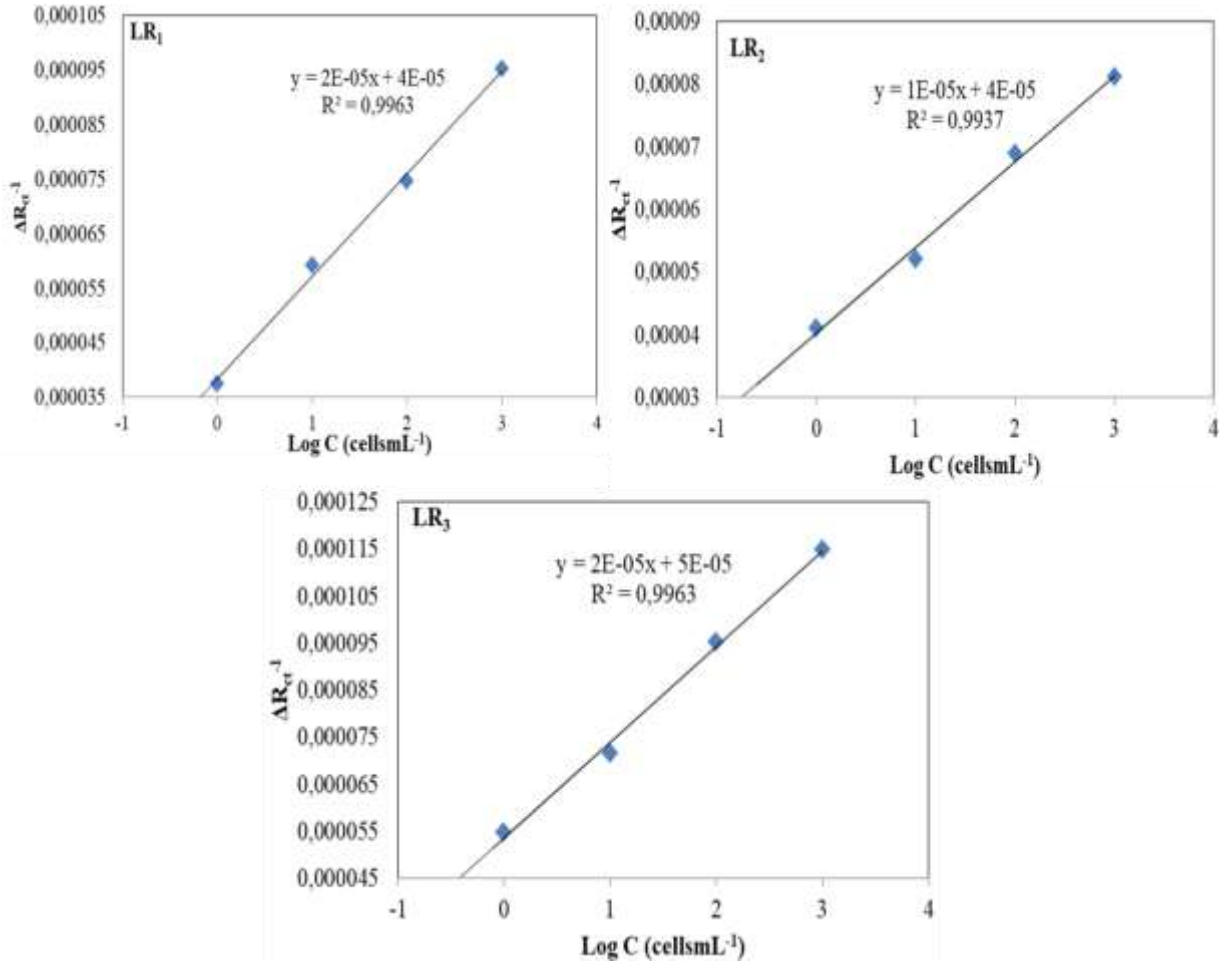

Appendix VI: Standard calibration curve for determination of *E. coli* in water samples collected from Atlantic Ocean, Cape Town, South Africa.

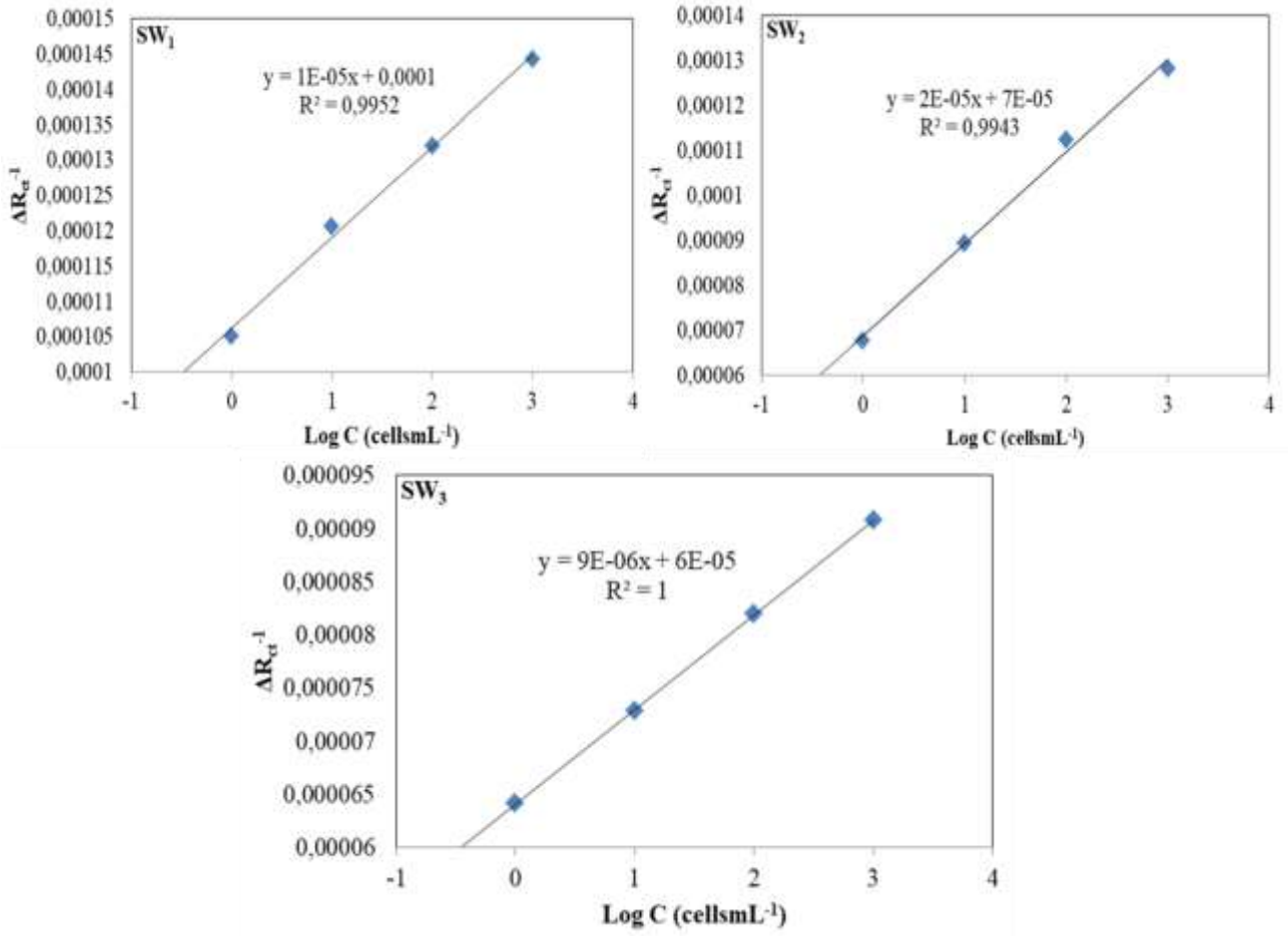

Appendix VII: Electrochemical parameters from the circle fitting and modeling of EIS data for the interaction between bimetallic Ag-Au (1:2) NPs and varying concentrations of *E. coli* (cells μL^{-1}) in 0.1 M PBS, pH 7.4 using IDAE

	R_s(Ω)	R_{ct}(Ω)	$Z_{CPE}\times10^{-6}$ (F)	α	Z_w	X^2
Ag-Au (1:2) NPs	1006.85±0.04	10514.33±1.25	-	0.8347	-	0.0900
8.0×10^1 cellsμL^{-1}	488.00±0.74	89622.00±1.63	3.99	0.8442	0.0001	0.0881
1.6×10^2 ''	514.75±0.01	82215.00±0.82	11.92	0.6448	-	0.0109
3.2×10^3 ''	806.16±0.42	59967.00±0.81	11.39	0.6562	-	0.0263

CPE=$Z_{CPE} = \frac{1}{Y^0(jw)^\alpha}$ where; α - frequency exponent, α = 1 for an ideal capacitor; the estimated errors for all the fitting values were less than 1%.

Appendix VIII: Electrochemical parameters from circle fitting and modelling of EIS data for the interactions between bimetallic Ag-Au (1:2) NPs and varying concentrations of *S. typhimurium* in 0.1 M PBS, pH 7.4 using GCE.

	R_{ct} (kΩ)	R_s (kΩ)	$Z_{CPE}/F\times10^{-5}$	α	X^2
Ag-Au (1:2) NPs	63.93±0.16	0.25±0.24	2.5742	0.8950	0.0437
8×10^1 cellsmL^{-1}	46.02±0.63	0.35±0.34	2.5904	0.8764	0.0460
1.6×10^2 ''	40.95±0.33	0.35±0.32	2.5499	0.8816	0.0543
2.4×10^3 ''	30.02±0.30	0.35±0.31	2.3169	0.9054	0.0840
3.2×10^4 ''	30.00±0.30	0.33±0.23	2.3574	0.8982	0.0992
4.0×10^5 ''	33.72±0.67	0.25±0.25	2.6268	0.8886	0.1176
4.8×10^6 ''	32.81±0.14	0.26±0.18	2.7611	0.8657	0.0413
5.6×10^7 ''	19.21±0.92	0.20±0.53	2.5574	0.9083	0.1711

CPE=$Z_{CPE} = \frac{1}{Y^0(jw)^\alpha}$ where; α -frequency exponent, α = 1 for an ideal capacitor; the errors of the fitting values were all <1%.

Appendix IX: Electrochemical parameters from the circle fitting and modeling of EIS data for the interaction between bimetallic Ag-Au (1:2) NPs and varying concentrations (cellsμL^{-1}) of *S. typhimurium* in 0.1 M PBS, pH 7.4 using IDAE

	R_s (Ω)	**R_{ct} (Ω)**	**$Z_Q\times10^{-3}$**	α	**Z_w**	***X^2***
Ag-Au (1:2) NPs	826.67±0.02	5223.40±0.10	0.02	0.85	1.1×10^{12}	0.02
8.0×10^1 cellsμL^{-1}	779.68±0.01	4268.90±0.10	0.02	0.86	0.0038	0.01
1.6×10^2 ''	237.89±0.01	716.37±0.01	7.51	0.56	0.0015	0.03
3.2×10^3 ''	716.32±0.01	3508.57±0.15	0.02	0.88	-	0.01